Liquid Processing in Rotating Packed Beds

Zur Erlangung des akademischen Grades eines

Dr.-Ing.

von der Fakultät Bio- und Chemieingenieurwesen
der Technischen Universität Dortmund
genehmigte Dissertation

vorgelegt von

M.Sc. Dennis Alexander Wenzel

aus

Berlin

Tag der mündlichen Prüfung: 10.12.2019

1. Gutachter: Prof. Dr.-Ing. Andrzej Górak
2. Gutachter: Prof. Dr.-Ing. Gerhard Schembecker

Dortmund 2020

ABSTRACT

Rotating Packed Beds (RPBs) are one of the most promising concepts for intensified modular equipment in the chemical industry. Based on flexible design and by means of centrifugal force, their operation can be adjusted according to the respective process requirements. Despite the large potential of RPBs, many years of research, and although RPBs have been successfully applied to numerous processes on a pilot scale, their industrial implementation is still scarce. One of the key reasons is that the technology is often considered insufficiently mature, with a particular lack of knowledge in the field of liquid processing.

Therefore, liquid processing in RPBs is investigated experimentally and analytically in this thesis, with respect to liquid phase reactive mixing, liquid-liquid extraction, and liquid-gas processing, in order to further develop the current RPB technology. The applicability of RPBs to these different processes is critically studied and rules of RPB design and operation are deduced.

On this account, the current state of the art is analyzed, and the available methodology is adapted to RPBs. In experimental investigations, the role and importance of liquid distribution design, packing design, and residence time distribution in the apparatus are elucidated. These investigations are complemented by modeling results and a comparison to conventional devices and processes for each respective application.

It is shown that RPBs are especially capable of providing fast liquid processing at high liquid flow rates and high viscosities and offer more operational degrees of freedom than their conventional counterparts. However, their utilization is also restricted based on limitations in the current design. Therefore, guidelines and recommendations for preferable RPB operation, RPB design, and the most reasonable industrial implementation of RPBs are presented, together with an alternative apparatus design.

ZUSAMMENFASSUNG

Rotierende Stoffaustauschmaschinen (Rotating Packed Beds, RPBs) sind eines der vielversprechendsten Konzepte für intensiviertes und modulares Equipment in der chemischen Industrie. Ihr Betrieb kann auf Grundlage eines flexiblen Aufbaus and mithilfe von Zentrifugalkräften an die jeweiligen Prozessanforderung angepasst werden. Trotz des großen Potentials von RPBs, langjähriger Forschungsbemühungen und obwohl RPBs im Pilotmaßstab bereits erfolgreich in vielen Prozessen Anwendung finden, ist eine industrielle Verwendung noch selten. Eine der Hauptursachen ist die verbreitete Einstufung als nicht hinreichend ausgereifte Technologie. Eine besonders gravierende Wissenslücke besteht dabei noch bei Prozessen in der Flüssigphase.

Aus diesem Grund wird die Flüssigkeitsverarbeitung in RPBs in dieser Arbeit experimentell und analytisch untersucht, um die derzeitige RPB Technologie weiterzuentwickeln. Dies geschieht im Hinblick auf reaktive Flüssig-Flüssig-Mischungsprozesse, Flüssig-Flüssig-Extraktionsprozesse und Flüssig-Gas-Prozesse. Die Möglichkeit RPBs für diese unterschiedlichen Prozesse zu verwenden wird kritisch untersucht und Richtlinien zu Auslegung und Betrieb von RPBs werden abgeleitet.

Zu diesem Zweck wird der derzeitige Stand der Technik analysiert und die verfügbare Methodik für Untersuchung in RPBs angepasst. Die Bedeutung von Flüssigkeitsverteilung, Packungsgestaltung, und Verweilzeitverteilung werden auf Basis experimenteller Ergebnisse erläutert. Zusätzlich werden Modellierungsergebnisse vorgestellt und Vergleiche zu konventionellen Apparaten und Prozessen auf dem jeweiligen Gebiet gezogen.

Dabei wird gezeigt, dass sich RPBs insbesondere zur Verarbeitung von großen Flüssigkeitsströmen eignen und mehr operative Freiheitsgrade bieten als konventionelle Apparate. Nichtsdestotrotz bleibt ihre Anwendung auf Grundlage derzeitiger Designeigenheiten eingeschränkt. Aus diesem Grund werden Empfehlungen für den Betrieb und die Auslegung von RPBs, sowie die sinnvolle industrielle Anwendung von RPBs, präsentiert, ergänzt durch die Vorstellung eines alternativen Gerätedesigns.

TABLE OF CONTENT

NOTATION

Latin letters		
A_{outlet}	Cross-sectional area of the nozzle outlet	m^2
a_{ox}	Activity of the oxidized species	-
a_{red}	Activity of the reduced species	-
b	Radial packing depth	m
c	Partial reaction order of H^+	-
C	Reference concentration	mol m^{-3}
C(t)	Tracer concentration at time t	mol m^{-3}
$C_{B,total}$	Total buffer concentration	mol m^{-3}
C_i	Concentration of ion i	mol m^{-3}
C_j	Concentration of species j	mol m^{-3}
$C_{j,1}$	Concentration of species j in liquid volume 1	mol m^{-3}
$C_{j,10}$	Concentration of species j in the surrounding liquid	mol m^{-3}
$C_{j,2}$	Concentration of species j in liquid volume 2	mol m^{-3}
C_{total}	Total reference concentration	mol m^{-3}
$< C_j >$	Mean concentration of species j	mol m^{-3}
d	Optical path length through a sample	m
E	Electrode potential	V
E(t)	Differential distribution curve	-
E^0	Electrode potential against the standard hydrogen electrode	V
F	Faraday's constant	C mol^{-1}
F(t)	Cumulative residence time fraction curve	-
F_g	Gas capacity factor	$Pa^{0.5}$
g	Growth function	-
h	Axial packing height	m
$[i,_0]$	Initial concentration of component i before mixing	mol m^{-3}
[i]	Final concentration of component i after mixing and the occurrence of reactions (i) to (iii)	mol m^{-3}
$[i]_0$	Reference concentration of component i	mol m^{-3}
$[i]_{eq}$	Equilibrium concentration of component i	mol m^{-3}
I	Ionic strength	mol m^{-3}
K_{a2}	Second dissociation constant of sulfuric acid	mol m^{-3}
K_{eq}	Equilibrium constant of reaction (iii)	m^3 mol^{-1}
k_i	Reaction rate constant of n^{th}-order-reaction i	$(m^3\ mol^{-1})^{n-1}\ s^{-1}$

K_i	Capacity of solvent with respect to component i	-
K_La	Volumetric mass transfer rate	s^{-1}
L	Premixed distributor length	m
L_1	Buffer solution	-
L_2	Acid solution	-
LL	Liquid load	$m^3\ m^2\ h^{-1}$
pH	Negative of the base 10 logarithm of the molar acid concentration	-
pH*	Equilibrium pH value	-
$pH_{average}$	Average working pH	-
P	Electric power consumption	W
R	Universal gas constant	$J\ K^{-1}\ mol^{-1}$
r_i	Inner packing radius	m
R_j	Reaction rate of species j	$mol\ s^{-1}\ m^{-3}$
$R_{k,1}$	Reaction rate of a species in reaction k in liquid volume 1	$mol\ s^{-1}\ m^{-3}$
$R_{k,2}$	Reaction rate of a species in reaction k in liquid volume 2	$mol\ s^{-1}\ m^{-3}$
r_k	Reaction rate of reaction k	$mol\ s^{-1}\ m^{-3}$
r_o	Outer packing radius	m
$S_{S/C}$	Selectivity of solvent with respect to solute and carrier	-
t	Time	s
t_{50}	Median of the residence time distribution	s
t_{90}	90^{th} percentile of the residence time distribution	s
t_{100}	Complete residence time	s
t_{DS}	Characteristic time scale of diffusion and shear	s
t_m	Characteristic time scale of mixing	s
t_{mix}	Micromixing time parameter	s
t_r	Characteristic reaction time scale	s
T	Temperature	K
u_{out}	Liquid outlet velocity from the nozzle	$m\ s^{-1}$
u_{tang}	Tangential velocity of the rotor	$m\ s^{-1}$
V_1	Surrounding volume	m^3
V_2	Aggregate volume	m^3
V_{20}	Initial aggregate volume	m^3
V_{L1}	Volume of the buffer	m^3
V_{L2}	Volume of the acid	m^3
V_{PM}	Perfectly mixed volume	m^3
V_{ST}	Segregated volume	m^3

$\dot{V}_{acid}$	Flow rate of the acid	$m^3\ s^{-1}$
$\dot{V}_{buffer}$	Flow rate of the buffer	$m^3\ s^{-1}$
$\dot{V}_G$	Total gas flow rate	$m^3\ s^{-1}$
$\dot{V}_L$	Total liquid flow rate	$m^3\ s^{-1}$
X_S	Segregation index	-
Y	Ratio of protons bound in reaction (ii) to protons initially added to the mixture	-
Y_{ST}	Y-value for a state of total segregation	-
z_e	Number of transferred electrons	-
z_i	Charge number of ion i	-
Greek letters		
α_{diss}	Degree of dissociation	-
α_{mix}	Micromixedness ratio	-
α_{vol}	Volume fraction	-
β	Premixed distributor pipe angle	°
δ	Nozzle distribution angle	°
ε	Energy dissipation rate	$W\ kg^{-1}$
ε_N	Molar extinction coefficient	$m^2\ mol^{-1}$
ζ_L	Power consumption due to the acceleration of liquid	W
Θ	Dimensionless time	-
μ	Dynamic viscosity	Pa s
ν	Kinematic viscosity	$m^2\ s^{-1}$
ρ_G	Gas density	$kg\ m^{-3}$
ρ_L	Liquid density	$kg\ m^{-3}$
τ	Residence time	s
$\bar{\tau}$	Average residence time	s
φ	Nozzle orientation angle	°
ω	Rotational speed	s^{-1}

Abbreviations	
AV	Anisidine value
ButA	Butyl acetate
CD	Complete dissociation
CFD	Computational fluid dynamics
CFP	Ceramic foam packing
CT	Computed tomography
FF	Flat fan
FID	Flame ionization detector

FJ	Full jet
GC	Gas chromatography
GOED	Global Organization for EPA and DHA
GVL	γ-Valerolacton
HSM	High Shear Mixer
ID	Incomplete dissociation
IEM	Interaction-by-Exchange-with-the-Mean model
IIR	Isobutylene-isoprene rubber
MDA	Methylene diphenyl dianiline
MDI	Methylene diphenyl diisocyanate
NMR	Nuclear magnetic resonance
NNP	Non-modified nickel foam packing
OD	Optical density
OD_0	Initial optical density
ODE	Ordinary differential equation
ppi	Pores per inch
PUFA	Polyunsaturated fatty acids
PV	Peroxide value
RPB	Rotating Packed Bed
RRR	Rotating Ring Reactor
RTD	Residence time distribution
SDR	Spinning Disc Reactor
SNP	Surface-modified nickel foam packing
TRL	Technology Readiness Level
WHO	World Health Organization
WMP	Wire mesh packing

GLOSSARY

Term	Meaning
Axial packing height	Extension of the packing in direction of the rotational axis. Also known as packed bed height, axial packing size, or height of the packing.
HiGee equipment	Equipment exploiting centrifugal forces higher than the gravitational force for phase processing. Also known as Higee equipment or High-g equipment.
Liquid load	Liquid flow rate per cross-sectional area of packing at the inner radius of the packing.
Radial packing depth	The distance between the inner packing radius and the outer packing radius. Also known as length of the packing, packed bed size, radial packing size, or packed bed length.
Rotational axis	The rotational axis of the rotor shaft. Therefore, an RPB with a vertically oriented rotor has a horizontal axis of rotation and an RPB with a horizontally oriented rotor has a vertical axis of rotation.
Rotational speed	The angular velocity of the rotor around the rotational axis, in contrast to the tangential velocity at a certain rotor radius.
Rotor eye	Void, inner part of the rotor, enclosed by the eye ring.

1 INTRODUCTION*

1.1 Motivation and Gap Analysis

Both the intensification and the modularization of production processes are fields of great scientific and economic interest in the chemical industry (Keil 2018). Process intensification is an important driver for the development of innovative technologies and process concepts (Skiborowski 2018). Intensified devices tend to have higher energy and cost efficiency and a lower volume than conventional equipment (Baldea et al. 2017; Skiborowski 2018). In contrast, the application of modular equipment can increase the production flexibility and allows for a shorter time to market (Baldea et al. 2017; Radatz et al. 2017). Furthermore, modularity tends to save investment costs if modules can be recycled and enables a smart scale-up of existing processes (DECHEMA e.V. 2017).

Ideally, the concepts of process intensification and modularity are complementary. Modularity based on process intensification can be understood as an approach beyond the conventional unit operations; Instead of designing multiple apparatuses, each dedicated to one particular unit operation, different fundamental functions are combined into tasks that are solved by only one piece of equipment (Baldea et al. 2017). Therefore, the ideal intensified module could be considered „one apparatus for all unit operations“. Such an inherently flexible module would enable fast changes between production processes without the need for varying equipment. Furthermore, the production of new products could be tested expeditiously and based on existing know-how, accelerating the development cycles (DECHEMA e.V. 2017).

An example of intensified, modular devices are rotating high-gravity apparatuses, which were suggested by *Ramshaw* under the term “HiGee technology” as a concept of process intensification (Ramshaw 1983). Since then, many authors have underlined the importance of HiGee devices for improving existing processes.

---

* Parts of this chapter have been published as:
Review and Analysis of Micromixing in Rotating Packed Beds (2018), Wenzel, D.; Górak, A.; Chem. Eng. J. (345), pp. 492-506.
Liquid Distribution and Mixing in Rotating Packed Beds (2019); Wenzel, D.; Ojeda, L.S.; Gerdes, N.; Steinbrink, M.; Górak, A.; Ind. Eng. Chem. Res. 58 (15), pp. 5919-5928.
Reactive mixing in rotating packed beds: on the packing's role and mixing modeling (2019); Wenzel, D.; Nolte, K.; Górak, A.; Chem. Eng. Proc.: P.I. (143), published online, doi: 10.1016/j.cep.2019.107596.

By replacing gravity by centrifugal force, the mass transfer efficiency can be dramatically increased and the equipment size remarkably decreased (Kelleher and Fair 1996). Thus, the hold-up of liquids, gases, and solids is reduced, allowing for more expensive coating materials and reducing potentially hazardous situations (Visscher et al. 2013).

One of the most promising and flexible HiGee concepts are Rotating Packed Beds (RPBs, (Neumann et al. 2018a)). Within RPBs, centrifugal forces up to three orders of magnitude higher than Earth's gravity can be reached to intensify the contact between two or more phases (Agarwal et al. 2010; Rao et al. 2004). The rotational speed can be adjusted according to the process requirements, which offers an additional operational degree of freedom in comparison to gravity-based devices (Sudhoff et al. 2015). Moreover, the integration of RPBs into conventional processes was shown to lead to synergistic effects (Qian et al. 2018). RPBs have been successfully applied to the deaeration of seawater, the production of hypochloric acid, and the preparation of nanoparticles, with a broad range of other processes being investigated as possible fields of application (Zhao et al. 2010). Nevertheless, the European chemical industry is still skeptical of this technology and has not yet taken full advantage of its potential – in contrast to the chemical industry in China, Taiwan, and Japan (Sudhoff et al. 2015; Górak et al. 2017; EUROPIN 2007).

Current obstacles are that practical rules of design are still missing and that the construction of RPBs is often done on a case-to-case basis (Neumann et al. 2017). Generally, one of the most important reasons for the sparse implementation of intensified devices is their complexity in combination with the lack of standardized equipment, as well as a limited understanding of their proper design and operation (Bielenberg and Bryner 2018). Therefore, it is necessary to investigate the influence of different design and operational parameters in RPBs in a structured approach and with respect to promising applications.

Three of the potentially most promising applications of RPBs can be found in the field of liquid processing, namely liquid phase reactive mixing, liquid-liquid extraction, and liquid-gas processing.

The performance of most industrial liquid phase processes is affected by the mixing of miscible fluids and mass transfer between immiscible fluids. Therefore, mixing in chemical reactors is an important unit operation and the design and optimization of well-mixed reactors are of large practical importance (Mao and Yang 2017). An intense and fast mixing process is crucial for high selectivity and turnover in fast complex reaction schemes, for a defined particle size distribution in precipitation processes, or for defined molecular weight distribution in polymerization reactions (Hofinger 2013;

Mao and Yang 2017). In particular, mixing at the molecular scale (micromixing) is believed to be very important when the characteristic reaction time scale is on the same order of magnitude or smaller than the characteristic time scale of mixing (Zhao et al. 2010). The idea of applying RPBs to mixing processes has been discussed in the literature for more than 15 years since first being investigated by *Chen et al.* (Chen et al. 2004). A comprehensive overview of the state of the art in this field is presented in chapter 4. However, previous investigations have often not been conducted in a systematic manner and have left many questions open. Furthermore, different types of equipment have been compared on the basis of concentration-dependent parameters or unvalidated models in the past.

In contrast, liquid-liquid extraction is a key method to obtain natural substances in high purity (Modak et al. 2016). However, for economic operation, the size of the extraction apparatus should be kept small, whereas the capacity and the mass transfer rate should be as large as possible. All three conditions could be met by RPBs (Li and Qi 2004; Liu et al. 2003; Modak et al. 2016). Nevertheless, studies in the field are currently confined to the laboratory scale and no concept for a pilot-scale RPB process is available from the literature so far.

Moreover, the countercurrent processing of liquid and gas phases is of large interest to the chemical industry. Particularly for liquids with high viscosity and low thermal stability, the combination of high shear forces, short residence times, and high mass transfer rates in an RPB could be promising. An exemplary process in this field is the refining of vegetable oils for food and pharmaceutical application. However, no studies on this matter have been published so far.

1.2 Objectives

The overall objective of this thesis is the further development of the RPB technology for the task of liquid processing. This shall be done on the basis of the previous state of the art, with an emphasis on the applicability of RPBs to different liquid processes and with a focus on industrially relevant processes. Since previous studies on liquid processing in RPBs have left many questions open, one objective of this thesis is to answer the most important questions with respect to the liquid distribution and packing design. Furthermore, the applicability of RPBs and other devices shall be compared by means of concentration-independent and validated model parameters. For this objective, the most suitable methods of investigation must be first identified and validated. For the application of RPBs in industrial liquid processing, three different case studies shall further be considered. Firstly, liquid phase reactive mixing processes in

RPBs, for which condensation and polymerization reactions shall be investigated. Secondly, liquid-liquid extraction processes in RPBs, for which a process concept shall be developed and compared to a conventional process. Thirdly, liquid-gas processing in RPBs, for which a pilot-plant setup shall be designed and experimentally investigated. Overall, RPBs are competing with many other intensified and non-intensified types of equipment. While the literature claims a large potential for the RPB technology, their use in the industry is still scarce. For a more wide-spread and courageous use of RPBs, more guidance on their design, operation, and reasonable application are necessary but currently missing. Therefore, guidelines and conclusions for the most reasonable utilization of RPB technology shall be derived in this thesis, in comparison to other HiGee devices and conventional equipment. Ultimately, conclusions on the most reasonable application of RPBs and alternative HiGee concepts in the field of liquid processing shall be drawn.

1.3 Structure of This Thesis

An overview of this thesis' structure is shown in Fig. 1. The context, the motivation, and the objectives are presented in this chapter. Then, general fundamentals are presented in chapter 2. In contrast, fundamentals that are only important for one section of this thesis are presented in the respective chapters.

The focus of this work lies on liquid phase reactive mixing, which is investigated on three scales: literature study, laboratory-scale experiments, and pilot-scale experiments. In chapter 3, the methodology used in the subsequent chapters on liquid phase reactive mixing is introduced and the optimal utilization of the method for experiments in RPBs is investigated on a laboratory scale. In chapter 4, the state of the art in the field of liquid phase reactive mixing in RPBs is presented and a detailed gap analysis on this topic is conducted. However, the concentration-dependent comparison of RPBs with other devices, conducted in chapter 4, will be shown to be limited. Therefore, suitable mixing models are evaluated and validated in chapter 5 and a concentration-independent comparison of RPBs with other devices is conducted. On the basis of chapters 3 and 4, the introduced methodology is further used in chapter 5 to close the identified gaps in the knowledge on operation and design of RPBs by means of pilot-scale experiments. Subsequently, the application of RPBs to liquid processing is investigated by means of three case studies in chapter 6. First, the investigations on liquid phase reactive mixing in RPBs are extended to the industrial scale in chapter 6.2, with an experimental and literature case study on relevant industrial processes. Second, a suitable framework to implement a liquid-liquid

extraction process in multiple RPBs is investigated in chapter 6.3 and a detailed process concept is presented. Third, the liquid-gas processing in RPBs is investigated in chapter 6.4 in the scope of an oil refining process.

In chapter 7, recommendations on the design, operation, and application of RPBs for liquid processing are made, based on the insights obtained in the previous chapters. Operation, design, and scaling guidelines are derived, the technology readiness levels of the processes investigated in chapter 6 are assessed, and a decision chart for the application of RPBs is presented. Furthermore, based on the drawbacks of the current RPB design that were identified in the previous chapters, a novel HiGee device design is recommended. Finally, the achievements of this thesis and the most reasonable fields of application for RPBs and alternative concepts are summarized in chapter 8 and an outlook on future research is given.

<table>
<tr><th colspan="3">Introduction and Fundamentals</th></tr>
<tr><td colspan="2">Chapter 1
Introduction</td><td>Chapter 2
Fundamentals</td></tr>
<tr><th colspan="3">Method and Technology Development</th></tr>
<tr><td>Chapter 3
Method Development</td><td>Chapter 4
Literature Study</td><td>Chapter 5
Operation, Design, and Modeling</td></tr>
<tr><th colspan="3">Application Case Studies</th></tr>
<tr><td>Chapter 6.2
Case Study: Liquid Phase Reactive Mixing</td><td>Chapter 6.3
Case Study: Liquid-Liquid Extraction</td><td>Chapter 6.4
Case Study: Liquid-Gas Processing</td></tr>
<tr><th colspan="3">Insights and Conclusions</th></tr>
<tr><td colspan="2">Chapter 7
Recommendations</td><td>Chapter 8
Achievements and Future Research</td></tr>
</table>

Fig. 1. Structure of this thesis.

2 FUNDAMENTALS *

In this chapter, the fundamentals of the Rotating Packed Bed technology will be presented. Also, the state of the art of liquid-liquid processing and liquid-gas processing in Rotating Packed Beds is elucidated. Finally, the Rotating Packed Bed design variants considered in this thesis are introduced.

2.1 Rotating Packed Bed Technology

A schematic drawing of an RPB for liquid processing is shown in Fig. 2. In general, RPBs contain a rotating part and a static part, which are connected through bearings and sealings. The rotating part consists mostly of the rotor, which is connected through a shaft to a motor.

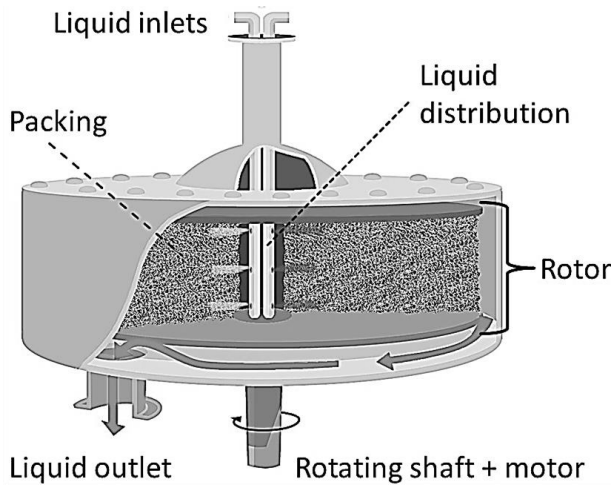

Fig. 2. Schematic drawing of the liquid-liquid processing in an RPB with a vertical axis of rotation.

* Parts of this chapter have been published as:
Review and Analysis of Micromixing in Rotating Packed Beds (2018), Wenzel, D.; Górak, A.; Chem. Eng. J. (345), pp. 492-506.
Liquid Distribution and Mixing in Rotating Packed Beds (2019); Wenzel, D.; Ojeda, L.S.; Gerdes, N.; Steinbrink, M.; Górak, A.; Ind. Eng. Chem. Res. 58 (15), pp. 5919-5928.
Reactive mixing in rotating packed beds: on the packing's role and mixing modeling (2019); Wenzel, D.; Nolte, K.; Górak, A.; Chem. Eng. Proc.: P.I. (143), published online, doi: 10.1016/j.cep.2019.107596.

The rotor usually contains an annular packing and, in many RPBs, a perforated ring at the inner radius of the packing. This so-called eye ring is required as a spacer in case of separated rotor plates and serves as packing support (Neumann et al. 2017). As in gravity-based equipment, the packed bed can either consist of structured packings or of non-structured packings. Structured packings are usually made of wire mesh, ceramic foam or metal foam. The static part contains the casing and the static components of the motor. Within the center void of the rotor (referred to as the rotor eye), the liquid feed is distributed onto the rotating packing. The motor can be placed either underneath or to the side of the machine, depending on the rotational axis. The rotational axis of the shaft can be either horizontal or vertical, with the orientation of the rotor varying correspondingly. Furthermore, the speed of rotation can be adjusted according to the respective process demands.

2.2 Liquid-Liquid Processing in RPBs

While countercurrent operation is common for liquid-gas processing in RPBs (Chapter 2.3), only cocurrent operation has been investigated for liquid-liquid processing in RPBs so far. For this, the liquid streams are distributed in the eye of the rotor, impinge on the rotating packing, flow through the packing in the direction of the applied centrifugal force to the outer rim, and are then ejected into the casing, leaving the whole apparatus through the liquid outlets. To distribute liquids onto the rotating packing, three different approaches have been published (Fig. 3).

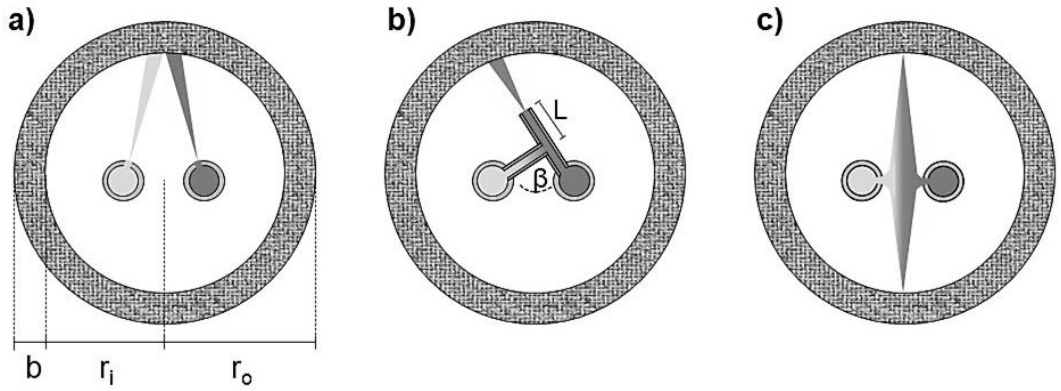

Fig. 3. Schematic drawing of the rotating packing and the three most common forms of liquid distribution in an RPB, as seen from the top, where r_o is the outer packing radius, r_i is the inner packing radius, and b is the radial packing depth. a) Distribution pipes; b) Premixed distributor, with distributor length L and pipe angle β; c) Impinging stream distribution.

The first involves distribution pipes and consists of two separate pipes with small holes at the lower end to spray liquid onto the rotating packing (Fig. 3a). The second involves premixed distributors, in which two separate pipes are located at the lower end and are connected to only one pipe with one opening (Fig. 3b). Thus, the two formerly separate liquids are already macromixed within the liquid distributor. The third involves impinging streams, which are sprayed against each other in the eye of the rotor before splashing onto the rotating packing (Fig. 3c). The way in which liquid flows through different packings is still under investigation. Based on a visual study, *Burns and Ramshaw* proposed that liquid flow through the bulk zone of the packing can be categorized as pore flow, droplet flow and film flow (Burns and Ramshaw 1996). The authors found that pore flow dominated at a lower rotational speed, leaving most of the packing starved of liquid. However, for increasing rotational speed, a more evenly distributed droplet flow set in, while for the highest rotational speed, film flow was suggested. Similar results were presented by *Guo et al.*, who found that in most of the rotating packing, except for the inner rim (impingement zone), liquid flows along the inner surface of the packing, with liquid drops flying across the voids (Guo et al. 2000). This description is in agreement with the droplet and film flow described by *Burns and Ramshaw*. The authors quantified the impingement zone to cover the first 7 – 10 mm of the packing. Furthermore, *Burns et al.* measured the liquid hold-up in a rotating packing and found that the liquid hold-up was inversely proportional to the packing radius, with the highest liquid hold-up in the center, whereas the flow through the packing could best be described by the inertial pore flow model (Burns et al. 2000). Based on computed tomography (CT) scans, *Yang et al.* found that for different packing types, liquid flow rates, and rotational speed, different flow patterns through the packing can be observed (Yang et al. 2015a). Consequently, the packing could be differentiated into the impingement zone with a high liquid hold-up, the bulk zone with a lower hold-up, and the outer rim with again an increased hold-up. From the outer rim of the packing, drops and strings of liquid are ejected into the casing.

2.3 Liquid-Gas Processing in RPBs

A schematic drawing of liquid-gas processing in RPBs is shown in Fig. 4. In contrast to the processing of liquid alone, gas flows countercurrently through the RPB. It enters the RPB through a gas inlet in the RPB casing, flows through the rotating packing, and leaves the RPB through the gas outlet in the rotor eye.

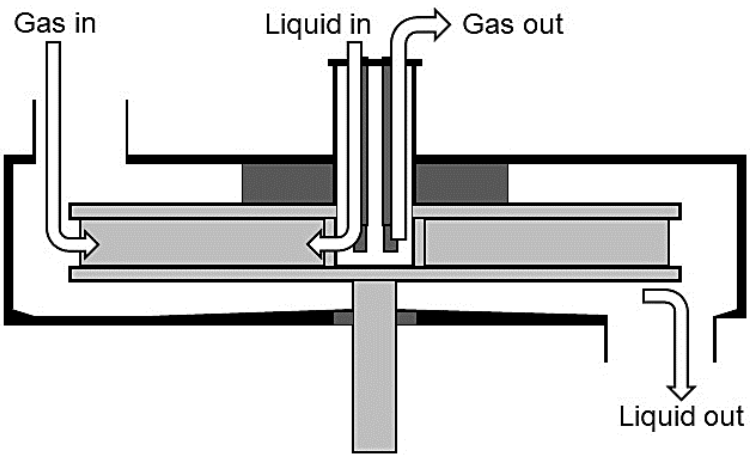

Fig. 4. Schematic drawing of the liquid-gas processing in an RPB. Moving parts are shown in in light grey.

In order to prevent gas from bypassing the rotor, an upper sealing must be installed between the rotor and casing. This upper sealing is commonly realized in the form of a labyrinth seal or a liquid ring seal. The relationships between gas flow rate, liquid flow rate, and packing dimensions can be expressed in terms of the gas capacity factor F_g (Eq. (1)) and the liquid load LL (Eq. (2)) (Neumann et al. 2017). Both parameters are given with respect to the cross-sectional area of the packing at the inner packing radius.

$$F_g = \frac{\dot{V}_G}{3600 * 2\pi * r_i * h} * \sqrt{\rho_G} \quad (1)$$

$$LL = \frac{\dot{V}_L}{2\pi * r_i * h} \quad (2)$$

where $\dot{V}_G$ is the total gas flow rate, $\dot{V}_L$ is the total liquid flow rate, ρ_G is the gas density, h is the axial packing height, and r_i is the inner packing radius.

For liquid-gas processing, *Guo et al.* found that countercurrent gas flow had almost no influence on either liquid flow pattern or liquid distribution within the packing in the investigated range (Guo et al. 2000). This is in agreement with previous results by *Burns et al.*, who found that a gas flow has only little effect on the liquid hold-up in the packing below the flooding point (Burns et al. 2000).

2.4 RPB Design Variants

Multiple RPB design variants are reported in the literature (Neumann et al. 2017). From these, three RPB design variants are considered in this thesis. These are the RPB 1.0 design and the RPB 2.0 design, which were used for liquid-liquid processing, and the Andritz RPB design, which was used for liquid-gas processing.

2.4.1 The RPB 1.0 Design

The RPB 1.0 design is schematically depicted in Fig. 5. The distance between the rotor and the casing are 96 mm. The casing inner diameter is 792 mm. Thus, for a 600-mm rotor, the ratio between the casing inner radius and the rotor radius is 1.32. The RPB contains four liquid outlets, which are each 16 mm in inner diameter and close to the rotor shaft. Thus, the liquid outlets occupy about 0.16 % of the casing bottom in the RPB 1.0 design. Further details and dimensions are given in Tab. 14 (Appendix C.1).

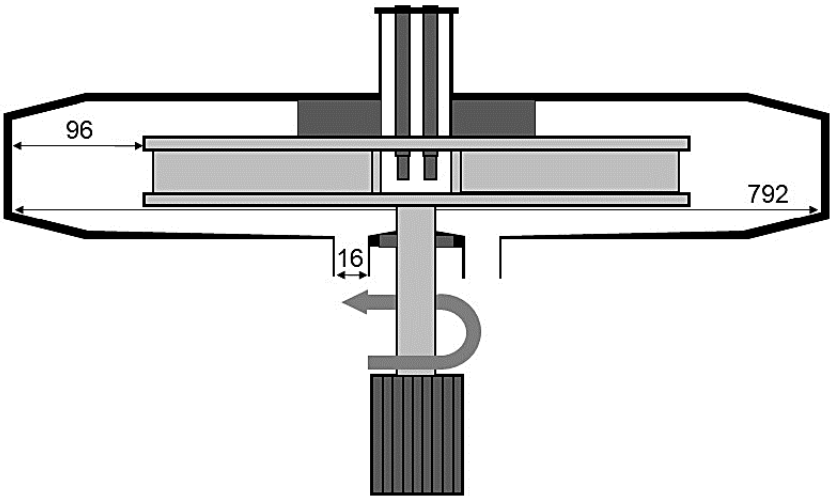

Fig. 5. Schematic drawing of the RPB 1.0 design. All dimensions are given in mm. Moving parts are shown in light grey.

2.4.2 The RPB 2.0 Design

Fig. 6 schematically depicts the RPB 2.0 design. The distance between the rotor and the casing are 39 mm. The casing inner diameter is 678 mm. Thus, for a 600-mm rotor, the ratio between the casing inner radius and the rotor radius is 1.13, which is 14.4 % less than in the RPB 1.0 design. The RPB 2.0 contains three liquid outlets, which are each 80 mm in inner diameter and close to the RPB casing. Thus, the liquid outlets occupy about 4.0 % of the casing bottom in the RPB 2.0 design, which is 25 times more than in the RPB 1.0 design.

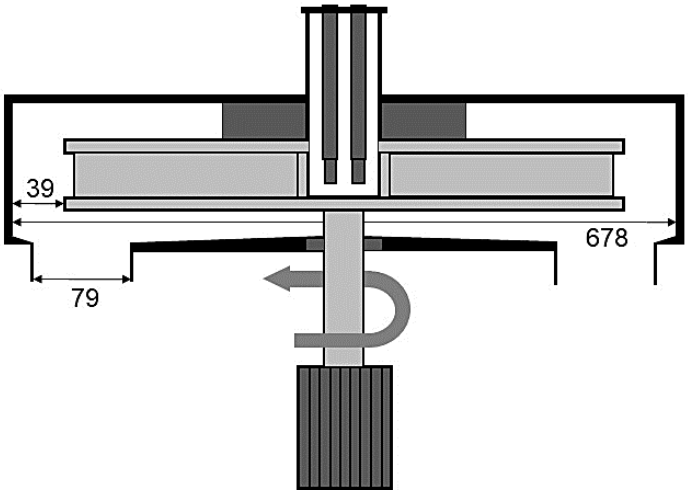

Fig. 6. Schematic drawing of the RPB 2.0 design. All dimensions are given in mm. Moving parts are shown in light grey.

2.4.3 The Andritz RPB Design

The Andritz RPB design is schematically depicted in Fig. 7. This compact RPB setup was designed and constructed by Andritz AG (Graz, Austria) in a way that the motor can be placed to the side of the casing, driving a hollow shaft via a belt. In contrast to the RPB 1.0 and RPB 2.0 design, the liquid is supplied from the bottom of the apparatus. Furthermore, gas can be fed into the RPB casing from the top side, leaving the RPB through the bottom of the hollow shaft after passing through the packing. Further details and dimensions are given in Tab. 24 (Appendix D.5). Photographies of the setup are shown in Fig. 79 and Fig. 80 (Appendix D.5).

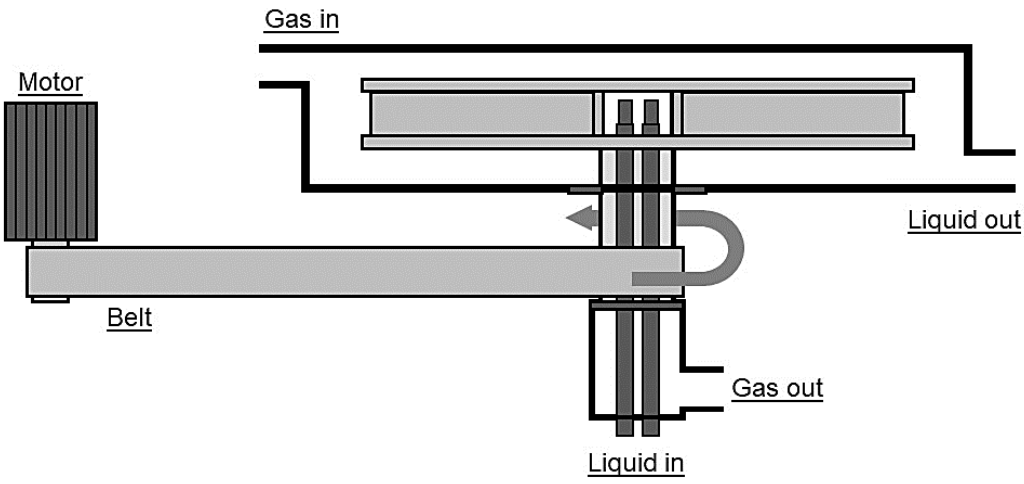

Fig. 7. Schematic drawing of the Andritz RPB design. Moving parts are shown in light grey.

3 METHOD DEVELOPMENT *

In this chapter, one of the most prominent methods for the investigation of fast mixing processes, the Villermaux-Dushman protocol, will be developed further and adjusted to investigations in RPBs. First, the fundamentals of mixing processes, how to quantify mixing processes, and how to utilize the Villermaux-Dushman protocol for this purpose are introduced. Second, the influence of different acid and buffer substances and concentrations on the obtained results will be experimentally investigated. Finally, conclusions on a reaction protocol design best suitable for the investigation of reactive mixing processes in RPBs will be drawn.

3.1 Introduction

Many industrial production processes involve the immediate reaction of two contacted liquids. Therefore, it is essential to develop tools that allow the characterization of the mixing process (Villermaux and Falk 1994). Once this tool is at hand, it can then be used to systematically investigate the influence of different parameters on mixing efficiency, selectivity, and product quality. A comprehensive overview of available methods to characterize mixing was presented by *Bałdyga and Bourne* (Bałdyga and Bourne 1999) and *Aubin et al.* (Aubin et al. 2010). However, while the measurement of heat and mass transfer is quite straightforward, the measurement of mixing phenomena is often much more difficult, as their influence on the overall result can be difficult to isolate (Commenge and Falk 2011).

One promising approach is the use of a competitive consecutive reaction system, for example, the Villermaux-Dushman protocol, suggested by the working group of *Villermaux, Falk, and Fournier* (Fournier et al. 1996a, 1996b).

***** The scientific work published in this chapter was performed by D. Wenzel and supported by H. Rossen and M. Lopattschenko in the framework of bachelor theses. Scientific advice was given by A. Górak.

* Parts of this chapter have been published as:
On the Reactant Concentration and the Reaction Kinetics in the Villermaux-Dushman Protocol (2018); Wenzel, D.; Assirelli, M.; Rossen, H.; Lopattschenko, M.; Górak, A.; Chem. Eng. Proc.: P.I. (130), pp. 332-341.
Review and Analysis of Micromixing in Rotating Packed Beds (2018), Wenzel, D.; Górak, A.; Chem. Eng. J. (345), pp. 492-506.
Liquid Distribution and Mixing in Rotating Packed Beds (2019); Wenzel, D.; Ojeda, L.S.; Gerdes, N.; Steinbrink, M.; Górak, A.; Ind. Eng. Chem. Res. 58 (15), pp. 5919-5928.

This protocol has been used to study the mixing process in, for example, stirred tank reactors (STRs) (Assirelli et al. 2008), V-type mixers (Kölbl et al. 2010), inline mixers (Habchi et al. 2014), and spinning disc reactors (SDRs) (Manzano Martínez et al. 2017). However, the correct use of the protocol's key components and the underlying kinetics are still part of an ongoing debate. Therefore, the aim of this chapter is to provide new insights into the use of different acid and buffer substances and to enable optimal utilization of the Villermaux-Dushman protocol for the investigation of RPBs. Additionally derived insights on the kinetics in the Villermaux-Dushman protocol are summarized in Appendix A.5.

3.2 Fundamentals

3.2.1 Mixing Processes

Mixing processes are usually considered to occur on three different scales, i.e., macromixing, mesomixing, and micromixing (Villermaux and Falk 1994). Macromixing describes the initial phase in the process of two liquids contacting. It occurs on the macroscopic scale of the complete mixing vessel (Bałdyga and Pohorecki 1995) before the composition is uniform. Afterward, the mesomixing phase occurs. The term mesomixing was coined by *Bourne*, based on the work of *Beek and Miller*, and can be characterized as "distribution of one fluid through the other and uniformization of average composition without decreasing local concentration variations" and "reduction of size of the regions of uniform composition and increase of contact between regions of different composition" (Beek, JR. and Miller 1959; Villermaux and Falk 1994). Mesomixing involves the disintegration of liquid elements from an initial, macroscopic scale towards the Kolmogorov scale (Bourne 2003). Finally, micromixing describes the mixing of two liquids near the molecular scale (Bourne 2003). It is the last stage of a turbulent mixing process and is dominated by viscous-convective deformation of liquid aggregates, the shrinkage of liquid aggregates, and ultimately molecular diffusion (Bałdyga and Pohorecki 1995). As diffusion itself is a rather slow process, it is necessary to achieve liquid slabs a few microns in size to achieve molecular diffusion on the order of milliseconds, which is also the characteristic reaction time scale of fast reactions, such as the Dushman reaction (Falk and Commenge 2010). However, the diffusion process can be accelerated by the viscous-convective deformation and shrinkage of fluid elements, which is considered an important principle of micromixing (Bałdyga and Pohorecki 1995). The characteristic time scale of diffusion and shear (t_{DS}) necessary to further decrease the size of a liquid slab from Kolmogorov scale to

Batchelor scale can be described approximately by Eq. (3) (Bałdyga and Pohorecki 1995).

$$t_{DS} \approx \left(\frac{\nu}{\varepsilon}\right)^{\frac{1}{2}} * \ln\left(\frac{\nu}{D}\right) \quad (3)$$

where v is the kinematic viscosity, ε is the energy dissipation rate, and D is the diffusivity. More precise relations are presented by *Bourne* (Bourne 2003) and *Falk and Commenge* (Falk and Commenge 2010).

3.2.2 Quantifying Micromixing

Three different approaches to quantify micromixing are commonly used (Commenge and Falk 2011). The first approach is the visualization of a dye. However, this method is not suitable for investigating micromixing in RPBs because it requires the mixing apparatus to be made from a transparent material (Commenge and Falk 2011). The second approach is the use of reactions that generate colored species or a color change, which was found to be particularly suitable for split-and-recombine mixers (Wong et al. 2004). However, this approach is also partially based on the use of transparent apparatuses (Commenge and Falk 2011). The third approach is the use of competing reactions. This type of reaction system involving two competing parallel reactions is used in the Villermaux-Dushman protocol, which is currently the most popular reaction scheme to characterize continuous flow mixers (Kölbl and Schmidt-Lehr 2010; Commenge and Falk 2011). To evaluate mixing results with appropriate sensitivity, it is necessary to consider the relationship between the micromixing time t_m and the characteristic reaction time scale t_r. The micromixing time is the characteristic time scale necessary to achieve homogeneity between the two mixed liquids on the molecular scale (Commenge and Falk 2011; Kölbl and Schmidt-Lehr 2010). The micromixing time can be described through different mixing models, as discussed in chapter 5.2.2. However, the actual, physical micromixing time should not be confused with the model parameter of the same name (Kölbl and Schmidt-Lehr 2010) that will also be introduced in chapter 5.2.2. The characteristic reaction time is determined by the reaction kinetics and usually defined as the time after which the reaction would be completed with the initial reaction rate at t = 0 (Guichardon and Falk 2000).

In a chemical reaction system, the reaction rates are controlled by the intrinsic kinetics without the influence of micromixing when $t_m < t_r$ and controlled or influenced by micromixing when $t_m > t_r$ (Zhao et al. 2010; Bourne 2003). These considerations are explained in more detail in the following.

For conditions under which $t_m >> t_r$, the reaction is completed under incomplete

micromixing and dominated by macro- and mesomixing. Thus, a low sensitivity towards the influences of micromixing on the complete mixing process is obtained. This effect can be observed, e.g., when very high liquid flow rates are fed into a semi-batch reactor. The mixing results then become a function of the feed rate (Assirelli et al. 2002; Bałdyga and Bourne 1999). Additionally, if t_r is too low in a reaction system, for example, due to high reactant concentrations, the decreased relative difference between the reaction rates of two reactions can lead to low sensitivity of mixing results towards changes in the operating conditions and the reactor setup (Guichardon and Falk 2000).

For conditions under which $t_r >> t_m$, the reaction is completed almost entirely under micromixing conditions. Again, only a low sensitivity towards changes in the operating conditions and the reactor setup is obtained. For this case, *Guichardon and Falk* recommend increasing the reactant concentration to increase t_r (Guichardon and Falk 2000). However, if the concentrations are increased too much, low sensitivity is again encountered. Furthermore, t_m depicts a "cut-off" condition in the case of an instantaneous reaction as all reactants will be consumed at this point. For conditions under which t_r is in the same range as t_m, the reaction is partly dominated by macromixing conditions and partly dominated by micromixing conditions. In this case, the highest sensitivity of the investigation method is achieved (Guichardon and Falk 2000).

3.2.3 The Villermaux-Dushman Protocol

The Villermaux-Dushman protocol consists of two competing reactions: a redox-reaction and a neutralization reaction. While the neutralization reaction can be realized with any buffer reaction, most commonly, a boric acid buffer solution ($H_2BO_3^-/H_3BO_3$) is used (reaction (i)). The redox-reaction is fixed to be the iodide-iodate reaction, long known as Dushman reaction (Dushman 1904) (reaction ii), including the subsequent equilibrium reaction between iodine (I_2), iodide (I^-), and triiodide (I_3^-) (reaction (iii)).

$$H_2BO_3^- + H^+ \rightarrow H_3BO_3 \quad \text{(i)}$$

$$5\,I^- + IO_3^- + 6\,H^+ \rightarrow 3\,I_2 + 3\,H_2O \quad \text{(ii)}$$

$$I_2 + I^- \leftrightarrow I_3^- \quad \text{(iii)}$$

While reactions (i) and (iii) are usually considered to be quasi-instantaneous, the reaction velocity of reaction (ii) is believed to be very fast but considerably slower than the neutralization reaction (Commenge and Falk 2011). To use this set of reactions to assess the mixing efficiency of an apparatus, two solutions must be prepared. The first

one is a buffer solution (L_1) containing every reactant except for H^+. The second solution is an acidic solution (L_2), providing the protons. This acidic solution must be prepared in a way that a stoichiometric shortage of protons to buffer ions is obtained when these two solutions are mixed. Thus, only reaction (i) will take place under perfectly fast mixing conditions. However, a local surplus of protons over buffer ions will lead to the formation of iodine and triiodide through reactions (ii) and (iii) under slow mixing conditions. The optical density (OD, in the following assumed to be identical to the absorbance of triiodide) of a mixture sample can then be obtained by UV-vis spectrophotometry at 353 nm, i.e., the absorption maximum of triiodide (Fournier et al. 1996b). From the OD, the concentration of triiodide can be calculated according to Lambert-Beer's law (Eq. (4)).

$$[I_3^-] = \frac{OD}{\varepsilon_N * d} \tag{4}$$

where ε_N is the molar extinction coefficient and d is the optical path length through a sample. Furthermore, the concentration of iodine in a mixture sample can be calculated from the measured triiodide concentration, for a large surplus of iodide, according to Eq. (5).

$$K_{eq} \approx \frac{[I_3^-]}{[I_2][I_0^-]} \tag{5}$$

where $[I^-_0]$ is the initial iodide concentration before mixing and K_{eq} is the equilibrium constant of reaction (iii), which is a function of the temperature (Palmer et al. 1984) (Eq. (6)).

$$\log_{10}(K_{eq}) = \frac{555}{T} + 7.355 - 2.575 * \log_{10}(T) \tag{6}$$

To use the obtained iodine and triiodide concentrations to quantify the mixing process in an apparatus, the dimensionless segregation index X_S is commonly used (Eq. (7)).

$$X_S = \frac{Y}{Y_{ST}} \tag{7}$$

where Y is the ratio of protons bound in reaction (ii) to protons initially added to the mixture (Eq. (8)) and Y_{ST} is defined as the Y value under total segregation (Eq. (9)).

$$Y = \frac{2\left(n_{I_2} + n_{I_3^-}\right)}{n_{H_0^+}} = 2\,\frac{(V_{L_1} + V_{L_2}) * ([I_2] + [I_3^-])}{V_{L_2} * [H_0^+]} \tag{8}$$

$$Y_{ST} = \frac{6\,[IO_{3,0}^-]}{6\,[IO_{3,0}^-] + [H_2BO_{3,0}^-]} \quad (9)$$

where V_{L1} and V_{L2} are the volumes of buffer and acid, respectively, [i] is the final concentration of component i after mixing and the occurrence of reactions (i) to (iii), and [i,$_0$] is the initial concentration of component i before mixing. Consequently, the segregation index X_S can take values between 0 for perfect mixing conditions, where no iodine and triiodide are formed, and 1 for a state of total segregation, where iodine and triiodide are formed in an ideally stoichiometric ratio.

From a more hydrodynamic point of view, the mixing process can also be described by the ratio between the perfectly mixed volume V_{PM} and the still-segregated volume V_{ST} during the occurrence of reaction (ii). Consequently, this micromixedness ratio α_{mix} is also a function of the segregation index X_S (Eq. (10)) (Commenge and Falk 2011).

$$\alpha_{mix} = \frac{V_{PM}}{V_{ST}} = \frac{1 - X_S}{X_S} \quad (10)$$

As the Villermaux-Dushman protocol is based on the different velocities of the two competing reactions, the term “fast micromixing” should be generally preferred over “good micromixing” or “high micromixing”, as the phase of micromixing – the mixing of all components on the molecular scale – will eventually be entered in all mixing devices (for two phases of the same, fully miscible liquid) but within a different period of time.

3.2.4 Investigations on the Buffer

As discussed by *Guichardon and Falk* (Guichardon and Falk 2000; Guichardon 1996), a suitable buffer solution for a Villermaux-Dushman protocol must fulfill the following two conditions with respect to the dismutation pH (pH*) of iodine:

(1) pH > pH*

(2) $pH_{average}$ close to pH*

These requirements are based on the consideration that no iodine can be formed from iodate and iodide if the pH is above the equilibrium pH (pH*) (Fournier et al. 1996a). However, the formed iodine will also be thermodynamically unstable if the pH is too far above pH*. Therefore, the average working pH ($pH_{average}$) should be as close as possible to pH* (Guichardon and Falk 2000). The exact pH* value for a certain total concentration of all iodine species can be obtained from the respective Pourbaix diagram (Appendix A.1). In addition, the buffer must be chemically inert to the other reactants, should also be easy to handle, and inexpensive to use in large amounts. Under these

constraints, only a few buffer solutions seem suitable. The following buffer systems have been used in the literature or could meet the stated requirements:

- boric acid buffer ($H_2BO_3^-/H_3BO_3$; pK_a: 9.2)
- sodium acetate buffer (NaAc/CH_3COOH; pK_a: 4.8)
- phosphate buffer ($H_2PO_4^-/H_3PO_4$; pK_a: 7.2)

Boric acid was first suggested as a suitable buffer substance in a Villermaux-Dushman protocol because it is a weak acid that allows for quantitative production of iodine (Villermaux et al. 1992). It is commonly used together with sodium hydroxide to obtain buffer solutions of pH ~9.2 (Fournier et al. 1996a; Guichardon et al. 2000). However, in this approach, only the first criterion (pH > pH*) is fulfilled, but not the second one ($pH_{average}$ close to pH*). Therefore, the dismutation of iodine could potentially bias the mixing results towards a lower triiodide yield. In addition to these considerations, boric acid has recently been identified as a CMR (cancerogenic/mutagenic/reprotoxic) substance by the European Commission (Pinot et al. 2014), which makes additional safety measures and a more complex waste treatment necessary. In contrast, sodium acetate buffer does not fulfill the first requirement (pH > pH*), which will bias the mixing results towards a higher triiodide yield. Nevertheless, this buffer was used by *Ehrfeld et al.* for mixing studies, reportedly leading to a significant formation of triiodide after completion of mixing (absorption increased from 0.04 to 0.5 within 15 min) (Ehrfeld et al. 1999). Consequently, a modified Villermaux-Dushman protocol based on the use of a phosphate buffer ($H_2PO_4^-/HPO_4^{2-}$) was suggested by *Pinot et al.* (Pinot et al. 2014). The average pH in this modified Villermaux-Dushman protocol was adjusted to be ~7.8, fulfilling both stated requirements. Assuming that the buffer base used in the Villermaux-Dushman protocol is fully interchangeable, reaction (i) and Eq. (9) could be rewritten according to reaction (iv) and Eq. (11).

$$\mathrm{HPO_4^{2-} + H^+ \rightarrow H_2PO_4^-} \qquad \text{(iv)}$$

$$Y_{ST} = \frac{6\,[IO_{3,0}^-]}{6\,[IO_{3,0}^-] + [HPO_{4,0}^{2-}]} \qquad (11)$$

Such a phosphate buffer was compared by *Baqueiro et al.* to the established boric acid buffer as a function of the stirrer speed (Baqueiro et al. 2018). It was found that the use of phosphate buffer resulted in a lower triiodide yield than the use of a boric acid buffer. However, the authors compared the two buffer substances at only one concentration, while an investigation over a larger concentration range and different combinations of $H_2BO_3^-/H_3BO_3$ and $H_2PO_4^-/HPO_4^{2-}$, as presented in this chapter, is necessary to obtain a thorough comparison.

3.2.5 Investigations on the Acid

It was previously discussed by *Kölbl et al.* (Kölbl 2008; Kölbl et al. 2010; Kölbl and Schmidt-Lehr 2010) and *Bourne* (Bourne 2008) that one of the main difficulties of the Villermaux-Dushman protocol lies in the choice of the acid. The following acids have been either used or discussed in the literature (Kölbl and Schmidt-Lehr 2010):

- Sulfuric acid (H_2SO_4; $pK_{a,1} = -2$; $pK_{a,2} = 1.92$)
- Perchloric acid ($HClO_4$; $pK_a = -10$)
- Hydrochloric acid (HCl; $pK_a = -7$)

Sulfuric acid is by far the most often utilized acid. However, *Kölbl and Schmidt-Lehr* found that a protocol using sulfuric acid resulted in lower triiodide concentrations than those of otherwise identical experiments with perchloric acid, assuming full dissociation of both acids (Kölbl and Schmidt-Lehr 2010). Furthermore, the stoichiometric addition of potassium sulfate to perchloric acid also resulted in a lower triiodide yield, which could be replicated by *Baqueiro et al*. for the addition of sodium sulfate to perchloric acid (Baqueiro et al. 2018). It was therefore considered that the full ionization of a comparatively weak acid such as sulfuric acid could not be assumed under all experimental conditions (Bourne 2008). In contrast, *Commenge and Falk* suggested that sulfuric acid could be assumed to be fully dissociated throughout almost the entire mixing process (Commenge and Falk 2011). While it should be noted that the authors used rather low concentrations in their study, an incomplete dissociation of sulfuric acid could still influence a more considerable part of the mixing process for higher acid concentrations, as will be shown in this chapter.

The use of perchloric acid is problematic due to its chemical properties. Perchloric acid is a strong mineral acid that is highly corrosive to metals even at low concentrations and can react violently with many oxidizable substances at higher concentrations (Carnegie Mellon University 2016). When brought into contact with hot surfaces or strong friction, both possibly present in an RPB, perchloric acid becomes highly unstable, leading to the severe danger of an explosion (Sigma-Aldrich 2015). These safety constraints have led to extensive regulations on perchloric acid. Consequently, the acid should be substituted with less hazardous chemicals whenever possible (Carnegie Mellon University 2016).

Regarding the use of hydrochloric acid, *Guichardon et al.* (Guichardon et al. 2000) warned about the possible formation of I_2Cl^- under the experimental conditions of a Villermaux-Dushman protocol. Such a formation could occur with iodine monochloride (ICl) as an intermediate step and would lead to an overall smaller triiodide yield in comparison to the use of other acids. However, this reaction is only possible in the

presence of highly concentrated hydrochloric acid (Pesavento 1983). Furthermore, a catalytic effect of chloride ions (Cl^-) on the Dushman reaction was reported, as summarized by *Schmitz* (Schmitz 1999). In this case, a higher overall triiodide yield in comparison to that of other acids should be observable. The only reported case of the use of hydrochloric acid in a Villermaux-Dushman protocol was conducted by *Ehrfeld et al.* (Ehrfeld et al. 1999). However, their results were biased by the use of acetate buffer, as discussed in chapter 3.2.4.

3.2.6 Dushman Kinetics

To this point, the exact kinetics of the Dushman reaction is still unclear, although many efforts have been put into its investigation. One of the reasons is that the Dushman reaction rate is too fast even for the best commercially available stopped-flow apparatuses to this day (Kölbl 2008). A comprehensive overview of studies investigating the Dushman kinetics can be found in the respective literature (Guichardon et al. 2000; Bourne 2008) and will not be repeated here in detail. Although exact knowledge of the kinetics is not necessary to determine the segregation index, it is crucial to compare different mixing processes and apparatuses through concentration-independent mixing model parameters.

One of the most commonly considered Dushman kinetics was suggested by *Guichardon et al.* (Guichardon et al. 2000), who found that the rate law of the Dushman reaction (reaction (ii)) at 298 K could be best expressed as denoted in Eq. (12).

$$r_{\mathrm{Guichardon(2000)}} = k_2\,[H^+]^{2.0}[I^-]^{2.0}[IO_3^-]^{1.0} \qquad (12)$$

Where k_2 is the reaction rate constant of reaction (ii). For their kinetics experiments, the authors used a spectrophotometer cell as a reactor. 0.002 l of an iodide/iodate solution were given into the cell, 0.001 l of sulfuric acid was injected through a syringe, and the resulting triiodide formation was recorded as a function of time. The time necessary for the reaction to finish was 100 s, while the time necessary for complete mixing, determined through preliminary experiments with a coloring substance, was in the range of 3 s.

However, *Bourne* argued that this kinetics model, along with six other Dushman kinetics models investigated by him, did not fulfill all necessary requirements to be applied in mixing experiment because the concentrations used for the kinetics measurements differed strongly from those used in the mixing experiments (Bourne 2008). Therefore, *Bourne* called for new kinetics studies on the Dushman reaction, under conditions relevant to mixing applications. Consequently, *Kölbl et al.* (Kölbl et al. 2013a) proposed

the kinetics shown in Eq. (13) for the Dushman reaction as part of a Villermaux-Dushman protocol to investigate mixing in STRs.

$$r_{\text{Kölbl(2013a)}} = k_2\,[H^+]^{0.6}[I^-]^{1.4}[IO_3^-]^{0.6} \tag{13}$$

The authors determined the kinetics in Eq. (13) by adding 0.020 l of perchloric acid or sulfuric acid over a time period of 300 s to 5 l of a stirred buffer solution containing boric acid buffer, iodide, and iodate. Furthermore, *Kölbl et al.* (Kölbl et al. 2013b) proposed different kinetics for a Villermaux-Dushman protocol for experiments in microstructured cyclone type mixers, using volumetrically equal inlet flows of buffer solution and acid. The obtained relationship is shown in Eq. (14).

$$r_{\text{Kölbl(2013b)}} = k_2\,[H^+]^{1.3}[I^-]^{2.0}[IO_3^-]^{1.0} \tag{14}$$

It should be noted that *Kölbl et al.* obtained kinetics for a buffered and unstoichoimetrically adjusted reaction system. For this reason and on the basis of own investigations (Appendix A.5), the kinetics published by *Kölbl et al.* will not be considered for modeling calculations in this thesis.

With respect to reaction rate constant k_2, it was initially stated by *Guichardon and Falk* (Guichardon and Falk 2000; Guichardon 1996) that its value was inversely related to the ionic strength of the solutions employed, following the relationships given in Eqs. (15) – (16).

$$\log k_2 = 9.28 - 3.66\sqrt{I} \quad ; I \leq 0.166\ \text{M} \tag{15}$$

$$\log k_2 = 8.38 - 1.51\sqrt{I} + 0.24\,I \quad ; I \geq 0.166\ \text{M} \tag{16}$$

where I is the ionic strength of a solution, given by Eq. (17).

$$I = \frac{1}{2}\sum_{\text{i=all species}} C_i z_i^2 \tag{17}$$

where C_i is the molar concentration of species i and z_i is its charge number.

Kölbl et al. (Kölbl et al. 2013a) tested various salts for their influence on the Dushman reaction and reported that no other salts besides sulfates (which were used in the studies of *Guichardon and Falk* (Guichardon and Falk 2000; Guichardon 1996)) seemed to have an effect on the triiodide yield in a Villermaux-Dushman protocol. Therefore, the authors suggested that a lower triiodide yield might actually be caused by sulfate acting as a base. In contrast, *Baqueiro et al.* investigated the influence of the ionic strength based on the addition of $NaClO_4$ (Baqueiro et al. 2018). The authors found

that an increase in the ionic strength also increased the triiodide yield. Moreover, *Guichardon et al.* conducted a revision on their kinetics in 2016. The authors reported that, contrary to their earlier work, the reaction rate constant k_2 was actually increasing with increasing ionic strength. These revised values were, however, determined exclusively for the use of sulfuric acid, keeping the fifth-order law (Eq. (12)) and considering the second dissociation constant of sulfuric acid (Guichardon and Ibaseta 2016). Fig. 8 shows a comparison of the relationship between the revised and the previously suggested reaction rate constant k_2 and the ionic strength of the solution. As can be obtained, the previously suggested values (Guichardon2000) are negatively influenced by the ionic strength and decrease by orders of magnitude from ~10^9 to ~10^7 for an ionic strength between 0 M and 1 M. In contrast, the revised reaction rate constant (Guichardon2016) increases with an increasing ionic strength and can be described by Eq. (18) with a coefficient of determination of 0.998. Thus, for I = 0.3 M the difference between the two reaction rate constants is two orders of magnitude and should be taken into consideration for modeling calculations (Chapter 5.2.2).

$$k_2 = 8.23 \cdot 10^8 \cdot e^{(5.01 * I)} \tag{18}$$

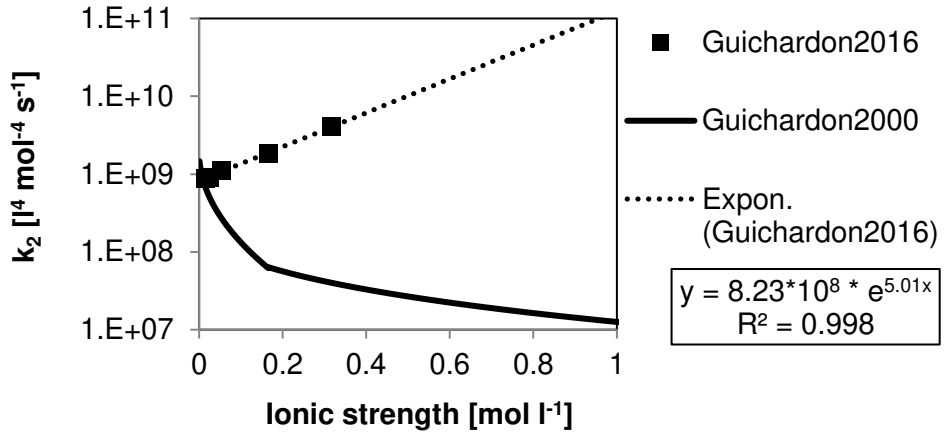

Fig. 8. Evolution of the reaction rate constant k_2 over the ionic strength as reported by *Guichardon et al.* in 2000 and 2016 (Guichardon and Ibaseta 2016; Guichardon et al. 2000).

The reaction rate (r_3) of the equilibrium reaction (iii) can be expressed as given in Eq. (19) and has not been disputed in the literature so far.

$$r_3 = k_3[I_2][I^-] - k_3'[I_3^-] \tag{19}$$

where k_3 is 5.9 · 10^9 l mol^{-1} s^{-1} and k_3' is 7.5 · 10^6 s^{-1} (Guichardon 1996; Guichardon et al. 2000).

3.3 Materials and Methods

3.3.1 Experimental Setup

The experimental setup in this chapter was designed to emulate an STR at the laboratory scale. As the mixing vessel, a 0.250-l Erlenmeyer flask (Schott, Mainz, Germany) was used. The liquid in this vessel was agitated by a magnetic stir bar with a size of 30.4 mm x 6.0 mm, which was propelled by a magnetic stir plate of the type RH basic 2 (IKA, Staufen, Germany). For the addition of acid, a syringe pump of the type Microlab 500 Series (Hamilton, Reno, USA) was equipped with a 0.0005-l syringe and connected to the acid feed tank and the acid outlet. The optical density of each sample was measured at 353 nm in a single-beam spectrophotometer of the type UVmini-1240 (Shimadzu, Kyoto, Japan) with quartz glass cuvettes of the type 104.002-QS (Hellma Analytics, Müllheim, Germany) with an optical path length of 10 mm. The pH value of the samples was measured with a pH meter of the type inoLab pH7110 and an electrode of the type SenTix81 (both WTW, Wertheim, Germany).

3.3.2 Experimental Procedure

3.3.2.1 Villermaux-Dushman Protocol

Each experiment was conducted according to the same protocol. First, a fresh batch of buffer solution was prepared, and 0.0117 mol l^{-1} of potassium iodide (KI) and 0.00233 mol l^{-1} of potassium iodate (KIO_3) were added under stirring. Thus, the total concentration of all iodine species was 0.014 mol l^{-1}, corresponding to a pH* of 7.1 (Appendix A.1). Then, 0.125 l of the buffer solution was added into the Erlenmeyer flask and positioned in the mixing setup. The stirrer was started to agitate the solution at a constant speed of 1000 rpm throughout all experiments. Then, the syringe pump was started. Subsequently, 0.0005 l of the respective acid was dropped into the stirred buffer solution over a time of 120 s in the form of single droplets. Thus, the volumetric ratio of both liquids was 250. The acid outlet of the syringe pump was positioned in a way that each droplet was impinging on the rim of the rotating vortex. After completing the acid addition, the stirrer was kept running for an additional 10 s before it was shut off, and a 0.001 l sample was taken from the mixture. The respective change in the buffer volume was considered in the calculation of the segregation index. The mixture sample's absorption at 353 nm was then measured photometrically and the respective triiodide concentration was calculated according to Eq. (4). In preliminary experiments, the molar

extinction coefficient was determined to be 2,462 $m^2\ mol^{-1}$. This value is in good agreement with values from the literature for other single-beam spectrometers (2,561 $m^2\ mol^{-1}$ (Hofinger 2013) and 2,396 $m^2\ mol^{-1}$ (Guichardon and Falk 2000)). The complete procedure (step) was successively repeated five times (run), according to the method of successive injections suggested by *Guichardon and Falk* (Guichardon and Falk 2000), to reduce the influence of the experimental error on the results. Consequently, the absorption of subsequent steps was calculated as a difference to the absorption of the preceding step. For each investigated concentration of acid and buffer, and each investigated combination, three runs were conducted. In this way, each value shown in the results section is the mean of 15 steps, with the error bar representing the standard deviation.

3.3.2.2 Investigations on the Buffer

To compare the commonly used boric acid buffer with the recently suggested phosphate buffer, the same experiments were conducted with both buffer substances at equal buffer concentrations. As the base case, the concentrations suggested by *Pinot et al.* (K_2HPO_4 = 0.09 mol l^{-1}, KH_2PO_4 = 0.02 mol l^{-1}) were used (Pinot et al. 2014). Both the buffer base and the buffer acid concentrations were then varied in subsequent experiments. All other concentrations and the hydrodynamic conditions were kept constant. For experiments with boric acid buffer, the respective concentrations of $H_2BO_3^-$ and H_3BO_3 were used. The concentration of H_2BO_3 was obtained by adding the equivalent amount of NaOH to a solution of H_3BO_3. The total buffer concentration $C_{B,total}$ in each experiment, i.e., the sum of all buffer ions in solution, was calculated according to Eq. (20).

$$C_{B,total} = [AH]_0 + [A^-]_0 \tag{20}$$

where $[AH]_0$ is the initial concentration of the respective buffer base ($H_2BO_3^-/HPO_4^{2-}$), before mixing with the acidic solution, and $[A^-]_0$ is the initial concentration of the respective buffer acid ($H_3BO_3/H_2PO_4^-$), also before mixing. The acid used in these experiments was HCl at 0.2 mol l^{-1}. An overview of all concentrations used in the investigations on the buffer concentration is given in Tab. 5 (Appendix A.2). To assess sample stability, the relative OD difference in regard to the OD value directly after mixing was calculated according to Eq. (21).

$$\text{Relative OD difference} = \frac{OD_0 - OD_t}{OD_0} \tag{21}$$

where OD_0 is the initial OD value directly after mixing and OD_t is the OD value at a given time.

3.3.2.3 Investigations on the Acid

To investigate the influence of the acid on the apparent mixing efficiency, the same experiments were conducted with HCl, H_2SO_4, and $HClO_4$ at varying concentrations. All acids – and H_2SO_4 in particular – were assumed to be fully dissociated for the design of experiments (dissociation degree $\alpha_{diss} = 1.00$). The added acid volume and all other concentrations, as well as the hydrodynamic conditions, remained constant. The buffer concentrations for these experiments were $HPO_4^{2-} = 0.09$ mol l^{-1} / $H_2PO_4^- = 0.02$ mol l^{-1} for the phosphate buffer and $H_2BO_3^- = 0.09$ mol l^{-1} / $H_3BO_3 = 0.09$ mol l^{-1} for the boric acid buffer. The concentration of $H_2BO_3^-$ was again obtained by adding the equivalent amount of NaOH to a solution of H_3BO_3.
To further investigate the influence of SO_4^{2-} independently of sulfuric acid, potassium sulfate (K_2SO_4) was added to the acidic solution in further experiments with HCl. Based on a similar experiment by *Kölbl et al.* (Kölbl et al. 2013a) with $HClO_4$, the concentration of SO_4^- was adjusted by adding K_2SO_4 in half-stoichiometric ratio to the acid. Furthermore, these experiments were conducted with phosphate buffer at the following concentrations: $HPO_4^{2-} = 0.09$ mol l^{-1} / $H_2PO_4^- = 0.02$ mol l^{-1}.
An overview of all concentrations utilized in the investigations on the acid concentration is given in Tab. 6 (Appendix A.2).

3.4 Experimental Results

3.4.1 Investigations on the Buffer

The two most important requirements for a buffer in the Villermaux-Dushman protocol are first its ability to facilitate reproducible experimental conditions over a wide concentration range and second its ability to provide stable samples. To investigate the first point, the resulting segregation indices as a function of the total buffer concentration of phosphate buffer and boric acid buffer are shown in Fig. 9.
As can be read from Fig. 9, the resulting segregation indices for the boric acid buffer are remarkably higher than those for the phosphate buffer for all investigated buffer concentrations. This finding is in agreement with the results from *Baqueiro et al.*, who investigated a total buffer concentration of 0.2 mol l^{-1} (Baqueiro et al. 2018). Furthermore, the segregation index is almost independent of the total buffer concentration for the boric acid buffer. This result would also be expected, as the amount of H_3BO_3 in solution should have no influence on the Villermaux-Dushman protocol and the amount of $H_2BO_3^-$ is taken into consideration in the segregation index (Eqs. (7) – (9)).

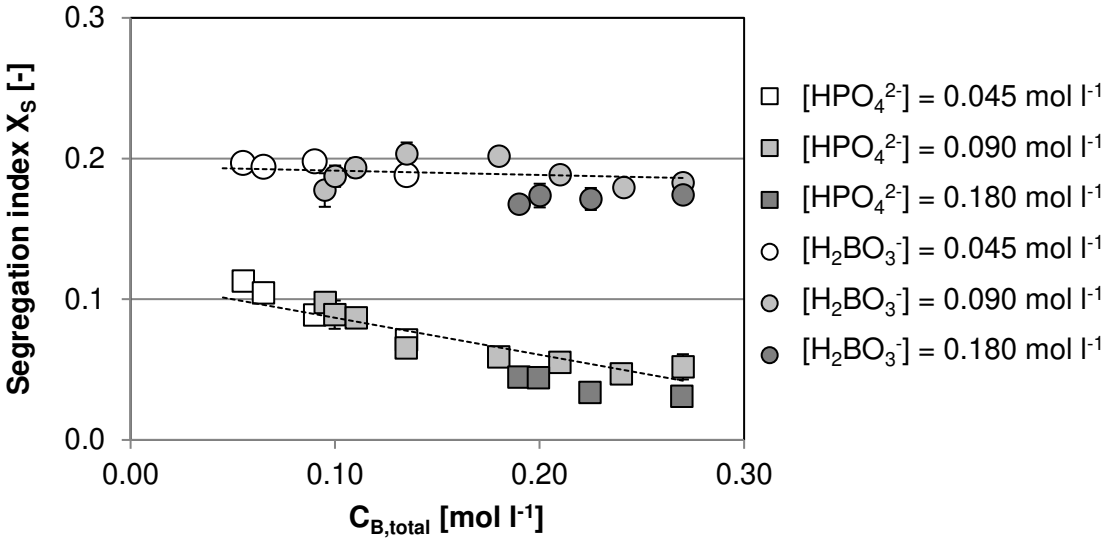

Fig. 9. Comparison of segregation indices for different total buffer concentrations of boric acid buffer and phosphate buffer. Lines are provided to guide the eye. Error bars depict the standard deviation.

However, for the phosphate buffer, decreasing segregation indices with an increasing total buffer concentration are obtained. These findings can be explained by the chemical nature of the phosphate buffer. In contrast to H_3BO_3, each $H_2PO_4^-$ molecule, acting as the buffer acid in the phosphate buffer solution, can bind one additional H^+ molecule depending on the H^+ concentration, i.e., the pH value. The dependency of each phosphate species' concentration on the pH value can be visualized in a Hägg diagram (Fig. 55, Appendix A.1). While the average working pH was adjusted to be between 6.4 and 8.2 for the phosphate buffer, the actual H^+ concentration in and around a diffusing acid droplet was significantly higher. In this way, some H^+ molecules were also bound by the buffer acid to form H_3PO_4 and therefore not available for the Dushman reaction. With a progressing mixing of the liquids, the pH value returned to the average working pH and the excess H^+ bound by $H_2PO_4^-$ was again released. However, due to the advanced state of mixing, no local surplus of protons necessary for the Dushman reaction could be formed anymore. Therefore, lower segregation indices were obtained for the phosphate buffer. Based on these observations, it can be concluded that the initial assumption, i.e., $H_2BO_3^-$ (Eq. (9)) is fully interchangeable with HPO_4^{2-} (Eq. (11)) as the buffer base in the Villermaux-Dushman protocol, is not valid at all concentrations. To investigate the buffers' influence on the sample stability before mixing, the absorption of the samples of each initial buffer base concentration was measured for 10 min after preparation. The resulting OD values after 10 min are shown in Fig. 10 as a function of the buffer solution's pH value. As can be obtained from the diagram, no influence on the absorption can be found for phosphate and boric acid buffers for

pH > pH* (pH* = 7.1 for a total iodine concentration of 0.014 mol l^{-1}). Below pH*, the solutions, however, start to form iodine and triiodide, as would be expected according to the corresponding Pourbaix calculations (Appendix A.1). This effect becomes stronger with decreasing pH value.

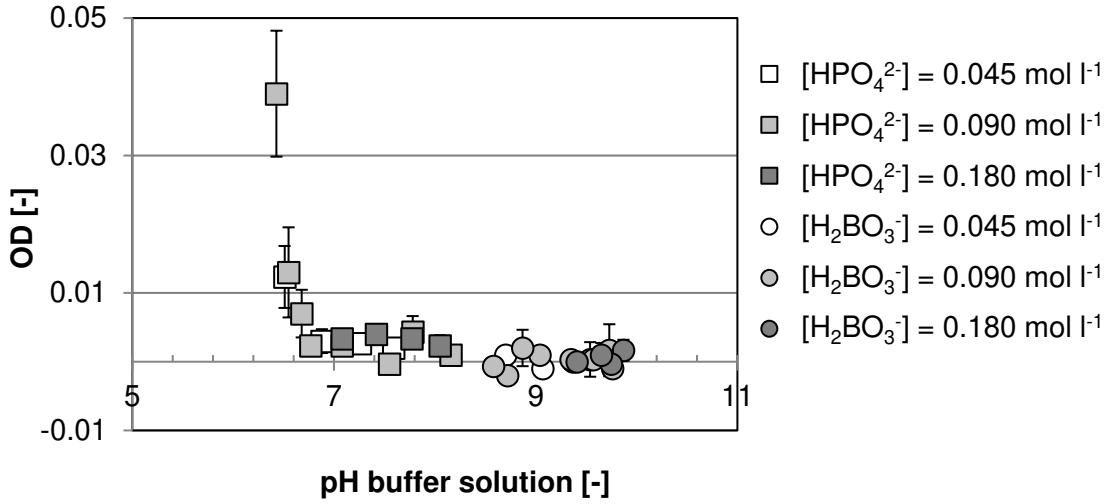

Fig. 10. OD of buffer solution samples before mixing with different initial buffer base concentrations at 353 nm, 10 min after preparation, as a function of the pH value of the prepared buffer solution. Error bars depict the standard deviation.

To further investigate the buffers' influence on the sample stability after mixing, the absorption of the samples of each initial buffer base concentration was measured once directly after mixing and then again 10 min after mixing. The resulting relative OD difference after 10 min, calculated according to Eq. (21), is shown in Fig. 11 as a function of the mixed solution's pH value. As can be drawn from Fig. 11, no clear trend with respect to the pH value can be deduced. Furthermore, the higher relative differences in absorption seem to be related to the higher buffer concentrations, which can be explained by a constant absolute difference. While it would be expected according to Appendix A.1 and the results from *Pinot et al.* (Pinot et al. 2014) that a lower pH value of the phosphate buffer would be beneficial, as it slows down the dismutation of iodine to iodate, no such effect is visible over 10 min. Instead, this relatively fast sample decay could be attributed to the evaporation of volatile iodine species (Lin 1981) or their reactive oxidation due to small amounts of oxygen dissolved in the mixed samples (Fournier et al. 1996b). Further data points on the sample stability over time are summarized in Appendix A.4.

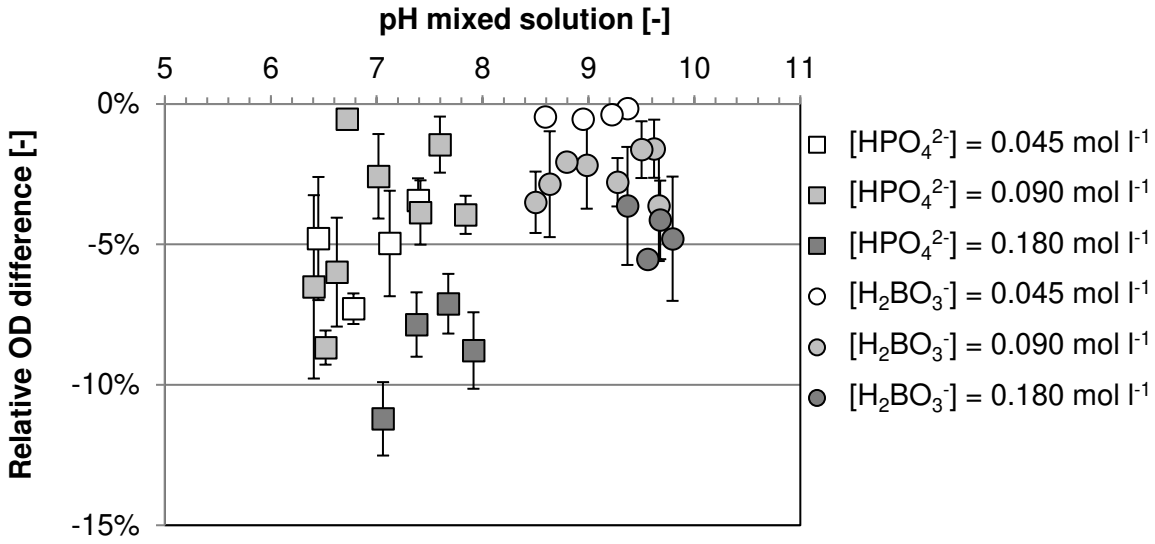

Fig. 11. Relative difference of OD of mixed solution samples with different initial buffer base concentrations at 353 nm, 10 min after mixing compared to directly after mixing, as a function of the pH value of the mixed solution. Error bars depict the standard deviation.

3.4.2 Investigations on the Acid

The OD values resulting from Villermaux-Dushman protocols with a boric acid buffer and H_2SO_4 and HCl are shown in Fig. 12 as a function of the nominal initial proton concentration of the acid. The respective OD values resulting from the experiments with a phosphate buffer and H_2SO_4, HCl, and $HClO_4$ are shown in Fig. 13 as a function of the nominal initial proton concentration of the acid. For this first comparison, all acids are initially assumed to be fully dissociated under all experimental conditions (dissociation degree $\alpha_{diss} = 1.00$).

As can be obtained from Fig. 12 and Fig. 13, remarkably smaller OD values are measured for H_2SO_4 than for HCl for the nominally same initial proton concentrations in the acidic solutions. In boric acid buffer (Fig. 12), a mean OD value of 0.578 is obtained with HCl at the highest initial proton concentration of 0.4 mol l^{-1}, but only a mean OD value of 0.260 is obtained with sulfuric acid. Thus, the mean OD value for H_2SO_4 is 55 % lower, despite the nominally same initial proton concentration.

Similarly, a mean OD value of 0.394 is obtained with 0.4 N HCl in phosphate buffer (Fig. 13), but a mean OD value of only 0.168 is obtained with 0.4 N H_2SO_4 (57 % difference). These differences can be attributed to two opposite effects.

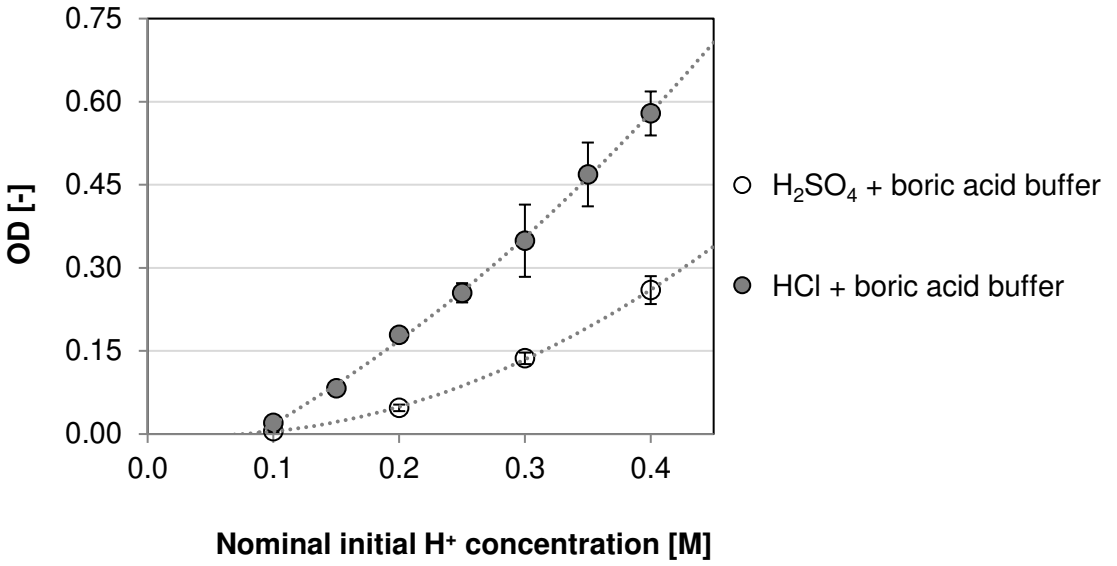

Fig. 12. OD as a function of the H^{+}_{0} concentration, obtained with boric acid buffer and HCl, and boric acid buffer and H_2SO_4. Both acids are assumed to be fully dissociated under all experimental conditions (α_{diss} = 1.00). Lines are provided to guide the eye. Error bars depict the standard deviation.

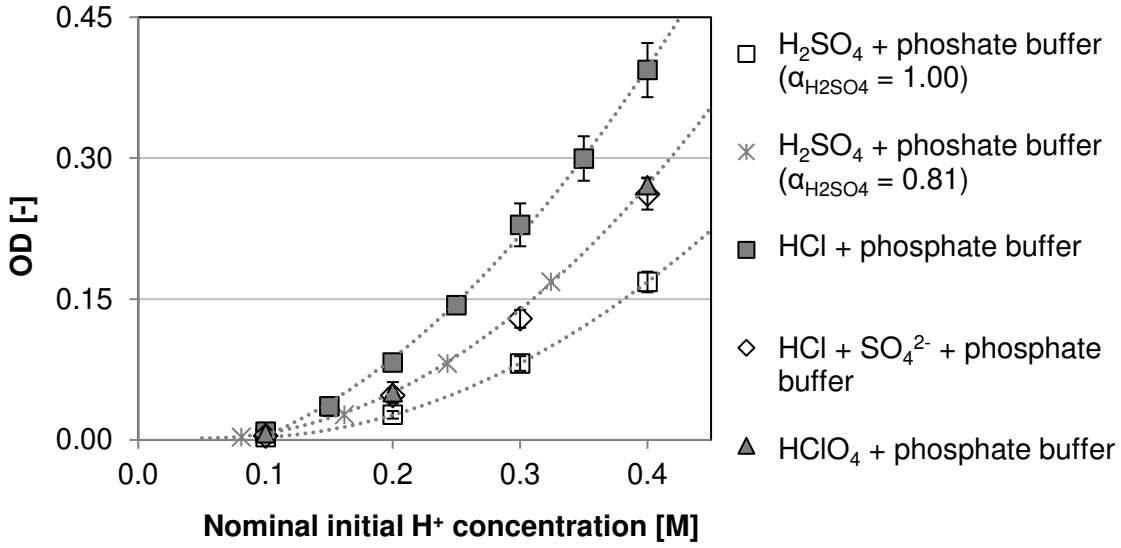

Fig. 13. OD as a function of the H^{+}_{0} concentration, obtained with phosphate buffer and HCl, a solution of HCl and potassium sulfate, H_2SO_4, and $HClO_4$. HCl and $HClO_4$ are assumed to be fully dissociated under all experimental conditions (α_{diss} = 1.00). Lines are provided to guide the eye. Error bars depict the standard deviation.

First, the initial assumption that H_2SO_4 was fully dissociated throughout the whole mixing process must be rejected for the utilized experimental conditions. A similar conclusion was drawn by *Kölbl et al.* (Kölbl et al. 2013a) and *Guichardon and Ibaseta* (Guichardon and Ibaseta 2016) from their experiments. However, the incomplete dissociation can now be quantified with respect to the experiments with $HClO_4$ (Fig. 13), which was suggested by *Kölbl et al.* (Kölbl and Schmidt-Lehr 2010) as a reliable base case. Assuming an average dissociation degree of H_2SO_4 ($\alpha_{H_2SO_4}$) of only 0.81 throughout the mixing process, the results for H_2SO_4 align with the curve for $HClO_4$ (Fig. 13). In this case, an initial H_2SO_4 concentration of 0.2 mol l^{-1} correlates to an effective proton concentration of 0.324 mol l^{-1} during the mixing process, instead of 0.4 mol l^{-1} for $\alpha_{H_2SO_4}$= 1.00. Second, a catalytic effect of chloride ions on the Dushman reaction can be confirmed. In the investigated concentration range, the OD values increase by up to 45 % with respect to ClO_4^- (Fig. 13). Such a catalytic effect was suggested by *Schmitz* (Schmitz 1999), based on earlier studies by *Beran and Bruckenstein* (Beran and Bruckenstein 1968). The author proposed a reaction mechanism involving I_2O_2 as the key intermediate. In contrast, the hypothesis of I_2Cl^- formation, as suggested by *Guichardon et al.* (Guichardon et al. 2000), is disproven, as it would have resulted in lower OD values for HCl than those for $HClO_4$. Additionally, the results obtained with phosphate buffer and a solution of HCl and potassium sulfate are shown in Fig. 13. Analogous experiments were conducted by *Kölbl et al.* (Kölbl et al. 2013b) with $HClO_4$ and potassium sulfate and by *Baqueiro et al.* with $HClO_4$ and sodium sulfate (Baqueiro et al. 2018). The authors found that the obtained OD values were almost identical to those obtained with the nominally equivalent concentration of H_2SO_4. This finding could not be replicated for HCl and potassium sulfate in this chapter. Instead, the results are almost identical to the OD values obtained with $HClO_4$ alone (Fig. 13). In this sense, the presence of chloride ions seems to facilitate the Dushman reaction to the same extent to that it is negatively affected by the incomplete dissociation of H_2SO_4 during the mixing process. Furthermore, *Guichardon and Ibaseta* reported that increasing the potassium sulfate concentration in combination with H_2SO_4 strongly accelerated the Dushman reaction (Guichardon and Ibaseta 2016). However, no such effect could be observed in this chapter with HCl and potassium sulfate. The concentration of the latter was increased half-stoichiometrically with the concentration of the acid. Instead, the OD values increase only as much as it would be expected due to the increase of the proton concentration. For good measure, the ionic strength for each combination of buffer and acid was also calculated (Tab. 7, Appendix A.3). However, no strong correlation to the results shown in Fig. 12 or Fig. 13 could be found.

3.5 Conclusions and Outlook

Due to the re-assessment of boric acid as a CMR substance, and due to considerations on sample stability, phosphate buffer was suggested by *Pinot et al.* as a viable alternative in a Villermaux-Dushman protocol. However, only limited information on the interchangeability of these two buffers was available so far. Therefore, these two buffers were compared under analogous conditions over a broad concentration range in this chapter. It was found that the use of phosphate buffer results in lower optical density values than those for the use of boric acid buffer for all investigated buffer concentration, and a dependency of the optical density values on the total buffer concentration was observed for phosphate buffer. It can be concluded that the ability of phosphate to bind an additional proton in combination with the initial pH peak during the mixing process is responsible for these effects. Furthermore, investigations on the sample stability before and after mixing revealed that boric acid buffer offers a wider concentration range for stable conditions. While it was assumed in the literature that phosphate buffer could offer more stable samples after mixing due to its more adequate pH range, no dependency of the sample stability on the final pH value could be found. Instead, the decay of Villermaux-Dushman samples after mixing is likely to be caused by the evaporation of iodine species or the reactive oxidation of iodine due to oxygen dissolved during the mixing process, rather than its thermodynamic dismutation. In practical terms, samples, e.g., from the mixing process in an RPB, should be immediately closed and analyzed swiftly. Overall, the phosphate buffer suggested by *Pinot et al.* is suitable for a Villermaux-Dushman protocol if used only within a limited concentration range. Otherwise, especially for comparison with literature data, phosphate buffer should be rejected in favor of a boric acid buffer. As a suitable compromise between sample stability and method sensitivity, the combination $[H_2BO_3^-]$ = 0.09 mol l^{-1} and $[H_3BO_3]$ = 0.02 mol l^{-1}, together with the iodide and iodate concentrations used in this chapter, appears reasonable for mixing experiments in an RPB and will be used in chapter 5. Furthermore, an acid once chosen for a Villermaux-Dushman protocol remains non-interchangeable, if results obtained at different concentrations should be quantitatively comparable. Especially for the investigation of very fast mixing processes, hydrochloric acid can, however, enable a higher sensitivity of the Villermaux-Dushman protocol than sulfuric acid or perchloric acid could. In addition, the influence of sulfate and chloride ions on the Dushman reaction – and their simultaneous interaction – could offer a new perspective on the reaction mechanism and should be investigated in more detail in future research.

4 LITERATURE STUDY *

In this chapter, the state of the art in the field of liquid phase reactive mixing in Rotating Packed Beds, as assessed by means of the Villermaux-Dushman protocol, is presented and critically analyzed. Thus, also gaps in the current knowledge are elucidated. Furthermore, a comparison with results for other mixing devices is conducted.

4.1 Introduction

In this chapter, the current literature knowledge on the utilization of RPBs for continuous reactive mixing is presented in the form of a literature study and results previously obtained by other authors are thoroughly analyzed. On this basis, general literature trends for the most important operational and design parameters are deduced.

As most publications on mixing in RPBs focus on the assessment of structured packings with a Villermaux-Dushman protocol, this combination will also be in the focus of this chapter. To further assess the technological potential in this field, mixing results from RPBs will be compared with the results of other continuous mixing devices.

Since many authors have used different concentrations of the key compounds of the buffer and the acid, a quantitative comparison based on the Villermaux-Dushman protocol can sometimes lead to misinterpretations. Therefore, this analysis focuses on a qualitative comparison. However, in the case of a direct comparison of segregation indices, the utilized concentrations are considered. A more thorough comparison of results based on a concentration-independent model parameter will be presented in chapter 5.6.

---

* Parts of this chapter have been published as:
Review and Analysis of Micromixing in Rotating Packed Beds (2018), Wenzel, D.; Górak, A.; Chem. Eng. J. (345), pp. 492-506.
Liquid Distribution and Mixing in Rotating Packed Beds (2019); Wenzel, D.; Ojeda, L.S.; Gerdes, N.; Steinbrink, M.; Górak, A.; Ind. Eng. Chem. Res. 58 (15), pp. 5919-5928.
Reactive mixing in rotating packed beds: on the packing's role and mixing modeling (2019); Wenzel, D.; Nolte, K.; Górak, A.; Chem. Eng. Proc.: P.I. (143), published online, doi: 10.1016/j.cep.2019.107596.

4.2 Fundamentals

4.2.1 Mixing in RPBs

The two key principles to ensure fast mixing in a continuous mixing device are (1) creating a region of high energy dissipation and (2) ensuring liquid streams pass through this region (Yang et al. 2005). Indeed, a high energy dissipation rate was found to be the only relevant parameter to obtain fast mixing in all continuous mixing devices (Falk and Commenge 2010). Therefore, to improve mixing processes in RPBs, operational parameters and design parameters need to be optimized to either increase the energy dissipation rate or improve the passage of liquid through the region of highest energy dissipation. All improvements in micromixing can further be attributed to a decreasing size of liquid aggregates and an increasing relative velocity of impingement among these liquid aggregates (Chen et al. 2004). An increasing relative velocity of impingement can again be related to a higher energy dissipation rate.
Because RPBs are active mixers, they are capable of providing high rates of energy dissipation. At the same time, liquids can be applied to the zone of most intense mixing in the form of small liquid aggregates by means of a proper liquid distribution design. Therefore, it seems reasonable to investigate RPBs for their utilization in mixing processes, as well as the liquid distribution design in RPBs in particular. To achieve a fair assessment of the micromixing capabilities of RPBs, it is further necessary to assess RPBs and other continuous mixing devices in the context of the same mixing task and by means of comparable parameters (Neumann et al. 2018a).

4.2.2 Adaptations of the Method

Boric acid ($H_2BO_3^-/H_3BO_3$) and sulfuric acid are most commonly used as the buffer substance and the acid in investigations on the continuous mixing in RPBs by means of the Villermaux-Dushman protocol. As shown in the previous chapter, hydrochloric acid could allow for higher sensitivity of the Villermaux-Dushman protocol in very fast mixing processes compared to sulfuric acid and would be especially suitable for the investigation of mixing in RPBs (Chapter 3.5). However, it has not been utilized for RPB investigations in the literature so far.

In order to calculate the segregation index for continuous mixing in RPBs, Eqs. (5) – (9) need to be adapted as presented in Eqs. (22) and (23).

$$K_{eq} \approx \frac{[I_3^-]}{[I_2] * \left([I_{,0}^-] * \frac{\dot{V}_{buffer}}{\dot{V}_{buffer} + \dot{V}_{acid}} \right)} \tag{22}$$

$$X_S = \frac{Y}{Y_{ST}} = \frac{\frac{2 * (\dot{V}_{buffer} + \dot{V}_{acid}) * ([I_2] + [I_3^-])}{\dot{V}_{acid} * [H_0^+]}}{\frac{6 * [IO_{3,0}^-]}{6 * [IO_{3,0}^-] + [H_2BO_{3,0}^-]}} \tag{23}$$

where $\dot{V}_{buffer}$ and $\dot{V}_{acid}$ are the volumetric flow rates of the buffer solution and the acid. The continuous ratio of these two flow rates can further be expressed in terms of the so-called volumetric ratio (Eq. (24)).

$$\text{volumetric ratio} = \frac{\dot{V}_{buffer}}{\dot{V}_{acid}} \tag{24}$$

4.2.3 Sensitivity of the Method

In addition to the considerations on sensitivity presented in chapter 3.2.2, also the residence time τ needs to be considered for continuous mixing processes. The residence time is the time in which a fluid element remains within the continuous flow apparatus.

For conditions under which t_m and t_r are in the same range but are both significantly shorter than the residence time τ, high sensitivity is achieved in the front part of the apparatus but influences in the back end are “cut off”. Thus, the results only show influences and changes made within the front part. In contrast, for conditions under which t_r and τ are in the same range but are both significantly shorter than the micromixing time t_m, the reaction is completed under incomplete mixing conditions. Thus, the results are dominated by macro- and mesomixing and influences “behind” the apparatus. For conditions under which t_m and τ are in the same range but are both significantly larger than the characteristic reaction time t_r, influences within the whole apparatus are described, but at the cost of sensitivity. Finally, conditions under which t_m, t_r, and τ are in the same range depict the ideal case, in which influences in the whole apparatus can be characterized with the highest possible sensitivity of the method.

4.2.4 Limitations of the Method

Generally, it should be kept in mind that competitive parallel reaction protocols cannot give space-resolved information for the applied mixer but only integral information over the whole mixing space-time (Falk and Commenge 2010; Kölbl et al. 2011). Thus, the

obtained results are not representative of all mixing processes occurring in the mixer (Kölbl et al. 2011). Instead, mixing processes in regions of stoichiometric H^+ deficiency are omitted, while mixing processes in regions of very high energy dissipation are over-represented. Therefore, the method is particularly suitable to describe the interaction of two fluids at the beginning of a mixing setup, such as the liquid distribution and impingement zone for RPBs, but unsuitable to properly quantify mixing phenomena that occur solely at the end of a mixing setup or even throughout a series of mixers (Panić et al. 2004). To counter this limitation, *Panić et al.* proposed to use the phase transfer of a solvatochromic dye between two immiscible fluids to complement the results obtained with the competitive parallel Villermaux-Dushman protocol (Panić et al. 2004). Further alternatives for mixing sensitive reaction schemes were given by *Bourne* (Bourne 2003).

Furthermore, the systematic presence of a gas phase in an RPB should be noted. Therefore, the sensitivity of the method could be reduced in the case of evaporation or oxidation of iodine species (Chapter 3.4). However, the influence of the gas phase in the RPB on the Villermaux-Dushman protocol has not been quantified in the literature so far.

Moreover, a comparison of different RPBs and different mixing apparatuses based on a universal, concentration-independent parameter from a mixing model or the energetic efficiency of mixing would be preferable to a comparison based on the segregation index X_S. However, several limitations currently restrict such an approach. The concept of energy efficiency of mixing was proposed by *Ottino et al.* (Ottino et al. 1979; Ottino and Macosko 1980) and has been used, e.g., to assess the performance of other continuous mixing devices as micromixers (Falk and Commenge 2010). Its calculation is based on knowing either the shear rate or the rate of energy dissipation. However, these parameters are not provided in the literature for RPBs. The rate of energy dissipation can further not be directly measured, but only be derived from correlations, e.g., from the pressure loss. Unfortunately, no such correlations are currently available for RPBs. For the sake of completeness, the approach of *Yang et al.* (Yang et al. 2005) should additionally be mentioned. The authors presented a way to derive the energy dissipation rate either through mixing models, which are based on multiple assumptions themselves as elaborated in chapter 5.2.2, or from assumptions regarding the film thickness, liquid velocity, and liquid flow pattern, which only apply to some mixing situations in an RPB. Therefore, a comparison based on such a parameter seems unlikely to give more accurate information than a comparison based on the segregation index.

4.3 Experimental Results in the Literature

The structure of the conducted literature study is shown in Fig. 14. With respect to operational parameters, literature results on the rotational speed, the total liquid flow rate, and the volumetric ratio are presented in this chapter. Supplementary results on the viscosity and correlations between operational parameters and the segregation index are presented in Appendices B.2 and B.3. In addition to the operational parameters, the influence of important RPB design parameters on the segregation index is investigated. These design parameters include characteristics of the packing as well as characteristics of the liquid distribution.

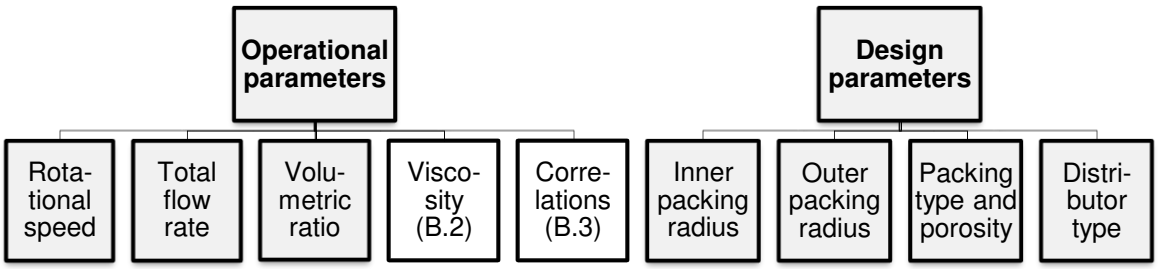

Fig. 14. Schematic overview of the conducted analysis.

4.3.1 Operational Parameters

In this subchapter, literature results on the influence of different operational parameters on the segregation index are presented. An overview of the range of each parameter investigated in the analyzed publications is shown in Tab. 9 (Appendix B.1).

4.3.1.1 Rotational Speed

The influence of the rotational speed of the packing was investigated in all studied publications. It was unanimously found that the segregation index decreased with increasing rotational speed (Chen et al. 2004; Chen et al. 2006; Yang et al. 2015b; Yang et al. 2009; Chu et al. 2015; Jiao et al. 2012). This is to be expected: the higher the rotational speed of the packing, the more vigorously the impinging liquid particles are fragmented. This means that the liquid is subjected to a higher rate of energy dissipation, leading to faster micromixing. However, most authors reported that the influence of the rotational speed on the segregation index also decreased with higher rotational speed (Chen et al. 2004; Chen et al. 2006; Yang et al. 2015b; Jiao et al. 2012), while only *Chu et al.* reported a linear relationship (Chu et al. 2015).

The rotational speed of the packing can also be expressed as the tangential velocity at

a particular packing radius. As the impingement zone was found to be most influential for micromixing (Yang et al. 2005), the tangential velocities (u_{tang}) at the inner packing radius for the minimum and maximum rotational speed were calculated according to Eq. (25), where r_i is the inner packing radius and ω is the rotational speed. An overview of the results is given in Tab. 10 (Appendix B.1). Its influence on the segregation index will be discussed in chapter 4.3.2.1.

$$u_{tang} = 2\pi * r_i * \omega \quad (25)$$

4.3.1.2 Total Liquid Flow Rate

Another crucial operational parameter for liquid-phase processes in an RPB is the flow rate of the liquids. In an RPB, the liquid streams are distributed in the eye of the packing. They leave the liquid distributor in the form of a spray of droplets or a liquid jet before impinging on the rotating packing. As the cross-sectional area of the liquid distributors was fixed for each particular publication, the influence of different liquid flow rates on the segregation index for the same liquid distributor is discussed here, while the influence of the liquid distributor design is discussed in a later chapter. The investigated liquid flow rates in the literature are in the range of 10^0 l h^{-1} – 10^1 l h^{-1} (Chen et al. 2004; Chen et al. 2006; Yang et al. 2015b; Chu et al. 2015; Jiao et al. 2012) and 10^2 l h^{-1} (Yang et al. 2005; Yang et al. 2009; Jiao et al. 2012). For the rotational speed, the liquid flow rate was unanimously reported to be inversely related to the segregation index for the whole range. This could be explained by the higher velocity with which the liquid leaves the liquid distributor and impinges on the packing, leading to a higher rate of energy dissipation and faster micromixing. Furthermore, a higher liquid flow rate means a higher collision probability of fragmentized liquid elements within the packing (Chen et al. 2004). Nevertheless, most of the authors reported a sharply decreasing relative influence of the liquid flow rate on the segregation index (Yang et al. 2005; Yang et al. 2009; Chen et al. 2004; Chen et al. 2006; Yang et al. 2015b). In the lower liquid flow rate range, an increase of 250 % from 15.5 l h^{-1} to 54.0 l h^{-1} at 600 rpm decreased the segregation index by up to 45 % from 0.100 to 0.065 (Chen et al. 2006). In the higher liquid flow rate range, an increase of 33.3 % from 410.0 l h^{-1} to 546.5 l h^{-1} at 600 rpm (Yang et al. 2009) and an increase of 50 % from 410.0 l h^{-1} to 615.0 l h^{-1} at 900 rpm (Yang et al. 2005) were investigated. However, the segregation index only decreased by 8.3 % from 0.0024 to 0.0022 and by 11.8 % from 0.0068 to 0.0060, respectively. In contrast, two different authors reported a rather linear relationship (Chu et al. 2015; Jiao et al. 2012).

4.3.1.3 Volumetric Ratio

In addition to the rotational speed and the total liquid flow rate, the volumetric ratio of the two supplied liquid streams (Eq. (24)) plays an important role. However, only two authors have investigated the influence of this parameter on the segregation index (Chu et al. 2015; Jiao et al. 2012). For an RPB with an impinging stream distributor, the volumetric ratio was varied between 1 and 15 for a buffer flow rate of 70.0 l h^{-1} and a rotational speed of 1630 rpm (Jiao et al. 2012). Under these conditions, the segregation increased with an increasing volumetric ratio. Furthermore, a linear relationship between the two parameters was shown. This effect was explained by the author by the less intense impinging of the two liquid streams at higher volumetric ratios for a fixed liquid flow rate. For an RPB with a premixed distributor, the volumetric ratio was varied between 12 and 18 for buffer flow rates between 21.6 l h^{-1} and 64.5 l h^{-1} at 1200 rpm (Chu et al. 2015). Again, it was found that the segregation index increased with an increasing volumetric ratio. This can be explained in two ways. First, the increasing volumetric ratio was realized by decreasing the acid flow rate at a constant buffer flow rate, overall decreasing the liquid flow rate. However, a lower liquid flow rate also increases the segregation index, as explained above. Second, the acid concentration was increased with a decreasing acid flow rate to keep the number of protons constant. This increase in acid concentration favored the Dushman reaction under macro- and mesomixing conditions. These could be especially influential for a premixed distributor, as explained in the design parameters section. Thus, higher segregation indices were obtained for the nominally same amount of protons.

Overall, these considerations illustrate a general problem: the volumetric ratio cannot be adjusted independently from acid concentration and total liquid flow rate without changing the effective acid concentration throughout the mixing process and thus influencing the strongly concentration-dependent segregation index, which in turn leads to an unfair comparison of different volumetric ratios. This problem will continue to arise as long as no mixing model is available that is validated for all volumetric ratios.

4.3.2 Design Parameters

In this subchapter, literature results on the influence of different design parameters on the segregation index are presented. The most important packing characteristics, such as inner packing radius, outer packing radius, and packing material, are summarized in Tab. 11 (Appendix B.1), together with other key packing parameters, such as rotational axis, axial packing height, and packing porosity. The most important liquid distribution characteristics, such as distribution type, buffer outlet diameter, and acid outlet

diameter, are given in Tab. 12 (Appendix B.1). Additionally, the resulting outlet velocities for the maximum reported liquid flow rates are presented.

4.3.2.1 Inner Packing Radius

The influence of the inner packing radius on the segregation index consists of the influence of the tangential velocity at a given rotational speed and the influence of the distance from the liquid distributor. Despite this relationship, the influence of the latter has never been investigated as an independent parameter in RPBs. However, the distance from the packing can be assumed to be proportional to the inner packing radius.

Chen et al. varied the inner packing radius between 10 mm and 50 mm in their RPB-1, with a liquid flow rate of 34.3 l h^{-1} and a fixed outer radius of 60 mm (Chen et al. 2006). Thus, the packing depth also varied between 50 mm and 10 mm. The authors found that the segregation index decreased with an increasing inner radius and attributed this effect to a higher tangential velocity with increasing inner radius. The effect of an increasing distribution distance to the packing was not discussed. However, when the segregation indices at the minimum and maximum rotational speed (600 rpm and 1500 rpm) are plotted as a function of the tangential velocity (Fig. 15a) and the inner packing radius (Fig. 15b), it can be observed that the distance of the liquid distributor from the packing has a significant influence on the segregation index. While a general trend can also be identified for the tangential velocity, the curves for the minimum and maximum rotational speed are shifted (Fig. 15a). However, a clear relationship for the liquid distribution distance can be obtained if it is assumed to be proportional to the inner packing radius (Fig. 15b). This becomes especially evident when the ratio of the segregation indices at minimum and maximum rotational speed (X_S ratio, Eq. (26)) and the respective ratio of the tangential velocities (u_{tang} ratio, Eq. (27)) are plotted as a function of the inner packing radius (Fig. 16): the segregation index ratio increases with an increasing inner packing radius, while the ratio of the tangential velocity stays constant.

In conclusion, the improved micromixing with an increasing radial distance cannot only be attributed to a higher tangential velocity but also to the larger distance of the liquid distributor from the rotating packing. This positive influence on the micromixing could be explained by greater droplet dispersion for increasing distribution distances. Thus, the specific surface area of the liquid is larger, the wetting of the packing is improved, impingement occurs more vigorously, the energy dissipation rate is higher, and micromixing is accelerated.

$$X_S \text{ ratio} = \frac{X_S^{600\text{rpm}}}{X_S^{1500\text{rpm}}} \tag{26}$$

$$u_{tang} \text{ ratio} = \frac{u_{tang}^{600\text{rpm}}}{u_{tang}^{1500\text{rpm}}} \tag{27}$$

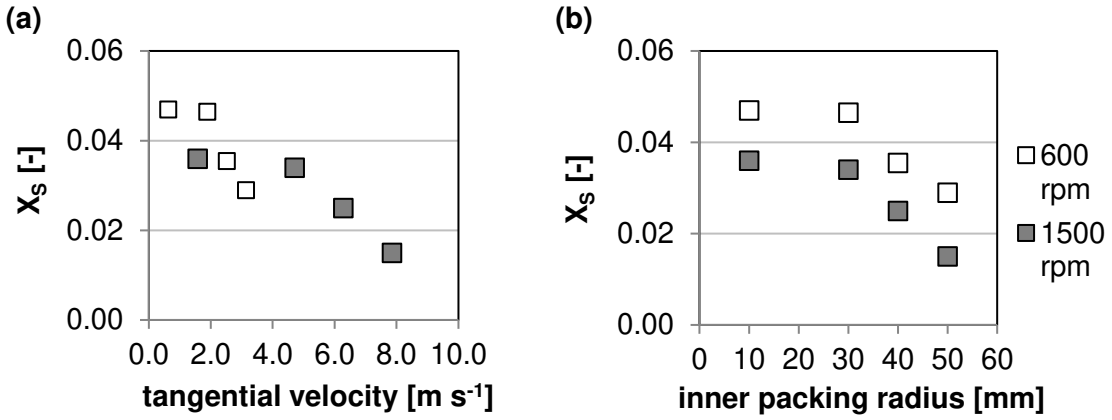

Fig. 15. Segregation index X_s at the minimum and maximum reported rotational speed as a function of (a) the tangential velocity at the inner radius and (b) the inner packing radius. Data points obtained from *Chen et al.* (Chen et al. 2006).

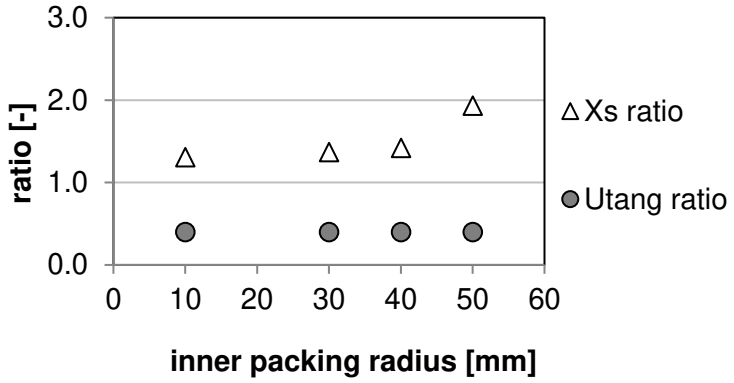

Fig. 16. Segregation index ratio and tangential velocity ratio as a function of the inner packing radius. Data points obtained from *Chen et al.* (Chen et al. 2006).

4.3.2.2 Outer Packing Radius and Radial Packing Depth

In addition to the inner packing radius, the influence of the outer packing radius was also investigated by *Chen et al.* (Chen et al. 2006). The authors varied the outer radius from 20 mm to 60 mm for their RPB-1, with a liquid flow rate of 34.3 l h^{-1} and an inner radius of 10 mm. Thus, the radial packing depth varied between 10 mm and 50 mm. The authors found that the segregation index decreased with an increasing outer radius.

However, the differences were rather small, with no clear trend at 600 rpm and 900 rpm, and a maximum difference of 12.5 % at 1500 rpm for a packing depth increase of 400 % from 10 mm to 50 mm. This minor influence was explained by the authors as an indication that the most intense micromixing occurred in the impingement zone in the first 10 mm of the packed bed. Thus, the total radial packing depth was also rather unimportant for the mixing result. This finding is in agreement with the results for the influence of the inner packing radius, where the lowest segregation index was found for the smallest radial packing depth.

Another method to investigate the influence of the packing radius and the radial packing depth on the segregation index was used by *Yang et al*. (Yang et al. 2005; Yang et al. 2009), who constructed an RPB with two symmetric rows of 11 sampling positions each, with an angular distance of 15° and a radial distance of 17 mm. The innermost sampling point was positioned at a radius of 40 mm, corresponding to a radial packing depth of 10 mm. The outermost sample point was at a radius of 210 mm, corresponding to a radial packing depth of 180 mm. However, only results up to the sample point at 159 mm were reported. The samples for each position were collected through sample tubes within the packing, which were aligned to holes in the bottom of the casing. Data points for the segregation indices in this RPB at 600 rpm and 1200 rpm, as obtained from *Yang et al.* (Yang et al. 2005), are shown in Fig. 17a as a function of the radial sampling position. The total liquid flow rate was 455.0 l h^1, the volumetric ratio was 12, and distributor pipes were used to inject the liquids. The sampling radius can also be expressed as the tangential velocity. Thus, the segregation indices are also plotted as a function of the respective tangential velocity in Fig. 17b.

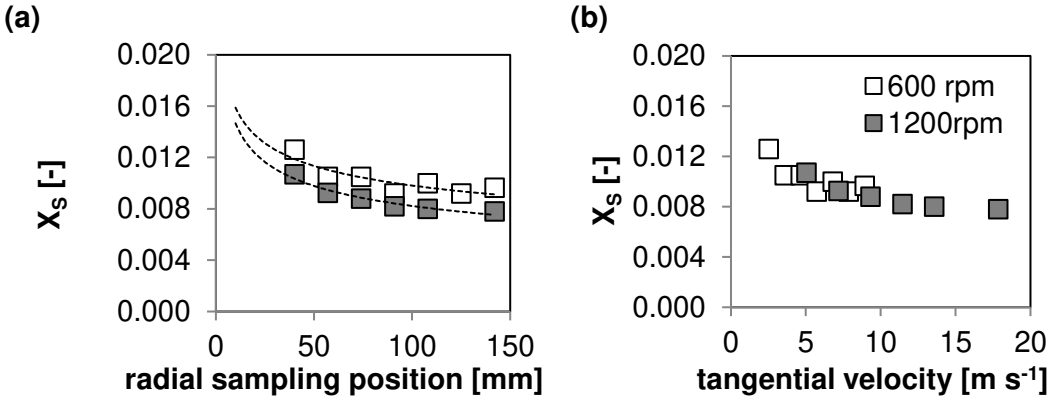

Fig. 17. Segregation index X_S at 455.0 l h^{-1} and a volumetric ratio of 12 as a function of (a) the radial sampling position and (b) the respective tangential packing velocity. Data points obtained from *Yang et al*. (Yang et al. 2005). Lines provided to guide the eye.

As can be obtained from the figures, the segregation index seems to be directly related to the tangential velocity of the packing at the respective sampling position. This influence is nevertheless rather small and decreases with an increasing radial sampling position.

For the same RPB, but with a premixed liquid distributor, additional data points were reported by *Yang et al.* (Yang et al. 2009), which are shown in Fig. 18. The total liquid flow rate of 200.0 l h^{-1} was approximately 56 % lower than in the authors' previous study, while the volumetric ratio was 9. The results for 200 rpm, 400 rpm, and 600 rpm show a rather linear dependency. However, a very different relationship is found at 1200 rpm, similar to the one shown in Fig. 17. This abrupt change in behavior could imply a shift between different flow patterns within the packing, e.g., from pore flow to droplet flow, with 900 rpm being the transition state. Thus, beneficial flow conditions that allow for faster micromixing despite the same tangential velocity could be achieved, possibly due to a better utilization of the initial packing volume. However, the results also imply that at the highest rotational speed of 1200 rpm, micromixing was already achieved before the first sampling position (40 mm), i.e, mostly in the impingement zone.

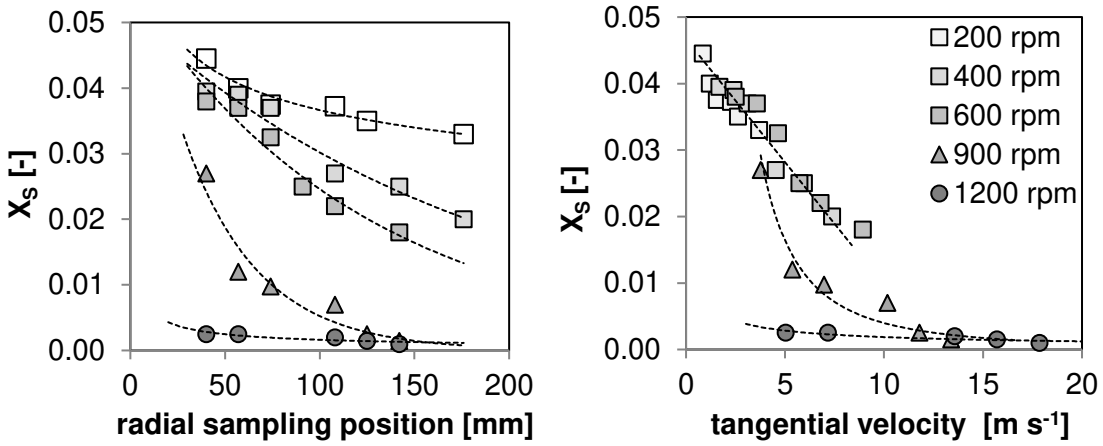

Fig. 18. Segregation index X_S as a function of the radial sampling position and the respective tangential packing velocity for a total liquid flow rate of 200 l h^{-1} and a volumetric ratio of 9. Data points obtained from *Yang et al.* (Yang et al. 2009). Lines provided to guide the eye.

4.3.2.3 Packing Type and Porosity

The influence of differently structured packing types on the segregation index was studied by *Chu et al.* (Chu et al. 2015). The authors compared a surface-modified nickel foam packing (SNP) with a non-modified nickel foam packing (NNP) and stainless steel wire mesh packing (WMP). Furthermore, NNP packings with 5 ppi (pores per inch) and

50 ppi were compared. To manufacture SNP, the NNP packing was subjected to a hydrophobic modification procedure developed by *Li et al.,* which increased the water contact angle by 26.3° from 108.5° to 134.8° (Li et al. 2007).

Overall, the foam packings allowed for lower segregation indices than the WMP. Furthermore, for the NNP lower segregation values were obtained for the packing with a smaller pore size (50 ppi). The authors attributed this to the more vigorous dispersion of the liquid into smaller elements, as well as an increased coalescence-dispersion frequency of the liquid particles (split-recombine-mixing). Additionally, the surface modification of the packing (SNP) further improved the results. This effect was attributed to a higher surface area of the liquid elements available for contact between liquid elements. Additionally, it can be assumed that the slip of the liquid elements was increased. In this way, the liquid elements could cover a longer radial distance of the packing, with more chances of coalescence-dispersion, before the tangential velocity of the packing was fully imparted on the liquid by friction and adhesion.

A comparison of WMP and ceramic foam packing (CFP) was conducted by *Zhang et al.,* who found that CFP yielded lower segregation indices than WMP (Zhang et al. 2014). Furthermore, the authors investigated ceramic foams with an aperture size of 0.83 mm and 0.25 mm and found a smaller aperture size to be beneficial for fast micromixing.

Yang et al. compared micromixing results for different WMPs with mesh diameters of 0.22 mm, 0.33 mm, 0.5 mm, and 0.8 mm (Yang et al. 2015b). The authors found that, at a volumetric ratio of 15, the segregation index decreased with a decreasing packing wire diameter, i.e., a decreasing pore size. Furthermore, it was found that the influence of the wire mesh diameter on the segregation index increased with increasing viscosity. These findings could imply a significant split-recombine-mixing effect within some parts of the packing, which would also be in agreement with the above results from *Chu et al*. (Chu et al. 2015).

4.3.2.4 Distributor Type

In the reviewed literature, the three different types of liquid distribution depicted in Fig. 3 (Chapter 2.2) were used: distributor pipes (Chen et al. 2006; Yang et al. 2005; Chen et al. 2004), premixed distributors (Yang et al. 2009; Yang et al. 2015b; Chu et al. 2015), and impinging stream distribution (Jiao et al. 2012). A detailed overview of their characteristics is given in Tab. 12 (Appendix B.1).

A direct comparison between distributor pipes and premixed distributors was conducted by *Yang et a*l. (Yang et al. 2009). For this comparison, the authors used the results from a previous study (Yang et al. 2005), where the buffer distributor pipe had 4 holes, each

3 mm in diameter, and the acid distributor pipe had 3 holes, each 1.5 mm in diameter. The premixed distributor had only one outlet with a diameter of 6 mm. The authors stated that by using the premixed distributor, the segregation indices could be reduced by two orders of magnitude. Interestingly, a longer distributor length L (Fig. 3) led to smaller segregation values. The authors attributed this to a more uniform macroscopic reactant distribution, i.e., better macromixing, before entering the RPB. Additionally, a smaller pipe angle β led to smaller segregation values. However, this result has not been discussed by the author. It should be noted that this type of investigation is based on the attempt to reduce segregation values as much as possible, not to characterize the RPB as such. Because the premixing distributor design had a large influence on the results, it is obvious that the distributor was mostly characterized, rather than the RPB. A different approach to liquid distribution is the impinging stream RPB, which was introduced by *Jiao et al*. The authors claimed that the device was an ideal micromixing reactor. However, for the same concentrations, rotational speed, volumetric ratio, and liquid flow rate, *Chen et al.* obtained a segregation index of 0.015 with distributor pipes (Chen et al. 2004), while *Jiao et al.* obtained a segregation index of 0.018 (Jiao et al. 2012). In combination with the above results for the volumetric ratio, it can be stated that the impinging stream liquid distribution is roughly as effective as the distributor pipes but distinctively harder to adjust and less flexible in operation.

4.3.2.5 Other Design Parameters

In addition to the type of distributor, the velocity, angle, and orientation at which the two liquid streams are distributed may influence the resulting segregation indices. However, no systematic investigation of the influence of these parameters was reported in the literature. Other design parameters that could have an important influence on the segregation index but have not been investigated so far are the axial height of the packing, the alignment of the packing at the inner or the outer end of the rotor (if not filling the complete rotor volume), and the rotational axis. Especially for relatively low liquid flow rates, the latter could have a large influence on the segregation index, because an evenly wetted packing may be more easily realized with a horizontal axis of rotation.

4.4 Comparison with Other Mixing Devices

In this subchapter, the above-considered RPBs with structured packings are compared to RPBs with non-structured packings and other continuous mixing devices, and differences in their mixing abilities are discussed based on the influence of operational and design parameters on the segregation index. A comparison of RPBs with other mixing devices based on model parameters is conducted in chapter 5.6.

4.4.1 RPBs with Non-Structured Packings

Lin and Tsai investigated micromixing with a Villermaux-Dushman protocol in RPB-like apparatuses with rotating blades (Lin and Tsai 2016). The 12 blades were positioned with a 30° radial distance and wrapped in stainless steel wire mesh packing. The rotational axis was vertical, and the liquids were distributed through two distributor pipes. Contrary to RPBs with a structured packing, an increasing influence of the rotational speed on the segregation index could be found for the blade-packing RPBs. Furthermore, an increasing influence of the liquid flow rate on the segregation index was reported (Lin and Tsai 2016), again contrary to the RPBs with structured packing. With an increasing viscosity, the segregation index first increased but then decreased for higher viscosities. The effect was even more pronounced at 1800 rpm than at 600 rpm. This unexpected behavior could be caused by a viscosity-induced shift of the characterized mixing zone towards the outer diameter, with a higher radial velocity and thus a higher local rate of energy dissipation. Despite these very unusual characteristics, the authors concluded that the overall micromixing efficiency was lower than that for a comparable RPB with a structured packing. However, it should be noted that *Lin and Tsai* obtained a segregation index of 0.04 for the blade packing (Lin and Tsai 2016), while *Chen et al*. obtained a similar segregation index of 0.03 with a structured wire mesh packing (Chen et al. 2004) for the corresponding tangential velocity (at r_i) and the same concentration set, volumetric ratio, and liquid flow rate. Furthermore, RPBs with non-structured packings, consisting of packing elements, such as glass beads, Raschig rings, and Pall rings, were investigated by *Jun et al.* (Jun et al. 2011). They found that the segregation index increased with an increasing volumetric ratio and increasing Pall ring size, i.e., an increasing packing porosity, and decreased with increasing rotational speed and liquid flow rates. These findings are in agreement with the findings for RPBs with a structured packing. However, no quantitative comparison has been conducted so far. Among the investigated non-structured packing elements, the fastest micromixing was achieved for the Pall rings, followed by the Raschig rings.

4.4.2 Spinning Disc Reactor, High Shear Mixer and T-mixer

A comparison of an RPB and an SDR was reported by *Chen et al.* (Chen et al. 2006). It was shown by the authors that the SDR provides faster micromixing at low and intermediate liquid flow rates. However, the difference between the two devices decreases with increasing liquid flow rates, especially for lower rotational speed. This means that RPBs could be superior for providing fast and intense micromixing at high volumetric capacities. This assumption is supported by the finding of *Chen et al.* (Chen et al. 2006), in which the size of synthesized magnesium hydroxide nanoparticles decreased with an increasing liquid flow rate in the RPB but sharply increased for the SDR. However, future work should compare the two reactor types based on the same power input or energy density instead of the same rotational speed, to obtain a fair comparison.

For an inline high shear mixer (HSM), *Qin et al*. reported segregation indices of approximately 0.002 (Qin et al. 2017). The same value was obtained in an RPB by *Yang et al.* for the same concentrations and almost the same operational conditions (Yang et al. 2009). However, a direct comparison of the micromixing characteristics has not been conducted yet and should include the power consumption of HSM and RPB. *Yang et al.* compared their RPB with a T-mixer with wire mesh packing (Yang et al. 2015b). The authors reported that the use of an RPB seems especially advantageous for highly viscous fluids. While the segregation indices for the RPB are also lower for an aqueous solution, the largest benefit is achieved at the highest viscosity of 179 mPa s. This effect can be attributed to the high shear forces in RPBs. However, the difference in power consumption was also not discussed and should be included in a future comparison.

4.5 Conclusions and Outlook

In the presented literature study, the fundamentals of assessing micromixing in an RPB by means of the Villermaux-Dushman protocol were elucidated. Subsequently, general trends for fast micromixing in RPBs were deduced, and gaps in the current knowledge analyzed. First, the influence of the most important operational parameters on the segregation index was investigated. For increasing rotational speed and liquid flow rates, the segregation index decreases. This can be explained by the higher relative velocity difference between the packing and the liquid and thus a higher rate of energy dissipation. While the influence of the liquid flow rate on the segregation index sharply decreases with increasing liquid flow rates, no negative influence on the micromixing is observed, as is the case for other mixing devices. High rotational speed and liquid flow

rates seem therefore advisable for liquid mixing in RPBs. Furthermore, the influence of the rotational speed on the segregation index is especially pronounced at higher viscosities, independent of the liquid flow rate, demonstrating the elevated importance of higher shear forces – as imposed by a faster rotating packing – for the mixing of highly viscous liquids in an RPB. Additionally, the segregation index was found to increase for an increasing volumetric ratio between the two liquid streams. Based on these results, mixing in RPBs should be conducted with equal flow rates, if feasible. However, it is currently not possible to fully distinguish between stoichiometric and hydrodynamic effects. Instead, a complete interpretation would require a detailed mixing model, validated for the mixing process in RPBs at all volumetric ratios. Such a model is currently not available but should be a part of future work in the field.

Second, an overview of different RPB designs was presented, and the influence of these design parameters on the segregation index was discussed. Based on calculations for the tangential packing velocity, it was found that not only the rotational speed but also the distance to the liquid distribution has an influence on the mixing process. This could be explained by a greater droplet dispersion and thus higher effective surface area and better wetting of the packing. Based on these results, a highly disperse distribution of the liquids seems advisable for cocurrent liquid phase applications in an RPB and mixing in particular. Overall, it can be stated that the inner radius seems to be a more important design parameter for liquid application than the outer packing radius and the radial packing depth. Consequently, reducing the rotor size to an optimum seems reasonable to reduce the energy consumption of the motor and the investment costs of the RPB. Based on results from radial sampling positions and the respective tangential velocities, it was found that different flow patterns may occur at packing positions of identical tangential velocity for different rotational speed. Furthermore, the results for different structured packing types were discussed, as well as results from non-structured RPB packings and results for other continuous mixing devices. The comparison of structured and non-structured RPB packings supports the finding that lower porosities are beneficial for mixing, making the use of structured packing more reasonable. Structured foam packings, such as ceramic and metal foam packings, were found to allow for faster micromixing than wire mesh packings. By hydrophobically modifying the foam, the mixing could be improved even further. Additionally, a lower porosity was found to be beneficial for all packing types. This could be explained by a more significant split-recombine mixing within the packing. The positive influence of a lower porosity was especially pronounced at an increased viscosity, which underlines its importance for processing highly viscous liquids in an RPB. With respect to the liquid distribution, distributor pipes were compared to

premixed distributors and impinging streams. While the impinging stream RPBs yielded higher segregation indices than an RPB with distributor pipes under comparable conditions, the premixed distributor seems to be beneficial for mixing. However, it should be noted that this approach aims at decreasing the segregation indices as much as possible, not at characterizing the RPB itself. For the highest sensitivity towards mixing effects in the RPB, the feed should be supplied non-premixed. Other design parameters, such as the liquid outlet velocity, the axial height of the packing, the packing alignment, and the rotational axis, were either not reported systematically in the literature or could not be analyzed due to the lack of comparability of different concentration sets in the Villermaux-Dushman protocol, based on the concentration-dependency of the segregation index.

5 OPERATION, DESIGN, AND MODELING *

In this chapter, based on the gap analysis conducted in the previous chapter, pilot-scale experiments on operational and design parameters are discussed. Furthermore, suitable models to describe the mixing process in RPBs are assessed, and a comparison with other mixing devices based on a concentration-independent model parameter is conducted.

5.1 Introduction

As deduced in the previous chapter, the rotational speed, the design of the liquid distribution, and the packing's impingement zone are three of the most influential parameters for mixing in RPBs. However, many authors only reported a vague illustration of their liquid distribution design, whereas a specific description of details such as the outlet velocity, liquid distribution profile, and spraying angle, would be necessary for a meaningful comparison of different design variants. Consequently, a systematic approach to classifying different liquid distribution designs is suggested in this chapter, and the results of respective experimental investigations are presented, based on the Villermaux-Dushman protocol. Furthermore, the conditions under which the packing and its radial depth play an important role in fast mixing are clarified. In addition to the results for the segregation index, the Interaction-by-Exchange-with-the-Mean (IEM) model and the incorporation model are applied to derive a concentration-independent model parameter. Values of this model parameter for RPBs are then compared to those for other continuous mixing devices.

***** The scientific work published in this chapter was performed by D. Wenzel and supported by M. Steinbrink, E. Bredehorn, L. S. Ojeda, N. Gerdes, and K. Nolte in the framework of internships, bachelor theses, and master theses. Scientific advice was given by A. Górak.

* Parts of this chapter have been published as:
Review and Analysis of Micromixing in Rotating Packed Beds (2018), Wenzel, D.; Górak, A.; Chem. Eng. J. (345), pp. 492-506.
Liquid Distribution and Mixing in Rotating Packed Beds (2019); Wenzel, D.; Ojeda, L.S.; Gerdes, N.; Steinbrink, M.; Górak, A.; Ind. Eng. Chem. Res. 58 (15), pp. 5919-5928.
Reactive mixing in rotating packed beds: on the packing's role and mixing modeling (2019); Wenzel, D.; Nolte, K.; Górak, A.; Chem. Eng. Proc.: P.I. (143), published online, doi: 10.1016/j.cep.2019.107596.

Overall, the investigations in this chapter can be distinguished into two complementary approaches, based on the results of chapter 3. For the investigation of the rotational speed and the liquid distribution design, hydrochloric acid was used as the proton donator to obtain the highest possible sensitivity. For the comparison with other continuous mixing devices from the literature and for results which are the basis of model calculations, sulfuric acid was used. This was necessary to obtain a fair comparison and because no kinetics incorporating the influence of hydrochloric acid on the Dushman reaction is available from the literature.

5.2 Fundamentals

5.2.1 Liquid Distribution Design

Three different liquid distribution designs are commonly used in the literature for liquid mixing processes in RPBs (Chapter 4): distribution pipes, premixed distributors, and impinging stream distribution (Fig. 3). A further development of the distribution pipes design was presented by *Neumann et al*. (Neumann et al. 2017), based on previous work by *Acharya et al.* (Acharya et al. 1990) and *Trent and Tirtowidjojo* (Trent and Tirtowidjojo 2003). Instead of drilling holes directly into the distribution pipes, the authors used different types of nozzles that could be attached and exchanged at the end of the distribution pipes. These distribution nozzles can then be further distinguished by their type, their number of holes, and the distribution angle δ, that they cover. *Neumann et al.* introduced the full jet nozzle type that distributes the liquid in the form of a full jet without splitting up the liquid flow into droplets and the flat fan nozzle type that distributes the liquid in the form of a fan-shaped spray (Neumann et al. 2017). While the flat fan nozzles only have one hole by design, the full jet nozzles can have one or multiple holes. Furthermore, the arrangement of these holes and the exact design of the nozzle tongue can lead to different distribution angles that can range from covering one point of the packing (δ = 0°) to covering the complete packing (δ = 360°).

To allow for a meaningful comparison of different liquid distribution designs, the schematic shown in Fig. 19 is proposed for the use of two nozzles. However, this schematic could also be further extended to incorporate other liquid distribution designs. To quantify different nozzle orientations with respect to each other and with respect to the rotating packing, the polar orientation angle φ is introduced, which describes the angle between the center point of the RPB and the two center points of the liquid streams impinging on the packing. Fig. 20 shows an illustration of this concept

for an overlapping liquid distribution (φ = 0°, two nozzles spraying onto the same point of the packing) and an opposite liquid distribution (φ = 180°, two nozzles spraying onto two directly opposite points on the packing).

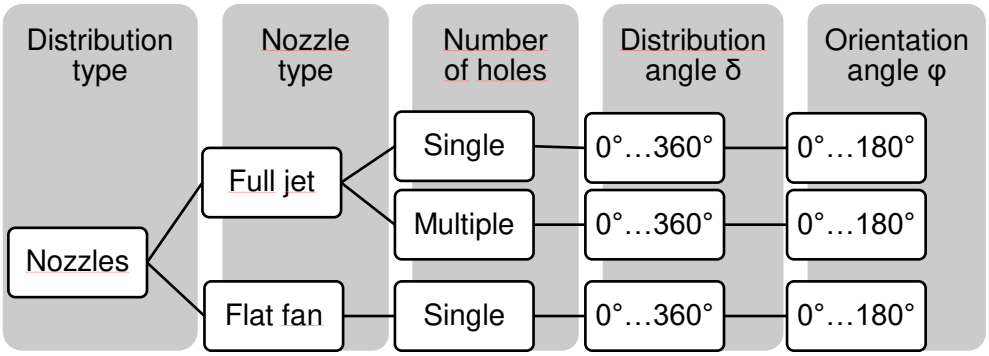

Fig. 19. Proposed schematic of liquid distribution designs.

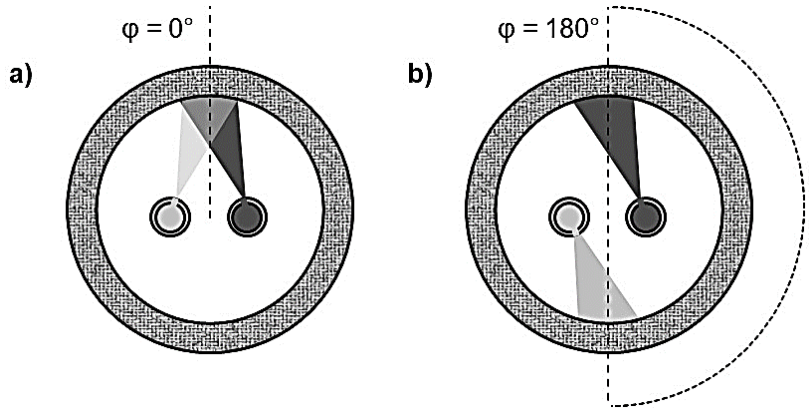

Fig. 20. Schematic drawing of the liquid distribution in the rotor eye of an RPB.
a) Liquid distribution with two nozzles at an overlapping orientation of φ = 0°.
b) Liquid distribution with two nozzles at an opposite orientation of φ = 180°.

5.2.2 Mixing Modeling

To solve the problem that the segregation index is a highly sensitive, concentration-dependent parameter, *Commenge and Falk* proposed the concept of “mixing time”, a concentration-independent model parameter, to compare mixing results (Commenge and Falk 2011; Falk and Commenge 2010). This parameter can be derived from appropriate mixing models, e.g., the IEM model and the incorporation model, which will be considered in this thesis. However, this “mixing time” should not be confused with the actual, characteristic time required to achieve complete homogeneity by mixing that was introduced in chapter 3.2.1. Instead, it is only a parameter of the respective model,

which provides an estimation of the order of magnitude of the characteristic mixing time on the molecular level (Kölbl and Schmidt-Lehr 2010). Therefore, it will be named micromixing time parameter t_{mix} in this thesis.

5.2.2.1 IEM Model

The IEM model assumes the mixing process to be a reversible exchange between segregated regions and their mean environment. The characteristic time scale of this exchange can be expressed in terms of the micromixing time parameter t_{mix} (Villermaux and Falk 1994). However, the IEM model only yields the order of magnitude of the characteristic time scale of mixing, without giving a detailed description of the mixing phenomena involved (Falk and Commenge 2010).
For each chemical species' concentration in the liquid flows that are mixed, Eqs. (28) – (30) can be set up for the time evolution, assuming plug flow and thus no backmixing (Falk and Commenge 2010).

$$\frac{dC_{j,1}}{dt} = \left(< C_j > - C_{j,1}\right) * \frac{1}{t_{mix}} + R_{j,1} \tag{28}$$

$$\frac{dC_{j,2}}{dt} = \left(< C_j > - C_{j,2}\right) * \frac{1}{t_{mix}} + R_{j,2} \tag{29}$$

$$< C_j > = \alpha_{vol} * C_{j,1} + (1 - \alpha_{vol}) * C_{j,2} \tag{30}$$

where $C_{j,1}$ and $C_{j,2}$ are the concentrations of species j in liquids 1 and 2 that are mixed, $< C_j >$ is the mean concentration of species j, $R_{j,1}$ is the reaction rate of species j in the liquid volumes 1 and 2, α_{vol} is the volume fraction of the total liquid flow rate of liquid 1, and $(1 - \alpha_{vol})$ is the volume fraction of the total liquid flow rate of liquid 2. For t = 0, the iodide-iodate-mixture of the buffer solution is, e.g., concentrated in liquid volume 1 (V_{L1}) and the acid solution is concentrated in liquid volume 2 (V_{L2}). The volumes in this model are considered constant over time (Baldyga and Bourne 1990). A more detailed description of the IEM model's equations in case of the Villermaux-Dushman protocol and how to solve them numerically is given in Appendix C.6.
However, to enable other authors to easily estimate the micromixing time parameter t_{mix} from Villermaux-Dushman experiments at equal liquid flow rates without numeric calculations, *Commenge and* Falk (Commenge and Falk 2011) presented a master curve for the IEM model. This IEM master curve was shown to be sufficiently accurate for certain concentration sets, e.g., 1b and 2b (Tab. 17), which will be used in this thesis for equal liquid flow rates. From this master curve, t_{mix} can then be obtained as a function

of the species' concentrations and the measured optical density (OD) per mm (Eq. (31)).

$$t_{mix} = 0.33 * (\text{OD per mm}) * [H^+]^{-4.55} * [KI]^{-1.5} * [KIO_3]^{5.8} * [NaOH]^{-2} * [H_3BO_3]^{-2} \quad (31)$$

5.2.2.2 Incorporation Model

The still most commonly utilized model to calculate the micromixing time parameter t_{mix} for RPBs is the so-called incorporation model, which is based on earlier work of *Baldyga and Bourne* on the engulfment model (Bałdyga and Bourne 1988, 1989). It assumes that micromixing is controlled by the incorporation of a small volume of one liquid by another surrounding liquid, consequently forming a continuously growing aggregate in which the reactions occur (Villermaux et al. 1993). The characteristic time scale for this incorporation process is assumed to be equal to the characteristic mixing time on the molecular level (Villermaux et al. 1993; Yang et al. 2005). The growth of the aggregate volume (V_2) due to the incorporation by a surrounding liquid V_1 can be described according to the incorporation function shown in Eq. (32) (Villermaux et al. 1993).

$$V_2 = V_{20} * g(t) \quad (32)$$

where V_{20} is the initial aggregate volume and g is the growth function. This function can either describe an exponential (Eq. (33)) or a linear growth (Eq. (34)) of volume V_2 over time (Fournier et al. 1996a).

$$g(t) = \exp\left(\frac{t}{t_{mix}}\right) \quad (33)$$

$$g(t) = 1 + \left(\frac{t}{t_{mix}}\right) \quad (34)$$

For exponential growth, the incorporation flow is proportional to the aggregate volume.

Finally, the time evolution of the concentration of each species j in reaction volume 2 can be expressed as shown in Eq. (35) (Fournier et al. 1996a).

$$\frac{dC_j}{dt} = \left(C_{j,10} - C_j\right) * \frac{1}{g} * \frac{dg}{dt} + R_j \quad (35)$$

where the subscript 10 denotes the surrounding liquid and R_j denotes the reaction rate of species j. A more detailed description of the incorporations model equations and how to solve them numerically is given in Appendix C.6.

5.2.2.3 Mixing Model Choice and Limitations

The incorporation model was initially suggested for mixing in an STR with very high volumetric ratios and thus very large volumetric differences between the two liquid flow rates. For only moderately high volumetric ratios, micromixing will be affected by the phenomenon of self-engulfment, a slowing-down of the reaction zone growth by engulfment of the same fluid (Bałdyga and Pohorecki 1995), which cannot be described through the incorporation model in its current form. Particularly, no exponential growth can be assumed, as shown by *Baldyga and Bourne* for the underlying engulfment model (Baldyga and Bourne 1990). In contrast, the prediction quality of a model assuming constant volumes over time, as the IEM model, decreases with increasing volumetric ratios (Baldyga and Bourne 1990; Lemenand et al. 2017). Consequently, the IEM model should only be considered for modeling the mixing process of two equally large liquid flow rates, but not for higher volumetric ratios. It should additionally be noted that, in an RPB, the maldistribution of the liquids may exist on multiple levels, and the exact process of mixing may be much more complicated than assumed by these models (Yang et al. 2005).

Also, solving the models' equations in an exact way requires exact knowledge about the reaction rate constants, i.e., the underlying kinetics (Assirelli et al. 2008; Guichardon et al. 2000). However, the kinetics of the Dushman reaction is part of an ongoing scientific debate (Chapter 3), so that quantitative results should be treated cautiously. Furthermore, if sulfuric acid is used, its incomplete dissociation should be included in the kinetics or the model equations (Bourne 2008; Kölbl and Schmidt-Lehr 2010). Two respective approaches have been published by *Hofinger* (Hofinger 2013) and *Guichardon and Ibaseta* ((Guichardon and Ibaseta 2016), chapter 3.2.6) but have not been implemented in RPB studies so far. Therefore, the latter will be taken into consideration in this chapter.

5.3 Material and Methods

5.3.1 Experimental Setup

The experimental setup used for the experiments in this chapter is shown schematically in Fig. 21. It consists of the two feed containers for the acid and the buffer solution, the acid pump, the buffer pump, and a single-stage RPB.

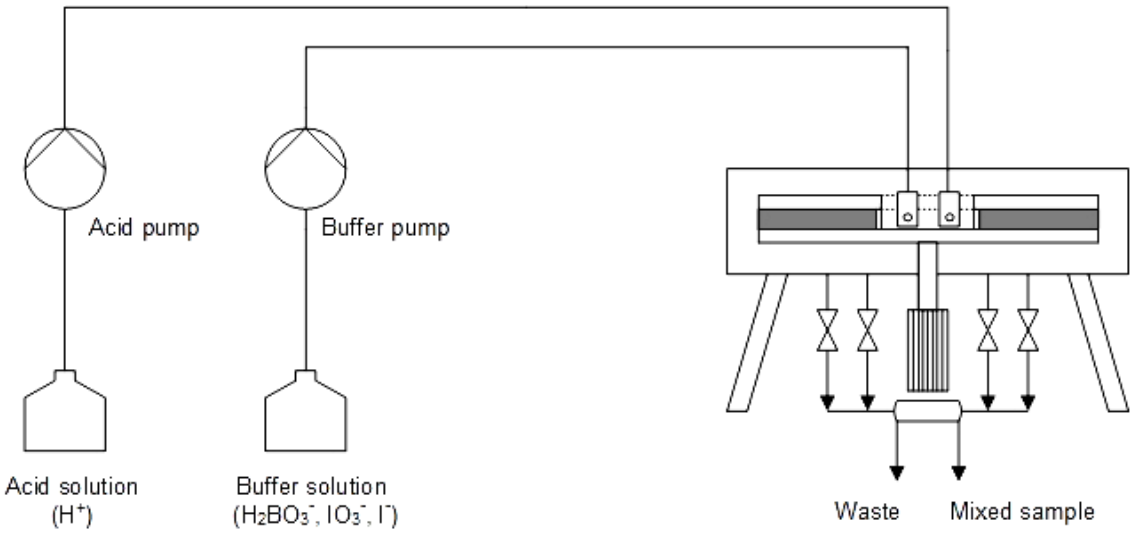

Fig. 21. Schematic drawing of the experimental setup used in chapter 5.4.

The feed containers were each placed on a DS 65K0.5 platform scale from KERN & Sohn GmbH (Balingen, Germany). From the feed containers, the solutions were pumped separately into the RPB. For experiments at volumetric ratios between 1 (equal flow rates) and 6, both the acid and the buffer solution were pumped separately by an Ismatec MCP-Z-Standard from Cole-Parmer GmbH (Wertheim, Germany), equipped with an MI0023 pump head from Micropump (Vancouver, Canada). For a volumetric ratio of 8, the acid was pumped by an Ismatec Reglo-Z from Cole-Parmer GmbH equipped with an MI0131 pump head from Micropump. The buffer solution was pumped by an Ismatec MCP-Z-Standard from Cole-Parmer GmbH, equipped with an MI0023 pump head from Micropump.

An overview of the RPB design variants used in this chapter is given in Tab. 14 (Appendix C.1). The two rotor plates, containing the packing, were separated by spacers at the outer end and by the eye ring at the inner end. Pictures of the 600-mm rotor (Fig. 60) and the eye ring (Fig. 61) are shown in Appendix C.1. Details on the different packing configurations are summarized in Tab. 15 (Appendix C.1). All metal foam packings were supplied by Recemat BV (Dodewaard, The Netherlands).
Two different nozzle types were used in this chapter, which can be distinguished by their features, according to Fig. 19, into flat fan nozzles (FF) and full jet nozzles (FJ). A picture of an FF-type nozzle and an FJ-type nozzle is shown in Fig. 59 (Appendix C.1). An overview of the nozzle parameters distribution angle δ, number of holes, and cross-sectional outlet area A_{outlet} of each nozzle is given in Tab. 13 (Appendix

C.1). All nozzles were installed in a manner such that the liquid was only impinging on the rotating packing and the eye ring. With respect to the nozzle orientation φ, three different cases were considered: overlapping liquid distribution (φ = 0°), adjacent liquid distribution (φ = 140°), and opposite liquid distribution (φ = 180°), The FF-type nozzles were manufactured by Lechler GmbH (Metzingen, Germany). The FJ-type nozzles were manufactured in TU Dortmund University's own workshops. In combination with packing configurations A, B, and F (Tab. 15), varying nozzles types were used, but always the same for the buffer and the acid solutions. In combination with packing configurations C.1, C.2, D, and E (Tab. 15), an FF-I nozzle was used for the buffer solution and an FF-III nozzle was used for the acid solution. Furthermore, some experimental runs were conducted without any packing. In that case, the rotor only contained the two rotor plates, the eye ring at the inner rim, and spacers at the outer rim. This configuration is denoted in the experimental section as "no packing".

The resulting mixed solution left the RPB through the liquid outlets and was collected in a siphon. From there, samples were withdrawn for further analysis. The rest of the mixed solution was collected and properly disposed of. The absorption of each sample was measured in the UV-vis spectrometer UVmini-1240 from Shimadzu Corporation (Kyoto, Japan) in a quartz glass cuvette from Hellma Analytics (Müllheim, Germany) with an optical path length of 10 mm. When the absorption value in this 10-mm cuvette was above 2.0, the sample's absorption was further determined in a quartz glass cuvette from Hellma Analytics (Müllheim, Germany) with an optical path length of 2 mm.

5.3.2 Experimental Procedure

Before the start of each experiment, the feed solutions were prepared according to Tab. 17 (Appendix C.3). Three concentration sets containing HCl were considered (FVT-a/FVT-b/FVT-c), based on the results of chapter 3, as well as two concentration sets containing H_2SO_4 (FVT-d/FVT-e). In these concentration sets, the buffer composition that was identified in chapter 3 as the most suitable was utilized. Furthermore, two H_2SO_4-based concentration sets used in the literature to investigate micromixers, namely the concentration sets 1SC and 2SC suggested by *Kölbl et al.* (Kölbl et al. 2008) (named 2b and 1b by *Commenge and Falk* (Commenge and Falk 2011)), were considered. Further details on the Villermaux-Dushman protocol used in this chapter are given in Appendix C.3. All solid components were weighed on the NewClassic MF scale from Mettler Toledo (Columbus, USA), while all liquid components were weighed on the DS 65K0.5 scale from KERN & Sohn GmbH (Balingen, Germany). The exact weight and concentration of each chemical were considered in the calculation of the segregation index. Afterward, the rotational speed

of the rotor was adjusted to a fixed value. Then, the pumps were started to pump the two liquid flows into the RPB at a fixed volumetric ratio and a fixed total liquid flow rate. The liquid flow rates of the acid and the buffer solution were controlled through the digital display of the pumps and further verified by measuring the weight of each feed tank before and after each experiment. Both liquids were used at ambient conditions. The ambient temperature was determined through a digital thermometer from VWR chemicals (Radnor, USA). All samples were taken at operating conditions that ensured stable operation. Directly afterward, the extinction value of the samples was determined in the UV-vis spectrometer at 353 nm. The accuracy of the scales, the digital temperature sensor, and the UV-vis spectrometer is given in Tab. 16 (Appendix C.1). To verify the reproducibility of the results, each experimental run was performed twice, unless noted otherwise. Thus, the results are presented as the mean value, with error bars depicting the sample standard deviation.

5.3.3 Mixing Modeling

For the experiments at equal liquid flow rates, the obtained values for OD mm^{-1} $\Pi[C_i]^{-k}$ were at maximum $0.0335\ \mathrm{mm}^{-1}\left(\frac{\mathrm{mol}}{\mathrm{l}}\right)^{4.25}$ for concentration set 1SC and at maximum $0.0285\ \mathrm{mm}^{-1}\left(\frac{\mathrm{mol}}{\mathrm{l}}\right)^{4.25}$ for concentration set 2SC. Therefore, the master curve described in Eq. (31) could be used to calculate the micromixing time parameter t_{mix} from the IEM model with sufficient accuracy. H_2SO_4 was assumed to be fully dissociated under all experimental conditions for these calculations.

For modeling calculation based on the experiments at a volumetric ratio of 8, the exponential and the linear approach of the incorporation model were assessed. Fourteen different kinetics approaches, including the different reaction rate constants suggested by *Guichardon et al.* (Chapter 3.2.6), as well as the complete and incomplete dissociation of sulfuric acid, were investigated for their accuracy in preliminary modeling calculations (Fig. 73, Appendix C.7). Based on the lowest sum of squared deviation between measured and predicted segregation indices for packing configuration E, values obtained with the revised kinetics by *Guichardon and Ibaseta* (Eq. (18)), are presented in the results section. Because this kinetics approach implicitly incorporates the incomplete dissociation of sulfuric acid, it was not additionally considered in the model equations.

In detail, the resulting systems of ordinary differential equations (ODE; Appendix C.6) were implemented in the software Matlab (MathWorks, Massachusetts, USA). Because the systems are described as stiff ODE-systems, the ode15s solver was used to solve the set of equations. This solver is a variable-step, variable-order solver based on

numerical differentiation formulas of orders 1 to 5. It can also use backward differentiation formulas and is recommended by Matlab for stiff ODE-problems (Shampine and Reichelt 1997). Finally, the accuracy of each modeling approach was checked by comparing predicted segregation indices with experimentally determined segregation indices.

5.4 Experimental Results

5.4.1 Operational Parameters

In this subchapter, experimental results on the influence of the rotational speed and of the total liquid flow rate on the segregation index are discussed. As no results for equal liquid flow rates were reported in the literature (Chapter 4), the influence of the total liquid flow rate will be shown and discussed for such conditions. These results will further be the basis of a comparison with other continuous mixing devices in chapter 5.6.1.

Additional and supporting information to this chapter is shown in Appendix C. For example, results on the residence time distribution in the RPB 1.0 and the RPB 2.0 design variants, which are investigated in this chapter, are presented (Appendix C.5). Also, for the sake of completeness, results for the influence of the volumetric ratio on the segregation index are shown (Fig. 63, Appendix C.4). These are in agreement with results from the literature (Chapter 4.3.1.3) but will not be discussed here in detail due to the noted lack of direct comparability without a suitable mixing model for all volumetric ratios.

5.4.1.1 Rotational Speed

The influence of the rotational speed on the segregation index is shown in Fig. 22 for two data series obtained with different parameter sets. As shown, the segregation index is strongly dependent on the rotational speed. The relationship between the two parameters can be described by the power law. These results are in excellent agreement with the findings obtained from the literature (Chapter 4) and can be explained by the higher rate of energy dissipation for higher rotational speed.

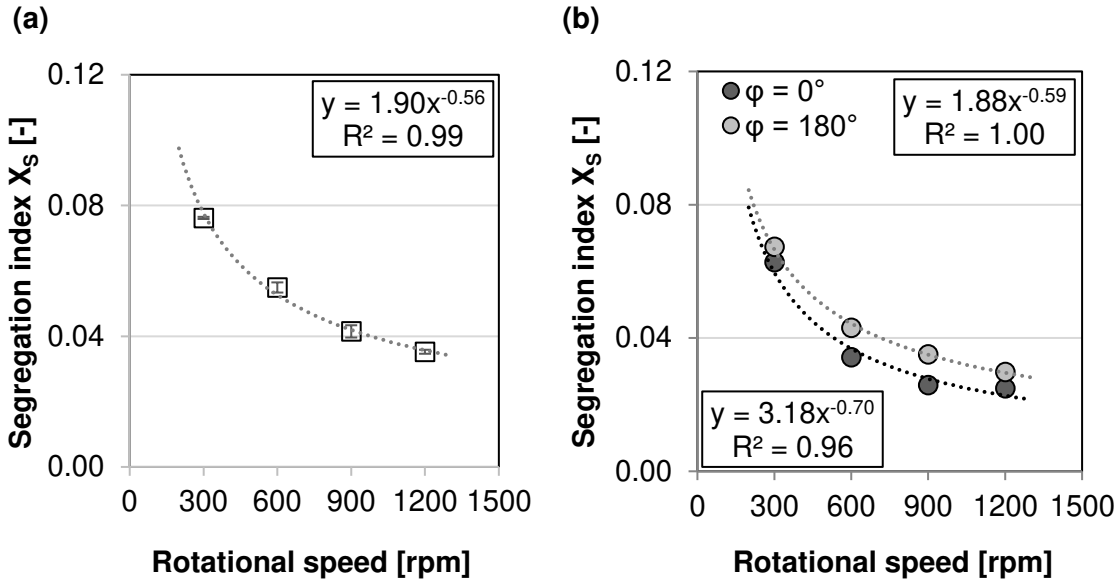

Fig. 22. Segregation indices as a function of the rotational speed for two different operating conditions. (a) Packing configuration E, FF-I/FF-III nozzles (φ = 180°), 140 l h^{-1}, volumetric ratio: 8, concentration set FVT-d. (b) Packing configuration F, FF-III nozzles (φ = 180°/ 0°), 60 l h^{-1}, volumetric ratio: 3, concentration set FVT-a. Error bars denote the sample standard deviation, figure b) shows single-point measurements. Dotted lines show data regression by the power law.

Although the two considered data sets differ in several operational and design parameters, the trendline equations of the power-law regressions are very similar, particularly for an opposite liquid distribution (φ = 180°). The obtained exponents are further in good agreement with the correlation from *Chen et al.* (Chen et al. 2004), who suggested a power-law relationship with an exponent of -0.64 (Appendix B.3).

5.4.1.2 Total Liquid Flow Rate

In this subchapter, the mixing process of two equally large inlet streams is investigated over a range of the total liquid flow rate $\dot{V}$ between 60 l h^{-1} and 100 l h^{-1} by means of the concentration sets 1SC and 2SC. As can be observed from Fig. 23, the segregation index decreases with an increasing total liquid flow rate. This relationship can be described by the power law, given in Eq. (36) for concentration set 2SC and in Eq. (37) for concentration set 1SC. The positive influence of a higher total liquid flow rate on the mixing process is in agreement with the findings from the literature for higher volumetric ratios (Chapter 4). It could be explained qualitatively by a combination of multiple effects: a higher liquid outlet and impingement velocity at higher flow rates, a better

wetting of the packing, or a higher collision probability of fragmentized liquid elements within the packing (Chapter 4).

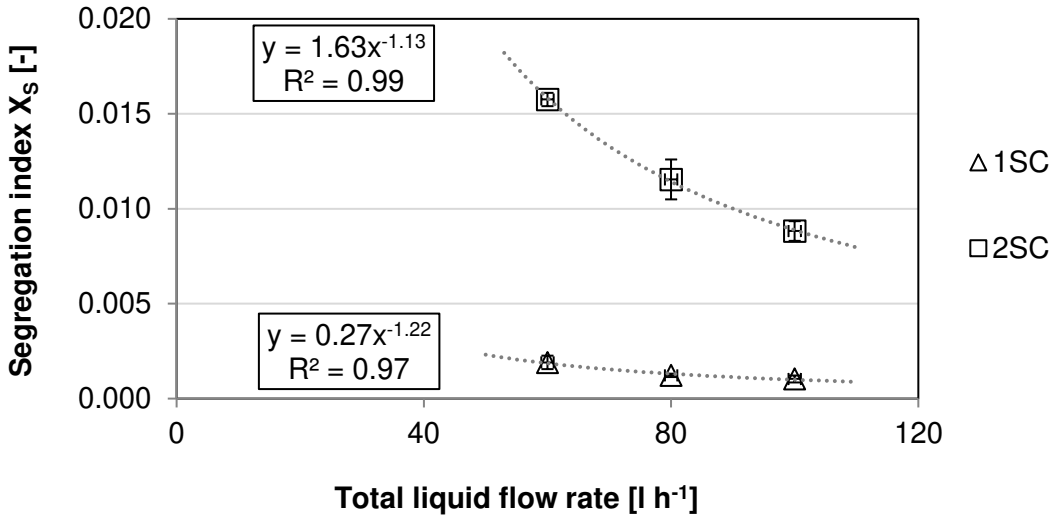

Fig. 23. Segregation indices obtained for equal liquid flow rates at different total liquid flow rates. Packing configuration B, FF-III nozzles (φ = 0°), 1200 rpm, concentration sets 1SC/2SC. Error bars depict the sample standard deviation. Power-law functions given as dotted lines.

$$X_S\,(2SC) = 1.63 * \dot{V}_L{}^{-1.13} \tag{36}$$

$$X_S\,(1SC) = 0.27 * \dot{V}_L{}^{-1.22} \tag{37}$$

However, based on the correlation between liquid outlet velocity and segregation index that is obtained in chapter 5.4.2 in the form of Eq. (38), a more precise assessment is possible. When the total liquid flow rate increased from 60 l h^{-1} to 100 l h^{-1}, the outlet velocity of the buffer increased from 16.67 m s^{-1} to 27.78 m s^{-1}. Based on Eq. (38), this increased outlet velocity should decrease the segregation index by 42.4 %. The actually observed decrease is 43.9 % for 2SC and 46.1 % for 1SC (Fig. 23). Therefore, it can be assumed that the positive influence of a higher total liquid flow rate is mainly due to the higher outlet and impingement velocity of the liquid and only secondarily due to other effects such as better utilization of the packing volume.

5.4.2 Design Parameters

Because it was found in the literature study (Chapter 4) that information on the liquid distribution design and the role and importance of the packing are currently insufficient, they will be investigated in more detail in this subchapter. Additional and supporting information to this chapter is shown in Appendix C.

5.4.2.1 Liquid Distribution Design

To investigate the influence of different liquid distribution parameters on the mixing process, the segregation indices obtained for three flat fan nozzles and four full jet nozzles in an orientation of φ = 180° at a total liquid flow rate of 60 l h^{-1} are investigated. They are shown in Fig. 24 as a function of the respective outlet velocity of the buffer solution ($u_{out,buffer}$) that was, based on the continuity equation for stationary flow, obtained by dividing the fixed buffer flow rate by the cross-sectional area of the respective nozzle summarized in Tab. 24 (Appendix C.1). Because the volumetric ratio was kept constant at 3, the respective acid outlet velocities can be derived by dividing the X-axis values by three. Furthermore, respective segregation indices for the FF-II nozzle and the FJ-IV nozzle are shown in Fig. 25. Both nozzles have the same cross-sectional area, and thus the same liquid outlet velocity, but a different distribution profile.

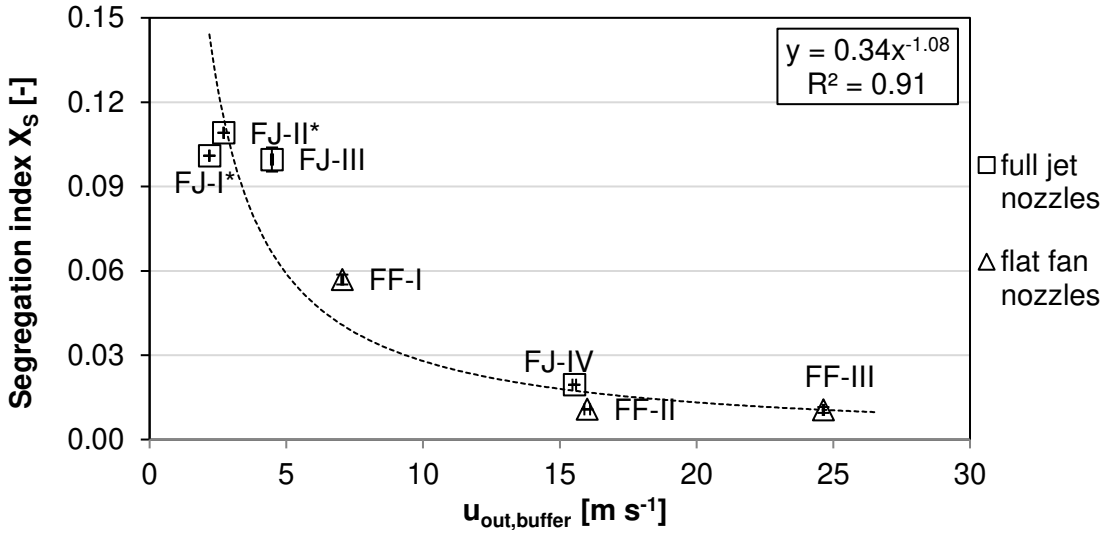

Fig. 24. Segregation indices obtained for the seven investigated FF and FJ nozzles in an orientation of φ = 180° as a function of the respective outlet velocity of the buffer. Packing configuration A, 60 l h^{-1}, 600 rpm, volumetric ratio: 3, concentration set FVT-a. Error bars depict the sample standard deviation. (*) denotes single-point measurements. A power-law function for all nozzles is given as dotted line.

As can be obtained from Fig. 24, the segregation index decreases with an increasing outlet velocity. However, the influence of the outlet velocity on the segregation index diminishes for very high outlet velocities. This relationship can be described by the power law, as given in Eq. (38), and more generally by $X_S \sim \frac{1}{u_{out}}$.

$$X_S = 0.34 * u_{out,buffer}{}^{-1.08} \quad (38)$$

This inverse relationship between the segregation index and outlet velocity can be explained as follows: the higher the outlet velocity is at the nozzle, the higher the liquid's velocity is when it impinges on the packing, and the higher the energy dissipation rate is. Thus, the liquid is fragmented into smaller aggregates, which offer a higher surface area for mixing than larger aggregates. Additionally, the liquid penetrates the packing further, which increases the wetting and utilization of the initial packing volume. This finding is further in agreement with the suggestion of *Chen et al.* that all improvements of micromixing in an RPB can be attributed to a decreasing size of liquid aggregates and an increasing relative velocity of impingement among these liquid aggregates (Chen et al. 2004). In contrast, the resulting segregation index is rather independent of the nozzle type, distribution angle, and number of nozzle holes at an opposite nozzle orientation (φ = 180°, Fig. 24). Furthermore, the nozzle orientation itself has only a slight influence on the resulting segregation indices in the case of FF nozzles (Fig. 25). These findings indicate that the liquid flow is synchronized with the rotational speed of the packing within a few milliseconds following the impingement. Such behavior was previously suggested by *Guo et al.* based on a computational fluid dynamics (CFD) study (Guo et al. 2017). Additionally, it can be obtained from Fig. 25 that the segregation index increases only slightly for the FF-II nozzle when changing from φ = 180° to φ = 0°. However, a drastic increase of the resulting segregation index can be observed for the FJ-IV nozzle. This can be explained with respect to the different distribution angles (Tab. 13, Appendix C.1). While the FF nozzles distribute the liquid over a wide angle (δ = 140°), the FJ-IV nozzles distribute the liquid onto a very small part of the packing (δ = 0°).

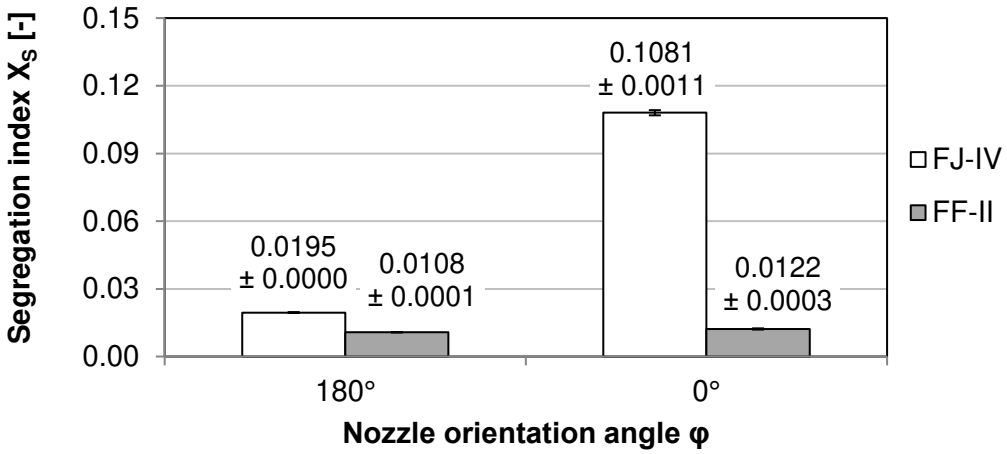

Fig. 25. Segregation indices obtained for the nozzles FJ-IV and FF-II at an orientation of φ = 180° and φ = 0°, respectively. Packing configuration A, 60 l h^{-1}, 600 rpm, volumetric ratio: 3, concentration set FVT-a. Error bars depict the sample standard deviation.

Therefore, when the nozzle orientation is also narrow (φ = 0°), the liquid load at this point is relatively high and the two liquid flows come into contact in the form of larger aggregates. Thus, larger parts of the two competing reactions will take place under mesomixing conditions instead of micromixing conditions, resulting in higher segregation indices.

The assumption of an excessive liquid load per area packing, i.e., an excessive liquid hold-up at the inner rim of the rotating packing for a very narrow liquid distribution, is also in agreement with recent experimental and CFD results by *Ouyang et al.* (Ouyang et al. 2018a; Ouyang et al. 2018b).

Furthermore, it was proposed in chapter 4 that a higher distance between packing and liquid distribution could have a positive influence on the mixing process due to a finer droplet dispersion. This finding was based on results from *Chen et al.* obtained at φ = 180° with two liquid distributor pipes similar to the FJ design (Chen et al. 2006). While finer droplet dispersion was also observed to have a slightly positive effect on the mixing process in this chapter (Fig. 25, φ = 180°, FF vs. FJ), the initially proposed mechanism should be extended as follows: with an increasing distribution distance, an increasing cross-sectional area at the inner rim of the packing is wetted. Therefore, an increasing distribution distance results in a lower liquid load per area packing and a lower liquid hold-up at the inner packing radius. Consequently, the mixing process is accelerated.

Overall, it can be concluded that the exact liquid distribution profile is rather irrelevant for the mixing process, if the nozzles are pointing away from each other (φ = 180°) or the liquid is distributed over a wide angle (e.g., with FF nozzles), but that a sufficiently high liquid outlet velocity is essential to achieve a fast mixing process.

5.4.2.2 Packing Design and Depth

While it was noted in chapter 5.4.2.1 that the liquid flow is probably synchronized with the packing within the first milliseconds, this does not necessarily mean that the packing has no influence on the mixing process; it only shows the comparatively high influence of the liquid outlet and impingement velocity as long as the rotor contains a packing. Therefore, the influence of the packing and its depth will be investigated separately in this subchapter for two different operating conditions.

First, the influence of the packing on the mixing process at equal liquid flow rates (volumetric ratio: 1) is investigated. The respective segregation indices obtained for a rotor with full packing (packing configuration B) and without any packing (no packing) are shown in Fig. 26. As displayed, using no packing substantially increased the segregation index from 0.0019 ± 0.0004 to 0.0076 ± 0.0002 at equal liquid flow rates.

This means that the rotating eye ring and rotor plates alone are insufficient for fast mixing under these conditions. Instead, the liquid hold-up and the residence time in the rotor can be assumed to be too low to complete the mixing process within the region of highest energy dissipation.

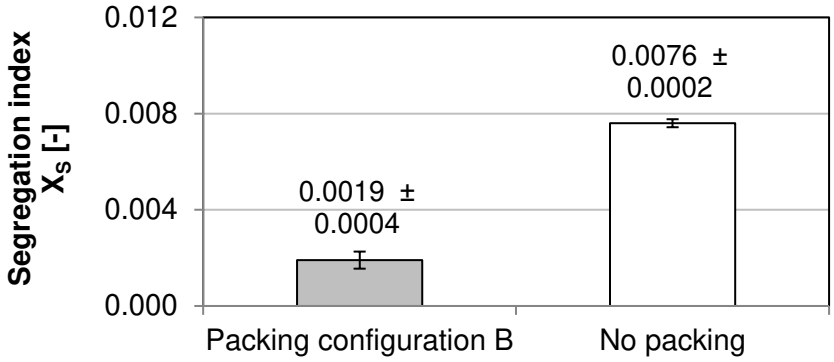

Fig. 26. Segregation indices obtained for equal liquid flow rates for a rotor with packing (packing configuration B) and without packing (no packing), FF-III nozzles, overlapping liquid distribution (φ = 0°), 60 l h^{-1}, 1200 rpm, concentration set 1SC. Error bars depict the sample standard deviation.

Second, segregation indices obtained at a volumetric ratio of 8 with different packing configurations and without packing are shown in Fig. 27, Fig. 28, and Fig. 29 as a function of the rotational speed. Since results for concentration sets with H_2SO_4 (concentration sets FVT-d/e) and HCl (concentration sets FVT-b/c) are qualitatively very similar, only results for concentration sets FVT-d/e are shown here, while results for concentration sets FVT-b/c are presented in Appendix C.4.

Segregation indices for a rotor with packing configuration E and a rotor without packing, obtained with an overlapping liquid distribution (φ = 0°), are presented in Fig. 27 as a function of the rotational speed. As shown in the figure, almost no influence of the packing on the segrgeation index is visible under these conditions. The largest, but still slight, positive influence of the packing on the segregation index can be found for the highest rotational speed: at 1200 rpm, the segregation index decreased from 0.0632 to 0.0541, on average, which corresponds to a decrease by 14.4 %. This suggests that, under these operating conditions, the mixing process is for the largest part finished before the liquids enter the packing. It can be assumed that the two liquids, when supplied in an overlapping fashion, already come in contact in form of droplets between liquid distributor and rotor and are mixing almost instantaneously on impact onto the rotating eye ring (radial depth: 7 mm) and the rotating rotor plates. While no other mixing

investigations with respect to the eye ring are reported in the literature, these results are in agreement with the study by *Chen et al.* on the influence of the radial packing depth on mixing results ((Chen et al. 2006), Chapter 4.3.2.2). The authors varied the outer packing radius and the radial packing depth at a total flow rate of 34.3 l h^{-1} and a volumetric ratio of 7. For these conditions, no clear influence of the radial packing depth on the segregation index could be found at 600 rpm and 900 rpm, and a maximum difference of only 12.5 % at 1500 rpm for an increase in the radial depth of 400 % from 10 mm to 50 mm. Therefore, the authors concluded the first 10 mm of the rotor to be most important for the mixing process. This consideration is in agreement with the results by *Guo et al.*, who quantified the zone of most intense mixing to be the first 7 mm to 10 mm of the rotor ((Guo et al. 2000), Chapter 2.2).

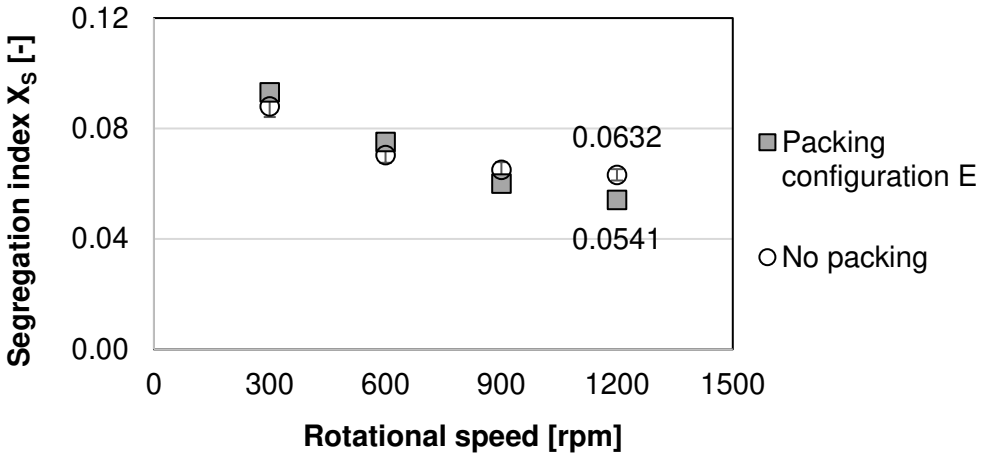

Fig. 27. Segregation indices as a function of the rotational speed for packing configuration E and a rotor without packing. FF-I/FF-III nozzles, overlapping liquid distribution (φ = 0°), 140 l h^{-1}, volumetric ratio: 8, concentration set FVT-e. Error bars denote the sample standard deviation.

In contrast, the segregation index decreased on average by 75.0 % for equal liquid flow rates (volumetric ratio: 1) and the same rotational speed (Fig. 26). This suggests an inverse relationship between volumetric ratio and importance of the packing at an overlapping liquid distribution. This consideration is further supported by results from preliminary experiments at a volumetric ratio of 6, in which the segregation index in experiments with a packing was on average 27.0 % lower than in experiments without a packing (Fig. 64, Appendix C.4).

Additionally, segregation indices for an opposite liquid distribution (φ = 180°) are presented in Fig. 28 and Fig. 29 as a function of the rotational speed. In Fig. 28, results obtained without packing are compared to those for packing configuration D (radial

packing depth: 67 mm) and packing configuration E (radial packing depth: 207 mm) with concentration set FVT-d. In Fig. 29, results obtained without packing are compared to those for packing configuration E, packing configuration C.1 (radial packing depth: 17 mm, average pore size: 1.4 mm), and packing configuration C.2 (radial packing depth: 17 mm, average pore size: 2.3 mm) with concentration set FVT-e.

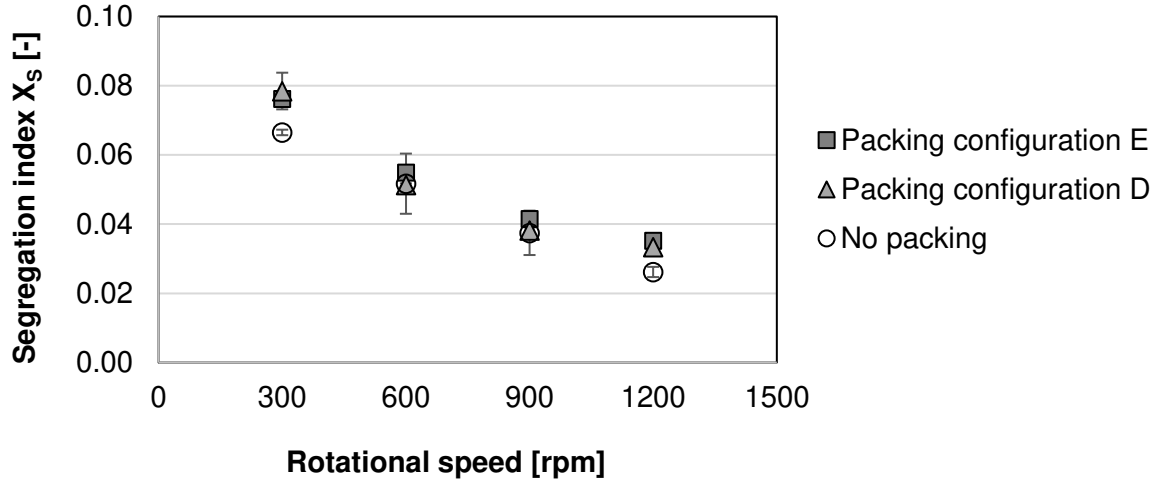

Fig. 28. Segregation indices obtained for packing configurations E, packing configuration D, and without packing as a function of the rotational speed. FF-I/FF-III nozzles, opposite liquid distribution (φ = 180°). 140 l h^{-1}, volumetric ratio: 8, concentration set FVT-d.

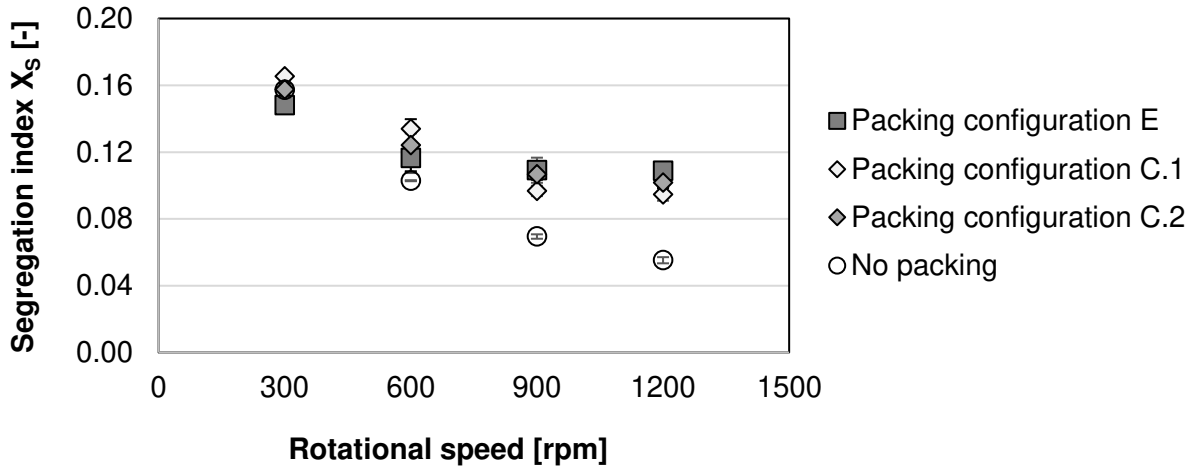

Fig. 29. Segregation indices obtained for packing configurations E, C.1, C.2, and without packing as a function of the rotational speed. FF-I/FF-III nozzles, opposite liquid distribution (φ = 180°). 140 l h^{-1}, volumetric ratio: 8, concentration set FVT-e.

As can be obtained from Fig. 28 and Fig. 29, for none of the investigated packing configurations a positive influence of the packing on the segregation index could be found under the investigated operating conditions. Decreasing the radial depth of the packing from 207 mm (configuration E) to 67 mm (configuration D) or 17 mm (configurations C.1 and C.2) had no influence on the resulting segregation index. Moreover, the influence of the packing pore size (configurations C.1 and C.2) can be considered negligible in the investigated range. In contrast, the lowest segregation index at the reference rotational speed of 1200 rpm was obtained without any packing. This trend is even more pronounced in Fig. 29, which can be explained by the use of different concentration sets. Since concentration set FVT-e includes a higher acid concentration than concentration set FVT-d, its sensitivity towards early effects in the mixing setup is also more pronounced (Chapter 4.2.3). The same observations as shown for H_2SO_4 can be made for the experiments with HCl as proton donator (concentration sets FVT-b/c, Fig. 65, Appendix C.4). Likewise, using a rotor without packing led to lower segregation indices at a high rotational speed, and higher sensitivity for the high-acid concentration set (FVT-c) was obtained.

Several explanations for the above observations are possible. However, based on the finding that the initial millimeters of the rotor are most important for the mixing process, the above considerations on the sensitivity of the method, the missing influence of the packing's radial depth, and the observations in chapter 5.4.2.1, it is reasonable to assume that an increased liquid load and hold-up at the inner packing radius negatively influences the mixing process. This consideration can be illustrated as follows: at 1200 rpm, the packing turns by 180° in 25.0 ms. Due to the wide liquid distribution angle of $\delta = 140°$, the minimum distance of the acid and buffer impingement zones is 40°, which is covered in 5.6 ms at 1200 rpm (Fig. 74a, Appendix C.8). Therefore, an increased liquid hold-up at the inner packing radius over a time scale of a few milliseconds could already be sufficient to increase the local acid surplus in the buffer impingement zone. Thus, the segregation index would be increased due to the packing at an opposite liquid distribution, as observed in Fig. 28 and Fig. 29. In contrast, acid and buffer are impinging together in the case of an overlapping liquid distribution. The resulting distance of the mutual impingement zone between two revolutions is 220° (Fig. 74b, Appendix C.8), corresponding to 30.6 ms at 1200 rpm. Thus, no such additional acid surplus could build up and the segregation index would not be negatively affected by the packing, as observed in Fig. 27.

Additionally, a back-splashing of liquid from the packing or intense local evaporation of iodine behind the eye ring's struts could contribute to the observed differences in the segregation indices at higher rotational speed.

By direct comparison of the results from Fig. 27 and Fig. 29 for an overlapping and an opposite liquid distribution (Fig. 66, Appendix C.4) it can further be deduced that in combination with a packing, an overlapping liquid distribution (φ = 0°) is beneficial for mixing at a volumetric ratio of 8. In contrast, it is only somewhat beneficial at a volumetric ratio of 3 (Fig. 22b), and no major difference is found for a sufficiently wide distribution at a volumetric ratio of 1 (Fig. 25, FF-II). Therefore, an overlapping liquid distribution onto the packing seems to be particularly important at increased volumetric ratios, which is in agreement with the assumption of an elevated influence of the impingement zone on the segregation index under these conditions. For a rotor without packing, no significant difference between an opposite liquid distribution (φ = 180°) and an overlapping liquid distribution (φ = 0°) could be found at a rotational speed above 600 rpm (Fig. 66).

5.5 Modeling Results

5.5.1 IEM Model Calculations

To allow a concentration-independent comparison of the results shown in Fig. 23 with results from the literature (Chapter 5.6), the respective micromixing time parameters t_{mix} were calculated based on the IEM model master curve, as obtained from Eq. (31). The resulting t_{mix} values are plotted in Fig. 30 as a function of the total liquid flow rate.

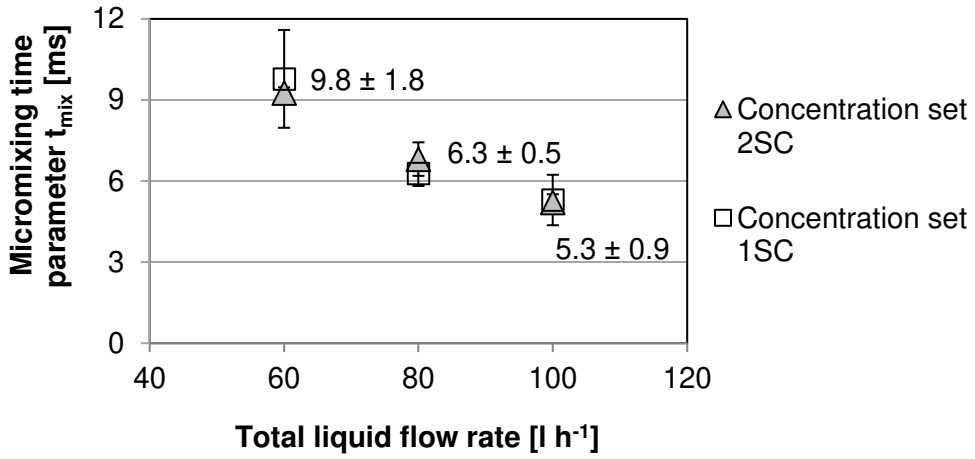

Fig. 30. Micromixing time parameter t_{mix} of the IEM model, as obtained from Eq. (31) for concentration sets 1SC and 2SC as a function of the total liquid flow rate. The underlying segregation indices are shown in Fig. 23. Error bars depict the sample standard deviation. Values are given for the concentration set 1SC.

As depicted in Fig. 30, micromixing time parameters between 9.8 ± 1.8 ms at a total liquid flow rate of 60 l h^{-1} and 5.3 ± 0.9 ms at 100 l h^{-1} are obtained from the IEM model master curve for equal flow rates (volumetric ratio: 1). While the rather small margins of error depict good experimental accuracy, the margin of error for the IEM model itself was considered by *Falk and Commenge* (Falk and Commenge 2010) to be within one order of magnitude. Therefore, the characteristic time scale of mixing for this range of liquid flow rates can only be determined to be on the order of 10^0 ms.

5.5.2 Incorporation Model Calculations

Based on the results shown in chapter 5.4.2.2, the micromixing time parameter t_{mix} was calculated for the results obtained with packing configuration E and without packing. For this calculation, the exponential and the linear approach of the incorporation model were considered. The results are shown in Fig. 31. As can be obtained from the figure, micromixing time values in the range of 10^0 ms to 10^{-1} ms are obtained from the incorporation model for the considered total liquid flow rate of 140 l h^{-1} at a volumetric ratio of 8. Because the underlying segregation indices for packing configuration E and for a rotor without packing were very similar (Fig. 28), also the corresponding micromixing time values are within a close range: at 1200 rpm, t_{mix} values of 0.67 ± 0.01 ms and 0.41 ± 0.15 ms, respectively, were obtained from the linear approach.

To further assess the quality of the two different incorporation model approaches, the t_{mix} values shown in Fig. 31, obtained with concentration set FVT-d at a rotational speed between 300 rpm and 1200 rpm, were used to predict segregation values for concentration set FVT-e at the same rotational speed. These predicted X_S values were then compared to the experimentally obtained X_S values (Fig. 29). The resulting parity plot is presented in Fig. 32, whereas the corresponding sum of squared deviation between the predicted and experimentally obtained X_S values is presented in Fig. 33. This assessment shows that both modeling approaches do not describe the reactive mixing process completely accurately. The exponential approach predicts X_S values in a range between -41 % and +1 % of the experimentally measured X_S values, whereas the linear approach predicts X_S values in a range between -26 % and +24 % of the experimentally measured X_S values. However, the sum of squared deviation for the linear approach is smaller than that for the exponential approach, particularly for experiments without a packing (Fig. 33).

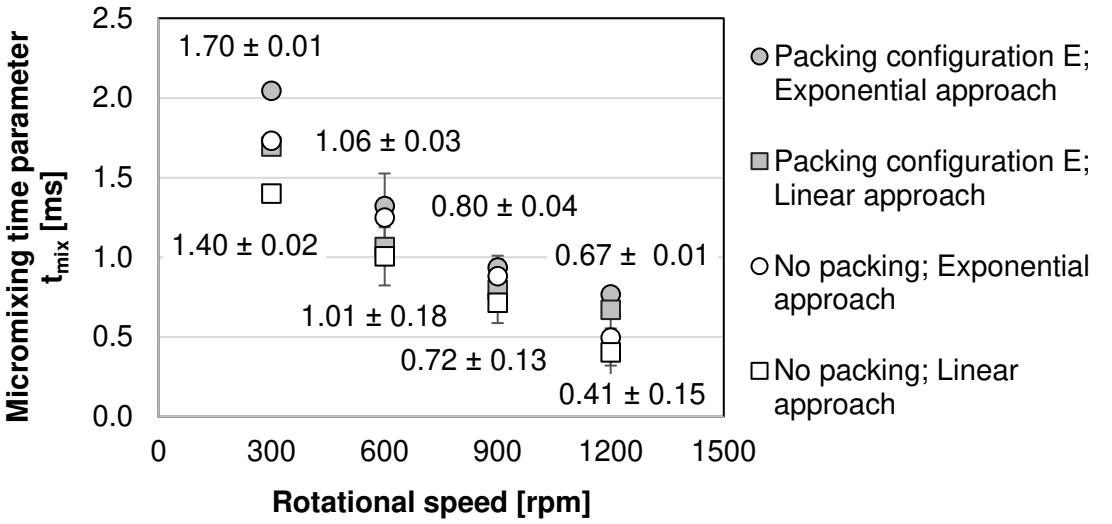

Fig. 31. Micromixing time parameter t_{mix} obtained from the incorporation model's exponential and linear approaches for packing configuration E and a rotor without packing as a function of the rotational speed. The underlying segregation indices are shown in Fig. 28 (opposite liquid distribution, concentration set FVT-d). Error bars depict the sample standard deviation. Values are given for the linear approach.

This observation of a slightly better fit for the linear approach could be explained by three mechanisms. First, since the volumetric ratio is still comparatively low, self-engulfment could be significant enough to slow down the growth process. Second, the liquid volume growth could be dominated by two-dimensional growth over a constant surface, as it would be the case for larger liquid aggregates, e.g., a film of liquid at the inner rim of packing and eye ring (Fig. 75, Appendix C.8). This would be in agreement with the results in chapter 5.4.2.2, suggesting an increased hold-up at the inner packing radius. In contrast, the surface of discrete liquid aggregates, e.g., small droplets at the inner packing rim, would increase over time based on three-dimensional growth. In this case, a better fit for the exponential growth term would be expected. Third, the liquid volume cannot grow exponentially because fresh liquid for the growth is not supplied fast enough. However, for the third mechanism, a decreasing fit of the exponential approach would be expected for an increasing rotational speed, which is not the case (Fig. 32).

For the sake of completeness, a comparison to results predicted by the IEM model is given in Fig. 68 (Appendix C.4). As to be expected, the overall fit of the IEM model predictions is very low for the volumetric ratio of 8 (combined sum of squared deviation: 108.8 %, Fig. 69). However, while the sum of squared deviation is particularly large for packing configuration E, it is in the same range as the incorporation model for a rotor

without packing. Since plug flow is one of the central assumptions of the IEM model, this finding suggests that backmixing takes places when the rotor contains a packing, but not without packing. Because backmixing within the packing itself seems unlikely based on the results in chapter 5.5.1 and in the literature, this result also supports the previous suggestion of backmixing in form of a liquid hold-up at the inner radius of the packing.

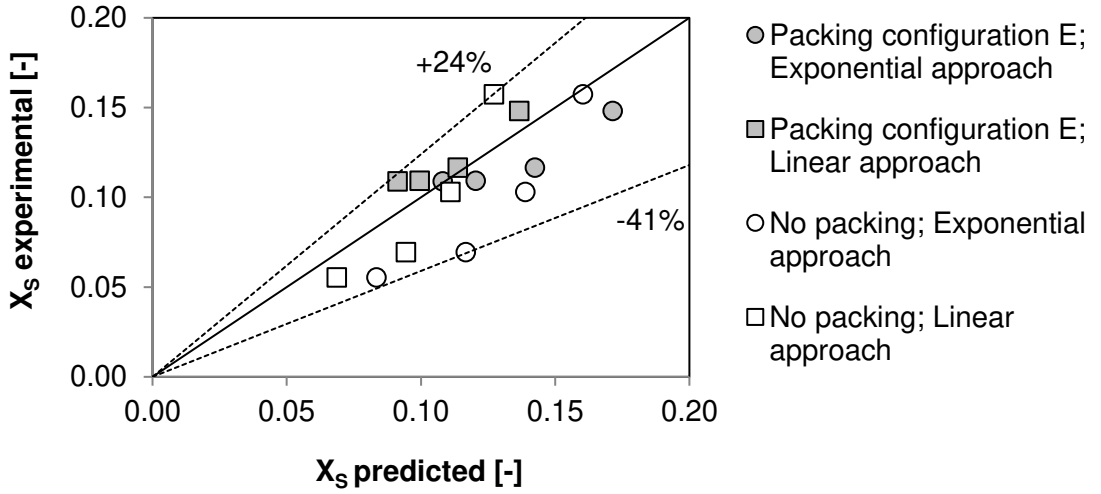

Fig. 32. Parity plot of experimentally measured X_S values (Fig. 29, FVT-e) and X_S values predicted by the linear and the exponential approach of the incorporation model (based on results shown in Fig. 28, FVT-d). The underlying experimental X_S values correspond to a decreasing rotational speed from left to right. Dotted lines are given to denote the positive and negative deviation from parity.

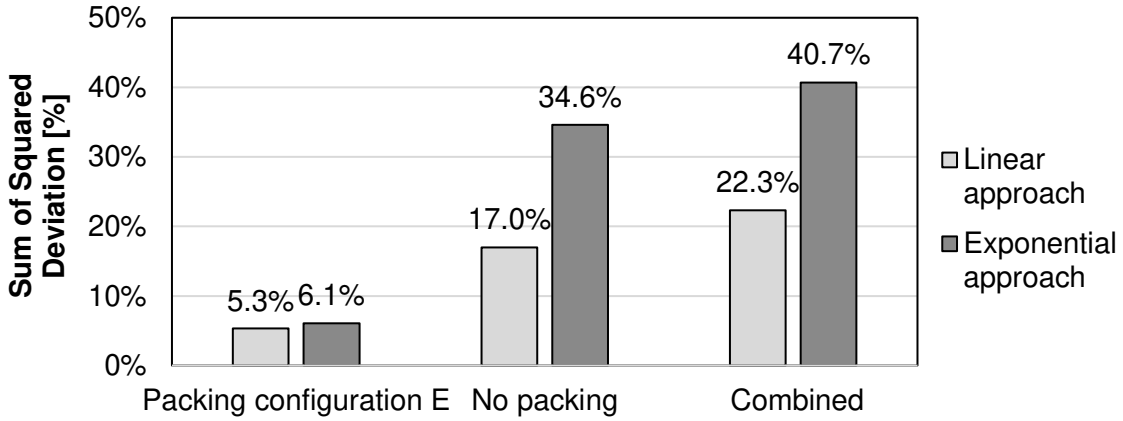

Fig. 33. Sum of squared deviation between experimentally measured X_S values (Fig. 29, FVT-e) and values predicted by the linear and the exponential approach of the incorporation model (based on results shown in Fig. 28, FVT-d), for packing configuration E, a rotor without packing, and the combination of both values.

5.6 Comparison with Other Mixing Devices

5.6.1 Mixing at Equal Liquid Flow Rates

Falk and Commenge presented an overview of the micromixing time parameter t_{mix} for mixing at equal liquid flow rates in different micromixers (Falk and Commenge 2010). The authors showed that the lower results range on the order of magnitude of 10^0 ms to 10^1 ms, which is the same order of magnitude as obtained in chapter 5.5.1 for the RPB 1.0 design. However, the total liquid flow rates in RPBs are usually significantly higher than those in micromixers. Therefore, a more detailed comparison with respect to the utilized liquid flow rates and the resulting pressure drop is given below. For the RPB 1.0 configuration used in chapter 5.5.1, the pressure drop over the nozzles was between 1.3 bar for a total liquid flow rate of 60 l h^{-1} and 3.6 bar for a total liquid flow rate of 100 l h^{-1}.

For a Villermaux-Dushman protocol with concentration set 1SC, *Commenge and Falk* analyzed data reported by *Kölbl et al.* (Kölbl et al. 2008) on their s100-12foils mixer (subsequently reported as a Zk10-12foils mixer (Kölbl et al. 2010)) to obtain micromixing time parameters (Commenge and Falk 2011). The authors applied the IEM model equations and concluded on a minimum micromixing time parameter of approximately 90 ms, as presented in Tab. 1. In addition, the results obtained for the mixer with the highest reported total liquid flow rate (Zk10-24foils; $\dot{V} \approx 25$ l h^{-1}; OD ≈ 0.1) and the mixer with the lowest reported OD (Zk10-2foils, $\dot{V} \approx 8$ l h^{-1}; OD ≈ 0.008) are given. The respective micromixing time parameters were likewise calculated according to the method presented by *Commenge and Falk* (Commenge and Falk 2011). While the best results in a V-type mixer can be obtained by minimizing the number of foils and thus increasing the exit velocity (Kölbl et al. 2010), this approach is limited by the strongly increasing pressure drop. The minimum micromixing time parameter is obtained for the Zk10-2foils mixer at 14 ms. However, the pressure drop at the corresponding liquid flow rate of 8 l h^{-1} was reported to be approximately 17.5 bar (Kölbl et al. 2010). Moreover, *Kölbl et al.* reported on the continuous mixing of equal liquid flow rates in cyclone-type mixers (Kölbl et al. 2011). The highest total liquid flow rate for the mixer with the lowest reported OD (mixer 4; 0.3) was 10 l h^{-1}. Applying the IEM model's master curve, a micromixing time parameter of only 0.06 ms can be obtained. This is, however, in agreement with the reported hydraulic residence time of 0.2 ms. Similar to the V-type mixer, a high pressure drop of approximately 16 bar is, nevertheless, reported for this comparably small liquid flow rate.

Tab. 1. Comparison of RPB data and data reported in the literature for other continuous mixing devices with equal inlet flow rates; micromixing time parameter for V-type mixer and cyclone-type mixer calculated according to *Commenge and Falk* (Commenge and Falk 2011).

Mixer	Maximum reported liquid flow rate [l h^{-1}]	Corresponding pressure drop [bar]	Corresponding micromixing time parameter [ms]	Characteristic time scale of mixing (order of magnitude) [ms]
RPB (Chapter 5.5.1)				
RPB 1.0	100	3.6	5.3 ± 0.9	10^0
V-type mixer (Kölbl et al. 2010)				
Zk10-12foils	11	4.5	90	10^1-10^2
Zk10-24foils	25	3.5	180	
Zk10-2foils	8	17.5	14	
Cyclone-type mixer (Kölbl et al. 2011)				
mixer 4	10	16.0	0.06	10^{-2}
T-jet mixer (Krupa et al. 2014)				
W6w1d6	45	n/a	35	10^1

Krupa et al. utilized the reaction between 1-naphthol/2-naphthol and diazotized sulfanilic acid to investigate continuous mixing processes with equal inlet flow rates in T-jet mixers (Krupa et al. 2014). For a maximum total liquid flow rate of 45 l h^{-1}, the authors reported a minimum micromixing time parameter of 35 ms, obtained through *Corrsin's* model. Overall, the results summarized in Tab. 1 demonstrate that RPBs are capable of mixing high and equal liquid flow rates within a few milliseconds. At the same time, the maximum reported liquid flow rates of the compared static mixers are considerably smaller and restricted by a high pressure drop. In contrast, static mixers only rely on the power input to the pumps, while active mixers such as RPBs require an additional power input. However, the liquid flow rate only contributes to this additional power input in RPBs to a small extent (Appendix C.2). Furthermore, the power input to the pumps can be kept low even at higher liquid flow rates by adjusting the nozzle type and thus reducing the pressure drop. Therefore, the use of RPBs instead of static mixers could be particularly beneficial for mixing large liquid flow rates.

5.6.2 Mixing at Higher Volumetric Ratios

In this chapter, the results of chapter 5.5.2 are assessed specifically in the context of intensified rotating devices, i.e, RPBs and SDRs. On this account, micromixing time parameters obtained in the literature through the incorporation model and the engulfment model at higher volumetric ratios than unity are considered. A more general comparison of different devices for reactive mixing was previously presented by *Visscher et al.* (Visscher et al. 2013).

As shown in chapter 5.5.2, micromixing time parameters in the range of 10^{-1} ms to 10^{0} ms are obtained for mixing in the RPB 2.0 design at a total liquid flow rate of 140 l h^{-1} and a volumetric ratio of 8 by means of the incorporation model. While it should be kept in mind that quantitative results rely strongly on the underlying model kinetics, this range is in agreement with results from the literature. *Chu et al.* reported micromixing time parameters in the order of 10^{0} ms for an RPB with metal foam packing, a total liquid flow rate of 31.2 l h^{-1}, and a volumetric ratio of 12 (Chu et al. 2015). For an RPB with liquid distribution pipes, *Yang et al.* reported that t_{mix} was 10^{-1} ms at a total liquid flow rate of up to 615.0 l h^{-1} and a volumetric ratio between 7.2 and 12 (Yang et al. 2005). For experiments in an RPB with a premixed distributor, even t_{mix} values as low as 10^{-2} ms were reported by the authors for a total liquid flow rate of up to 50.0 l h^{-1} and a volumetric ratio between 9 and 15 (Yang et al. 2015b).

Furthermore, *Jiao et al.* calculated that the micromixing time parameter for an RPB with impinging stream liquid distribution, a total liquid flow rate of 160.0 l h^{-1}, and a volumetric ratio of 7 was in the range of 10^{-2} ms to 10^{-1} ms (Jiao et al. 2012). However, it should be noted that these micromixing time parameters could not be reproduced in own calculations on the basis of the concentrations and segregation indices reported by the authors. Instead, the incorporation model equations used in this thesis (Chapter 5.2.2.2 and Appendix C.6) yield t_{mix} values in the range of 10^{-1} ms to 10^{0} ms.

In comparison, micromixing time parameters in the range of 10^{-1} ms to 10^{0} ms were reported by *Manzano Martinez et al.* for continuous mixing in an SDR (Manzano Martínez et al. 2017). However, these results were obtained at a total liquid flow rate of only 27.5 l h^{-1}, at a volumetric ratio of 50.

Overall, these results demonstrate that also at increased volumetric ratios, fast mixing of comparatively high liquid flow rates can be achieved in an RPB, as already shown for a volumetric ratio of 1 in chapter 5.6.1.

5.7 Conclusions and Outlook

The influence of the operational parameters rotational speed and total liquid flow rate on the segregation index can be concluded to be in agreement with the results from the literature (Chapter 4.3), as well as the overall trend for the influence of the volumetric ratio. For the influence of design parameters on the segregation index, it can further be concluded that the exact liquid distribution profile is less relevant for a fast mixing process than initially expected. Instead, it is important that the outlet velocity of the liquid is adjusted sufficiently high and that both the orientation angle and the distribution angle of the liquid distribution are chosen in a way that prevents excessive liquid loads on single spots of the packing. The investigations in this chapter further demonstrate that both a very high and a very low liquid hold-up at the inner rim of the packing can negatively affect the mixing process, making a sophisticated rotor and packing design an important factor for liquid mixing in RPBs. In this context, it is worth noting that *Neumann et al*. (Neumann et al. 2017) suggested a narrow liquid distribution for gas-liquid countercurrent contacting in RPBs, opposite the results in this chapter for cocurrent liquid phase mixing. This finding demonstrates that a fundamental understanding of RPBs is important to design them in such a manner that allows for their full potential to be utilized for each particular application. Overall, RPBs show a large potential for fast mixing of high total liquid flow rates at a low pressure drop, which is complemented by their capability to process viscous media (Chapter 4.5) and their inherent flexibility. To increase the production capacity, numbering-up is usually necessary with conventional equipment. In contrast, RPBs offer the possibility of adjusting the rotational speed and the liquid distribution design. Thus, constant mixing time and pressure drop values could be realized for different liquid flow rates over a large operating range and it can be concluded that RPBs offer one additional degree of freedom in comparison to active in-line mixers and two additional degrees of freedom in comparison to static mixers. However, RPBs also rely on the energy input of the motor and their moving parts are more likely to require maintenance than static mixers. Therefore, future research should add operation and maintenance costs to this comparison. Additionally, it was demonstrated that the packing is especially important at volumetric ratios close to 1. In contrast, only a smaller packing or just a rotating eye ring may be necessary for fast mixing at higher volumetric ratios, particularly in combination with an opposite liquid distribution. It should be noted that the investigations without packing, where the rotor only contained the eye ring and the spacers, have a strong analogy to the blade-packing RPB investigated by *Lin and Tsai*, which also showed promising results ((Lin and Tsai 2016), Chapter 4.4.1). Furthermore, it was reported in the literature that a smaller packing pore size had a positive influence

on the segregation index (Chapter 4.3.2.3). No such effect could be found in this chapter. Therefore, the range of investigated pore sizes in combination with the investigated volumetric ratio should be extended in future work.

By means of improvements between the RPB 1.0 design and the RPB 2.0 design, as well as a more suitable operation, the average residence time in the complete RPB could be drastically reduced (Appendix C.5). However, the RTD curves for the RPB 2.0 design are still unsatisfyingly broad if an RPB should be applied for industrial applications, as will be shown in more detail in chapter 6.

With respect to the utilized mixing models, it can be concluded that, despite its simple nature, the IEM model is sufficient to describe the mixing of two equal inlet streams under the investigated conditions. This could implicate that plug flow, the basic assumption of the IEM model, is fulfilled for liquid mixing in RPBs as long as liquid load and liquid hold-up are moderately high. However, more thorough investigations are necessary to validate the model for the whole range of possible operating conditions in combination with equal liquid flow rates in RPBs. In contrast, the mixing of a volumetric flow ratio of 8 was not well described by the IEM model, but best described by the linear approach of the incorporation model. Furthermore, recently published kinetics, which implicitly incorporate the incomplete dissociation of sulfuric acid, were successfully implemented. A limitation with respect to a concentration-dependency of the linear approach, as reported by *Assirelli et al.* (Assirelli et al. 2008), could not be confirmed in this chapter. Nevertheless, an overall model or approach that is capable of describing and comparing the whole possible range of RPB operation is still to be found. All micromixing time values obtained from the linear approach for a volumetric ratio of 8 were in the order of milliseconds, even for a rotor without packing. Therefore, it appears reasonable to design an HiGee apparatus that combines the mixing efficiency of an RPB with a much smaller rotor volume and a further reduced residence time. A respective design will be presented in detail in chapter 7.5.

Ultimately, the results presented in this chapter have to be considered black box investigations, which can only show the integral result of the mixing process over the complete RPB setup. Therefore, future methods which allow for detailed investigations would be preferable. Also, all investigations should be repeated with a different method to evaluate the meaningfulness of the results and exclude an influence of the method's sensitivity on the results.

6 APPLICATION CASE STUDIES *

In this chapter, three different case studies for liquid processing in RPBs are discussed. First, the production of methylene diphenyl dianiline (MDA) is investigated in a case study on liquid phase reactive mixing (Chapter 6.2). These results are supplemented by a literature study on the RPB-based production of methylene diphenyl diisocyanate (MDI, Appendix D.2) and the production of isobutylene-isoprene rubber (IIR; Appendix D.3). Second, the liquid-liquid extraction of γ-Valerolacton by means of an RPB-based three-stage process is presented in a case study on liquid-liquid extraction. Third, the RPB-based refining of vegetable oil is investigated in a case study on liquid-gas processing.

6.1 Introduction

For the design and the construction of industrial liquid phase processes, two factors are most important for an economically feasible operation. On the one hand, suitable equipment, capable of satisfying requirements on product quality and yield, must be determined. On the other hand, the required production capacity must be met, which commonly dictates the necessary equipment size. Especially for processes including fast chemical reactions, the first requirement can drastically restrict the equipment choice. In contrast, solving both tasks in a reduced equipment volume through process intensification can yield remarkable benefits over common equipment. Mechanical agitation, as one means for process intensification, can result in equipment size reductions by a factor of up to 100 (Ramshaw 1995; Stankiewicz, A.I., Moulijn, J.A. 2000). This lower equipment volume reduces investment costs, lowers the risk of potentially dangerous situations and allows for the application of more expensive coating materials, improving the durability as well as the range of applications (Visscher et al. 2013).

---

* The scientific work published in this chapter was performed by D. Wenzel and supported by A. J. Minor and T. Pyka in the framework of bachelor theses. Scientific advice was given by A. Górak.

* Parts of this chapter have been published as:
A guide on the industrial application of rotating packed beds (2018), Neumann, K.; Gladyszewski, K.; Groß, K.; Qammar, H.; Wenzel, D.; Górak, A.; Skiborowski, M.; Chem. Eng. Res. Des. 134, pp. 443–462.

However, besides RPBs there is also a wide range of established conventional equipment and competing technologies for intensified liquid processing, such as micromixers and SDR (Falk and Commenge 2010; Visscher et al. 2013). Therefore, the industrial applicability of RPBs must be critically reviewed in the context of available alternatives and conventional production processes. This will be done in the framework of the following case studies.

6.2 Case Study: Liquid Phase Reactive Mixing

6.2.1 Introduction

The reactive mixing of aniline and formaldehyde to obtain MDA is the first step to produce MDI (Appendix D.2), one of the most important raw materials for the polyurethane industry (Six et al. 2003). This condensation reaction is typically very rapid and strongly exothermic. Furthermore, inefficient mixing in the reactor can lead to a non-uniform concentration distribution (Zhao et al. 2010). Therefore, undesirable by-products are often formed in the conventionally utilized reactors, like STRs and jet mixers (Hua et al. 2007). Also, local overheating (Ding et al. 2007b) and blockage of pipes due to the presence of viscous by-products (Zhao et al. 2010) have been reported. Taking this into account, it seems necessary to conduct the condensation reaction under very efficient mixing conditions, as they could be provided by RPBs, while closely controlling and regulating the reactor's temperature. Indeed, two promising studies on product yield and composition are available for the production of MDA in RPBs.

For a pilot-scale RPB process, *Hua et al.* reported to have reduced the concentration of one of the key by-products, by 80 % from 0.78 wt.% in the conventional production process in an STR to 0.16 wt.% in the RPB (Hua et al. 2007). At the same time, the MDA yield was increased from 97.4 % in the STR to 99.3 % in the RPB. In comparison, a cascade of three STRs only achieved a by-product reduction of 42 % and an MDA yield of 98.4 % – at a remarkably larger equipment volume. According to the authors, this benefit could be contributed to the intense micromixing inside of RPBs. Unfortunately, the authors did not give any details on the process itself or the utilized RPB. Additionally, *Ding et al.* patented an RPB process for the production of MDA (Ding et al. 2007b). In a direct comparison of the same recipe produced in an STR alone and a combined RPB and STR process, the concentration of one of the key by-products could be reduced by 60 % from 0.23 wt.% to 0.09 wt.%, while slightly increasing the MDA yield from 70.93 wt.% to 71.14 wt.%. Nevertheless, the authors did not include

any details on their RPB and no information on the temperature control in an RPB has been published for an MDA production process so far.

6.2.2 Fundamentals

MDA is formed from aniline and formaldehyde in the presence of hydrochloric acid as a catalyst (reaction (v)). The educts and the key product 4,4'-MDA are shown schematically in Fig. 34.

$$C_6H_7N + CH_2O \xrightarrow{HCl} C_{13}H_{14}N_2\ (MDA) + H_2O \qquad (v)$$

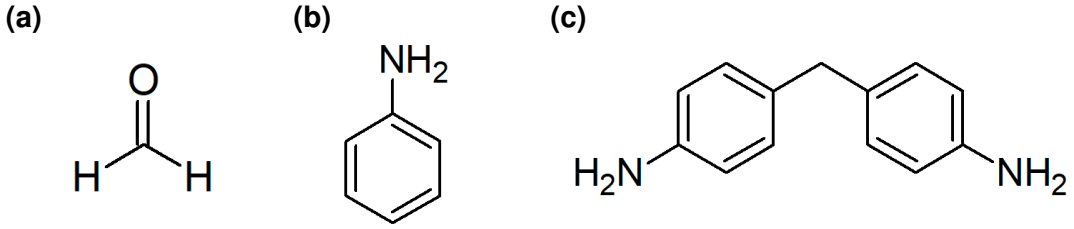

Fig. 34. Schematic drawings of the reactants of reaction (v). (a) aniline; (b) formaldehyde; (c) 4,4'-MDA.

Besides the mostly desired *para*-isomer 4,4'-MDA, also the *ortho*-isomeres 2,4'-MDA and 2,2'-MDA can be formed. The distribution of the MDA isomers depends on the ratio of aniline to formaldehyde, the acid concentration, and the reaction conditions (Six et al. 2003). In addition to these primary amines with two and more aromatic rings, by-products such as N-methylated compounds (Fig. 35 (a)), quinazolines (Fig. 35 (b)), secondary amines (Fig. 35 (c) and (d)), and oligomeric and polymeric amines (triamines, tetramines, etc.) can be formed through side-reactions (Nayar and Francis 1978; Botella et al. 2011; Corma et al. 2004; Wegener et al. 2001). N-methylated compounds are particularly undesirable because they cannot be transformed into isocyanates through reaction with phosgene in the subsequent production of MDI (Appendix D.2), in contrast to the intended primary amines (Botella et al. 2011; Wegener et al. 2001).

Overall, suitable MDA crude should not contain more than 1 % of N-methylated compounds; preferably, less than 0.5 % (Botella et al. 2011). With respect to secondary amines, a final concentration below 0.5 % is desirable (Botella et al. 2011).

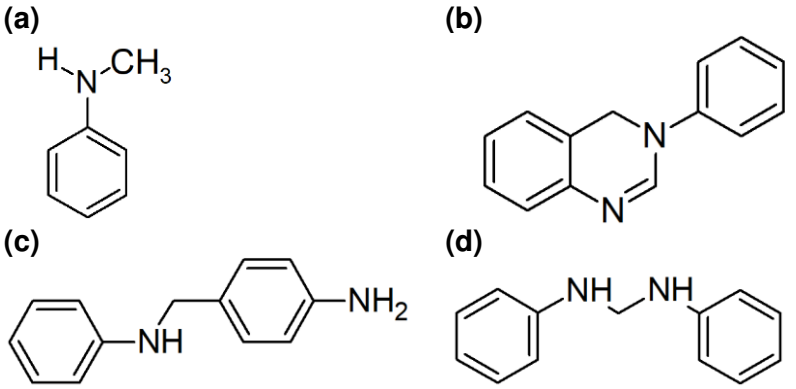

Fig. 35. By-products from the reaction of aniline with formaldehyde.
(a) N-methylaniline, one of the various possible N-methylated compounds;
(b) quinazoline; (c) aminobenzylaniline (ABA); (d) dianilinomethane.

Practically, reaction (v) is realized by premixing aniline and hydrochloric acid, before adding formaldehyde (Benneker et al. 2016; Botella et al. 2011). The process is commercially conducted in an STR at a temperature of 60°C to 80°C and with a molar ratio of aniline to formaldehyde of 2:1 (Botella et al. 2011). After completion of the formaldehyde addition, a mixture of primary and secondary amines is obtained. The exact proportion is mostly dependent on the acid concentration (Santhanalakshmi 1988). Since the disposal of large amounts of saltwater is considered a major drawback of the conventional process, hydrochloric acid is usually added in sub-stoichiometric amounts (Botella et al. 2011). This, however, favors the formation of secondary amines. Consequently, the mixture must be transferred to an isomerization section and heated to 90°C to 160°C for about 2 h to 3 h to convert secondary amines to primary amines through an interconversion reaction (Botella et al. 2011; Benneker et al. 2016; Ding et al. 2007b). The acidic mixture is then neutralized by sodium hydroxide (Benneker et al. 2016). Afterward, the resulting organic and aqueous phases are separated and worked up. By removing un-consumed aniline from the organic phase by means of distillation, MDA is obtained, which can then be used for the production of MDI (Benneker et al. 2016).

Ideally, a high primary amine concentration and very low concentrations of N-methylated compounds and secondary amines should be present at this point. However, a maximum 4,4'-MDA concentration cannot be considered the overall goal of an ideal process. Instead, being able to exactly control the proportion of *para*- and *ortho*-isomers, as well as the proportion of monomeric and polymeric MDA, would be desirable (Wegener et al. 2001). Furthermore, one of the key difficulties of the conventional process is the addition of the formaldehyde. A formaldehyde excess

favors the formation of by-products and results in local hot-spots (Benneker et al. 2016; Hua et al. 2007). This is particularly problematic since the reactants mixture typically has a viscosity in the range of 40 mPas to 80 mPas (Hua et al. 2007). Therefore, formaldehyde must be added over a substantial period of time or over multiple stages in the conventional process (Benneker et al. 2016; Hua et al. 2007).

6.2.3 Materials and Methods

6.2.3.1 Experimental Setup and Chemicals

The chemicals used in the experimental investigations are summarized in Tab. 18 (Appendix D.1). The experimental setup and procedure of the MDA experiments were kept close to the setup and procedure described and patented by *Ding et al.* (Ding et al. 2007b). The experimental setup is shown in Fig. 36.

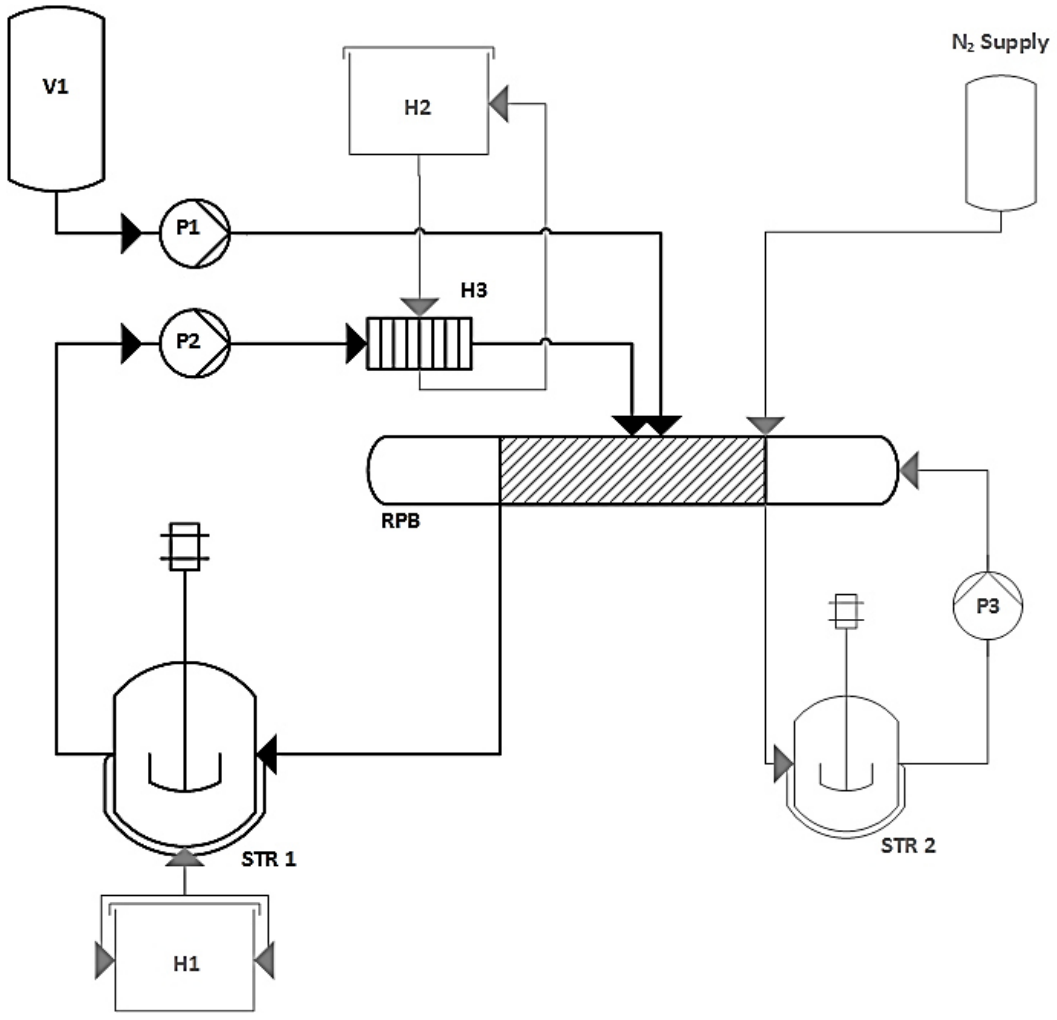

Fig. 36. Experimental setup of the pilot plant used in the MDA experiments. Primary equipment is shown in black, secondary equipment is shown in grey.

The aniline and the HCl were premixed in feed STR 1, which was equipped with a heating mantle heated by oil bath H1. Afterward, the aniline-HCl-mixture was pumped to the RPB by pump P2, passing through a plate-type heat exchanger (H3), which was connected to thermostat H2 and could either cool or heat the feed. In parallel, formaldehyde was pumped from tank V1 to the RPB by pump P1. The two feed streams were fed to the RPB by means of a nozzle liquid distribution (Tab. 20, Appendix D.1). The liquids would then flow through the packing and leave the RPB through the liquid outlets. From the four liquid outlets of the RPB, one was connected back to STR 1 (re-circulation), one outlet was connected to the rinsing circuit (closed during experimental runs), and two outlets were permanently closed. Thus, the reacted mixture was continuously circulated over RPB and STR 1. In order to push the liquid out of the RPB, nitrogen was used to build up a slight overpressure of 0.5 barg within the RPB casing. Additionally, the RPB could be connected to a rinsing circuit, comprising STR 2 and pump P3, to rinse the RPB with pure aniline, methanol, or water. The RPB used in these experiments was the RPB 1.0 design with packing configuration A (Tab. 14 and Tab. 15, Appendix C.1).

6.2.3.2 Experimental Procedure

For the preparation of the experiments, the supplied aqueous formaldehyde solution (formalin; Tab. 18, Appendix D.1) was diluted down from 44 wt.% to 37 wt.% by adding water. Similarly, the supplied hydrochloric acid was diluted down from 37 wt.% to 30 wt.% by adding water. The aniline was used as supplied. Then, 5503 g of aniline were mixed with 2584 g of the 30 wt.% hydrochloric acid solution to obtain 8087 g of premixed aniline-HCl-solution. An overview of the experiments conducted with the combination RPB and STR 1 is given in Tab. 19 (Appendix D.1). At the beginning of each experiment, STR 1 was started and heated up by heater H1. Then, the premixed aniline-HCl-solution was added to STR 1. The RPB was started and set to a rotational speed between 600 rpm and 1200 rpm. By circulating the heated aniline-HCl-mixture from STR 1 over the RPB, the RPB was heated up prior to the start of the formaldehyde addition. However, for a first set of experiments, the RPB was left cold until the start of the formaldehyde addition (cold start). Followingly, the circulation flow was put to its set point (between 1000 g min^{-1} and 3000 g min^{-1}) and the formaldehyde addition was started. The formaldehyde was added at a rate between 83 g min^{-1} and 100 g min^{-1} over a time of 23 min and 19 min, respectively. Then, the formaldehyde addition and the circulation flow were stopped and all liquid was allowed to flow back to STR 1. The final molar ratio of aniline/formaldehyde/HCl thus was 2.5/1.0/0.9. After a resting time of 10 min, STR 1 was heated to 90°C. It was kept at 90°C for 2 h to allow for the

interconversion reaction to occur. Afterward, a 0.05 l sample was taken and neutralized with NaOH. All samples were then analyzed by means of gas chromatography (GC) and nuclear magnetic resonance (NMR) analysis. GC values are reported for the 4,4'-MDA and the total MDA content, corrected for the remaining aniline content. NMR values are reported for the content of quinazolines, N-methylated compounds, secondary amines, and primary amines, with respect to the moles of formalin used for the reaction. After the end of each experiment, the RPB was flushed with aniline, methanol, and water. First, pure aniline was heated to 50°C in STR 2 and circulated over the RPB for 15 min. Afterward, pure methanol was heated to 50°C in STR 2 and circulated over the RPB for 10 min. Finally, water was fed to the still hot STR 2 and circulated over the RPB until coming out clear. For comparison, the same recipe was also once prepared in a well-stirred, well-tempered small scale STR (1 l) and once in STR 1 alone. For this experiment, aniline and HCl were first mixed, before the formaldehyde was added over a time of 132 min. STR 1 had a volume of 10 l and was equipped with an anchor stirrer (0.09 m in diameter), running at 250 rpm. STR 2, used in the rinsing circuit, had a volume of 6 l and no stirrer.

6.2.4 Experimental Results

A comparison of the reference values presented in "Example 1" of *Ding et al.'s* patent (Ding et al. 2007b) and experimentally obtained values for the 4,4'-MDA content, the overall MDA content, and the concentration of N-methylated compounds, the key impurities, is shown in Fig. 37. As can be obtained, the values of the patent could not be reproduced in own experiments. While the combination of STR 1 and RPB is slightly superior the use of STR 1 alone, the resulting values do not exceed those obtained by using the conventional method, i.e., a well-stirred, well-tempered small scale STR. The details of these findings will be investigated in more detail in the following.

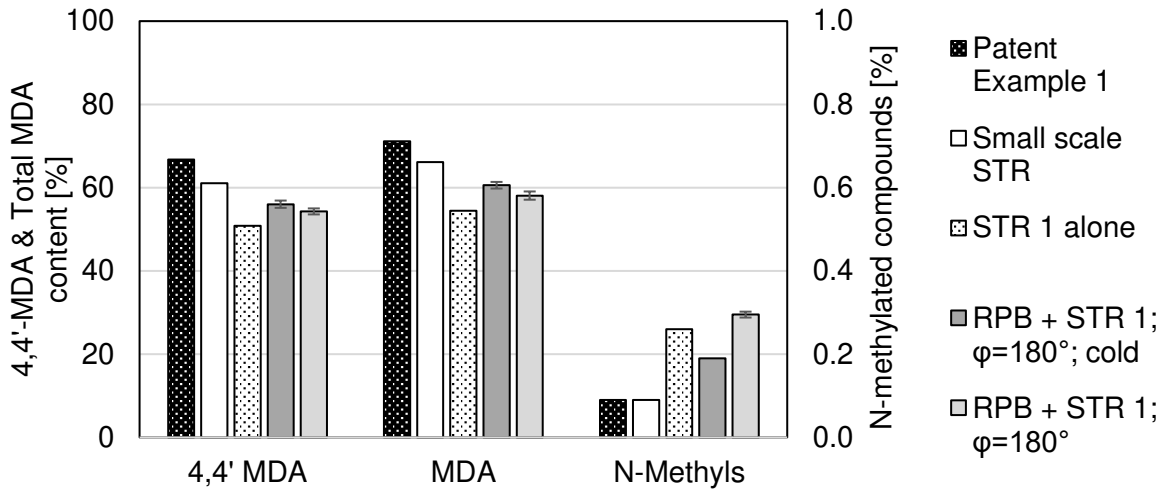

Fig. 37. Comparison between reference values presented in "Example 1" of *Ding et al.'s* patent, values obtained in the small scale STR, STR 1 alone, and RPB + STR 1 together (values are given for regular start and cold start conditions).

In a first set of experiments, the influence of the position of the formaldehyde addition, the initial temperature of the RPB, and two different ways of liquid distribution on the final sample composition were investigated. In order to analyze the influence of these parameters on the process, the key and by-product concentrations in the final samples, according to the NMR analysis, are shown in Fig. 38. The concentration of the by-products quinazolines, N-methylated compounds, and secondary amines are shown on the primary Y-axis, while the concentration of the primary amines is shown on the secondary Y-axis.

As can be obtained from Fig. 38, the results for a formaldehyde addition to the STR and a formaldehyde addition to the RPB are either virtually identical or very similar, both for an initially cold RPB and for regular start conditions. This means, that the time of intense mixing in the RPB packing can be assumed negligibly small in comparison to the residence time in the rest of the setup. In contrast, the influence of temperature is much more pronounced.

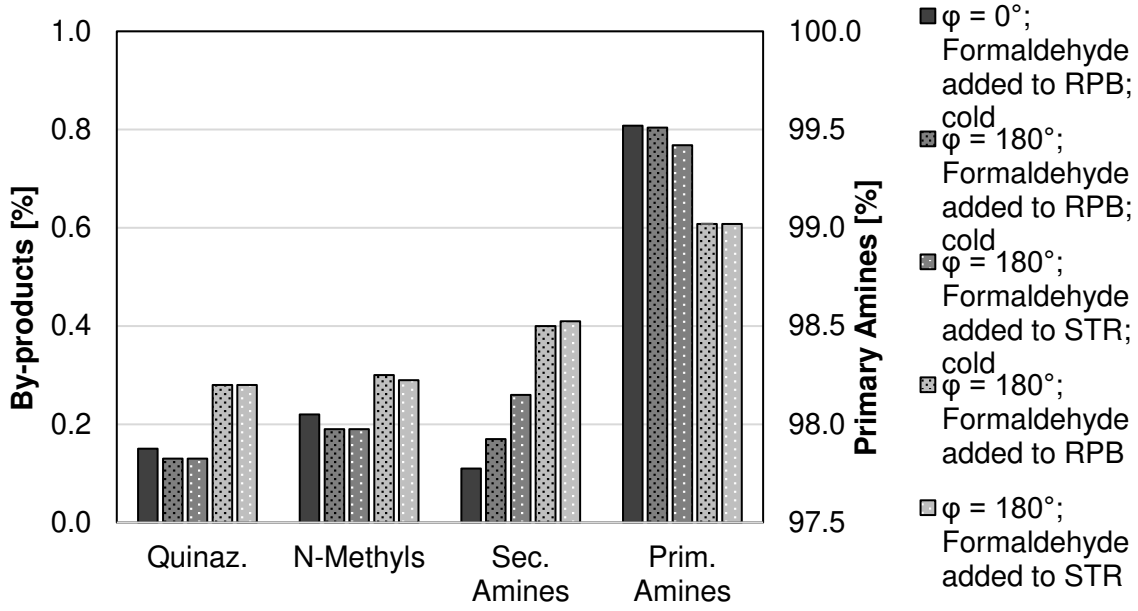

Fig. 38. Influence of the position of the formaldehyde addition, the initial temperature of the RPB, and two different ways of liquid distribution on the final sample composition. Final concentrations of quinazolines, N-methylated compounds, secondary amines, and primary amines, as obtained by NMR analysis.

As shown, increasing the initial RPB temperature significantly increases the by-product concentration, whereas the primary amine concentration decreases. Because the feed position of the aniline also had almost no influence on the results, it can be assumed that these results reflect a significant liquid hold-up in the very ill-mixed RPB casing bottom and on the RPB casing walls. Since increasing the temperature increases the reaction velocities, the residence time in these zones of bad mixing becomes more pronounced with an increasing initial temperature of the RPB. Furthermore, the influence of the liquid distribution is ambiguous but rather small. While the amount of primary amines is slightly increased for an overlapping liquid distribution (φ = 0°), so is the amount of quinazolines and N-methylated compounds. Under practical terms, however, an orientation angle of φ = 0° does not seem reasonable as it was observed to lead to significant fouling in the experiments (Fig. 76, Appendix D.1). This kind of fouling was not observed in the case of an opposite liquid distribution (φ = 180°), even for an initially cold RPB. Consequently, all further experiments were conducted at a nozzle orientation of φ = 180°.

In conclusion of Fig. 38, the influence of the RPB can be distinguished into the primary influence of the RPB on the mixing of the two liquids, and the secondary influence of the RPB on the reaction temperature. The first influence was investigated further by

varying the rotational speed. The temperature profiles in the RPB and in STR 1 are given in Fig. 39 as a function of the formaldehyde addition time, whereas the resulting by-product and primary amine concentrations are shown in Fig. 40. As can be obtained from Fig. 39, no influence of the rotational speed on the temperature profiles – as a measure of the reaction intensity – in the RPB can be observed. In the same way, the influence on the temperature profiles in STR 1 can be assumed to be not significant.

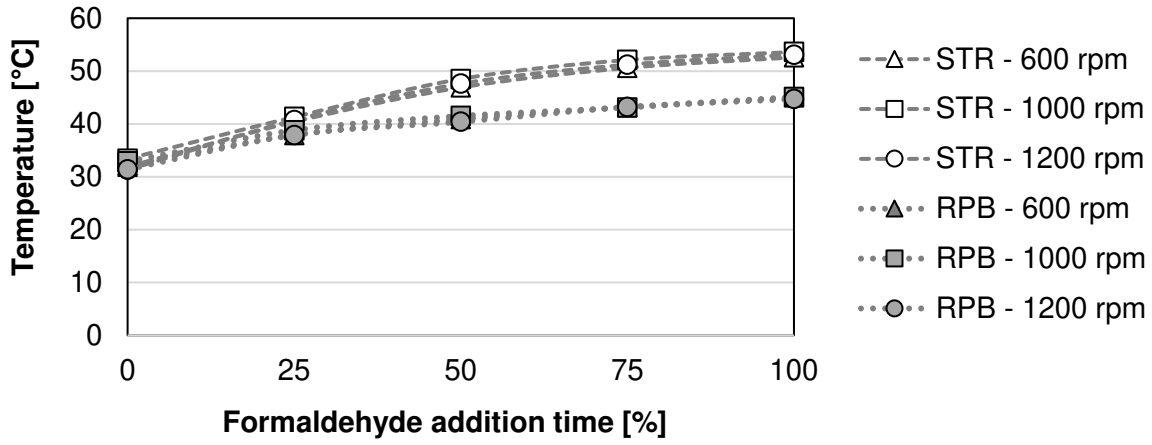

Fig. 39. Influence of the rotational speed on the temperature profiles in the RPB and in STR 1, as a function of the formaldehyde addition time.

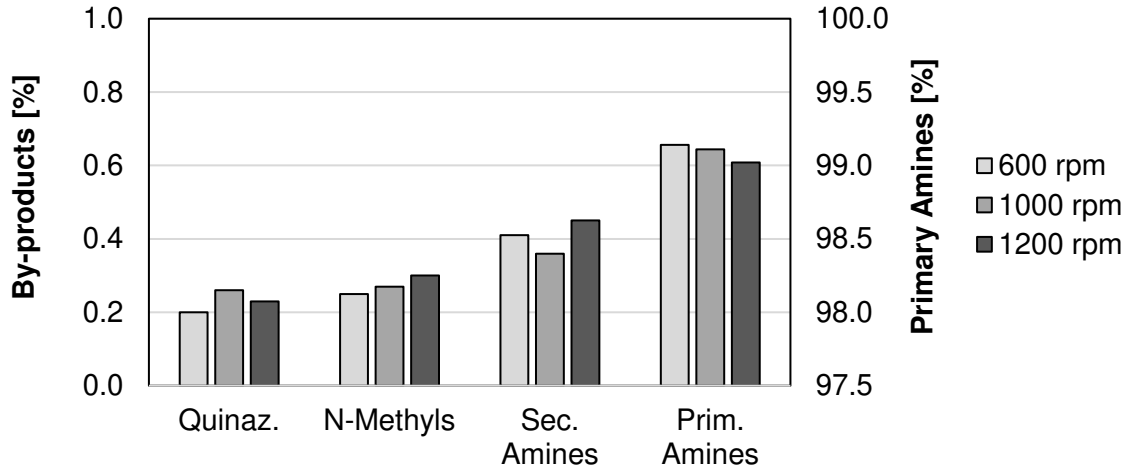

Fig. 40. Influence of the rotational speed on the final sample composition. Final concentrations of quinazolines, N-methylated compounds, secondary amines, and primary amines, as obtained by NMR analysis.

In combination with the concentration results shown in Fig. 40, it can be concluded that increasing rotational speed is either negatively influencing the product composition – or not at all. This is in strong contrast to the literature results and the initial key assumption

that a higher rotational speed would strongly and positively influence the product composition due to a more intense micromixing.

The secondary influence of the RPB on the reaction temperature can be further investigated by comparing the temperature increase in STR 1 for different operation conditions. Fig. 41 shows the temperature difference in STR 1 between the start and the end of the formaldehyde addition over the formaldehyde addition time for STR 1 alone, for the operation of RPB and STR 1 together for a circulation flow of 1000 g min^{-1}, 2000 g min^{-1}, and 3000 g min^{-1}, as well as for a circulation flow of 2000 g min^{-1} and an 18 % shorter formaldehyde addition time. Furthermore, the formaldehyde addition time is given. The corresponding final sample concentrations are shown in Fig. 42.

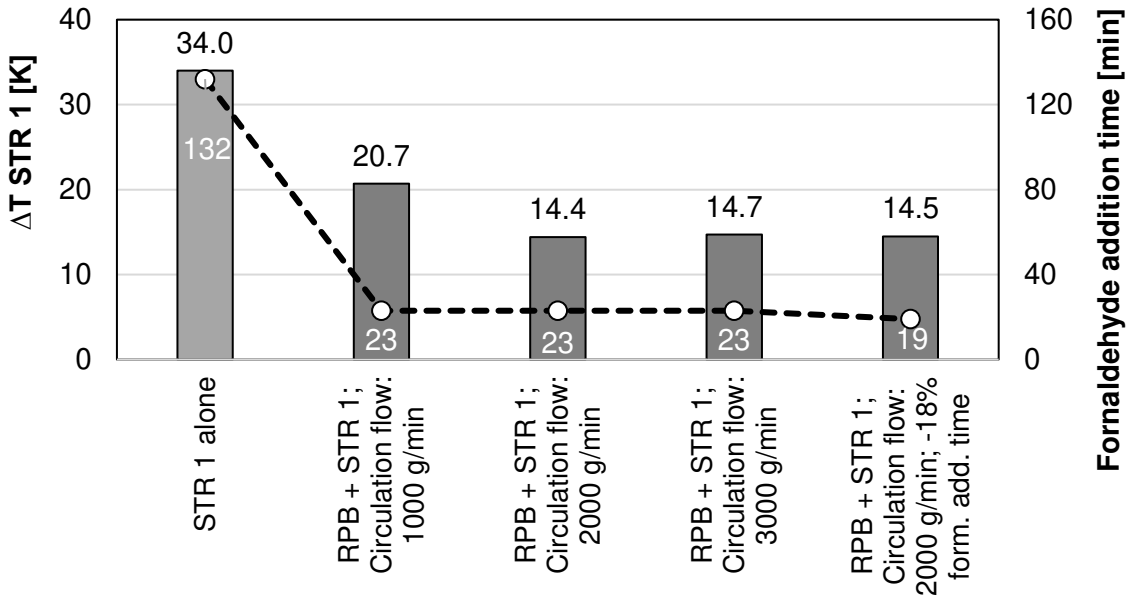

Fig. 41. Delta T in STR 1 (black numbers, primary Y-axis) and formaldehyde addition time (white numbers, secondary Y-axis) for STR 1 alone, for the operation of RPB and STR 1 together for a circulation flow of 1000 g min^{-1}, 2000 g min^{-1}, and 3000 g min^{-1}, as well as for a circulation flow of 2000 g min^{-1} and an 18 % shorter formaldehyde addition time. The formaldehyde addition time is given as dotted line.

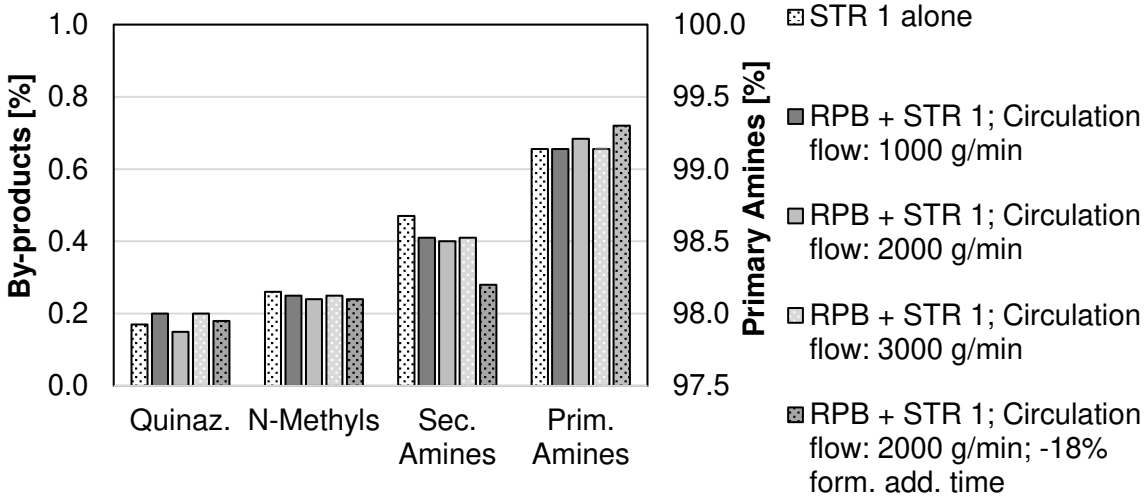

Fig. 42. Influence of different feed rates on the final sample composition. Final concentrations of quinazolines, N-methylated compounds, secondary amines, and primary amines, as obtained by NMR analysis.

It can be obtained from Fig. 41 and Fig. 42 that the additional utilization of the RPB facilitates a much faster formaldehyde addition while reducing the temperature difference in STR 1. This effect is more pronounced for a higher circulation flow rate, which can be explained by a lower relative formaldehyde surplus. However, also a 20 % faster formaldehyde addition did not negatively affect this influence. Instead, the by-product concentration did not change significantly (quinazolines and N-methylated compounds) or even decreased (secondary amines), whereas the concentration of primary amines slightly increased.

6.2.5 Conclusions and Outlook

In contrast to findings in the literature, the combination of RPB and STR was not found to be superior to the conventional method, using an STR alone. Furthermore, the sensitivity of the process results towards changes in RPB operation and design parameters was very low. This indicates that the results largely reflect the mixing process in the STR, the piping, and the RPB casing, instead of the mixing process in the RPB rotor.

It is shown in Appendix C.5 that the average hydraulic residence time τ of liquid in the RPB 1.0 design is 54.3 s for a similar flow rate of 54.0 l h^{-1}, whereas the residence time in the rotor can be assumed to be in the range of only 0.2 s to 1.4 s (Yang et al. 2015a). In contrast, *Ladwig et al.* calculated a conversion half-life period of formaldehyde of 6 s and a total formaldehyde conversion time of 150 s for a similar recipe (1.7/1/0.85), a

reactor temperature of 70°C and an ideal plug flow reactor (Ladwig et al. 1991; Ladwig et al. 1989). Under these assumptions, only 15 % of the added formaldehyde would be consumed within the first 1.4 s. Also, a large set of equilibrium reactions with characteristic reaction times in a similar order results from the many possible by-products and intermediate products (Ladwig et al. 1989). This allows for two general conclusions. Firstly, the Villermaux-Dushman protocol alone might be unsuitable to accurately model the parallel-competitive set of reactions occurring during the reactive mixing of formaldehyde and aniline. Secondly, constant intense mixing could be considered more reasonable than very fast initial mixing followed by slow mixing.

Additionally, the residence time in dead zones on the RPB's casing walls and in the casing bottom, as well as residence time in the pipes, and the STR can be assumed to be much more influential than the residence time in the RPB rotor and packing. Furthermore, it was found in chapter 5.5 that the micromixing time for a similar total liquid flow rate and volumetric ratio changes in the range of 10^{-3} s – 10^{-4} s for a rotational speed increase from 600 rpm to 1200 rpm. Therefore, if the characteristic reaction time is much higher (as can be expected based on *Ladwig et al.'*s results) the sensitivity of experimental results towards the rotational speed may indeed be negligible. Instead, a higher rotational speed will lead to a lower residence time in the packing and more splashing on the casing walls. This is particularly problematic in the utilized RPB 1.0 design with a large distance between the rotor and the casing (Fig. 5). An additional problem was found to arise from fouling in case of an overlapping liquid distribution. Instead, an opposite liquid distribution seems reasonable under practical terms.

The main advantage of an RPB utilization in the conducted experiments was an improved temperature control due to the thick casing walls of the RPB 1.0 design. Given the casing's very large heat capacity, the formaldehyde addition time could be reduced from 132 min in STR 1 alone to 19 min in the combination of STR 1 and RPB. This equals an almost 7-fold capacity increase. However, it should be noted that under real continuous operation this advantage would become irrelevant as soon as thermal steady state conditions are reached. With respect to *Ding et al.*'s patent, several conclusions can be drawn. The patent claims to describe a continuous preparation of MDA with an RPB as mixer-reactor. However, the described process steps are those of a semi-batch process where the liquid is mixed in an STR for the majority of the time. This is particularly important with respect to the fact that the MDA and N-methyl values in the patent are very similar to those obtained in the well-mixed, well-tempered small scale STR (Fig. 37). Furthermore, as no results for parameter variations of the RPB are presented, it remains unclear if the patent process is sensitive to RPB operation and design changes. Interestingly, the patent describes a comparatively low rotational

speed of 450-1500 rpm to be most preferable, while 3000 rpm would be technically possible in the authors' RPB. Indeed, only 1000 rpm are used in the reference *Example 1*. Therefore, it can be concluded – with respect to the above presented experimental results – that the ascribed benefit of the RPB could actually lie in an improved temperature control, instead of a faster initial mixing of the reactants.
For future MDA experiments in an RPB, several design parameters should be adapted. Most importantly, the residence time in the casing needs to be drastically decreased, while the residence time in the rotor and the packing should be increased. The casing size and the distance between the rotor and the casing should be significantly reduced and the size of the liquid outlets significantly increased. In order to further facilitate a low liquid hold-up in the casing, a horizontal rotational axis would be preferable. A respective design of a more suitable, novel type of HiGee equipment will be presented in chapter 7.5.
Furthermore, many attempts have been published to reduce the necessary amount of hydrochloric acid. One of the most promising attempts is the use of heterogeneous catalysis over zeolite type structures (Wegener et al. 2001; Botella et al. 2011). One field of application for these catalysts could be the packing in an improved RPB design. By changing the packing, a quick and easy change between different zeolite types would be possible. Thus, also the final product composition could be controlled.

6.3 Case Study: Liquid-Liquid Extraction

6.3.1 Introduction

The dependence of the transport sector on fossil fuels is one of the biggest political and environmental concerns at the beginning of the 21st century. An alternative for fossil fuels could be fuels obtained from sustainable, bio-based platform chemicals (Serrano-Ruiz et al. 2010). One of the currently most promising bio-based platform chemicals for fuel production is γ-Valerolacton (GVL), which can further be used to obtain polymers and fine chemicals (Albani et al. 2017). However, the current extraction methods have not yet met their full potential, leaving room for new, innovative approaches (Serrano-Ruiz et al. 2010). In the conventionally utilized liquid-liquid extraction process, an economically necessary reduction of equipment volume and amount of solvent is restricted by residence time and mass transfer limitations. In contrast, an RPB-based liquid-liquid extraction process requires little space, has a high processing capacity, and is potentially very efficient, with a reported extraction efficiency of close to 100 % (Yang et al. 2018; Li and Qi 2004; Modak et al. 2016). Therefore, the utilization of RPBs for

the liquid-liquid extraction of GVL could be a viable possibility to overcome the current limitations and will be investigated in this case study.

6.3.2 Fundamentals

GVL is a stable, colorless liquid at room temperature. Its chemical structure is shown in Fig. 43.

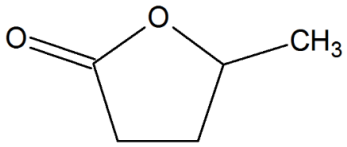

Fig. 43. Chemical structure of GVL.

GVL can be obtained from water-rich lignocellulosic biomass waste by means of hydrolysis and hydration, with levulenic acid or ethyl luvinate as intermediates (Alonso et al. 2013; Serrano-Ruiz et al. 2010). Consequently, the GVL has to be extracted from a thin aqueous solution, typically by liquid-liquid extraction (Alonso et al. 2013).
Liquid-liquid extraction processes typically comprise four streams: the feed, which consists of the key component (solute) and a carrier liquid, the solvent, the extract (solute-rich solvent), and the raffinate (solute-lean carrier). Furthermore, liquid-liquid extraction processes can be characterized by the capacity K (Eq. (39)) and the selectivity S (Eq. (40)) of the utilized solvent (Pfennig et al. 2011).

$$K_i = x_i^E / x_i^R \tag{39}$$

$$S_{S/C} = \frac{K_S}{K_C} = \frac{x_S^E / x_S^R}{x_C^E / x_C^R} \tag{40}$$

Where K_i is the capacity of the solvent with respect to component i, x_i^E and x_i^R are the molar fractions of component i in the extract and in the raffinate, respectively, $S_{S/C}$ is the selectivity of the solvent with respect to solute and carrier, x_S^E and x_S^R are the molar fractions of the solute in the extract and in the raffinate, respectively, and x_C^E and x_C^R are the molar fractions of the carrier in the extract and in the raffinate, respectively.
Due to its relatively low costs and high selectivity, butyl acetate is currently believed to be one of the most promising solvents for GVL extraction (Braden et al. 2011). However, no phase diagram of GVL/water/butyl acetate or experimental data on selectivity and capacity are available from literature so far.

6.3.3 Material and Methods

6.3.3.1 Experimental Setup and Chemicals

The chemicals utilized for this chapter are given in Tab. 21 (Appendix D.4). All chemicals were used in a purity of ≥ 99.9 %. The gas chromatograph of the type GC 14B from Shimadzu (Kyoto, Japan) contained a column of the type FS-Supreme-5ms HT from CS-Chromatographie-Service (Langerwehe, Germany). It had a length of 30 m, a diameter of 0.32 m and a film thickness of 0.15 µm. Helium was utilized as the carrier gas and acetonitrile as the internal standard. For each run, 0.4 g of sample were mixed with 0.2 g of acetonitrile. The gas chromatograph was further equipped with a flame ionization detector (FID) operated with hydrogen and synthetic air. Each sample was heated at 105°C for 2.40 minutes, then the temperature was increased by 30°C per minute until the run was finished at 160°C and 4.23 minutes.

6.3.3.2 Experimental Procedure

Samples of GVL/water/butyl acetate with a total volume of 0.015 l were weighed and mixed together at ambient pressure and 22°C. The samples were then stirred by a magnetic stir bar for two hours. Afterward, the samples were allowed to rest for 48 h at ambient pressure and either 22°C or 10°C. Samples of 0.002 l were then carefully drawn from the formed phases with a syringe and analyzed by means of gas chromatography. Finally, the mass of each component in the samples was obtained by comparison with calibration curves. Each sample composition was investigated in duplicate and afterward analyzed three times, respectively.

6.3.3.3 Results Evaluation and Concept Design

To determine the miscibility gap of the system GVL/water/butyl acetate, the binodals, and the tie lines, the respective molar fractions were calculated from the GC results and drawn into a ternary diagram. The binodals were then obtained by polynomial regression and the tie line by connecting the adjacent points on the binodals resulting from the samples two phases. Additional tie lines for unknown compositions could be drawn by means of a conjugate line. Thus, a countercurrent extraction process could be designed. According to *Goedeke,* extraction processes with high energy demand, as it would potentially be the case for an RPB-based process, should be limited to three to four stages to be economically feasible (Pfennig et al. 2011). Therefore, a three-stage process was considered in this case study. As a further basis, exemplary values

reported by *Murat Sen et al.* for feed flow rate, feed composition, and necessary raffinate purity were used (Murat Sen et al. 2012). Additionally, a pure solvent stream of 20 kmol h^{-1} was assumed, based on calculations for the minimum required amount of solvent for the considered three stage countercurrent extraction process. Based on the very high extraction efficiency reported for RPBs in the literature, ideal extraction stages (η = 100 %) were assumed. Furthermore, ambient pressure and temperature (22°C) were assumed for the process. The stages for the countercurrent process were obtained by means of a pole construction.

6.3.4 Experimental Results

The ternary diagram for GVL/water/butyl acetate is shown for 22° C in Fig. 44 and for 10°C in Fig. 45. The mixing points are given as grey triangles in the diagrams and connected to the resulting phase compositions (black dots) by the tie lines. For both investigated temperatures, a closed miscibility gap with steep tie lines was obtained. The miscibility gap obtained for 10°C is slightly larger than for 22°C, as would be expected. However, this temperature sensitivity is rather small. Furthermore, the points for the water-rich phase could be reproduced accurately, whereas the measured composition of the GVL-rich phase strongly deviated along the tie lines for both temperatures. The range of these variations will be called area of uncertainty in the following and can be defined by an inner border regression (dotted line) and an outer border regression (full line).

No systematic influence, which could explain these variations, could be identified in the design of experiments and a systematic error due to temperature fluctuations seems unlikely based on the above results. However, the formation of discrete liquid drops on the glass wall of the sample tubes and in the organic phase could be observed after 48 h of separation. These could be formed by water that condensed on the glass walls, depending on the gas-liquid equilibrium above the organic phase and the humidity of the air enclosed in the sample tube, and could have ran down into the organic phase. Alternatively, the formation of a microemulsion during mixing of the components could have lead to parts of aqueous phase being entrapped in the organic phase. Such an observation was made by *Anton and Vandamme* for a similar ternary system (Anton and Vandamme 2011). As both considerations would lead to an erroneously small miscibility gap, the outer border regressions of the uncertainty area will be considered as binodals in the following. Exemplary compositions on the binodal for 22°C and the corresponding capacities and selectivities along the tie lines are given in Tab. 22 (Appendix D.4).

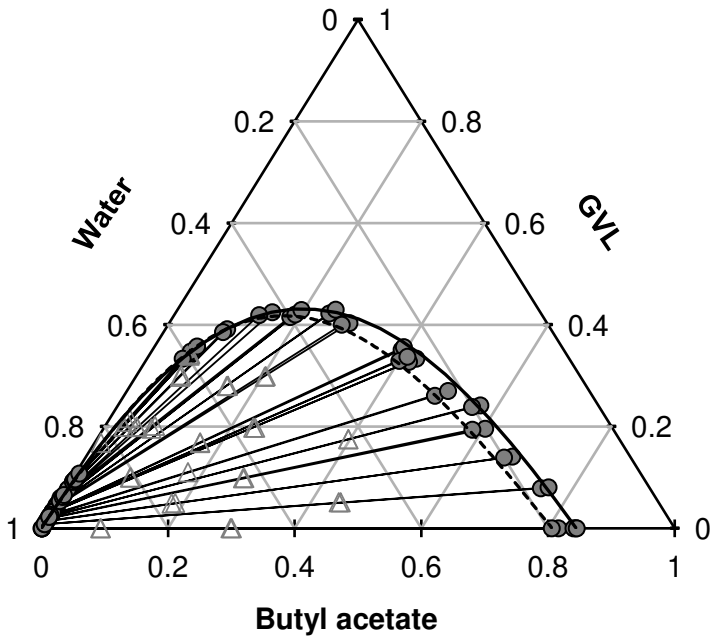

Fig. 44. Ternary diagram for GVL/water/butyl acetate at a temperature of 22°C. Mixing points are given as triangles and the resulting phase samples as dots. Binodals are given as regression, with an inner border (dotted line) and an outer border (dotted line) of the miscibility gap, with the area of uncertainty in between.

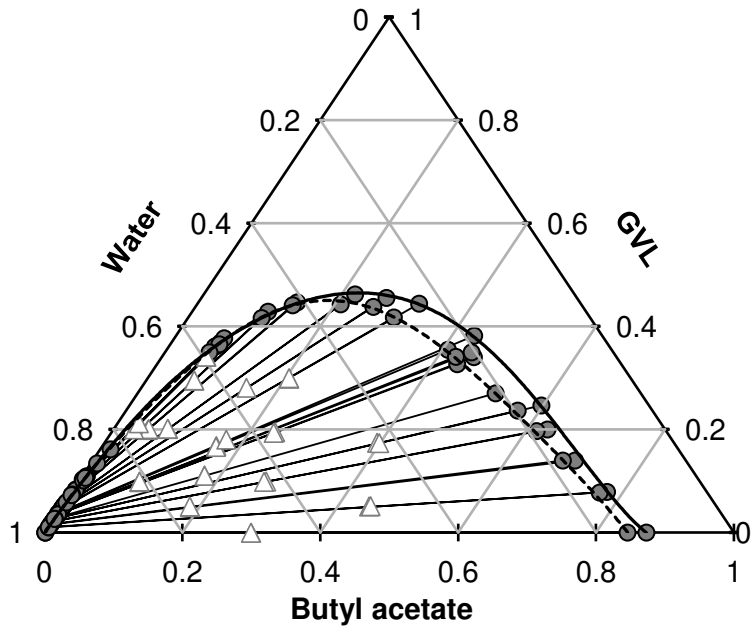

Fig. 45. Ternary diagram for GVL/water/butyl acetate at a temperature of 10°C. Mixing points are given as triangles and the resulting phase samples as dots. Binodals are given as regression, with an inner border (dotted line) and an outer border (dotted line) of the miscibility gap, with the area of uncertainty in between.

6.3.5 Process Concept

A complete concept design for the considered RPB-based three-stage countercurrent process is shown in Fig. 46. The underlying flow rates and the stage construction in the ternary diagram are shown in Tab. 23 and Fig. 78 (Appendix D.4), respectively.

Fresh solvent (E4, pure butyl acetate) is supplied at a rate of 20 kmol h^{-1} from container C4 and pumped to the third RPB unit (RPB3) by pump P9. In RPB3, it is contacted with raffinate R2 from the second RPB unit (RPB2). Both phases leave RPB3 through the liquid outlets (238 kmol h^{-1}) and are pumped to the third centrifuge unit (S3), where they are separated into the final GVL-lean raffinate (R3, 210 kmol h^{-1}) and the first extract (E3, 28 kmol h^{-1}). The final raffinate is stored in container C3, while the extract is pumped to RPB2 by pump P7. Here, the extract is contacted with raffinate R1 from the first RPB unit (RPB1). After leaving the second RPB unit, the liquid stream (253 kmol h^{-1}) is pumped to the second centrifuge unit (S2) by pump P5. There, the liquid stream is separated into the raffinate phase (R2, 218 kmol h^{-1}), which is pumped to RPB3 by pump P6, and the extract phase, which is pumped to RPB R1 by pump P4 (E2, 35 kmol h^{-1}). Here, the extract is contacted with the water-rich feed solution (R0), which is stored in container C1 and pumped to RPB1 by pump P1 (261 kmol h^{-1}). After leaving RPB1, the liquid stream (296 kmol h^{-1}) is pumped to the first centrifuge unit (S1) by pump P2. In centrifuge unit S1, the liquid is separated into the GVL-rich final extract phase (E1, 71 kmol h^{-1}), which is stored in container C2, and the first raffinate (R1, 225 kmol h^{-1}), which is pumped to the second RPB unit R2 by pump P3.

The final extract E1 contains 41.5 % GVL, whereas the final raffinate contains 1.2 % GVL. With respect to the feed composition, 92.4 % of the initial GVL amount could be extracted in the RPB-based concept process with three stages and 20 kmol h^{-1} of pure solvent, resulting in a raffinate purity of 98.8 %. In comparison, *Murat et al*. assumed an extraction column with 20 stages and 90 kmol h^{-1} of solvent stream (70 wt.% butyl acetate, 30 wt.% water) to be necessary to achieve the same raffinate purity in a conventional liquid-liquid extraction process.

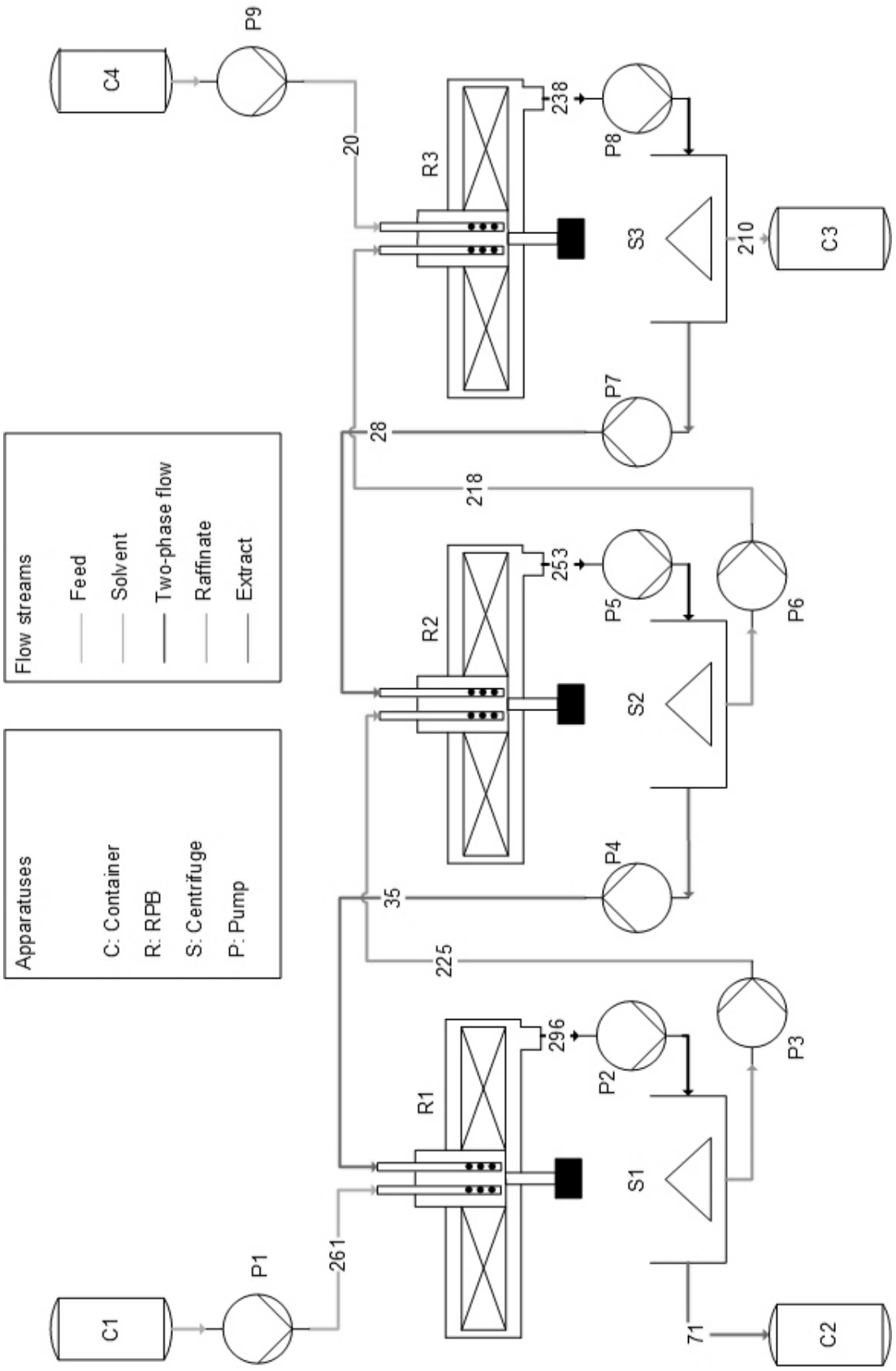

Fig. 46. Concept design for the three-stage countercurrent RPB extraction process.

6.3.6 Conclusions and Outlook

Based on the ternary diagrams obtained for extraction temperatures of 22°C and 10°C and the derived solvent capacities and selectivities, it can be concluded that the considered solvent butyl acetate is indeed very well suitable for the extraction of GVL from a bio-based water-rich feed. A promising process concept for the implementation of such an extraction process by means of three countercurrently connected RPBs with associated centrifuge units was successfully designed in this case study.

In such a process, a final raffinate purity of up to 98.8 % could be achieved within three stages due to the very high efficiency of RPBs for mixing and extraction tasks, which implies high competitiveness in comparison to the conventional extraction process assumed in the literature. However, the experimental results also showed that the mass transfer limitations in the system GVL/water/butyl acetate are comparatively low. Therefore, RPBs with a high radial packing depth, as in the current design, might not be necessary to meet the raffinate constraints. Moreover, investment and operation costs of RPBs are typically higher than those of conventional equipment. A more suitable HiGee design for the investigated extraction process could offer sufficiently high mass transfer rates, reduced equipment volume, lower investment costs, and a lower residence time in each stage (Chapter 7.5).

For a system with higher mass transfer limitations or high viscosities, however, the utilization of RPBs could be a reasonable alternative. Therefore, such a suitable system for an RPB extraction process should be identified in future research and the suggested concept process should be realized under pilot-scale conditions. The obtained results could then be compared to those from conventional equipment and those from other intensified equipment for liquid-liquid extraction, such as Podbielniak contactors and annular centrifugal extractors (Podbielniak 1935; Vedantam and Joshi 2006).

Furthermore, extraction processes in RPBs could be used in the future to gain additional knowledge on the influence of different operational and design parameters on the liquid processing in RPBs by comparison of extraction results with such obtained from mixing studies.

6.4 Case Study: Liquid-Gas Processing

6.4.1 Introduction

High-quality oils with an elevated content of polyunsaturated fatty acids (PUFA) are suggested as dietary and health supplements (Horrocks and Yeo 1999). In their

unrefined form, such oils can emit a characteristic, unpleasant odor, which reduces their commercial value. Therefore, a refining and deodorization process is necessary, in which off-flavors, but also other unwanted volatile components, such as free fatty acids, can be removed economically (Greyt 2013). State-of-the-art for the refining of vegetable oil and the removal of undesired compounds is the countercurrent contacting with a hot gas or vapor stream (stripping). In the conventional stripping column process, a time frame of several hours, temperatures of up to 270°C, and large amounts of steam or nitrogen are necessary, which results in high operating costs (Greyt 2013; Decap et al. 2004). Moreover, commercial PUFA-rich oils should only be heated as short as possible, due to their low oxidation stability, high heat sensitivity, and the necessary high product quality (Motallebi et al. 2015; Greyt 2013). Therefore, alternative and intensified means of processing are under investigation. Gravity-based intensified equipment has been considered, but either, the mass transfer was too slow with respect to the short residence time, e.g., in the case of a short path evaporator (Greyt 2013), or the investment and operating costs were too high, e.g., in the case of supercritical CO_2 processing (Greyt 2013), or an additional separation step was required, e.g., in the case of organic solvent nanofiltration (Fang et al. 2018). By means of liquid-gas contacting in HiGee equipment, however, the time the oil is subjected to high temperatures could be drastically reduced, whereas the stripping efficiency could be significantly increased, thus reducing the operating costs. Therefore, it seems reasonable to utilize RPBs for the production of a refined and odorless vegetable oil, which will be investigated in this case study.

6.4.2 Fundamentals

Four of the most important characteristic parameters of PUFA-rich oils are the peroxide value (PV), the anisidine value (AV), the TOTOX value, and the acid value.

The PV is a parameter for the amount of primary oxidation products in oils and is reported in milliequivalent of active oxygen per kilogram of oil sample (meq O_2 kg^{-1}). During the aging and decay of an oil, the PV first increases due to the formation of hydroperoxide and autoxidation products and then decreases again due to the subsequent degradation of peroxides (Matissek et al. 2014). PV values are typically < 6 for unoxidized oil and need to be < 10 for food-grade refined oil, according to the WHO's *Codex Alimentarius* (Matissek et al. 2014) and the *European Pharmacopoeia* (*Ph. Eur.*) (Vestland et al. 2017). A stricter upper limit of PV < 5 is defined by the Global Organization for EPA and DHA (GOED) (Vestland et al. 2017). The AV is a dimensionless parameter for the amount of secondary oxidation products such as α,β-unsaturated aldehydes. During the aging and decay of an oil, the AV value is

typically inversely related to the PV (Matissek et al. 2014). According to *Ph. Eur.*, the maximum acceptable AV is 30, whereas the GOED determines an upper limit of < 20 (Vestland et al. 2017). From the combination of the PV and the AV, the TOTOX value can be obtained (Eq. (41)), which describes the total amount of primary and secondary oxidation products in an oil sample (DG Fett 2012).

$$\mathrm{TOTOX} = \mathrm{AV} + 2 * \mathrm{PV}\ [\mathrm{meq}] \tag{41}$$

Calculating the respective values according to Eq. (41), *Ph. Eur.* considers the maximum acceptable TOTOX value to be 50. In contrast, the GOED determines an upper limit of < 26 (Vestland et al. 2017).

In addition, the acid value describes the amount of fatty acids in an oil that is not bound, e.g., in the form of glycerin. It is given as milligrams of sodium hydroxide necessary to neutralize all free fatty acids in 1 g of oil sample. It typically increases with the increasing degradation of an oil (Matissek et al. 2014). Consequently, a lower acid value reflects higher oxidation stability and a higher overall quality of an oil (Frede 2010; Fang et al. 2018).

6.4.3 Material and Methods

6.4.3.1 Experimental Setup and Chemicals

The utilized stripping gas was bottled nitrogen from Messer (Bad Soden am Taunus, Germany) with a purity of > 99.5 %. The experimental setup, which was built into a 1.8 m x 4.0 m ventilated housing, is shown schematically in Fig. 47 and as photography in Fig. 79 (Appendix D.5). It consists of four consecutively numbered process streams (stripping gas, vegetable oil, mantle heating, sealing coolant) and its central part, the RPB (V0.1) from Andritz (Fig. 7, chapter 2.4.3). Detailed specifications of the RPB are given in Tab. 24 (Appendix D.5). The RPB, the heat exchangers, and all heated pipe connections were insulated with rock wool (Fig. 80, Appendix D.5). The stripping gas was pre-heated by passing through two plate-type heat exchangers (H1.2 & H1.3) from Alva Laval (Lund, Sweden) and then fed to the RPB (N1). Marlotherm-SH oil from Sasol (Sandton, South Africa), continuously heated by a heater (H1.1) of the type teco tt from GWK (Meinerzhagen, Germany), was passed countercurrently through the heat exchangers H1.2 and H1.3. Additionally, the pipe section between H1.3 and the RPB was heated by a wire heating of the type ELK-HS from eltherm GmbH (Bubach, Germany).

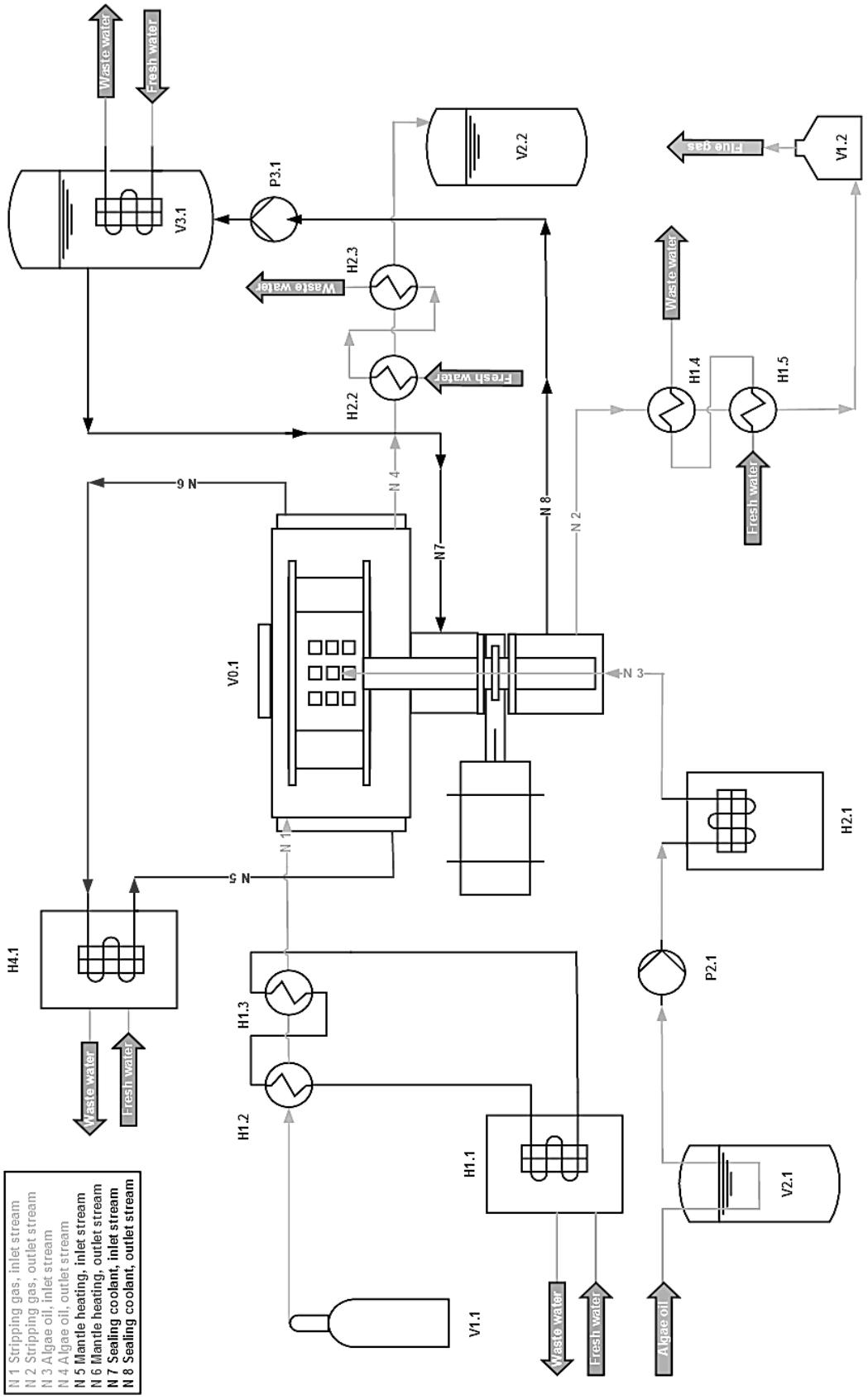

Fig. 47. The experimental setup used for the liquid-gas processing of vegetable oil.

After leaving the RPB (N2), the flue gas was cooled by tap water in two plate type heat exchangers (H1.4 & H1.5), led through a liquid trap (V1.2) to collect potentially entrained liquid, and then discarded into the ventilation system.
The vegetable oil was pumped from the feed container V2.1 by a pump (P2.1) of the type Ismatec MCP-Z-Standard from Cole-Parmer GmbH (Wertheim, Germany), equipped with pump head MI0131 from Micropump (Vancouver, Canada). The oil first passed through the oil pre-heater (H2.1) of the type Proline P12 from Lauda (Lauda-Königshofen, Germany) and was then fed (N3) into the rotor eye of the RPB through a nozzle. The nozzle is further specified in Tab. 25 (Appendix D.5). Additionally, the pipe section between H2.1 and the RPB was heated by a wire heating of the ELK-HS from eltherm GmbH (Bubach, Germany). After leaving the RPB, the refined vegetable oil (N4) was cooled in two plate type heat exchangers (H2.2 & H2.3) by tap water and then collected in tank V2.2. Samples of the refined oil could be drawn directly at the connection to tank V2.2. The shaft sealing of the RPB was cooled by Marlotherm-SH oil from Sasol (Sandton, South Africa) which was stored in tank V3.1 and fed to the RPB by gravity and the application of a slight overpressure of 0.5 bar (N7).
After cooling the shaft sealing, the oil was pumped back (N8) to the storage tank by a pump (P3.1) of the type WD-100-EXE-250-40B-V4A from Jahns Hydraulik (Offenbach am Main, Germany) where it was cooled by tap water. Furthermore, the RPB was equipped with a mantle heating which was continuously fed (N5) with hot Marlotherm-SH heating oil from Sasol (Sandton, South Africa). The hot oil for the mantle heating was supplied by a heater (H4.1) of the type US6 from Lauda (Lauda-Königshofen, Germany) for experiments at 150°C and by a heater of the type unistat T305 from Huber Kältemaschinenbau AG (Offenbach, Germany) for experiments at 180°C. After heating the RPB, the oil was led back (N6) to the respective heater. The gas flow was measured by a rotameter of the type SHO-RATE 1355M from Brooks Instrument (Dresden, Germany) and the temperatures were measured by PT-100 thermoelements and digitally recorded.

6.4.3.2 Experimental Procedure

The fresh vegetable oil was stored frozen at -18°C. Shortly before the start of each experiment, the vegetable oil was thawed and given into feed container V2.1. The RPB was started and set to a rotational speed between 500 rpm and 2000 rpm. The gas supply was opened and adjusted to the setpoint of 16.8 l h^{-1} or 33.0 l h^{-1}. All heaters were started and set to 200°C, except for the mantle heating. However, despite the rock wool insulation and additional wire heating, the actual temperatures at the gas and liquid

inlets of the RPB were somewhat lower due to heat losses, as summarized in Tab. 26 (Appendix D.5). To further investigate the influence of temperature on the process, two identical sets of experiments were conducted at a mantle heating temperature of 150°C and 180°C, respectively. As soon as all temperatures were in steady-state, the experiments were started by feeding the vegetable oil at a rate of 5 kg h^{-1} to the RPB. Thus, the gas capacity factor F_g (Eq. (1)) was between $1.3 * 10^{-4}$ $Pa^{0.5}$ and $2.6 * 10^{-4}$ $Pa^{0.5}$ and the liquid load LL (Eq. (2)) was 0.19 m^3 m^2 h^{-1}. Both values are orders of magnitude below the operational limit of the RPB that can be expected based on the research of *Neumann et al.* (Neumann et al. 2017). Before taking the first sample and between two set points, 2 kg of oil were pumped through the setup to allow for the adjustment of a new steady state. At the end of one day of experiments, the setup was cooled down and thoroughly rinsed.

The determination of the PV value in oil samples was conducted according to the DIN EN ISO 3960 standard (DIN EN ISO 3960) by means of iodometric titration. The determination of the AV value was conducted according to the DIN EN ISO 6885 standard (DIN EN ISO 6885) by means of reaction with p-anisidine and subsequent photometric analysis. The acid value was determined according to the DIN EN ISO 660 standard (DIN EN ISO 660) by means of titration with sodium hydroxide.

For the identification of possible key compounds for a deodorization, oil samples were analyzed by gas chromatography in a GC 17 from Shimadzu. The chromatographic column of the type FS-Supreme-5ms HT from CS-Chromatographie-Service (Langerwehe, Germany) had a length of 30 m, a diameter of 0.32 m and a film thickness of 0.15 µm. Helium was utilized as the carrier gas, dibutyl ether as the internal standard, and n-decane as the solvent. The gas chromatograph was further equipped with a flame ionization detector (FID) operated with hydrogen and synthetic air. For comparison, pure aldehyde and ketone samples were analyzed accordingly.

6.4.4 Experimental Results

The resulting PVs and AVs of vegetable oil samples obtained after RPB processing at different RPM, a nitrogen flow rate of 16.8 l h^{-1} and 33.0 l h^{-1}, and a mantle heating temperature of 150°C and 180°C are shown in Fig. 48 and Fig. 49, respectively. Additionally, the average PVs, AVs, and TOTOX values of vegetable oil samples before RPB processing and after RPB processing at a nitrogen flow rate of 16.8 l h^{-1} and 33.0 l h^{-1} and a mantle heating temperature of 150°C and 180°C are shown in Fig. 50.

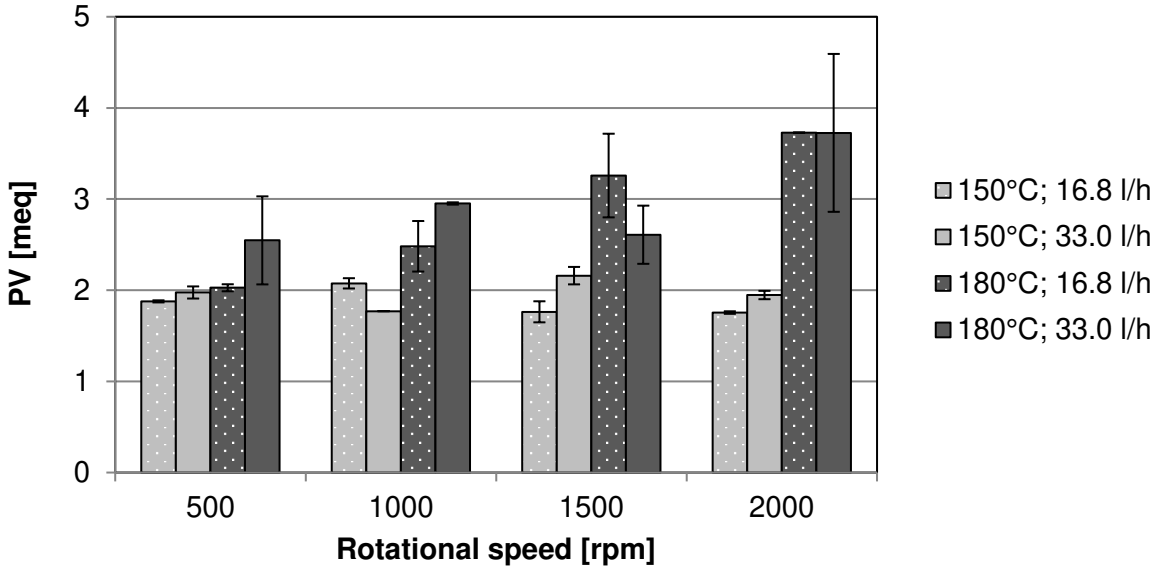

Fig. 48. PVs for varying rotational speed, a nitrogen flow rate of 33.0 l h^{-1} and 16.8 l h^{-1}, and a mantle heating temperature of 150°C and 180°C. Error bars depict the sample standard deviation.

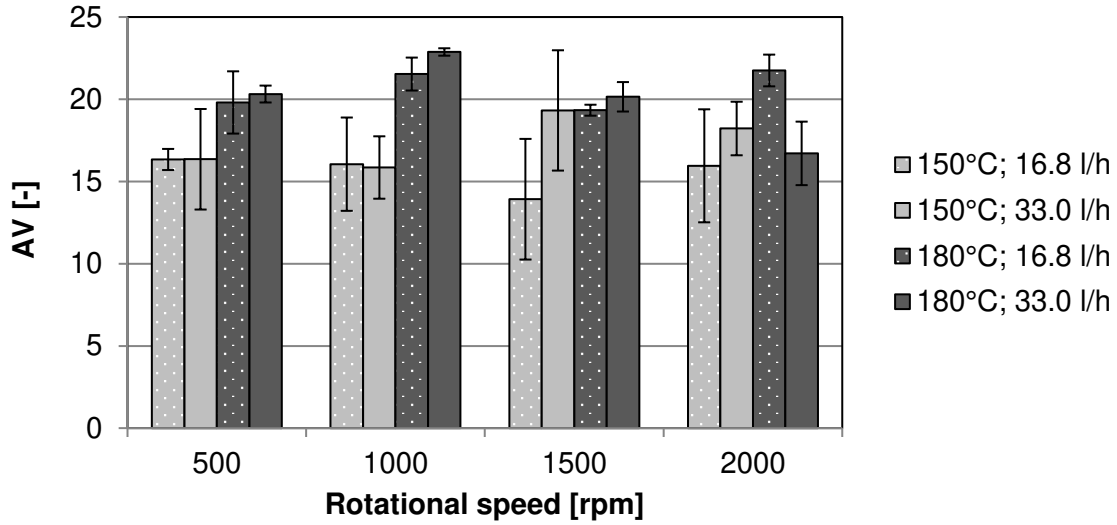

Fig. 49. AVs for varying rotational speed, a nitrogen flow rate of 33.0 l h^{-1} and 16.8 l h^{-1}, and a mantle heating temperature of 150°C and 180°C. Error bars depict the sample standard deviation.

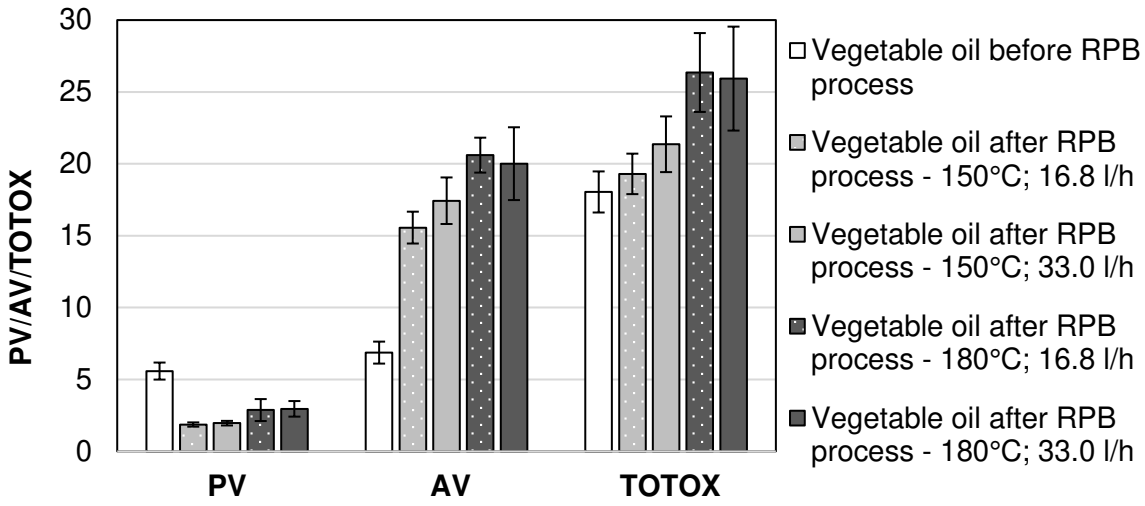

Fig. 50. PVs, AVs, and TOTOX values for oil samples before RPB processing and after RPB processing at a nitrogen flow rate of 16.8 l h^{-1} and 33.0 l h^{-1}. Error bars depict the sample standard deviation.

As can be obtained, no strong relationship between the investigated rotational speed and nitrogen flow rates and the resulting PVs (Fig. 48) and AVs (Fig. 49) is visible for a mantle heating temperature of 150°C. While a higher nitrogen flow rate seems to be correlated to slightly higher AVs at 1500 rpm and 2000 rpm, this trend is not statistically significant. At a mantle heating temperature of 180°C, the PV seems to be increasing with increasing rotational speed, whereas the AV remains again more or less constant. As for 150°C, no clear trend with respect to the influence of the gas flow rate on the AV and the PV is visible in the investigated range. From Fig. 50, it can further be obtained that the PVs decrease during the RPB processing, whereas the AVs increase. This effect is to be expected: during a deodorization process, peroxides are typically degraded into aldehydes, decreasing the PVs. While the volatile aldehydes are stripped out of the oil, some aldehydes are bound by triglyceride molecules and cannot be removed, increasing the AVs (Matissek et al. 2014; DG Fett 2012). With respect to the mantle heating temperature, it can be obtained that both the PVs and the AVs are higher after processing the vegetable oil at 180°C than at 150°C. This could mean that at higher temperatures fewer aldehydes are formed in total, whereas the proportion of non-volatile aldehydes is increased. While it is reported in the literature that the TOTOX should stay more or less constant throughout a deodorization process, this observation can thus only be made approximately for 150°C, but not for 180°C. With respect to the nitrogen flow rate, again no trend seems evident.

The average acid values for oil samples before RPB processing and after RPB processing at a nitrogen flow rate of 16.8 l h^{-1} and 33.0 l h^{-1} and a mantle heating temperature of 150°C and 180°C are shown in Fig. 51.

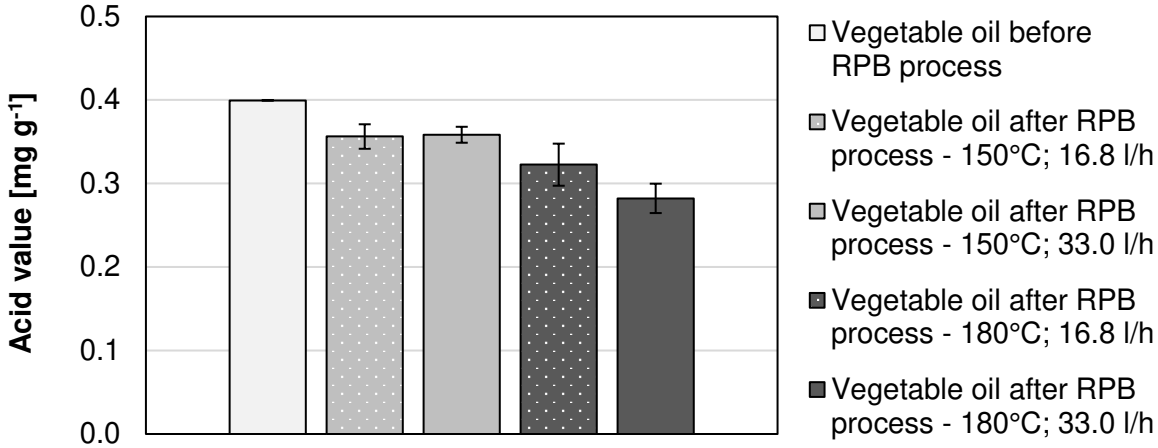

Fig. 51. The average acid values for oil samples before RPB processing and after RPB processing at a nitrogen flow rate of 16.8 l h^{-1} and 33.0 l h^{-1}. Error bars depict the sample standard deviation.

It is demonstrated that the acid value of the oil was decreased by processing it in the RPB by up to 29 %, on average, from 0.400 mg g^{-1} to 0.282 mg g^{-1}. The difference between the two different nitrogen flow rates is not statistically significant at 150°C, whereas a positive influence of an increased nitrogen flow rate may be present at 180°C. Moreover, the acid value decreased with an increasing mantle heating temperature, which can be explained by increased volatility of the free fatty acids at higher temperatures. In contrast, the acid value typically stays constant in the conventional steam stripping process. This is because some free fatty acids are stripped out, while some are newly formed due to the hydrolysis of triglycerides in the presence of water (Fang et al. 2018). In the absence of the second effect, a decreasing acid number could be observed with nitrogen as stripping gas in this case study. Overall, the results are shown in Fig. 51 demonstrate that stripping of components from the liquid phase was successfully realized.

The results of the GC analysis of an oil sample obtained before processing in the RPB is shown in Fig. 52. For comparison, the peaks obtained with propanal, propanone (acetone), butanal, and butanone (MEK) are also given. As can be obtained from the diagram, a slight offset between the oil sample peak I and the peaks of propanal and propanon is present. Therefore, the oil sample peak I could possibly be formed by

propenal, which could be expected at this position for the slightly polar column used in this GC analysis. The oil sample peaks II and III are in between propanal and butanal and could possibly be formed by a relatively high-boiling/polar C3-compound or a relatively low-boiling/non-polar C4-compound.

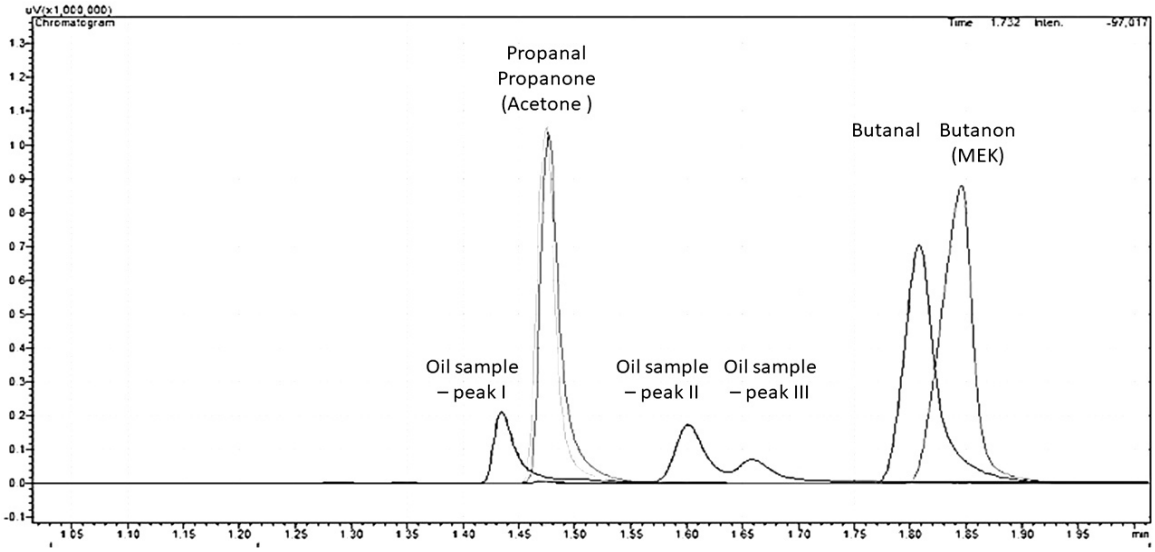

Fig. 52. Results of the GC-FID analysis of a vegetable oil sample and propanal, propanone, butanal, and butanone.

6.4.5 Conclusions and Outlook

With respect to the absolute values, all measured PV, AV, and TOTOX values after RPB processing are within the limits set by the *Codex Alimentarius* and the *Ph. Eur.* In addition, the acid value could be drastically decreased by up to 29 %, increasing the vegetable oil's quality. Whereas the AV and TOTOX values obtained at 180°C slightly exceed the recommendations made by the GOED, the PV could be reduced from an average value of 5.8 – above the GOED's limit – to average values below 2.0 (150°C) and 3.0 (180°C), respectively. Therefore, it can be concluded that the overall feasibility of an RPB-based vegetable oil stripping process with nitrogen could be shown in this case study.

However, no clear relationships could be found for the rotational speed and the gas flow rate in the investigated operation range. Therefore, the operation range should be extended for future investigations. Moreover, a trade-off for the influence of the temperature could be observed. Whereas an increased temperature of the RPB's mantle heating improved the stripping of free fatty acids and potentially also the

stripping of other volatile compounds, the AV and the TOTOX value increased slightly above the limits recommended by the GOED. To overcome this trade-off, the residence time of PUFA-rich vegetable oil in the RPB should be drastically reduced in the future, e.g., by an alternative HiGee design, as presented in chapter 7.5.

Furthermore, it should be noted that the TOTOX value for the vegetable oil before processing was already relatively high, which could imply advanced aging of the oil before receipt. Therefore, even better results may be obtained in the future if fresh vegetable oil is used. Additionally, the analytics of oil samples should be extended. During the GC analysis, the absolute height of the peaks was subject to high fluctuations, which could be due to the high viscosity of the oil samples. Therefore, a more suitable solvent and an internal standard should be adopted in the future to achieve higher accuracy and reproducibility. Finally, oil samples before and after the RPB should be compared by sensory analysis.

6.5 Conclusions and Outlook

In this chapter, three case studies on the industrial application of RPBs for liquid processing were investigated. With respect to liquid phase reactive mixing, it was reported in the literature that the production of MDA, MDI, and IIR could be significantly improved by the application of RPBs due to intense micromixing and high internal heat and mass transfer rates. However, it was not possible to reproduce any clear influence of RPB operation and design parameters on the MDA production process in own experimental investigations. This can most likely be explained by the large dead zones and the long residence time of liquid on the RPB's casing walls and in the casing bottom in the RPB 1.0 design. In contrast, the highest influence on the experimental results was found for the reactant and the equipment temperature before and during the experiments, which can be explained by kinetics effects. On the positive side, the large heat capacity of the RPB casing enabled a fast formaldehyde addition. Nevertheless, it should be noted that this effect would become irrelevant under steady-state conditions of continuous operation. Overall, the RPB 1.0 design has to be considered unsuitable for the MDA production.

With respect to liquid-liquid extraction, RPBs seem particularly interesting for liquid systems with high mass transfer limitations or high viscosities. Otherwise, the higher investment and operation costs in comparison to conventional equipment could make their utilization economically infeasible.

Promising results were obtained for the refining of vegetable oil in the liquid-gas processing case study, in which the amount of unwanted volatile components in the oil

could be strongly decreased. More extensive investigations should include the study of a broader operating range and the implementation of more comprehensive analytics.

Overall, the application of RPBs to industrial liquid processes still seems promising. For such processes, RPBs could be superior to conventional equipment, such as STR and tubular reactors, while offering a remarkable equipment volume reduction. With respect to micromixers and SDRs, RPBs offer more degrees of freedom and a higher capacity. However, these benefits come at an additional energy demand for the motor and potentially higher initial investment costs. Furthermore, the current RPB design does not reflect an optimum design for the investigated processes. A more suitable design will be presented and discussed in chapter 7.5.

7 RECOMMENDATIONS*

In this chapter, tools for assessing the current state and potential of the RPB technology from an industrial perspective are presented. For this purpose, guidelines for the operation and the design of RPBs for liquid processing are derived based on the previous chapters. Furthermore, the Technology Readiness Levels (TRL) of the considered applications are discussed and a decision chart is presented to help identify promising fields of RPB application. Finally, an improved HiGee device design is recommended.

7.1 RPB Operation Guidelines

In this subchapter, guidelines for the operation of RPBs are presented with respect to the rotational speed, the total liquid flow rate, the volumetric ratio, and the viscosity. For each operational parameter, recommendations are given on the basis of results from the literature and from own investigations, as presented in the previous chapters.

To make a decision on the rotational speed, a comparison of different design variants should always be conducted based on the tangential velocity at the inner packing radius, instead of the angular velocity (rpm) alone. In the literature, it was unanimously found that the mixing efficiency increases with an increasing tangential velocity at r_i between 0.6 m s^{-1} and 7.9 m s^{-1}. However, most authors reported that the influence of an increasing rotational speed on the mixing efficiency also decreased at a higher rotational speed, mostly following the inverse power law. In own experimental investigations in the RPB 1.0 and the RPB 2.0 design, it was observed that the mixing efficiency increases with increasing rotational speed up to the maximum investigated rotational speed of 1200 rpm (tangential velocity at r_i: 9.2 m s^{-1}).

* Parts of this chapter have been published as:
A guide on the industrial application of rotating packed beds (2018), Neumann, K.; Gladyszewski, K.; Groß, K.; Qammar, H.; Wenzel, D.; Górak, A.; Skiborowski, M.; Chem. Eng. Res. Des. 134, pp. 443–462.
Reactive mixing in rotating packed beds: on the packing's role and mixing modeling (2019); Wenzel, D.; Nolte, K.; Górak, A.; Chem. Eng. Proc.: P.I. (143), published online, doi: 10.1016/j.cep.2019.107596.
Rotierender Ring Reaktor (2019), Wenzel, D.; Górak, A; Application Nr.: DE102017119569A1.

However, the influence of an increasing rotational speed on the mixing efficiency decreased at a higher rotational speed, mostly following the inverse power law. Therefore, in many experiments, no strong additional benefit could be observed above 900 rpm (tangential velocity at r_i: 6.9 m s^{-1}). While the strongest influence of an increasing rotational speed could be found below 300 rpm (tangential velocity at r_i: 2.3 m s^{-1}) (Chapter 5, Appendix C.4). This finding is in agreement with results from the liquid phase reactive mixing and the liquid-gas processing case studies, in which a higher rotational speed had either no positive influence on the results, or no effect at all (Chapters 6.1 and 6.3), and with findings for distillation in RPBs by *Qammar et al.* (Qammar et al. 2018). Consequently, it can be recommended that the rotational speed should be chosen as high as necessary in respect to the necessary mixing time and as low as possible with respect to the operational costs. Therefore, a rotational speed corresponding to a tangential velocity of 7 m s^{-1} can be assumed a suitable compromise.
An increasing total liquid flow rate was unanimously reported in the literature to decrease the segregation index in the range of 20.2 l h^{-1} and 615.0 l h^{-1}. However, most authors reported that the influence of an increasing total flow rate on the mixing efficiency also decreased at higher total flow rates. Therefore, increasing the total flow rate from 15.5 l h^{-1} to 54.0 l h^{-1} decreased the segregation index by 45 %, whereas an increase from 410.0 l h^{-1} to 615.0 l h^{-1} decreased the segregation index only by 12 %. (Chapter 4)
In own experiments at a volumetric ratio of 1, the segregation index and the micromixing time parameter decreased in the RPB 1.0 design with an increasing total liquid flow rate between 60.0 l h^{-1} and 100.0 l h^{-1}, following the inverse power law. By comparison with other results, it could be shown that this positive effect was most likely based on the increased liquid outlet and impingement velocity. The obtained segregation indices could be correlated to a micromixing time parameter in the order of 10^0 ms, whereas the pressure drop over the nozzles was about 3.6 bar. In the RPB 2.0, a total liquid flow rate of up to 140.0 l h^{-1} (corresponding to a liquid load per void cross-sectional area at r_i of 30.5 m^3 m^{-2} h^{-1}) could be mixed at a volumetric ratio of 8 at a pressure loss over the nozzles of about 2.0 bar. The derived corresponding micromixing time parameter was in the order of 10^{-1} ms to 10^0 ms (Chapter 5). During preliminary investigations on the operation limits of the RPB 1.0 design, a total liquid flow rate of up to 480 l h^{-1} could be processed without flooding the casing. The maximum liquid load of RPB 2.0 has not yet been investigated but can be assumed to be significantly higher due to its larger liquid outlets (Chapter 2.4). The additional power consumption due to the liquid load can be calculated based on *Neumann et al.* to contribute only 3 % to the total power consumption in the RPB 1.0 design at a total liquid flow rate of 100 l h^{-1}, but 24 % at

1000 l h^{-1} ((Neumann et al. 2018b), Appendix C.2). Overall, it can be stated that RPBs are capable of processing comparatively large total liquid flow rates at a low pressure loss. The exact limit is determined by factors as the local liquid load on the inner cross-sectional area of the packing and the liquid outlets in the RPB casing, as well as the liquid outlet flow rate. For sufficiently large liquid outlets, the total flow rate should be chosen as high as possible.

The volumetric ratio was varied in the literature in the range between 1 and 15. It was found that the segregation index increased with an increasing volumetric ratio. In own experiments, volumetric ratios between 3 and 5 were studied in the RPB 1.0 design at a constant total proton concentration and a constant total liquid flow rate of 60 l h^{-1} (Appendix C.4). It was found that the segregation index increases with an increasing volumetric ratio. Furthermore, combining results from the RPB 1.0 and the RPB 2.0 design for volumetric ratios in the range of 1 to 8 (Chapter 5), it can be concluded with respect to the radial packing depth that the influence of the packing on the mixing process strongly decreases with an increasing volumetric ratio. Therefore, it can be recommended that for a sufficiently large radial packing depth, a low volumetric ratio, e.g. 1, should be chosen, if stoichiometrically possible. If the packing size should be as small as possible, a larger volumetric ratio should be chosen, e.g., 8. However, it should be noted that these recommendations are made on basis of the segregation index and that a truly concentration-independent investigation will only be possible as soon as a mixing model is available that has been validated for all volumetric ratios (Chapter 4).

With respect to the viscosity of the processed liquids, it was unanimously reported in the literature that the segregation index increases with an increasing viscosity in the range of 1 mPa s to 220 mPa s (Appendix B.2). Furthermore, it was found that the influence of the rotational speed on the mixing efficiency is higher at higher viscosities, independent of the liquid flow rate and the liquid distribution method. However, in comparison with a T-mixer, the use of an RPB resulted in 70 % smaller segregation indices for the mixing of viscous liquids of 179 mPa s (Chapter 4). In own experiments, the influence of viscosity was not investigated by means of the Villermaux-Dushman-protocol, or as a controlled parameter in any other experiment. In the liquid phase reactive mixing case study (Chapter 6.2), as well in the case study on liquid-gas processing (Chapter 6.4), liquids with an increased viscosity could be handled without problems. Overall, RPBs seem particularly suitable to process viscous liquids. However, small packing pore sizes, low total liquid flow rates, or a design causing a high residence time in the rotor eye or in the RPB casing could restrict their application and should be avoided.

7.2 RPB Design Guidelines

In this subchapter, guidelines for the design of RPBs are presented with respect to the casing design, the liquid distribution design, and the packing design. For each design parameter, recommendations are given on the basis of results from the literature and from own investigations, as presented in the previous chapters.

With respect to the rotor and casing design, it was found in the literature that the residence time in the rotor can be assumed to be in the range of 0.2 s to 1.4 s and is dependent on rotational speed, viscosity, and total liquid flow rate (Yang et al. 2015a). In contrast, the residence time in the complete RPB depends largely on the exact RPB casing design and partly on the operation and was not investigated in the literature, but in own experiments. The residence time within the complete RPB (from liquid distribution to outlet) was investigated by the tracer pulse method for the RPB 1.0 and the RPB 2.0 design (Appendix C.5). The results for the RPB 1.0 design showed that 90 % of all liquid elements leave the RPB within the first 96.5 s, while some few liquid elements stay up to 227.5 s in the RPB. Due to an improved design and operation, the total residence time could be reduced to 60.0 s in the RPB 2.0 design, whereas 90 % of all liquid elements leave the RPB within the first 37.4 s. Overall, an RPB should be constructed in a way that minimizes the dead volume on the walls and the bottom of the casing. The distance between the rotor and the wall should be kept small, e.g., 25 mm. All liquid outlets should be opened to reduce the dead volume and the liquid hold-up. If possible, the casing volume should be as small as possible, the liquid outlets as large as mechanically feasible and the bottom of the casing should be inclined towards the liquid outlets.

For the liquid distribution design, distribution pipes were compared with pre-mixed distributors and impinging stream distribution in the literature. It was reported that by using the premixed distributor, the segregation index could be reduced by two orders of magnitude. A longer distributor length and a smaller pipe angle between the two pipes further increased the mixing efficiency. On the impinging stream distribution it can be stated that it is roughly as effective as the distributor pipes, but distinctively harder to adjust and less flexible in operation. By further analysis of the results, it was found that an increasing distance from the packing leads to a decreasing segregation index. A liquid distribution by means of adjustable nozzles has not been investigated in the literature. In own experiments, it was found that the segregation index decreases with an increasing liquid outlet velocity in the range between 2 m s^{-1} and 25 m s^{-1}, independent of the nozzle type, following the inverse power law according to $X_S = 0.34 * u_{out}^{-1.08}$ (Eq. (38)). In the RPB 1.0 design, full jet nozzles showed varying results, whereas the use of flat fan nozzles resulted in low segregation indices and a

high experimental reproducibility over the complete investigated operation range. In the RPB 2.0 design, only flat fan nozzles were used. In combination with a packing, an overlapping liquid distribution (φ = 0°) was beneficial for mixing, whereas no difference between an opposite liquid distribution (φ = 180°) and an overlapping liquid distribution (φ = 0°) could be found for a rotor without packing for a rotational speed above 600 rpm (Appendix C.4). Overall, the influence of the nozzle orientation angle φ on mixing results was ambiguous, but particularly small in the case of flat fan nozzles and at high rotational speed (Chapter 5). In conclusion, a liquid distribution by means of flat fan nozzles can be recommended for mixing processes. Furthermore, an overlapping liquid distribution (φ = 0°) seems favorable in combination with this type of nozzles. In contrast, if full jet nozzles are used, an opposite liquid distribution (φ = 180°) seems preferable to prevent an excessive liquid load on single spots at the packing's inner radius. Furthermore, a narrow liquid distribution showed to be problematic in the liquid phase reactive mixing case study (Chapter 6.2) due to strongly intensified fouling. For this particular application, an orientation angle of φ = 180° can be recommended under practical terms. Additionally, it is important that the outlet velocity of the liquid is adjusted high enough by means of the nozzle outlet area and total flow rate; an outlet velocity of 10 m s^{-1} can be recommended. In the case of a volumetric ratio higher than unity, the nozzle size should be chosen individually for each stream to allow for the different flow rates.

On the packing design, it was found in the literature that the segregation index decreases with an increasing inner packing radius. This effect can be attributed to a higher tangential velocity with increasing inner radius, a finer droplet dispersion due to a larger distance from the liquid distribution, and a lower local liquid load and hold-up at the inner radius of the packing. Furthermore, it was found that the segregation index decreases with an increasing radial packing depth. However, the reported decrease was rather marginal. A comparison between a wire mesh packing and foam packings showed lower segregation indices for foam packings. Hydrophobic modification of the foam packing (wetting angle increase from 108° to 134°) further decreased the segregation indices. Moreover, pore sizes in the range between 0.22 mm and 0.8 mm were compared. It was found that a smaller pore size of the packing was related to lower segregation indices (Chapter 4). In own experiments, very similar results for wire mesh packing and foam packing were obtained with respect to the influence of the rotational speed on the segregation index. Combining results from the RPB 1.0 design and the RPB 2.0 design for volumetric ratios in the range of 1 to 8, it can further be concluded that the influence of the packing on the mixing process seems to decrease with an increasing volumetric ratio. While a strong influence of the packing was visible

at a volumetric ratio of 1 (radial depth: 5 mm (eye ring) vs. 107 mm) and some minor influence at volumetric ratio of 6 (radial depth 5 mm (eye ring) vs. 207 mm), no difference between using just an empty rotor (radial depth: 7 mm (eye ring)) or a rotor filled with packing (radial depth: 207 mm) could be found at a volumetric ratio of 8. Moreover, for an opposite liquid distribution (φ = 180°), the utilization of a packing resulted in a negative influence on the mixing results at a rotational speed above 600 rpm in the RPB 2.0 design (Chapter 5). In conclusion, it can be recommended that the inner radius of the packing should be chosen as large as possible with respect to other design parameters, and as small as necessary to facilitate a defined liquid distribution onto the packing and low investment costs. The radial packing depth and the outer diameter of the packing should be chosen as small as possible, but as large as necessary to facilitate complete processing within the packing. For a volumetric ratio of 8, a combined radial depth of 10 mm may be sufficient, whereas a combined radial depth of 100 mm may be necessary for a volumetric ratio of 1. In general, a larger packing seems to be necessary at low volumetric ratios. The packing should consist of foam or other regular, well-defined material. The pore size of the packing should be as small as possible, but as large as necessary to avoid a large liquid hold-up on the inner side of the packing, particularly for viscous liquids. The axial height of the packing should be large enough to allow for the processing of the chosen total liquid flow rates.

7.3 RPB Scaling Guidelines

So far, no scaling guidelines have been published in the literature for liquid processing in RPBs. However, on the basis of the previous chapters, several scaling rules can be deduced:

- When changing the inner diameter of the packing, the rotational speed needs to be compared based on the tangential velocity at the inner radius of the packing, instead of the angular velocity (rpm) alone.
- When changing the total liquid flow rate, the same order of the micromixing time parameter and a constant pressure drop can be achieved by adjusting the liquid distribution to obtain a similar liquid outlet velocity, providing additional degrees of freedom.
- Similar behavior should be observable for different total liquid flow rates and axial heights of the packing, as long as the liquid load per cross-sectional area of packing at the inner radius of the packing is kept constant.

- When increasing the total liquid flow rate, the axial packing height and the size of the liquid outlets should be increased. Vice versa, by increasing the size of the liquid outlets, the residence time for a given liquid flow rate can be reduced.

7.4 Technology Readiness Levels and Decision Chart

In order to assess the maturity of the RPB technology with respect to the processes investigated as case studies in this thesis, the respective Technology Readiness Levels (TRLs) are evaluated. This evaluation is conducted on the basis of the TRL definition by *Mankins* (Mankins 1995), as summarized in Tab. 27 (Appendix E). The resulting TRLs are given in Tab. 2, together with an evaluation on the improvements necessary to reach the next TRL.

As shown, the considered RPB-based processes have reached very different TRLs. However, no application can currently be rated at a TRL above 7. A similar observation was made by *Neumann et al.* and attributed to the finding that the application of RPBs in the industry is still very limited and often only comprises stand-alone setups (Neumann et al. 2018a). Consequently, more systematic studies and a more courageous implementation of RPBs in the actual industrial environment would be necessary to reach the next TRLs. For this reason, and to support informed decisions about the use of RPBs for industrial liquid processing, a decision chart is presented in Fig. 53.

The application of such a decision chart can be considered particularly reasonable in the case of space restrictions, for the retrofit of equipment, in the case of viscous media (e.g. MDA, Chapter 6.2), and in the case of temperature-sensitive materials (e.g. PUFA-rich vegetable oil, Chapter 6.4) (Neumann et al. 2018a). With respect to the reduced residence time for exothermic reactions stated in Fig. 53, it should be noted that the current design must be significantly improved to reduce the residence time, as elaborated in the previous chapters. Consequently, a more appropriate design will be presented in chapter 7.5.

Tab. 2. TRLs the RPB-based processes considered in this thesis. Partly adapted and modified from *Neumann et al.* (Neumann et al. 2018a).

Application	Description	TRL	Improvements necessary for next TRL
MDA production (Chapter 6.2)	Technology fully tested and validated in a pilot-plant, but in a laboratory environment	6-7	Systematic investigations in a relevant environment, additional rules of design, long-term industrial application
MDI production (Appendix D.2)	Technology concept formulated; Components of the technology implemented and successfully tested in a relevant environment	2-5	Investigation of the complete technology in laboratory and relevant environments and additional rules of design
IIR production (Appendix D.3)	Technology fully tested and validated in a laboratory environment	5-6	Systematic investigations in a relevant environment and additional rules of design
GVL extraction (Chapter 6.3)	Technology concept formulated; Components of the technology implemented and successfully tested in a laboratory environment	2-4	Investigation of the complete technology in laboratory and relevant environments
Vegetable oil de-odorization (Chapter 6.4)	Complete technology fully tested and validated in a pilot-plant, but in a laboratory environment	6-7	Systematic investigations in a relevant environment, additional rules of design, long-term industrial application

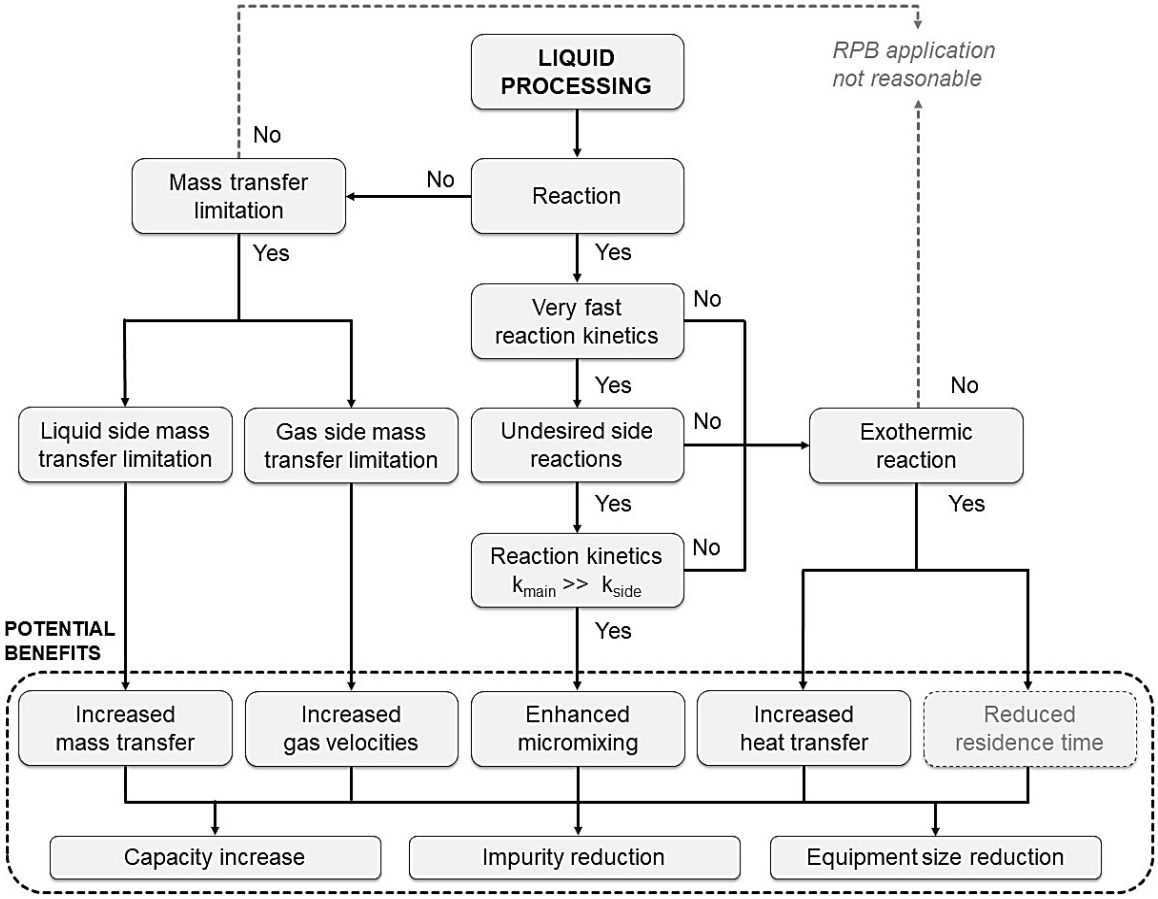

Fig. 53. Decision chart for liquid processing in RPBs. Partly modified and adapted from *Neumann et al.* (Neumann et al. 2018a).

7.5 Rotating Ring Reactor

As shown in chapters 4 and 5, the utilization of a large packing, or a packing at all, is only in certain cases important for fast mixing – i.e., at a low rotational speed and low volumetric ratios. However, high rotational speed was shown to result in the fastest mixing. Additionally, high volumetric ratios are relevant for many industrial reactive mixing processes, e.g., the MDA production and the IIR production (Chapter 6.2, Appendix D.3). With respect to the liquid distribution, it was shown in chapters 5 and 6 that a wide distribution is most reasonable under practical terms. Furthermore, it was shown in chapters 5 and 6, that the RPB casing was unnecessarily large for liquid processing, particularly with respect to the size of the liquid outlets. As a consequence, a wide RTD was identified to be a major drawback in the current RPB design. This was partly improved by the RPB 2.0 design. However, the RTD curves for the RPB 2.0 design are still unsatisfyingly broad if an RPB should be applied for industrial applications (Appendix C.5). In addition, it was concluded in chapter 6.2.5, that the distance between rotor and casing should be significantly reduced and that a horizontal rotation axis would be preferable in order to further facilitate a low liquid hold-up in the casing.

As a consequence of the above considerations, a novel type of HiGee equipment is presented in this chapter. It is called “Rotating Ring Reactor” (RRR) and depicted schematically in Fig. 54 (patent pending, “Rotierender Ring Reaktor”, DE102017119569A1 (Wenzel and Górak 2019)).

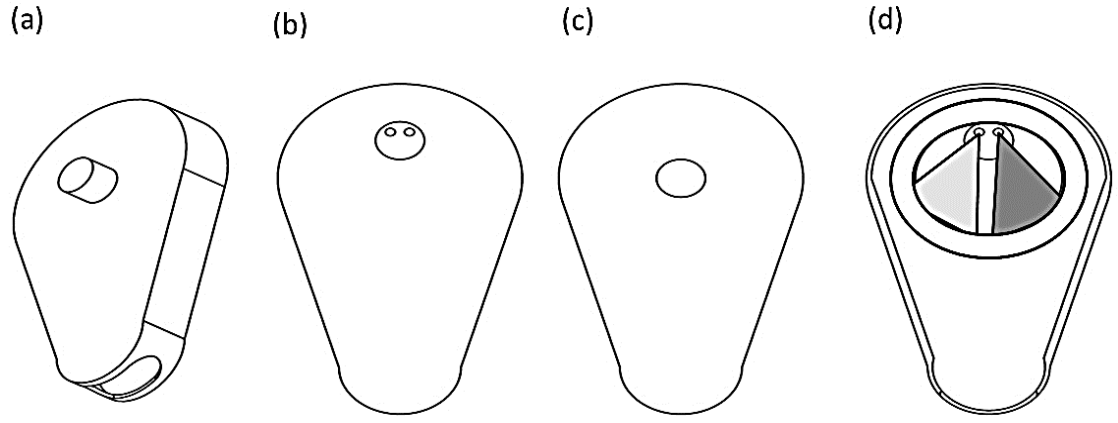

Fig. 54. Schematic drawing of the RRR. (a) Slanted view from the back; (b) front; (c) back; (d) back view with the back cover removed, nozzles spraying. Adapted from *Wenzel and Gorak* (Wenzel and Górak 2019).

As depicted in Fig. 54, the RRR comprises an annular rotor, which contains a perforated or structured metal ring or a thin ring of structured packing, and an elongated casing. The rotor is connected to a motor by the rotor shaft. The rotor shaft is sealed off against the casing and supported by bearings. From the front, liquid distribution pipes with nozzles can be introduced into the casing and the eye of the rotor. The key features of the RRR are:

- a small radial ring/packing depth,
- a wide liquid distribution
- a large wetted area at the inner rim of the ring/packing
- a horizontal axis of rotation
- a small distance between rotor and casing
- strongly inclined casing walls
- a large liquid outlet

As a result of these features, fast liquid processing combined with a low liquid hold-up and a very low residence time in the apparatus can be expected, which leads to a reduced equipment volume, reduced energy consumption, and reduced investment costs compared to an RPB.
It should be noted that also multiple RRR modules could be arranged in series, interconnected by pumps. Additionally, a recycle from and to one or more RRR would be easily possible to increase the frequency of liquid being processed in the rotor.

8 ACHIEVEMENTS AND FUTURE RESEARCH

8.1 Achievements

In this thesis, liquid processing in RPBs was investigated and evaluated with respect to the applicability of three different RPB design variants to liquid phase reactive mixing, liquid-liquid extraction, and liquid-gas processing. Rules of RPB design and operation were deduced for these processes and further guidance for the industrial implementation of RPBs was given. Finally, an alternative HiGee device concept was derived and presented.

For the investigation of liquid phase reactive mixing, the Villermaux-Dushman reaction scheme was adapted for optimal utilization of the method in RPB experiments. The choice of buffer and acid was experimentally investigated on a laboratory scale with respect to sample stability, interchangeability of the key compounds, and comparability with literature results. Boric acid and phosphate were considered for the buffer solution and hydrochloric acid, sulfuric acid, and perchloric acid for the acidic solution. It was demonstrated that boric acid buffer offers a wider concentration range for stable experimental conditions than phosphate buffer. Furthermore, hydrochloric acid was identified as particularly advisable for the investigation of very fast mixing processes, whereas the use of sulfuric acid allows for an accurate comparison with literature data. Based on these result, suitable concentration sets for experiments in RPBs were determined.

In the subsequent literature study, the state of the art in the field of liquid phase reactive mixing in RPBs was thoroughly analyzed and general trends for fast micromixing in RPBs were deduced. However, it was also demonstrated that many operational and design parameters were either not reported systematically in the literature, particularly for the liquid distribution, or could not be analyzed based on the concentration-dependent segregation index alone.

Consequently, a systematic approach to classifying different liquid distribution designs was introduced and results of respective pilot-scale RPB experiments were presented. In these experiments, also the influence of the rotational speed, the total flow rate, and the volumetric ratio of buffer and acid on the mixing results was investigated, and conditions in which the packing and its radial depth play an important role for fast mixing were determined. It was demonstrated that a high liquid outlet and impingement velocity is crucial for fast liquid mixing in RPBs and that an excessive liquid load per cross-sectional area at the inner packing radius should be avoided. Furthermore, it was shown

that both a very high and very low liquid hold-up at the inner rim of the packing can negatively affect the mixing process, depending on the operating conditions. Additionally, the influence of the packing on the mixing process was demonstrated to be dependent on the volumetric ratio and the nozzle orientation. For a volumetric ratio of 8 and an overlapping liquid distribution, the fastest mixing was observed without any packing, but with an empty rotor, comprising the rotating eye ring and rotor plates, alone. In addition to these experimental investigations, the IEM model, the linear approach of the incorporation model, and the exponential approach of the incorporation model were evaluated for their capability to accurately describe the mixing process in an RPB and to derive the concentration-independent micromixing time parameter. It was demonstrated that the mixing process of two equally large inlet streams is accurately described by the IEM model. In contrast, the mixing process at a volumetric ratio of 8 was not well described by the IEM model, but best described by the linear approach of the incorporation model. The lowest results of the micromixing time parameter were 5.3 ± 0.9 ms at equal flow rates and 0.41 ± 0.15 ms at a volumetric ratio of 8. In comparison with other continuous mixing devices, it was demonstrated that RPBs are capable of rapidly mixing comparatively large total flow rates at a low pressure drop. Moreover, it was shown that RPBs offer additional degrees of operational freedom based on their flexible liquid distribution design and the possibility to adjust the rotational speed.

Subsequently, the investigations on liquid phase reactive mixing in RPBs were extended to the industrial scale with a case study on the production of MDA, MDI, and IIR. An analysis of literature results revealed a large potential of RPBs for these processes. However, experimental investigations on the MDA process could not confirm a clear influence of RPB operation and design parameters on the product composition. Instead, large dead zones and a long residence time of liquid on the RPB's casing walls and in the casing bottom were discovered to be the largest drawbacks of the RPB 1.0 design. While it was demonstrated that the average residence time could be reduced from 54.3 s in the RPB 1.0 design to 20.5 s in the RPB 2.0 design by a more sophisticated design and operation, further advances were deemed necessary for a wide-spread industrial application of RPBs. Afterward, a case study on liquid-liquid extraction was conducted. In this framework, a detailed concept for a three-stage RPB process was presented. A final raffinate purity of up to 98.8 % could be achieved under the assumed process constraints. However, it was also demonstrated that the utilization of RPBs for extraction processes might only be economically feasible for systems with high mass transfer limitations or high viscosities. As a third application case study, the liquid-gas processing in RPBs was investigated experimentally. Thus, the overall

feasibility of an RPB-based refining process for PUFA-rich vegetable oil was demonstrated. The amount of undesired free fatty acid in the vegetable oil could be decreased by up to 29 %. However, no clear influence of the rotational speed and the gas flow rate on the product composition was found. Furthermore, it was shown that the residence time of PUFA-rich vegetable oil in the RPB should be drastically reduced to allow for higher process temperatures without negatively influencing the oil's quality.

On the basis of the gained insights, guidelines on the operation, design, and scaling of RPBs for liquid processes were derived. Furthermore, the TRLs of the investigated processes were assessed. It was demonstrated that none of the investigated industrial RPB application could currently be rated at a TRL above 7. In response, a decision chart was presented to support future advances on the process TRLs and foster informed decisions about the use of RPBs for industrial liquid processing. Furthermore, a novel HiGee device design, the Rotating Ring Reactor (RRR), was developed, that could combine rapid liquid processing with a reduced apparatus volume, low liquid hold-up, and short average residence time.

Ultimately, two main conclusions can be drawn for liquid processing in RPBs, based on the results in this thesis. For conditions under which "one apparatus for all unit operations" is demanded, RPBs offer large flexibility and more operational degrees of freedom than other devices. They can be concluded to be especially capable of providing fast liquid processing at high liquid flow rates and high viscosities. Also, RPBs are well-suited for the small-scale testing of different processes, eliminating the necessity to change equipment frequently. However, the current RPB design does also not reflect an optimum design for liquid processing – high residence times and large liquid hold-ups are the result. Consequently, for conditions under which a small and highly efficient apparatus for intensified continuous liquid processing is demanded, other HiGee devices seem more reasonable. One example is the Rotating Ring Reactor design, which was suggested as a promising alternative in this thesis.

8.2 Future Research

In future research, additional work should be conducted to more closely investigate liquid flow patterns in the rotor eye and at the inner rim of the rotor in an RPB. Experiments in this field could include high-resolution non-invasive techniques and high-speed imaging. Furthermore, investigations on the relationship between the volumetric ratio and the influence of the packing should be extended. Additionally, the influence of the total flow rate on this relationship could be studied in the future.

However, with respect to the assessment of liquid phase reactive mixing in RPBs and other continuous mixing devices, the Villermaux-Dushman protocol alone is limited, particularly with respect to the modeling of industrial reactive mixing processes. Therefore, alternative methods of investigation should also be considered in the future to complement results obtained with the Villermaux-Dushman protocol in order to verify or object the trends discussed in this thesis and exclude an influence of the method's sensitivity on the results. This could be, e.g., single- and multi-phase reaction schemes as the competitive neutralization of hydrochloric acid and the alkaline hydrolysis of ethyl chloroacetate (Makowski and Bałdyga 2011) and the competitive nitration of benzene and methylbenzene (Bourne 2003). More comprehensive mixing models should be developed based on the results in this thesis to make the comparison of a broader range of operating conditions possible and to accurately investigate the influence of different volumetric ratios on mixing results in particular. Furthermore, future work should compare the available data based on universal parameters, as the energy dissipation and the energetic efficiency of mixing, as soon as reliable correlations for their calculation have been found. Moreover, the introduction of dimensionless numbers could facilitate a more accurate comparison with other mixing devices. On a long-term basis, CFD simulations could add another layer of analysis and facilitate further validation of experimental results.

The operation range of all considered case studies should be extended in future investigations. Moreover, future cross-device comparisons should include data on power consumption and energy density of the apparatuses, as well as detailed cost functions for investment and operation.

Finally, trends observed in this thesis should be compared to such obtained from absorption, desorption, and distillation studies in future research. Thus, a more complete understanding of the interaction of multiple phases in RPBs could be obtained, as well as more comprehensive guidelines on the operation and design of RPB for liquid processing.

LITERATURE

Acharya, A.; Gottzmann, C. F.; Nowobilski; J.J. (1990): Airborne Rotary Air Seperator Study. Union Carbide Industrial Gases Inc., Linde Devision. National Aeronautics and Space Administration.

Agarwal, Lava; Pavani, V.; Rao, D. P.; Kaistha, N. (2010): Process Intensification in HiGee Absorption and Distillation: Design Procedure and Applications. In *Ind. Eng. Chem. Res.* 49 (20), pp. 10046–10058. DOI: 10.1021/ie101195k.

Albani, Davide; Li, Qiang; Vilé, Gianvito; Mitchell, Sharon; Almora-Barrios, Neyvis; Witte, Peter T. et al. (2017): Interfacial acidity in ligand-modified ruthenium nanoparticles boosts the hydrogenation of levulinic acid to gamma-valerolactone. In *Green Chem.* 19 (10), pp. 2361–2370. DOI: 10.1039/C6GC02586B.

Alonso, David Martin; Wettstein, Stephanie G.; Dumesic, James A. (2013): Gamma-valerolactone, a sustainable platform molecule derived from lignocellulosic biomass. In *Green Chem.* 15 (3), p. 584. DOI: 10.1039/c3gc37065h.

Anton, Nicolas; Vandamme, Thierry F. (2011): Nano-emulsions and micro-emulsions. Clarifications of the critical differences. In *Pharm. Res.* 28 (5), pp. 978–985. DOI: 10.1007/s11095-010-0309-1.

Assirelli, M.; Bujalski, W.; Eaglesham, A.; Nienow, A. W. (2002): Study Of Micromixing in a Stirred Tank Using a Rushton Turbine. In *Chem. Eng. Res. and Des.* 80 (8), pp. 855–863. DOI: 10.1205/026387602321143390.

Assirelli, M.; Bujalski, W.; Eaglesham, A.; Nienow, A. W. (2008): Macro- and micromixing studies in an unbaffled vessel agitated by a Rushton turbine. In *Chem. Eng. Sci.* 63 (1), pp. 35–46. DOI: 10.1016/j.ces.2007.07.074.

Aubin, J.; Ferrando, M.; Jiricny, V. (2010): Current methods for characterising mixing and flow in microchannels. In *Chem. Eng. Sci.* 65 (6), pp. 2065–2093. DOI: 10.1016/j.ces.2009.12.001.

Baldea, Michael; Edgar, Thomas F.; Stanley, Bill L.; Kiss, Anton A. (2017): Modular manufacturing processes: Status, challenges, and opportunities. In *AIChE J.* 63 (10), pp. 4262–4272. DOI: 10.1002/aic.15872.

Baldyga, J.; Bourne, J. R. (1984): Mixing and fast chemical reaction-VIII: Initial deformation of material elements in isotropic, homogeneous turbulence. In *Chem. Eng. Sci.* 39 (2), pp. 329–334. DOI: 10.1016/0009-2509(84)80031-7.

Baldyga, J.; Bourne, J. R. (1990): Comparison of the engulfment and the interaction-by-exchange-with-the-mean micromixing models. In *Chem. Eng. J.* 45 (1), pp. 25–31. DOI: 10.1016/0300-9467(90)80022-5.

Bałdyga, J.; Bourne, J. R. (1988): Calculation of micromixing in inhomogeneous stirred tank reactors. In *Chem. Eng. Res. and Des.* 66, pp. 33–38.

Bałdyga, J.; Bourne, J. R. (1989): Simplification of micromixing calculations. I. Derivation and application of new model. In *Chem. Eng. J.* 42 (2), pp. 83–92. DOI: 10.1016/0300-9467(89)85002-6.

Bałdyga, J.; Bourne, J. R. (1999): Turbulent mixing and chemical reactions. New York: Wiley.

Bałdyga, J.; Pohorecki, R. (1995): Turbulent micromixing in chemical reactors — a review. In *Chem. Eng. J. Bioch. Eng.* 58 (2), pp. 183–195. DOI: 10.1016/0923-0467(95)02982-6.

Baqueiro, Carlos; Ibaseta, Nelson; Guichardon, Pierrette; Falk, Laurent (2018): Influence of reagents choice (buffer, acid and inert salt) on triiodide production in the Villermaux–Dushman method applied to a stirred vessel. In *Chem. Eng. Res. Des.* 136, pp. 25–31. DOI: 10.1016/j.cherd.2018.04.017.

Beek, J., JR.; Miller, R. S. (1959): Turbulent transport in chemical reactors. In *Chem. Eng. Prog. Symp. Series* 55, pp. 23–28.

Benneker, Anne M.; van der Ham, Louis G.J.; Waele, Bart de; Zeeuw, Arend Jan; van den Berg, Henk (2016): Design and intensification of industrial DADPM process. In *Chem. Eng. Process.: P.I.* 109, pp. 39–50. DOI: 10.1016/j.cep.2016.08.009.

Beran, Premysl; Bruckenstein, Stanley (1968): Rotating-disk-electrode study of the catalytic wave produced by the reduction of iodine in the presence of iodate. In *J. Phys. Chem.* 72 (10), pp. 3630–3635. DOI: 10.1021/j100856a046.

Bielenberg, J.; Bryner, M. (2018): Realize the Potential of Process Intensification. In *CEP Mag. - Process Intensification: Its Time is Now*.

Botella, P.; Corma, A.; Carr, Robert H.; Mitchell, Christopher J. (2011): Towards an industrial synthesis of diamino diphenyl methane (DADPM) using novel delaminated materials: A breakthrough step in the production of isocyanates for polyurethanes. In *Appl. Catal. A: Gen.* 398 (1-2), pp. 143–149. DOI: 10.1016/j.apcata.2011.03.026.

Bourne, J. R. (2003): Mixing and the Selectivity of Chemical Reactions. In *Org. Process Res. Dev.* 7 (4), pp. 471–508. DOI: 10.1021/op020074q.

Bourne, J. R. (2008): Comments on the iodide/iodate method for characterising micromixing. In *Chem. Eng. J.* 140 (1-3), pp. 638–641. DOI: 10.1016/j.cej.2008.01.031.

Braden, Drew J.; Henao, Carlos A.; Heltzel, Jacob; Maravelias, Christos C.; Dumesic, James A. (2011): Production of liquid hydrocarbon fuels by catalytic conversion of biomass-derived levulinic acid. In *Green Chem.* 13 (7), p. 1755. DOI: 10.1039/c1gc15047b.

Burns, J. R.; Jamil, J. N.; Ramshaw, C. (2000): Process intensification: operating characteristics of rotating packed beds — determination of liquid hold-up for a high-voidage structured packing. In *Chem. Eng. Sci.* 55 (13), pp. 2401–2415. DOI: 10.1016/S0009-2509(99)00520-5.

Burns, J. R.; Ramshaw, C. (1996): Process intensification. Visual study of liquid maldistribution in rotating packed beds. In *Chem. Eng. Sci.* 51 (8), pp. 1347–1352. DOI: 10.1016/0009-2509(95)00367-3.

Carnegie Mellon University (2016): Guidelines for Using Perchloric Acid. Edited by Carnegie Mellon University. Available online at https://www.cmu.edu/ehs/chemical/Guidelines%20for%20Using%20Perchloric%20Acid.pdf, checked on 6/9/2016.

Chen, J. F. (2009): The recent developments in the HIGEE technology. GPE-EPIC. Venice, Italy, 2009, checked on 9/2/2016.

Chen, J. F.; Gao, Hua; Wu, Yi-Xian; Zou, Hai-Kui; Chu, Guang-Wen; Zhang, Lei (2010): Method for synthesis of butyl rubber. Patent no. US7776976B2.

Chen, Jian-Feng; Gao, Hua; Zou, Hai-Kui; Chu, Guang-Wen; Zhang, Lei; Shao, Lei et al. (2009): Cationic polymerization in rotating packed bed reactor. Experimental and modeling. In *AIChE J.* 25 (2). DOI: 10.1002/aic.11911.

Chen, Y.-S.; Clifford, Y.-D.T.; Ming-Hui, C.; Hwai-Shen, L. (2006): Characteristics of Micromixing in a Rotating Packed Bed. In *J. Chin. Inst. Chem. Engrs.* 37 (1), pp. 63–69.

Chen, Y.-S.; Liu, H.-S.; Lin, C.-C.; Liu, W.-T. (2004): Micromixing in a Rotating Packed Bed. In *J. Chem. Eng. Japan / JCEJ* 37 (9), pp. 1122–1128. DOI: 10.1252/jcej.37.1122.

Chu, G.-W.; Song, Y.-J.; Zhang, W.-J.; Luo, Y.; Zou, H.-K.; Xiang, Y.; Chen, J.-F. (2015): Micromixing Efficiency Enhancement in a Rotating Packed Bed Reactor with Surface-Modified Nickel Foam Packing. In *Ind. Eng. Chem. Res.* 54 (5), pp. 1697–1702. DOI: 10.1021/ie504407a.

Commenge, J.-M.; Falk, L. (2011): Villermaux–Dushman protocol for experimental characterization of micromixers. In *Chem. Eng. Process.: P.I.* 50 (10), pp. 979–990. DOI: 10.1016/j.cep.2011.06.006.

Corma, Avelino; Botella, Pablo; Mitchell, Chris (2004): Replacing HCl by solid acids in industrial processes: synthesis of diamino diphenyl methane (DADPM) for producing polyurethanes. In *Chemical communications (Cambridge, England)* (17), pp. 2008–2010. DOI: 10.1039/b406303a.

Decap, Philippe; Braipson-Danthine, Sabine; Vanbrabant, Béatrice; Greyt, Wim de; Deroanne, Claude (2004): Comparison of steam and nitrogen in the physical deacidification of soybean oil. In *J. Amer. Oil. Chem. Soc.* 81 (6), pp. 611–617. DOI: 10.1007/s11746-006-0950-3.

DECHEMA e.V. (2017): Modulare Anlagen. Flexible chemische Produktion durch Modularisierung und Standardisierung - Status quo und zukünftige Trends. Edited by Temporärer ProcessNet-Arbeitskreis „Modulare Anlagen“. Available online at https://processnet.org/dechema_media/modulareanlagen.pdf, checked on 12/4/2018.

DG Fett (2012): Hinweise zur Bestimmung der Totox-Zahl und den DGFEinheitsmethoden C-VI 6a (02) und C-VI 6e (05) zur Bestimmung der Peroxidzahl und der Anisidinzahl. Deutsche Einheitsmethoden zur Untersuchung von Fetten, Fettprodukten, Tensiden und verwandten Stoffen. Edited by Gemeinschaftsausschuss für die Analytik von Fetten, Ölen, Fettprodukten, verwandten Stoffen und Rohstoffen (GA Fett). Deutsche Gesellschaft für Fettwissenschaften e.V. Available online at http://www.dgfett.de/methods/hinweise_cvi6.pdf, checked on 9/18/2018.

Ding, J.; Chen, J. F.; Hua, W.; Chu, G.; Zou, H.; Luo, P. et al. (2007a): Process for preparing isocyanate. Applied for by Ningbo Wanhua Polyurethane Co. on 4/26/2007. App. no. CN:200710098040:B. Patent no. CN101104595B.

Ding, J.; Chen, J. F.; Zhang, H.; Zou, H.; Hua, W.; Zhang, P. et al. (2007b): Method of preparing polymethylene-polyphenyl-polyamine. Applied for by Ningbo Wanhua Polyurethanes Co., Ltd. (Ningbo), Beijing University of Chemical Technology (Beijing) on 10/16/2007. App. no. 11/873,056. Patent no. 20080249261.

Dushman, S. (1904): The rate of the reaction between iodic and hydriodic acids. [Toronto]: University Library (CIHM-ICMH Microfiche series = CIHM-ICMH collection de microfiches, no. 88080).

Ehrfeld, W.; Golbig, K.; Hessel, V.; Löwe, H.; Richter, T. (1999): Characterization of Mixing in Micromixers by a Test Reaction. Single Mixing Units and Mixer Arrays. In *Ind. Eng. Chem. Res.* 38 (3), pp. 1075–1082. DOI: 10.1021/ie980128d.

EUROPIN (2007): European Roadmap for Process Intensification. Available online at http://efce.info/EUROPIN.html, checked on 12/4/2018.

Falk, L.; Commenge, J.-M. (2010): Performance comparison of micromixers. In *Chem. Eng. Sci.* 65 (1), pp. 405–411. DOI: 10.1016/j.ces.2009.05.045.

Fang, Yizhou; Gu, Saiqi; Zhang, Jianyou; Liu, Shulai; Ding, Yuting; Liu, Jianhua (2018): Deodorisation of fish oil by nanofiltration membrane process. Focus on volatile flavour compounds and fatty acids composition. In *Int. J. Food Sci. Technol.* 53 (3), pp. 692–699. DOI: 10.1111/ijfs.13644.

Fournier, M.-C.; Falk, L.; Villermaux, J. (1996a): A new parallel competing reaction system for assessing micromixing efficiency—Determination of micromixing time by a simple mixing model. In *Chem. Eng. Sci.* 51 (23), pp. 5187–5192. DOI: 10.1016/S0009-2509(96)00340-5.

Fournier, M.-C.; Falk, L.; Villermaux, J. (1996b): A new parallel competing reaction system for assessing micromixing efficiency—Experimental approach. In *Chem. Eng. Sci.* 51 (22), pp. 5053–5064. DOI: 10.1016/0009-2509(96)00270-9.

Frede, Wolfgang (2010): Handbuch für Lebensmittelchemiker. Lebensmittel, Bedarfsgegenstände, Kosmetika, Futtermittel. 3. Aufl. Dordrecht: Springer.

Gal, J. (2012): To the rescue. 281 (7): ICIS Chemical Business.

Górak, A.; Gourdon, C.; Spits, F.; Stankiewicz, A. (2017): Importance of Knowledge and Technology Transfer in PI. In *NPT Procestechnologie* 4, pp. 18–19.

Greyt, Wim de (2013): Edible Oil Refining: Current and Future Technologies. In: Edible Oil Processing; 2nd Ed. (Eds.: Hamm, W.; Hamilton, R. J.; Calliauw, G.). Chichester, UK: John Wiley & Sons, Ltd.

Guichardon, P. (1996): Caracterisation Chimique du micromelange par la reaction iodure-iodate. PhD Thesis.

Guichardon, P.; Falk, L. (2000): Characterisation of micromixing efficiency by the iodide–iodate reaction system. Part I: Experimental procedure. In *Chem. Eng. Sci.* 55 (19), pp. 4233–4243. DOI: 10.1016/S0009-2509(00)00068-3.

Guichardon, P.; Falk, L.; Villermaux, J. (2000): Characterisation of micromixing efficiency by the iodide–iodate reaction system. Part II: kinetic study. In *Chem. Eng. Sci.* 55 (19), pp. 4245–4253. DOI: 10.1016/S0009-2509(00)00069-5.

Guichardon, P.; Ibaseta, N. (2016): Revision of the Dushman Reaction Kinetics for an Improved Micromixing Characterization. In *24th Int. Symp. Chem. Reac. Eng. (ISCRE),* Minneapolis, USA.

Guo, K.; Guo, F.; Feng, Y.; Chen, J.-F.; Zheng, C.; Gardner, N. C. (2000): Synchronous visual and RTD study on liquid flow in rotating packed-bed contactor. In *Chem. Eng. Sci.* 55 (9), pp. 1699–1706. DOI: 10.1016/S0009-2509(99)00369-3.

Guo, Tian-Yu; Cheng, Kun-Peng; Wen, Li-Xiong; Andersson, Ronnie; Chen, Jian-Feng (2017): Three-Dimensional Simulation on Liquid Flow in a Rotating Packed Bed Reactor. In *Ind. Eng. Chem. Res.* 56 (28), pp. 8169–8179. DOI: 10.1021/acs.iecr.7b01759.

Habchi, Charbel; Lemenand, Thierry; Della Valle, Dominique; Khaled, Mahmoud; Elmarakbi, Ahmed; Peerhossaini, Hassan (2014): Mixing assessment by chemical probe. In *J. Ind. Eng. Chem.* 20 (4), pp. 1411–1420. DOI: 10.1016/j.jiec.2013.07.026.

Hofinger, J. (2013): Micro- and Macromixing Studies in Two- and Three-Phase (Gas-Solid-Liquid) Stirred Chemical Reactors. Ph.D. thesis. University of Birmingham, Birmingham. College of Engineering & Physical Sciences.

Horrocks, L. A.; Yeo, Y. K. (1999): Health benefits of docosahexaenoic acid (DHA). In *Pharmacol. Res.* 40 (3), pp. 211–225. DOI: 10.1006/phrs.1999.0495.

Hua, W.; Ding, J.; Chen, J. F. (Eds.) (2007): Application of Rotating Packed Bed Rpb Reactor in Production of MDA. AIChE 2007 Annual Meeting. Catalysis and Reaction Engineering Division.

Jiao, Weizhou; Liu, Youzhi; Qi, Guisheng (2012): Micromixing Efficiency of Viscous Media in Novel Impinging Stream-Rotating Packed Bed Reactor. In *Ind. Eng. Chem. Res.* 51 (20), pp. 7113–7118. DOI: 10.1021/ie202586f.

Jun, J.; Hong, S.; Liu, J. (2011): Micromixing efficiency in high gravity reactor with different packing. 2011 International Conference on Chemical Engineering and Advanced Materials, CEAM 2011. In *Adv. Mater. Res.* 2011 (233-235), pp. 1184–1187. Available online at http://www.scopus.com/inward/record.url?eid=2-s2.0-79958285042&partnerID=40&md5=f57e7edf134bee89e44710745fc7e537.

Keil, Frerich J. (2018): Process intensification. In *Rev. Chem. Eng.* 34 (2), pp. 135–200. DOI: 10.1515/revce-2017-0085.

Kelleher, T.; Fair, J. R. (1996): Distillation Studies in a High-Gravity Contactor. In *Ind. Eng. Chem. Res.* 35 (12), pp. 4646–4655. DOI: 10.1021/ie950662a.

Kölbl, A. (2008): Further comments on the Iodide Iodate Reaction Method for characterising micromixing. In *Chem. Eng. J.* 145 (1), pp. 176–177. DOI: 10.1016/j.cej.2008.06.003.

Kölbl, A.; Desplantes, V.; Grundemann, L.; Scholl, S. (2013a): Kinetic investigation of the Dushman reaction at concentrations relevant to mixing studies in stirred tank reactors. In *Chem. Eng. Sci.* 93, pp. 47–54. DOI: 10.1016/j.ces.2013.01.067.

Kölbl, A.; Kraut, M.; Dittmeyer, R. (2013b): Kinetic investigation of the Dushman reaction at concentrations relevant to mixing studies in microstructured cyclone type mixers. In *Chem. Eng. Sci.* 101, pp. 454–460. DOI: 10.1016/j.ces.2013.07.008.

Kölbl, A.; Kraut, M.; Schubert, K. (2008): The iodide iodate method to characterize microstructured mixing devices. In *AIChE J.* 54 (3), pp. 639–645. DOI: 10.1002/aic.11408.

Kölbl, A.; Kraut, M.; Schubert, K. (2010): On the scalability of microstructured mixing devices. In *Chem. Eng. J.* 160 (3), pp. 865–872. DOI: 10.1016/j.cej.2010.02.037.

Kölbl, A.; Kraut, M.; Wenka, A. (2011): Design parameter studies on cyclone type mixers. In *Chem. Eng. J.* 167 (2-3), pp. 444–454. DOI: 10.1016/j.cej.2010.08.092.

Kölbl, A.; Schmidt-Lehr, S. (2010): The iodide iodate reaction method. The choice of the acid. In *Chem. Eng. Sci.* 65 (5), pp. 1897–1901. DOI: 10.1016/j.ces.2009.11.032.

Krupa, K.; Nunes, Maria I.; Santos, Ricardo J.; Bourne, John R. (2014): Characterization of micromixing in T-jet mixers. In *Chem. Eng. Sci.* 111, pp. 48–55. DOI: 10.1016/j.ces.2014.02.018.

Ladwig, H. J.; Oelmann, H.; Pippel, W.; Ringel, C. (1991): Reaktionsführung der Formaldehyd-Anilin-Kondensation in verschiedenen Reaktionsführungen - ein theoretischer Vergleich. In *Wiss. Z. Tech. Univ. Dresden* 40 (2).

Ladwig, H. J.; Pippel, W.; Ringel, C.; Oelmann, H. (1989): Einfaches kinetisches Modell der Anilin-Formaldehyd-Kondensation. In *Wiss. Z. Tech. Univ. Dresden* 38 (1).

Lemenand, T.; Della Valle, D.; Habchi, C.; Peerhossaini, H. (2017): Micro-mixing measurement by chemical probe in homogeneous and isotropic turbulence. In *Chem. Eng. J.* 314, pp. 453–465. DOI: 10.1016/j.cej.2016.12.001.

Leschinski, I.; Mattke, T.; Waters, G.; Stroefer, E. (2012): Process for preparing isocyanates and/or polyisocyanates. Applied for by BASF SE on 10/26/2012. Patent no. US 8686182 B2.

Li, M.; Xu, J.; Lu, Q. (2007): Creating superhydrophobic surfaces with flowery structures on nickel substrates through a wet-chemical-process. In *J. Mater. Chem.* 17 (45), p. 4772. DOI: 10.1039/B709665H.

Li, T.-C.; Qi, G.-S. (2004): Impinging stream rotating packed bed extractor. In *Petro-Chem. Equip.* 133 (14), pp. 26–28.

Lin, C.-C.; Tsai, C.-H. (2016): Micromixing in a rotating packed bed with blade packings. In *J. Taiwan Inst. Chem. Eng.* 63, pp. 33–38. DOI: 10.1016/j.jtice.2016.03.012.

Lin, Chien-Chang (1981): Volatility of iodine in dilute aqueous solutions. In *J. Inorg. Nucl. Chem.* 43 (12), pp. 3229–3238. DOI: 10.1016/0022-1902(81)80094-2.

Liu, Y.; Qi, G.; Yang, L. (2003): Study on the mass transfer characteristics in impinging stream rotating packed bed extractor. In *Chem. Ind. Eng. Prog.* 22 (10), pp. 1108–1111.

Makowski, Łukasz; Bałdyga, Jerzy (2011): Large Eddy Simulation of mixing effects on the course of parallel chemical reactions and comparison with k–ε modeling. In *Chem. Eng. Process.: P.I.* 50 (10), pp. 1035–1040. DOI: 10.1016/j.cep.2011.06.003.

Mankins, J. C. (1995): Technology Readiness Levels. A White Paper. Edited by Advanced Concepts Office, Office of Space Access and Technology, NASA. Available online at https://www.colorado.edu/ASEN/asen3036/TECHNOLOGYREADINESSLEVELS.pdf, checked on 5/2/2018.

Manzano Martínez, Arturo N.; van Eeten, Kevin M P; Schouten, Jaap C.; van der Schaaf, John (2017): Micromixing in a Rotor-Stator Spinning Disc Reactor. In *Ind. Eng. Chem. Res.* 56 (45), pp. 13454–13460. DOI: 10.1021/acs.iecr.7b01324.

Mao, Zaisha; Yang, Chao (2017): Micro-mixing in chemical reactors: A perspective. In *Chinese J. Chem. Eng.* 25 (4), pp. 381–390. DOI: 10.1016/j.cjche.2016.09.012.

Matissek, Reinhard; Steiner, Gabriele; Fischer, Markus (2014): Lebensmittelanalytik. 5., vollst. überarb. u. akt. Aufl. 2014. Berlin, Heidelberg: Springer Berlin Heidelberg (Springer-Lehrbuch).

Modak, Jayant B.; Bhowal, Avijit; Datta, Siddhartha (2016): Extraction of dye from aqueous solution in rotating packed bed. In *J. Hazard. Mater.* 304, pp. 337–342. DOI: 10.1016/j.jhazmat.2015.10.062.

Motallebi, Abbasali; Gharachorloo, Maryam; Mizani, Maryam (2015): The effects of refining steps on Kilka (Clupeonella delicatula) fish oil quality. In *Iran J. Fish. Sci.* 14 (2), pp. 382–392.

Murat Sen, S.; Henao, Carlos A.; Braden, Drew J.; Dumesic, James A.; Maravelias, Christos T. (2012): Catalytic conversion of lignocellulosic biomass to fuels. Process development and technoeconomic evaluation. In *Chem. Eng. Sci.* 67 (1), pp. 57–67. DOI: 10.1016/j.ces.2011.07.022.

Nayar, M.R.G.; Francis, J. D. (1978): Kinetics and mechanism of the aniline-formaldehyde reaction in acid medium. In *Makromol. Chem.* 179, pp. 1783–1790.

Neumann, Kolja; Gladyszewski, Konrad; Groß, Kai; Qammar, Hina; Wenzel, Dennis; Górak, Andrzej; Skiborowski, Mirko (2018a): A guide on the industrial application of rotating packed beds. In *Chemical Engineering Research and Design* 134, pp. 443–462. DOI: 10.1016/j.cherd.2018.04.024.

Neumann, Kolja; Hunold, Sira; Beer, Michiel de; Skiborowski, Mirko; Górak, Andrzej (2018b): Mass Transfer Studies in a Pilot Scale RPB with Different Packing Diameters. In *Ind. Eng. Chem. Res.* 57 (6), pp. 2258–2266. DOI: 10.1021/acs.iecr.7b04186.

Neumann, Kolja; Hunold, Sira; Groß, Kai; Górak, Andrzej (2017): Experimental investigations on the upper operating limit in rotating packed beds. In *Chem. Eng. Process.: P.I.* 121, pp. 240–247. DOI: 10.1016/j.cep.2017.09.003.

Ottino, J. M.; Macosko, C. W. (1980): An efficiency parameter for batch mixing of viscous fluids. In *Chem. Eng. Sci.* 35 (6), pp. 1454–1457. DOI: 10.1016/0009-2509(80)85142-6.

Ottino, J. M.; Ranz, William E.; Macosko, Christopher W. (1979): A lamellar model for analysis of liquid-liquid mixing. In *Chem. Eng. Sci.* 34 (6), pp. 877–890. DOI: 10.1016/0009-2509(79)85145-3.

Ouyang, Yi; Xiang, Yang; Gao, Xue-Ying; Li, Wen-Ling; Zou, Hai-Kui; Chu, Guang-Wen; Chen, Jian-Feng (2018a): Micromixing efficiency in a rotating packed bed with non-Newtonian fluid. In *Chem. Eng. J.* 354, pp. 162–171. DOI: 10.1016/j.cej.2018.07.141.

Ouyang, Yi; Zou, Hai-Kui; Gao, Xue-Ying; Chu, Guang-Wen; Xiang, Yang; Chen, Jian-Feng (2018b): Computational fluid dynamics modeling of viscous liquid flow characteristics and end effect in rotating packed bed. In *Chem. Eng. Process.: P.I.* 123, pp. 185–194. DOI: 10.1016/j.cep.2017.09.005.

Palmer, D. A.; Ramette, R. W.; Mesmer, R. E. (1984): Triiodide ion formation equilibrium and activity coefficients in aqueous solution. In *J. Solution Chem.* 13 (9), pp. 673–683. DOI: 10.1007/BF00650374.

Panić, S.; Loebbecke, S.; Tuercke, T.; Antes, J.; Bošković, D. (2004): Experimental approaches to a better understanding of mixing performance of microfluidic devices. In *Chem. Eng. J.* 101 (1-3), pp. 409–419. DOI: 10.1016/j.cej.2003.10.026.

Paul, Edward L.; Atiemo-Obeng, Victor A.; Kresta, Suzanne M. (2004): Handbook of industrial mixing. Science and practice. Hoboken N.J.: Wiley-Interscience.

Pesavento, M. (1983): Spectrophotometric titration of traces of iodide in concentrated chloride solution. In *Anal. Chim. Acta* 153 (756), pp. 249–255. DOI: 10.1016/S0003-2670(00)85509-9.

Pfennig, A.; Pilhofer, T.; Schröter, J. (2011): Kapitel 10: Flüssig-Flüssig-Extraktion. In *Fluidverfahrenstechnik - Grundlagen, Methodik, Technik, Praxis (Ed.: Goedecke, R.)*, 907-992.

Pinot, J.; Commenge, J.-M.; Portha, J.-F.; Falk, L. (2014): New protocol of the Villermaux–Dushman reaction system to characterize micromixing effect in viscous media. In *Chem. Eng. Sci.* 118, pp. 94–101. DOI: 10.1016/j.ces.2014.07.010.

Podbielniak, W. J. (1935): Centrifugal counter current contact apparatus. Applied for by Podbielniak, W. J. App. no. 476190. Patent no. US2004011A.

Qammar, H.; Hecht, F.; Skiborowski, M.; Górak, A. (2018): Experimental Investigation and Design of Rotating Packed Beds for Distillation. In *Chem. Engineer. Trans.* 69.

Qian, Zhi; Chen, Qi; Grossmann, Ignacio E. (2018): Optimal synthesis of rotating packed bed and packed bed: a case illustrating the integration of PI and PSE. In : 13th International Symposium on Process Systems Engineering (PSE 2018), vol. 44: Elsevier (Computer Aided Chemical Engineering), pp. 2377–2382.

Qin, H.; Zhang, C.; Xu, Q.; Dang, X.; Li, W.; Lei, K. et al. (2017): Geometrical improvement of inline high shear mixers to intensify micromixing performance. In *Chem. Eng. J.* 319, pp. 307–320. DOI: 10.1016/j.cej.2017.02.150.

Radatz, Heiko; Elischewski, Johannes Martin; Heitmann, Matthias; Schembecker, Gerhard; Bramsiepe, Christian (2017): Design of equipment modules for flexibility. In *Chem. Eng. Sci.* 168, pp. 271–288. DOI: 10.1016/j.ces.2017.04.021.

Ramshaw, C. (1983): 'HiGee' Distillation - An Example of Process Intensification. In *Chem. Eng. (London)* (389), pp. 13–14. Available online at http://www.scopus.com/inward/record.url?eid=2-s2.0-0020703517&partnerID=40&md5=b9a4cc58b693fec16135534b284ed073.

Ramshaw, C. (Ed.) (1995): The Incentive for Process Intensification. Proceedings, 1st Intl. Conf. Proc. Intensif. for Chem. Ind. London: BHR Group (18).

Rao, D. P.; Bhowal, A.; Goswami, P. S. (2004): Process Intensification in Rotating Packed Beds (HIGEE): An Appraisal. In *Ind. Eng. Chem. Res.* 43 (4), pp. 1150–1162. DOI: 10.1021/ie030630k.

Sangalov, I͡U. A.; Minsker, K. S.; Zaikov, Gennadiĭ Efremovich (2001): Polymers derived from isobutylene. Synthesis, properties, application. Utrecht, Boston: VSP (New concepts in polymer science).

Santhanalakshmi, J. (1988): A thermochemical kinetic study of interconversion reactions of aniline-formaldehyde products. In *Thermochim. Acta* 127, pp. 369–375. DOI: 10.1016/0040-6031(88)87513-0.

Schmitz, G. (1999): Kinetics and mechanism of the iodate–iodide reaction and other related reactions. In *Phys. Chem. Chem. Phys.* 1 (8), pp. 1909–1914. DOI: 10.1039/a809291e.

Serrano-Ruiz, Juan Carlos; Braden, Drew J.; West, Ryan M.; Dumesic, James A. (2010): Conversion of cellulose to hydrocarbon fuels by progressive removal of oxygen. In *Appl. Catal. B: Environ.* 100 (1-2), pp. 184–189. DOI: 10.1016/j.apcatb.2010.07.029.

Shampine, Lawrence F.; Reichelt, Mark W. (1997): The MATLAB ODE Suite. In *SIAM J. Sci. Comput.* 18 (1), pp. 1–22. DOI: 10.1137/S1064827594276424.

Sigma-Aldrich (2015): Safety Data Sheet - Perchloric acid. Available online at www.sigmaaldrich.com, updated on 6/10/2015, checked on 8/28/2017.

Six, Christian; Richter, Frank; Ullmann, Fritz (2003): Ullmann's Encyclopedia of Industrial Chemistry: Isocyanates, Organic // Ullmann's encyclopedia of industrial chemistry. 7th ed. [Hoboken, N.J.]: Wiley-VCH Verlag GmbH & Co. KGaA; John Wiley & Sons, 1/15/2003. Available online at http://onlinelibrary.wiley.com/doi/10.1002/14356007.a14_611/full.

Skiborowski, Mirko (2018): Process synthesis and design methods for process intensification. In *Curr. Opin. in Chem. Eng.* 22, pp. 216–225. DOI: 10.1016/j.coche.2018.11.004.

Stankiewicz, A.I., Moulijn, J.A. (2000): Process Intensification Transforming Chemical Engineering. In *Chem. Eng. Prog.* (96 (1)).

Stenstrom, M. K.; Rosso, D. (2003): Fundamentals of Chemical Reactor Theory. University of California, Los Angeles, USA. Civil & Environmental Engineering Department.

Sudhoff, D.; Leimbrink, M.; Schleinitz, M.; Górak, A.; Lutze, P. (2015): Modelling, design and flexibility analysis of rotating packed beds for distillation. In *Chem. Eng. Res. and Des.* 94, pp. 72–89. DOI: 10.1016/j.cherd.2014.11.015.

DIN EN ISO 6885, Juli 2016: Tierische und pflanzliche Fette und Öle - Bestimmung der Anisidinzahl (ISO 6885:2016); Deutsche Fassung EN ISO 6885:2016, checked on 5/22/2018.

DIN EN ISO 3960, Mai 2017: Tierische und pflanzliche Fette und Öle - Bestimmung der Peroxidzahl - Iodometrische (visuelle) Endpunktbestimmung (ISO 3960:2017), checked on 5/22/2018.

DIN EN ISO 660, Oktober 2009: Tierische und pflanzliche Fette und Öle – Bestimmung der Säurezahl und der Azidität (ISO 660:2009); Deutsche Fassung EN ISO 660:2009, checked on 5/22/2018.

Trent, D. L.; Tirtowidjojo, D. (2003): Intensifying the process. In *Chem. Eng. (London)* (742), pp. 30–31. Available online at http://www.scopus.com/inward/record.url?eid=2-s2.0-38349011685&partnerID=40&md5=39f4b38a3a0f83efbbba3be8bc9241c6.

van den Berg, Henk; van der Ham, Louis; Gutierrez, Hector; Odu, Samuel; Roelofs, Tobias; Weerdt, Jan de (2012): Phosgene free route to Methyl Diphenyl Diisocynate (MDI). A technical and economical evaluation. In *Chem. Eng. J.* 207-208, pp. 254–257. DOI: 10.1016/j.cej.2012.06.095.

Vedantam, S.; Joshi, J. B. (2006): Annular Centrifugal Contactors—A Review. In *Chem. Eng. Res. and Des.* 84 (7), pp. 522–542. DOI: 10.1205/cherd.05219.

Vestland, Tina Lien; Petersen, Lizette Balle; Myrset, Astrid Hilde; Klaveness, Jo (2017): Oxidative stability of omega-3 tablets. In *Eur. J. Lipid Sci. Technol.* 119 (2), p. 1500322. DOI: 10.1002/ejlt.201500322.

Villermaux, J.; Falk, L. (1994): A generalized mixing model for initial contacting of reactive fluids. In *Chem. Eng. Sci.* 49 (24), pp. 5127–5140. DOI: 10.1016/0009-2509(94)00303-3.

Villermaux, J.; Falk, L.; Fournier, M. (1993): Potential use of a New Parallel Reaction System to Characterize Micromixing in Stirred Reactors. In *AIChE Ann. Meet. Proceed.*

Villermaux, J.; Falk, L.; Fournier, M.-C.; Detrez, C. (1992): Use of Parallel Competing Reactions to Characterize Micromixing Efficiency. In *AiChe Symp. Series*.

Visscher, F.; van der Schaaf, J.; Nijhuis, T. A.; Schouten, J. C. (2013): Rotating reactors – A review. In *Chem. Eng. Res. and Des.* 91 (10), pp. 1923–1940. DOI: 10.1016/j.cherd.2013.07.021.

Wang, Wei; Zou, Hai-Kui; Chu, Guang-Wen; Weng, Zhan; Chen, Jian-Feng (2014): Bromination of butyl rubber in rotating packed bed reactor. In *Chem. Eng. J.* 240, pp. 503–508. DOI: 10.1016/j.cej.2013.10.095.

Wegener, Gerhard; Brandt, Matthias; Duda, Lothar; Hofmann, Jörg; Klesczewski, Bert; Koch, Daniel et al. (2001): Trends in industrial catalysis in the polyurethane industry. In *Appl. Catal. A: Gen.* 221 (1-2), pp. 303–335. DOI: 10.1016/S0926-860X(01)00910-3.

Wenzel, D.; Górak, A. (2019): Patent: Rotierender Ring Reaktor. App. no. DE102017119569A1.

Wong, S.; Ward, M.; Wharton, C. (2004): Micro T-mixer as a rapid mixing micromixer. In *Sens. Actuators, B* 100 (3), pp. 359–379. DOI: 10.1016/j.snb.2004.02.008.

Yang, H.-J.; Chu, G.-W.; Zhang, J.-W.; Shen, Z.-G.; Chen, J.-F. (2005): Micromixing Efficiency in a Rotating Packed Bed: Experiments and Simulation. In *Ind. Eng. Chem. Res.* 44 (20), pp. 7730–7737. DOI: 10.1021/ie0503646.

Yang, Kuang; Chu, Guang-Wen; Shao, Lei; Luo, Yong; Chen, Jian-Feng (2009): Micromixing efficiency of rotating packed bed with premixed liquid distributor. In *Chem. Eng. J.* 153 (1-3), pp. 222–226. DOI: 10.1016/j.cej.2009.06.006.

Yang, Peng-Fei; Luo, Shuai; Zhang, Dong-Sheng; Yang, Pei-Zhen; Liu, You-Zhi; Jiao, Wei-Zhou (2018): Extraction of nitrobenzene from aqueous solution in impinging stream-rotating packed bed. In *Chem. Eng. Process.: P.I.* 124, pp. 255–260. DOI: 10.1016/j.cep.2018.01.022.

Yang, Y.; Xiang, Y.; Chu, G.; Zou, H.; Luo, Y.; Arowo, M.; Chen, J.-F. (2015a): A noninvasive X-ray technique for determination of liquid holdup in a rotating packed bed. In *Chem. Eng. Sci.* 138, pp. 244–255. DOI: 10.1016/j.ces.2015.07.044.

Yang, Y.-C.; Xiang, Y.; Pan, C.; Zou, H.-K.; Chu, G.-W.; Arowo, M.; Chen, J.-F. (2015b): Influence of Viscosity on Micromixing Efficiency in a Rotating Packed Bed with Premixed Liquid Distributor. In *J. Chem. Eng. Japan / JCEJ* 48 (1), pp. 72–79. DOI: 10.1252/jcej.14we153.

Zhang, C.; Chu, G.; Luo, Y.; Xiang, Y.; Zou, H.; Chen, J. (2014): Micromixing in rotating packed bed with ceramic foam packing. In *J. Chem. Ind. and Eng.(China)* (8). DOI: 10.3969/j.issn.0438-1157.2014.08.018.

Zhao, H.; Shao, L.; Chen, J.; Zhao, Hong; Shao, Lei; Chen, Jian-Feng (2010): High-gravity process intensification technology and application. In *Chem. Eng. J.* 156 (3), pp. 588–593. DOI: 10.1016/j.cej.2009.04.053.

APPENDIX

A Supporting Information To Chapter 3: Method Development

A.1 The Hägg Diagram and the Pourbaix Diagram

A Hägg diagram gives an overview of the concentration of different species of a chemical compound as a function of a solution's pH value. Fig. 55 shows a Hägg diagram for phosphate.

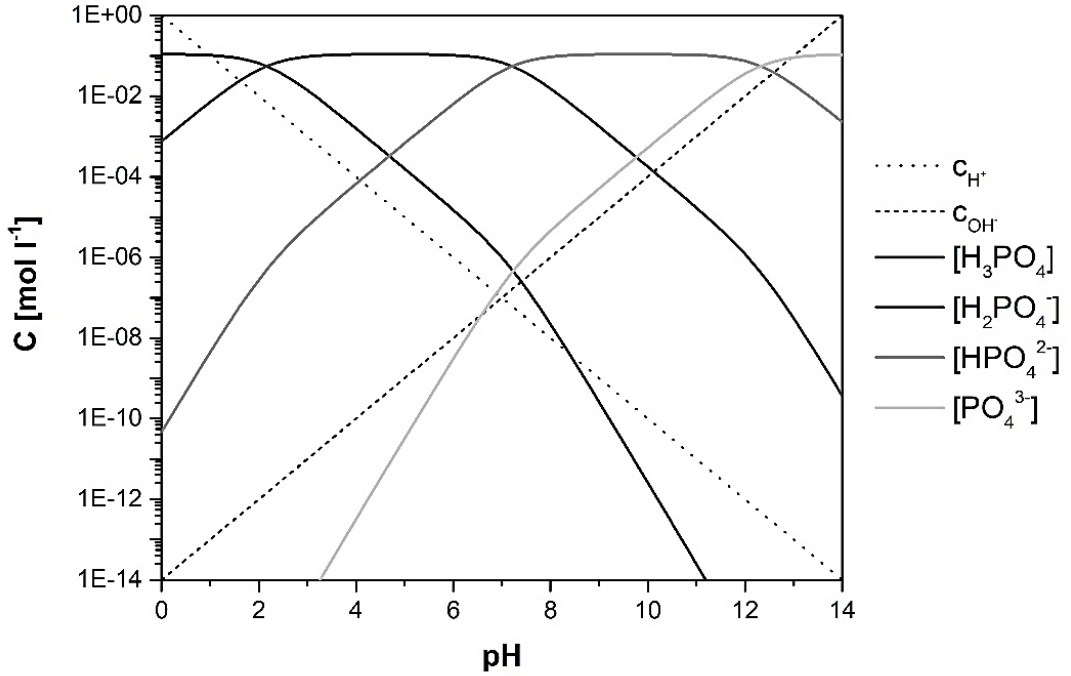

Fig. 55. Hägg diagram: concentration of each phosphate species as a function of the pH value for a total concentration of all phosphate species of 0.11 mol l^{-1}.

In addition, a Pourbaix diagram allows the prediction of species predominant at a given electrode potential and pH. Pourbaix diagrams can be constructed based on the Nernst equation (Eq. (42)).

$$E = E^0 + \frac{RT}{z_e F} * \ln\left(\frac{a_{Ox}}{a_{Red}}\right) \quad (42)$$

where E is the electrode potential, E^0 is the electrode potential against the standard hydrogen electrode, R is the universal gas constant, T is the temperature in Kelvin, z_e

is the number of transferred electrons, F is the Faraday's constant, and a_{Ox} and a_{Red} are the activities of the oxidized and the reduced species, respectively.

Each line in the Pourbaix diagram represents an electrochemical equilibrium and thus a state of equal activities. As an approximation, the involved species' activities can be assumed to be equal to their concentrations (Eq. (43)), although this assumption should be used carefully if the concentrations are above 0.001 mol l^{-1}.

$$E = E^0 + \frac{RT}{z_e F} * \ln\left(\frac{[C][D]}{[A][B]}\right) \tag{43}$$

The reactions involved in the Dushman reaction can be considered as a combination of five half-cell reactions (Fournier et al. 1996b). These half-cell reactions (reactions (vi) to (x)) are summarized in Tab. 3.

Tab. 3. Half-cell reactions involved in the Dushman reaction.

Reaction	Equation	E^0
(vi)	$3\,I^- \rightarrow I_3^- + 2e^-$	0.536 V
(vii)	$I^- + 3\,H_2O \rightarrow IO_3^- + 6\,H^+ + 6\,e^-$	1.085 V
(viii)	$2\,I_3^- \rightarrow 3\,I_2 + 2\,e^-$	0.789 V
(ix)	$I_3^- + 9\,H_2O \rightarrow IO_3^- + 18\,H^+ + 16\,e^-$	1.154 V
(x)	$I_2 + 6\,H_2O \rightarrow 2\,IO_3^- + 12\,H^+ + 10\,e^-$	1.178 V

For example, the according Nernst equation (at 25°C) for reaction (ix) can be given as stated in Eq. (44).

$$E = 1.154 + \frac{8.314 * 298.15}{16 * 96485} * \ln\left(\frac{[IO_3^-]^3[H^+]^{18}}{[I_3^-]}\right) \tag{44}$$

$$= 1.154 + 0.0592 * \frac{18}{16}\ pH + 0.0098 \log\left(\frac{[IO_3^-]^3}{[I_3^-]}\right)$$

As the concentrations are to be equal at equilibrium (see above), they can be substituted by a reference concentration C as shown in Eq. (45).

$$E = 1.154 + 0.0666\,pH + 0.0037 \log\left(\frac{C^3}{C}\right) \tag{45}$$

where C is defined as given in Eqs. (46) – (48) and C_{total} is the total reference concentration of the iodine species in equilibrium.

$$C = [IO_3^-]_{eq} = [I_3^-]_{eq} \quad (46)$$

$$[IO_3^-]_{eq} + [I_3^-]_{eq} = C_{total} \quad (47)$$

$$C = \frac{C_{total}}{2} \quad (48)$$

where $[i]_{eq}$ is the equilibrium concentration of component i. The overall equation system, which is only dependent on the pH value and the reference concentration C, is summarized in Tab. 4 (Fournier et al. 1996b).

Tab. 4. Nernst equations for the iodine-water system.

Reaction	Equation
(vi)	E = 0.536 – 0.0592 log C
(vii)	E = 1.085 – 0.0592 pH
(viii)	E = 0.789 + 0.0296 log C
(ix)	E = 1.154 – 0.0666 pH + 0.0074 log C
(x)	E = 1.178 – 0.0710 pH + 0.0059 log C

The corresponding Pourbaix diagram of the iodine-water system for a total iodine concentration of 0.014 mol l^{-1} is shown in Fig. 56.

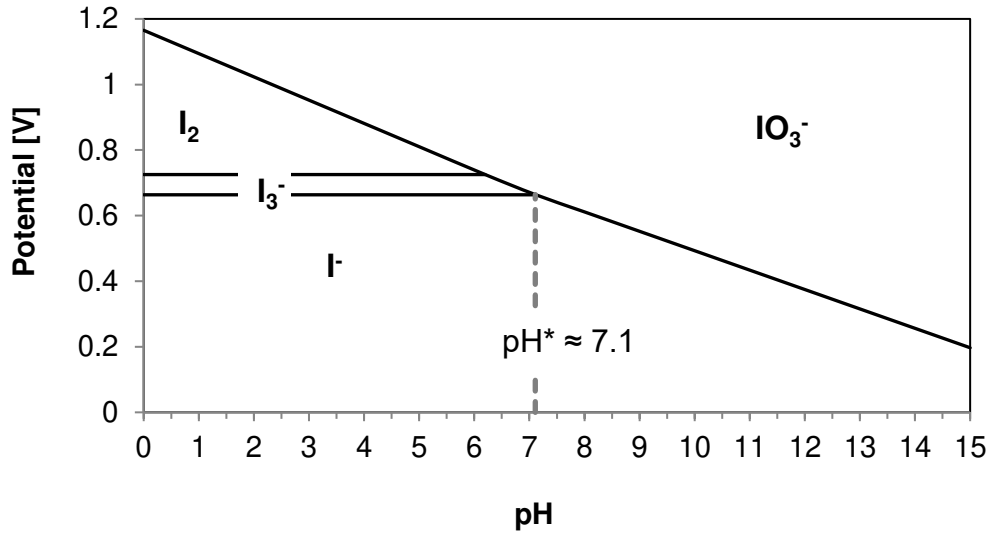

Fig. 56. Example of a Pourbaix diagram of the iodine-water system for a total concentration of all iodine species of 0.014 mol l^{-1}.

A.2 Concentration Overview of All Buffer and Acid Combinations

Tab. 5. Overview of the chemicals' concentrations used in the investigations on the buffer concentration in chapter 3.

Buffer solution [mol l^{-1}]	**Phosphate buffer**	**Boric acid buffer**
K_2HPO_4	0.045/0.09/0.18	-
KH_2PO_4	0.005/0.01/0.02/0.045/0.09	-
$NaOH/H_2BO_3^-$	-	0.045/0.09/0.18
H_3BO_3*		0.005/0.01/0.02/0.045/0.09
KI	0.0117	
KIO_3	0.00233	
Acid solution [mol l^{-1}]		
HCl	0.2	

* Resulting concentration after the addition of NaOH

Tab. 6. Overview of the chemicals' concentrations used in the investigations on the acid concentration in chapter 3 and the determination of Dushman kinetics in Appendix A.5.

Buffer solution [mol l^{-1}]	**Phosphate buffer**	**Boric acid buffer**
K_2HPO_4	0.09	-
KH_2PO_4	0.02	-
$NaOH/H_2BO_3^-$	-	0.09
H_3BO_3*	-	0.09
KI	0.0117	
KIO_3	0.0023	
Acid solution [mol l^{-1}]		
HCl	0.1/0.15/0.2/0.25/0.3/0.35/0.4/0.6***	
K_2SO_4**	0.05/0.1/0.15/0.2	
H_2SO_4	0.05/0.1/0.15/0.2/0.3***/0.4***	
$HClO_4$	0.1/0.2/0.4	

* Resulting concentration after the addition of NaOH; **Only for one part of the HCl experiments; ***Only for the determination of Dushman kinetics

A.3 Ionic Strength of All Buffer and Acid Combinations

Tab. 7. The ionic strength of all buffer and acid combinations investigated in chapter 3.

Combination	Ionic strength (Mixed samples) [mol l^{-1}]	Ionic strength (Only buffer solution) [mol l^{-1}]	Ionic strength (Only acid) [mol l^{-1}]
HCl + boric acid buffer	0.085	0.085	0.200
HCl + phosphate buffer	0.290	0.290	0.200
HCl + K_2SO_4 + phosphate buffer	0.292	0.290	0.800
H_2SO_4 + boric acid buffer	0.086	0.085	0.400
H_2SO_4 + phosphate buffer	0.290	0.290	0.400
$HClO_4$ + phosphate buffer	0.290	0.290	0.200

A.4 Stability of Mixed Samples

The relative OD difference of mixed samples with phosphate buffer and boric acid buffer was investigated over 20 min. While for one part of these samples the cuvette was covered by a cap, the other part was left open, without a cap. The results are shown in Fig. 57.

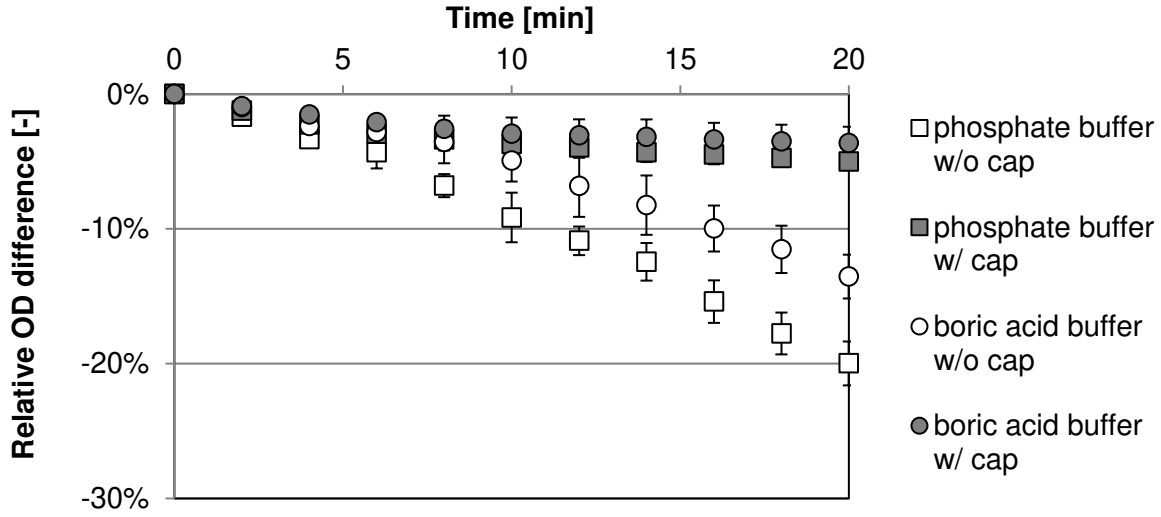

Fig. 57. The relative difference in OD at 353 nm over 20 min for mixed samples with phosphate buffer and boric acid buffer, measured in cuvettes with and without a cap. Phosphate buffer: $[HPO_4^{2-}]$ = 0.09 mol l^{-1} / $[H_2PO_4^-]$ = 0.02 mol l^{-1}. Boric acid buffer: $[H_2BO_3^-]$ = 0.09 mol l^{-1} / $[H_3BO_3]$ = 0.02 mol l^{-1}. Error bars depict the standard deviation.

On the one hand, the (negative) relative OD difference after mixing is constantly increasing for both mixed samples with phosphate buffer and boric acid buffer without a cap (Fig. 57). This increase seems to be larger for phosphate buffer than for boric acid buffer at first sight. However, the initial OD values which were used in Eq. (21) to calculate the relative OD difference were also higher for boric acid (Fig. 9), while the absolute difference was about the same. On the other hand, the curves for mixed samples with phosphate buffer and boric acid buffer samples that were covered with a cap show no such behavior. Instead, the relative OD difference seems to approach a constant value.

A.5 Investigations on the Dushman Kinetics

Information on the kinetics of the Dushman reaction can be obtained by varying the concentration of one reactant while keeping the concentrations of the other components and the mixing setup constant (Kölbl et al. 2013a) and measuring the influence on the resulting triiodide concentration. Therefore, to obtain the partial reaction order of H^+, the raw data from chapter 3 were processed according to the double-logarithmic linearization presented by *Kölbl et al.* (Kölbl et al. 2013a) (Eq. (49)).

$$\log\left(\frac{r}{r_0}\right) = \log\left(\frac{[I_3^-]}{[I_3^-]_0}\right) = c * \log\left(\frac{[H_0^+]}{[H_0^+]_0}\right) \tag{49}$$

where c is the partial reaction order of H^+ and $[i]_0$ is the reference concentration of component i. As factorization of the triiodide concentration, the logarithmic ratio of the optical density (Eq. (4)) can also be used to obtain kinetics data (Eq. (50)).

$$\log\left(\frac{OD}{OD_0}\right) = \log\left(\frac{\varepsilon_N * [I_3^-]}{\varepsilon_N * [I_3^-]_0}\right) = c * \log\left(\frac{[H_0^+]}{[H_0^+]_0}\right) \tag{50}$$

An overview of all concentrations utilized in the investigations on the acid concentration, and the Dushman kinetics, is given in Tab. 6 (Appendix A.2).

The raw data for all combinations of H_2SO_4, HCl, boric acid buffer and phosphate buffer were processed according to Eq. (50) to obtain the partial reaction order of H^+ in the utilized concentration range. The results are shown in Fig. 58 in a double-logarithmic plot. As an example for all combinations, the linear regression curve for H_2SO_4 and the boric acid buffer is presented.

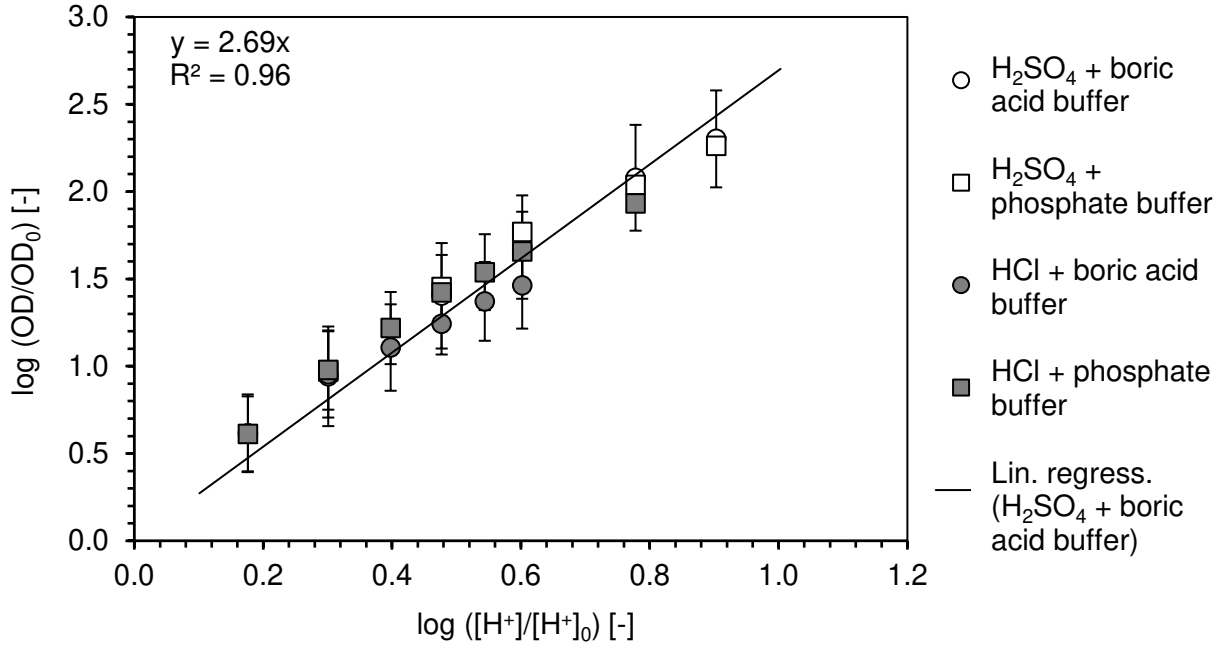

Fig. 58. Double-logarithmic plot of log (OD/OD_0) as function of log ($[H^+]/[H^+]_0$). Linear regression for H_2SO_4 + boric acid buffer. Error bars depict the propagated standard deviation.

Furthermore, the partial reaction order of H^+ was calculated for all investigated combinations of acid and buffer (Tab. 8). As denoted, a mean partial reaction order of H^+ of 2.68 ± 0.03 is obtained. For comparison, values from *Guichardon et al.* (Guichardon et al. 2000) (unbuffered Dushman reaction) and *Kölbl et al.* (Kölbl et al. 2013a; Kölbl et al. 2013b) (Villermaux-Dushman protocol), which were also obtained by linear regression based on results for the optical density, are additionally presented in Tab. 8.

As can be obtained from Tab. 8, the kinetics results of this thesis are not in agreement with the literature values, which themselves also do not provide a consistent number for the partial reaction order of H^+. While *Kölbl et al.* obtained two different partial reaction orders, both lower than those for the unbuffered reaction, the results in this thesis correspond to a partial reaction order of H^+ that is higher than that for the unbuffered system. These observations can be explained as follows.

Tab. 8. Partial reaction order of H^+ obtained by linear regression for log (OD/OD_0).

Combination	**Partial reaction order of H^+ (linear fit for log (OD/OD))**
This thesis	
HCl + boric acid buffer (this chapter)	2.62
HCl + phosphate buffer (this chapter)	2.77
H_2SO_4 + boric acid buffer (this chapter)	2.69
H_2SO_4 + phosphate buffer (this chapter)	2.70
$HClO_4$ + phosphate buffer (this chapter)	2.64
Ø (this chapter)	2.68 ± 0.03 (≅ 2.7)
Literature	
H_2SO_4 (unbuffered) (Guichardon et al. 2000)	1.90 (≅ 2.0)
H_2SO_4 /$HClO_4$ + boric acid buffer (Kölbl et al. 2013b)	1.34/1.32 (≅ 1.3)
H_2SO_4/$HClO_4$ + boric acid buffer (Kölbl et al. 2013a)	0.62/0.57 (≅ 0.6)

First, the underlying relationship between the characteristic reaction time scale t_r and the characteristic mixing time scale t_m must be taken into consideration. The reaction rate is controlled by intrinsic kinetics without the influence of mixing if $t_m < t_r$, and controlled or influenced by mixing and mass transfer when $t_m > t_r$ (Zhao et al. 2010; Bourne 2003). Therefore, the reaction order also becomes a function of the mixing efficiency if $t_m > t_r$, and only an apparent reaction order is obtained. As the Villermaux-Dushman protocol is by definition used to investigate imperfect mixing processes, the obtained (apparent) reaction orders are a function of the applied hydrodynamics. Therefore, *Kölbl et al.* obtained different partial reaction orders in a stirred tank reactor (Kölbl et al. 2013a) and a cyclone type mixer (Kölbl et al. 2013b). In contrast, in the unbuffered system of *Guichardon et al.* (Guichardon et al. 2000), the characteristic mixing time scale was in the range of 10^0 s, while the characteristic reaction time scale was in the range of 10^2 s. Therefore, it can be assumed that the values obtained by *Guichardon et al.* are very close to the actual partial reaction order of H^+.

The difference in deviation for a buffered system between this thesis and the results of *Kölbl et al.* can further be explained by a different experimental procedure. To obtain the partial reaction order of H^+, *Kölbl et al.* (Kölbl et al. 2013a; Kölbl et al. 2013b) varied the NaOH/H_3BO_3 concentration by the same factor as the acid concentration but left the

concentrations of iodide and iodate unchanged; this was done “to keep the iodine-active compartments constant” (Kölbl et al. 2013a). However, with respect to the stoichiometric ratio of reaction (i) and (ii), such an approach exaggerates the influence of the neutralization reaction (Commenge and Falk 2011). Instead, an attenuation effect occurs. Due to this attenuation, significantly lower iodine concentrations are obtained than it would be the case for a stoichiometrically increased buffer concentration. This effect is amplified with increasing acid concentrations and thus over-stoichiometrically increasing buffer concentrations. Consequently, also the (apparent) partial reaction order is remarkably lower than it would be in a system without attenuation.
Unlike in the work of *Kölbl et al.*, no adjustment of the buffer concentration was implemented in this thesis. Therefore, the relative attenuation of the Dushman reaction due to the presence of buffer ions decreases with an increasing acid concentration, and higher optical densities than for a system with the adjustment of the buffer concentration are obtained. Consequently, also the apparent reaction order is higher than that for an adjusted system (e.g., Kölbl et al. (Kölbl et al. 2013a)) or a system without any competing neutralization reaction (e.g., Guichardon et al. (Guichardon et al. 2000)).

Overall, it can be concluded that no buffer adjustment leads to an exaggerated partial reaction order of H^+ of 2.7 (this thesis) in comparison to the unbuffered system (~2.0, *Guichardon et al.*). Therefore, future investigations of concentrations relevant to mixing studies should be conducted with a stoichiometrically adjusted buffer solution, whereas a partial reaction order of 2.0 can be assumed to be close to the real value for H^+.

B Supporting Information To Chapter 4: Literature Study

B.1 Tabular Data on the Analyzed Publications

Tab. 9: Overview of analyzed operational parameter ranges. Publications sorted by authors and year of publication.

Publication		Rotational speed [rpm]	Total liquid flow rate [l h^{-1}]	Volumetric ratio [-]	Viscosity [mPa s]
Chen et al. (Chen et al. 2004)		600-1500	20.0-48.5	7.0	1.0-4.0
Chen et al. (Chen et al. 2006)	RPB-1	600-1500	34.3	7.0	1.0
	RPB-2	600-2300	15.5-54.0	11.0	1.0
Yang et al. (Yang et al. 2005)		200-1200	410.0-615.0	7.2-12.0	1.0
Yang et al. (Yang et al. 2009)		200-1500	200.0-546.5	7.2-12.0	1.0
Yang et al. (Yang et al. 2015b)		200-1600	5.0-50.0	9.0-15.0	1.0-220.0
Chu et al. (Chu et al. 2015)		500-2900	13.0-70.0	10.0-18.0	1.0
Jiao et al. (Jiao et al. 2012)		600-1500	48.0-160.0	1.0-15.0	5.0-70.0

Tab. 10. Overview of tangential velocities at the inner packing radius r_i.

Publication		Rotational speed [rpm]	Inner packing radius [mm]	Outer packing radius [mm]	Minimum tangential velocity at r_i [m s^{-1}]	Maximum tangential velocity at r_i [m s^{-1}]
Chen et al. (Chen et al. 2004)		600-1500	50	60	3.14	7.85
Chen et al. (Chen et al. 2006)	RPB -1	600-1500	10-50	20-60	0.63	7.85
	RPB -2	600-2300	20	40	1.26	4.82
Yang et al. (Yang et al. 2005)		200-1200	30	223	0.63	3.77
Yang et al. (Yang et al. 2009)		200-1500	30	223	0.63	4.71
Yang et al. (Yang et al. 2015b)		200-1600	20	40	0.42	3.35
Chu et al. (Chu et al. 2015)		500-2900	17.5	40	0.92	5.31
Jiao et al. (Jiao et al. 2012)		600-1500	30	50	1.88	4.71

Tab. 11. Overview of the RPB design variation used for the investigation of micromixing in the analyzed publications.

Publication		Rotational axis	Inner/ Outer packing radius [mm]	Axial packing height [mm]	Packing type/ material	Packing porosity
Chen et al. (Chen et al. 2004)		vertical	50/60	20	Stainless steel wire mesh (Diameter: 0.22 mm)	95 %
Chen et al. (Chen et al. 2006)	RPB -1	vertical	10-50/ 20-60	20	Stainless steel wire mesh (not specified)	not specified
	RPB -2	vertical	20/40	20	Stainless steel wire mesh (not specified)	not specified
Yang et al. (Yang et al. 2005)		vertical	30/223	50	Wire mesh (Cross section: 0.3 mm × 0.7 mm = 0.021 mm²)	97 %
Yang et al. (Yang et al. 2009)		vertical	30/223	50	Wire mesh (Cross section: 0.3 mm × 0.7 mm = 0.021 mm²)	97 %
Yang et al. (Yang et al. 2015b)		horizontal	20/40	20	Stainless steel wire mesh (Diameter: 0.22/0.3/0.5/ 0.8 mm)	not specified
Chu et al. (Chu et al. 2015)		horizontal	17.5/40	19	Stainless steel wire mesh	not specified
					Nickel foam	5-50 ppi
					Surface-modified nickel foam	not specified
Jiao et al. (Jiao et al. 2012)		horizontal	30/50	30	Stainless steel wire mesh (Diameter: 0.3 mm)	96 %

Tab. 12. Overview of types of liquid distribution in the analyzed publications.

Publication		Type of liquid distribution	Diameter of buffer injection [mm]	Diameter of acid injection [mm]	Maximum outlet velocity buffer [m s^{-1}]	Maximum outlet velocity acid [m s^{-1}]
Chen et al., (Chen et al. 2004)		2 distributor pipes	3 × 0.5	3 × 0.5	20.0	2.9
Chen et al., (Chen et al. 2006)	RPB -1	2 distributor pipes	3 × 0.5	3 × 0.5	14.2	2.0
	RPB -2	2 distributor pipes	3 × 0.5	3 × 0.5	23.3	2.1
Yang et al., (Yang et al. 2005)		2 distributor pipes	4 × 3.0	3 × 1.5	5.3	3.9
Yang et al., (Yang et al. 2009)		Premixed distributor; pipe angle β: 105 – 120°	1 × 6.0		5.4	
Yang et al., (Yang et al. 2015b)		Premixed distributor; pipe angle β: 90°	1 × 2.0		4.4	
Chu et al., (Chu et al. 2015)		Premixed distributor; pipe angle β: 90°	1 × 3.0		2.8	
Jiao et al., (Jiao et al. 2012)		2 impinging streams; impinging distance 3 mm; impinging angle: 180°	Not specified		n/a	

B.2 Literature Results on the Influence of Viscosity on the Segregation Index

Many liquid phase processes in the chemical industry involve the mixing of viscous liquids. Especially for processes with undesired side reactions, a preferably fast and uniform distribution of the components is crucial. Therefore, the influence of the viscosity on the micromixing results is an important field of investigation. The reported viscosities range from 1 mPa s for pure water to 4 mPa s (Chen et al. 2004), 70 mPa s (Jiao et al. 2012) and up to 220 mPa s (Yang et al. 2015b). In all cases, the increased viscosities were adjusted by using a water-glycerol mixture.

It was unanimously reported that the segregation index increased with an increasing viscosity (Chen et al. 2004; Jiao et al. 2012; Yang et al. 2015b). This is to be expected, as higher viscosities increase the average size of liquid fragments, decrease the rate of deformation and shrinkage of liquid elements for a given rate of energy dissipation, and decrease the coefficients of molecular diffusion (Yang et al. 2015b; Baldyga and Bourne 1984). Furthermore, it was found that the influence of the rotational speed on the segregation index is higher at higher viscosities, independent of the liquid flow rate (Yang et al. 2015b) and the liquid distribution method, be it distributor pipe (Chen et al. 2004), premixed distributor (Yang et al. 2015b), or impinging stream distribution (Jiao et al. 2012). This demonstrates the elevated importance of higher shear forces – as imposed by a faster rotating packing – for the mixing of highly viscous liquids in RPBs. However, the relative influence of the viscosity on the segregation index also decreased for increasing viscosities and increasing rotational speed (Jiao et al. 2012; Chen et al. 2004; Yang et al. 2015b).

B.3 Correlations between Segregation Index and Operational Parameters

Only a few authors have published model correlations and model parameters for micromixing in RPBs. This could be due to the complexity and the peculiarities of the Villermaux-Dushman protocol, e.g., the lack of comparability of results from different concentration sets, which makes it difficult to derive comprehensive equations for a variety of operational and design parameters. However, two correlations by *Chen et al.* (Chen et al. 2004) are presented below.

By considering the rotational speed ω, the total liquid flow rate $\dot{V}_L$, and the dynamic viscosity μ, the correlation shown in Eq. (51) was obtained by *Chen et al.* for a volumetric ratio of 7 (Chen et al. 2004). The segregation indices presented by the authors could be described by this equation with an accuracy of ± 30 %.

$$X_S = 2.2 * \omega^{-0.64} * \dot{V}_L{}^{-0.64} * \mu^{0.45} \tag{51}$$

Furthermore, the authors found that the segregation index X_S was directly related to the liquid-phase mass transfer coefficient K_La for dissolved oxygen stripping, as described by Eq. (52) (Chen et al. 2004). This implies that the mass transfer resistance may be reduced with increasingly fast micromixing, which would also be expected for an increasing rate of energy dissipation.

$$X_S = \frac{0.01}{K_L a} \tag{52}$$

C Supporting Information To Chapter 5: Operation, Design, and Modeling

C.1 Equipment Information

Tab. 13. Overview of nozzles used in chapter 5.

Nozzle type	δ	Number of holes	A_{outlet} [mm²]	Type
Flat fan nozzles				
FF-I	140°	1	1.8	686.528
FF-II	140°	1	0.8	686.408
FF-III	140°	1	0.5	686.368
Full jet nozzles				
FJ-I	90°	9	5.7	9HFJ
FJ-II	90°	3	4.6	3HFJ
FJ-III	0°	1	2.8	SSH
FJ-IV	0°	1	0.8	1HFJ

Tab. 14. Details on the RPB design variants used in chapter 5. Details on the Andritz RPB design are given in Tab. 24.

RPB design	RPB 1.0 a / b	RPB 2.0
Manufacturer	Omnikon, Łódź, Poland	Omnikon, Łódź, Poland
Rotor		
Rotor type	Two-plate rotor with eye ring	Two-plate rotor with eye ring
Rotor outer diameter	600 mm / 400 mm	600 mm
Eye ring		
Eye ring type	Squares, 90 % free cross-sectional area	Squares, 90 % free cross-sectional area
Eye ring inner diameter	136 mm	152 mm
Eye ring outer diameter	146 mm	166 mm
Eye ring radial depth	5 mm	7 mm

Tab. 15. Details on the packing configurations used in chapter 5. The respectively corresponding RPB configuration can be obtained from Tab. 14.

Packing configurations				
Packing	A / B	C.1 / D / E	C.2	F
Used with RPB design	RPB 1.0 a / RPB 1.0 b	RPB 2.0	RPB 2.0	RPB 1.0 a
Packing type	Nickel-chromium metal foam (NCX1116)	Nickel-chromium metal foam (NCX1116)	Nickel-chromium metal foam (NCX0610)	Knit mesh
Specific surface area packing	1000 $m^2\ m^{-3}$	1000 $m^2\ m^{-3}$	500 $m^2\ m^{-3}$	n/A
Voidage packing	92.0 %	92.0 %	92.0 %	86.7 %
Average pore size	1.4 mm	1.4 mm	2.3 mm	n/a
Packing outer diameter	580 mm / 380 mm	200 mm / 300 mm / 580 mm	200 mm	560 mm
Packing inner diameter	146 mm	166 mm	166 mm	146 mm
Radial packing depth	217 mm / 117 mm	17 mm / 67 mm / 207 mm	17 mm	107 mm
Axial packing height	10 mm	10 mm	10 mm	10 mm

Tab. 16. The accuracy of the equipment used in chapter 5.

Equipment	**Type**	**Accuracy**	**Unit**
Platform scale	DS 65K0.5 (KERN & Sohn GmbH)	0.5	g
Chemicals scale	NewClassic MF (Mettler Toledo)	0.001	g
Digital thermometer	Digitalthermometer (VWR Chemicals)	0.1	K
UV-vis spectrometer	UVmini-1240 (Shimadzu Corporation)	0.001	a.u.

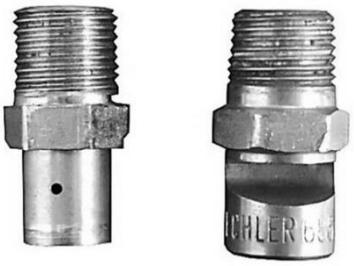

Fig. 59. Picture of an FJ-type nozzle (left) and an FF-type nozzle (right).

Fig. 60. RPB rotor with an outer diameter of 600 mm.

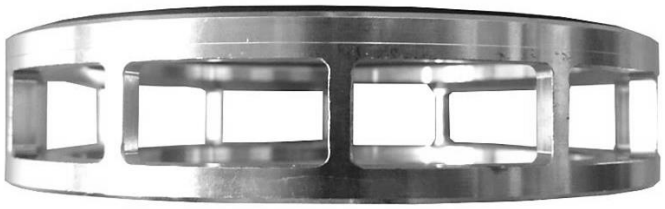

Fig. 61. Picture of the eye ring used to separate the two rotor plates and support the packing.

C.2 RPB Power Consumption

The total power consumption for each experimental run consisted of the power consumption of the pumps and the power consumption of the RPB. The average power consumption of the RPB 1.0 design at 100 l h^{-1} and 1200 rpm was 556 W. This power consumption consists of the power consumption due to friction in the bearings and sealings and the power consumption due to the acceleration of liquid (ζ_L). However, the latter is almost negligible and can be calculated according to *Neumann et al.* ((Neumann et al. 2018b), Eq. (53)) to be 17.2 W, contributing 3.1 % of the power consumption of the RPB and 2.0 % of the total power consumption.

$$\zeta_L = 0.5 * \rho_L * \dot{V}_L * (r_O * \omega)^2 \tag{53}$$

where ρ_L is the density of the liquid, $\dot{V}_L$ is the total liquid flow rate, r_o is the outer radius of the packing, and ω is the rotational speed.

From *Neumann et al.*'s measurements in the RPB 1.0 design, it is further known that the overall electric power consumption P increases linearly with an increasing rotational speed according to Eq. (54) (Neumann et al. 2018b).

$$P = 27.6 * \omega \tag{54}$$

The resulting total power consumption, the power consumption of the RPB, the power consumption of the bearings, and the power consumption due to the acceleration of liquid are given for 100 l h^{-1} and 1200 rpm in Fig. 62. The power consumption of the two pumps together was 300 W, contributing 35.0 % of the total power consumption.

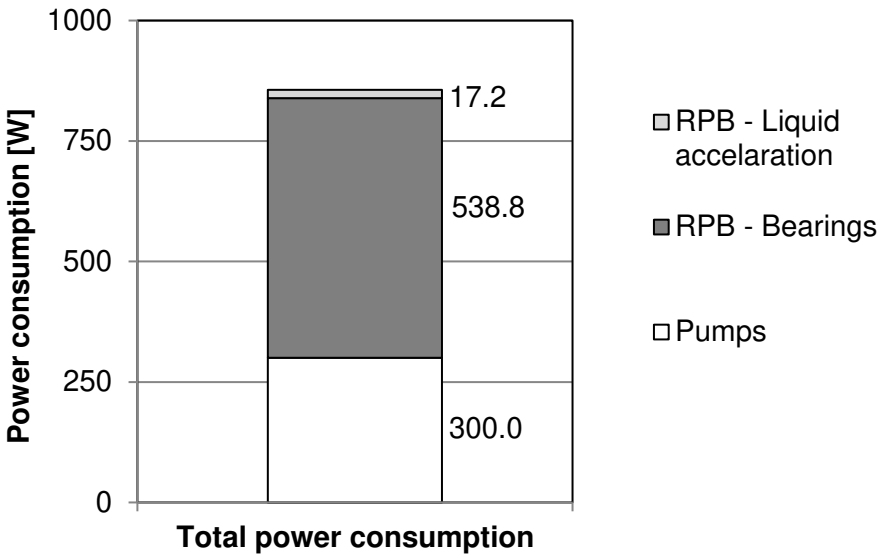

Fig. 62. The total power consumption, the power consumption of the pumps, the power consumption of the RPB, the power consumption of the bearings, and the power consumption due to the acceleration of liquid at 100 l h^{-1} and 1200 rpm.

C.3 Villermaux-Dushman Protocol

The chemical concentrations in the buffer solution and the acid solution used for the Villermaux-Dushman protocol experiments in chapter 5.4 are summarized in the form of concentration sets in Tab. 17.

Tab. 17. Overview of the concentration sets used in chapter 5.4.

Concentration set	**Buffer solution**				**Acid solution**	
	H_3BO_3 [mol l^{-1}]	NaOH [mol l^{-1}]	KI [mol l^{-1}]	KIO_3 [mol l^{-1}]	HCl [mol l^{-1}]	H_2SO_4 [mol l^{-1}]
FVT-a	0.110	0.090	0.0117	0.00233	0.080	-
FVT-b					0.160	-
FVT-c					0.240	-
FVT-d					-	0.080
FVT-e					-	0.120
1SC (2b)	0.045	0.045	0.0160	0.00318	-	0.015
2SC (1b)	0.090	0.090	0.0320	0.00636	-	0.030

For experiments in the RPB 1.0 design, the acid solution was prepared with 1 M HCl solution from Carl Roth (Karlsruhe, Germany) and deionized water for parameters sets FVT-a/b/c, and with 0.5 M (1 N) H_2SO_4 solution from VWR Chemicals (Radnor, USA) and purified water for parameter sets FVT-d/e and 1SC/2SC. To prepare the buffer solution, purified water, and 4 % boric acid solution from VWR Chemicals (Radnor, USA) were mixed. Afterward, solid NaOH from Carl Roth (Karlsruhe, Germany) was dissolved in this solution before adding solid KI from Carl Roth (Karlsruhe, Germany) and solid KIO_3 from PanReac AppliChem (Darmstadt, Germany) under constant stirring. For experiments in the RPB 2.0 design, all chemicals were provided by CHEMSOLUTE (Th. Geyer GmbH & Co. KG, Renningen, Germany) with a minimum purity of 99 %. The rest of the procedure was identical. Before the start of all experiments, it was verified that all solids were fully dissolved.

Based on the mixed samples' absorption value at 353 nm, the triiodide concentrations in each sample and the corresponding segregation index were determined according to chapters 3.2.1 and 4.2.2.

C.4 Additional Data

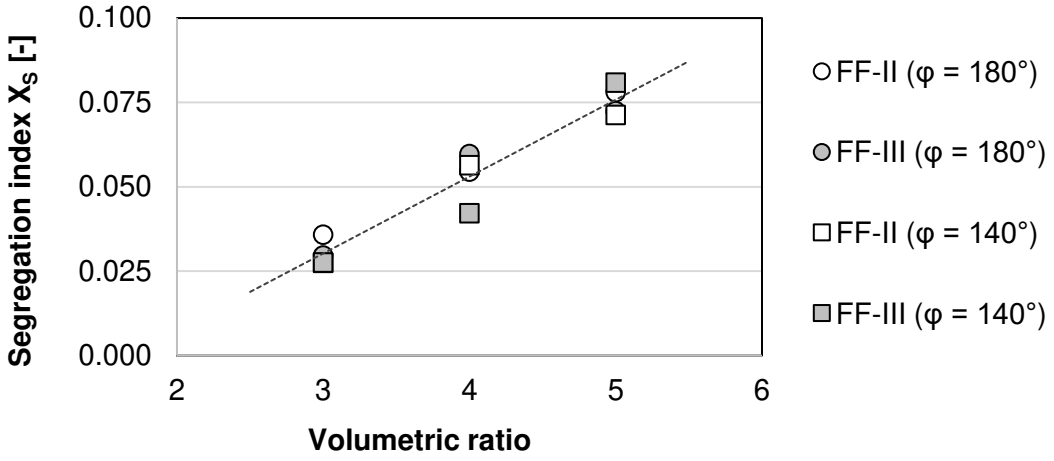

Fig. 63. Segregation indices for the nozzles FF-II and FF-III, at volumetric ratios between 3 and 5 and a nozzle orientation of φ = 140° (adjacent distribution) and φ = 180° (opposite distribution). Packing configuration A, 60 l h^{-1}, 600 rpm, concentration set FVT-a (acid concentration volumetrically adapted to be constant after mixing). Linear regression is given for all data points together.

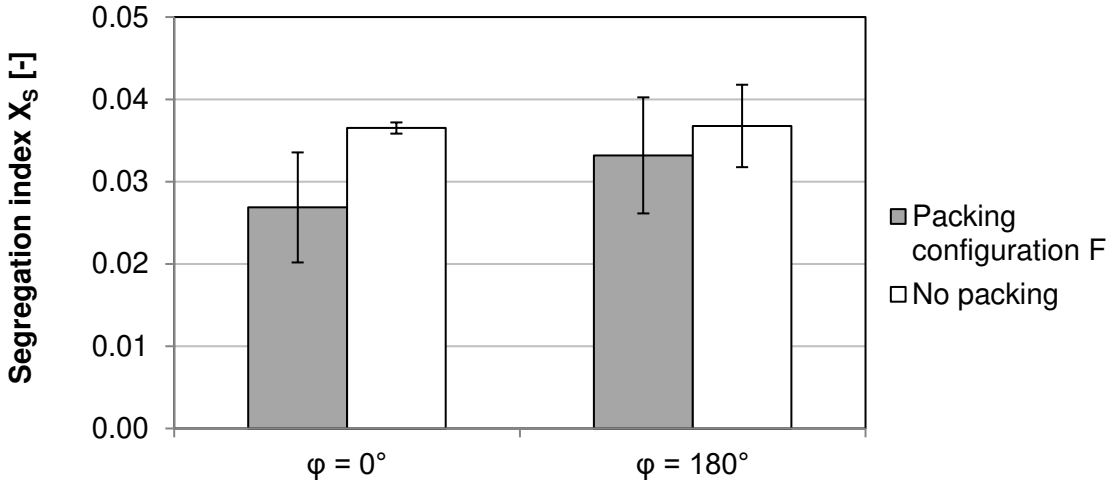

Fig. 64. Segregation indices for a volumetric ratio of 6 and a nozzle orientation of φ = 0° (overlapping distribution) and φ = 180° (opposite distribution) for packing configuration F and a rotor without packing. FF-II nozzles, 60 l h^{-1}, 600 rpm, concentration set FVT-a. Error bars depict the sample standard deviation.

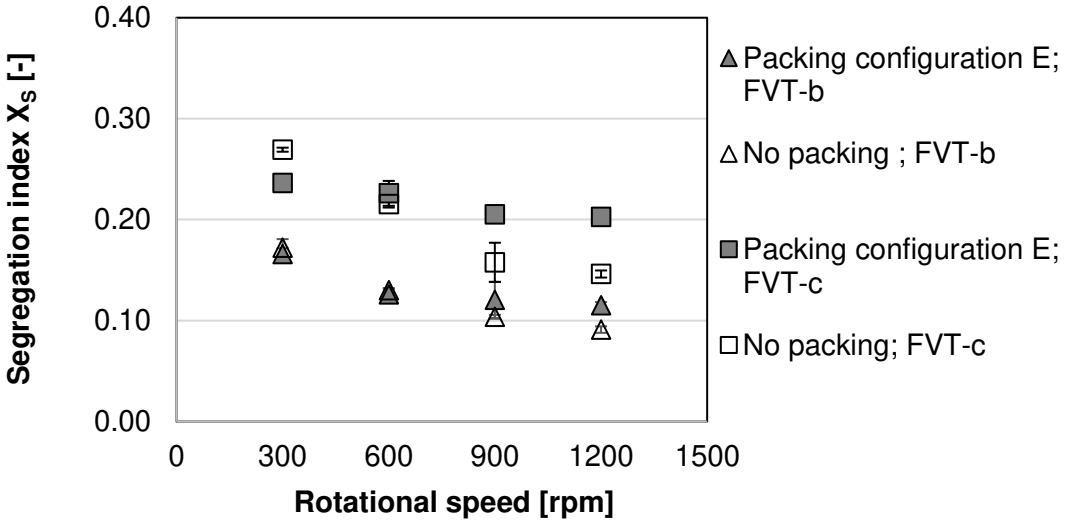

Fig. 65. Segregation indices obtained with concentration sets FVT-b and FVT-c as for packing configuration E and a rotor without packing as a function of the rotational speed. FF-I/FF-III nozzles, opposite liquid distribution (φ = 180°). 140 l h^{-1}, volumetric ratio: 8. Error bars depict the sample standard deviation.

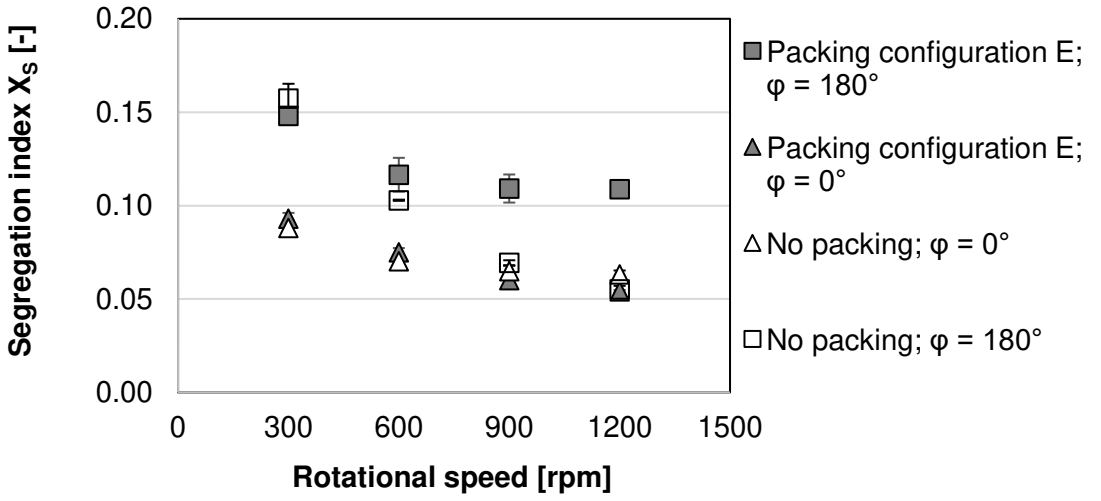

Fig. 66. Segregation indices obtained with concentration set FVT-e for an overlapping (φ = 0°) and an opposite (φ = 180°) liquid distribution and packing configuration E and a rotor without packing, respectively, as a function of the rotational speed. FF-I/FF-III nozzles, 140 l h^{-1}, volumetric ratio: 8. Error bars depict the sample standard deviation.

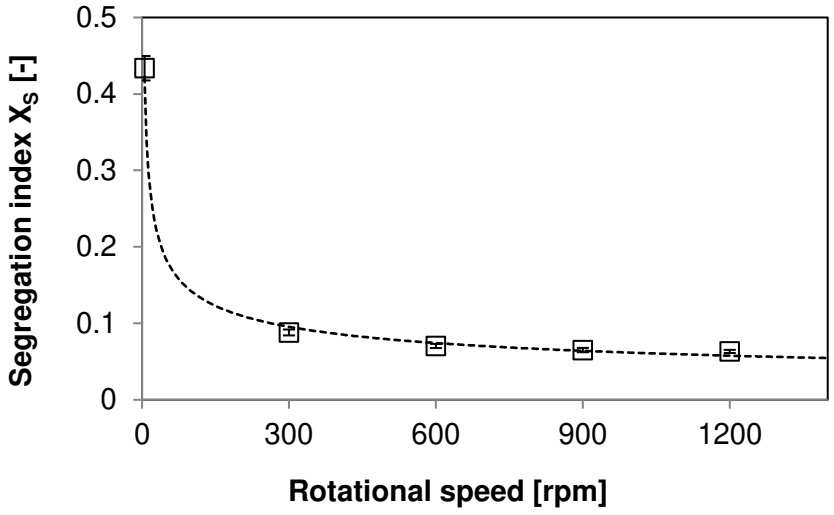

Fig. 67. Segregation indices obtained for a rotor without packing as a function of the rotational speed between 0 rpm and 1200 rpm. FF-I/FF-III nozzles, overlapping liquid distribution (φ = 0°). 140 l h^{-1}, volumetric ratio: 8, concentration set FVT-e. Error bars depict the sample standard deviation.

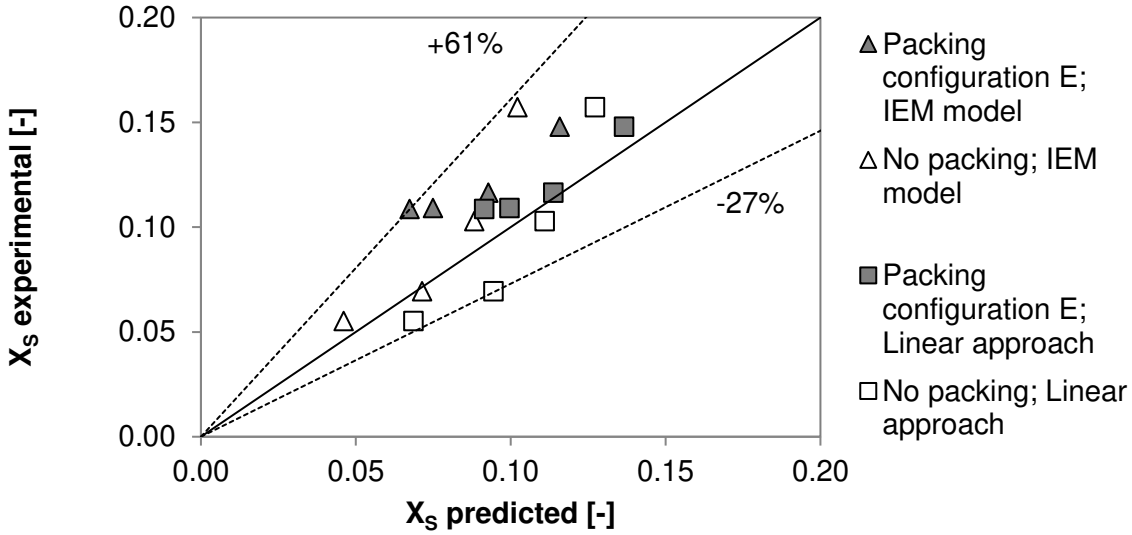

Fig. 68. Parity plot for experimentally measured X_S values (Fig. 29, FVT-e) and X_S values predicted by the IEM model and the linear approach of the incorporation model (based on results shown in Fig. 28, FVT-d). The underlying experimental X_S values correspond to a decreasing rotational speed from left to right. Dotted lines are given to denote the positive and negative deviation from parity. The values for the IEM model were calculated based on the equations given in Appendix C.6.

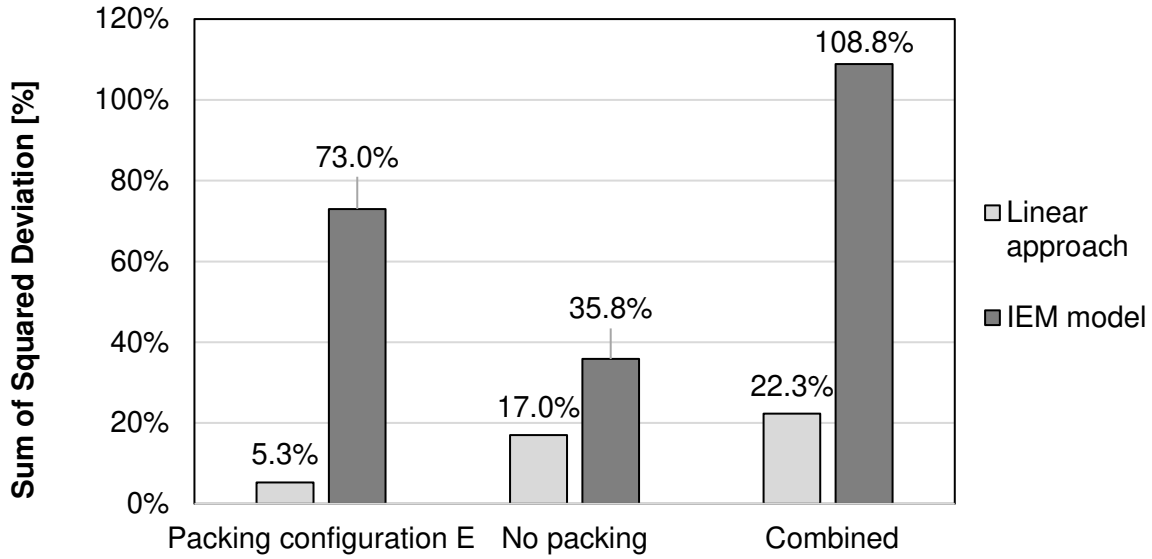

Fig. 69. Sum of squared deviation between experimentally measured X_S values (Fig. 29, FVT-e) and values predicted by the IEM model and the linear approach of the incorporation model (based on results shown in Fig. 28, FVT-d) for packing configuration E, a rotor without packing, and the combination of both values.

C.5 Residence Time Distributions

By means of the residence time distribution (RTD), the evolution of a reactant's concentration can be described over time. Usually, the RTD is expressed in form of the differential distribution curve (Eqs. (55) – (56)), also known as E function, which describes the concentration-time profile normalized over the area under the concentration curve, and the F function (Eq. (57)), which describes the cumulative distribution curve. (Stenstrom and Rosso 2003; Paul et al. 2004)

$$E(t) = \frac{C(t)}{\int_0^\infty C(t)dt} \tag{55}$$

$$\int_0^\infty E(t)\ dt = 1 \tag{56}$$

$$F(t) = \int_0^t E(t)\ dt = \frac{\int_0^t C(t)\ dt}{\int_0^\infty C(t)\ dt} \tag{57}$$

where C(t) is the concentration of the tracer at time t. Based on the E function, also the average residence time ($\bar{\tau}$) between the beginning of the setup and the probing position can be calculated (Eq. (58)). Furthermore, based on the F function, the median of the RTD (t_{50}), the 90th percentile of the RTD (t_{90}), and the complete residence time (t_{100}; here: F > 0.999) can be determined.

$$\bar{\tau} = \int_0^\infty t\,E(t)\,dt \tag{58}$$

To realize experiments on the RTD in the RPB 1.0 and the RPB 2.0 design, the space-time between rotor eye and liquid outlets was considered and determined by means of the Villermaux-Dushman protocol: RPB and buffer solution pump were started and adjusted to a setpoint. Then, 0.100 l of acid were added quickly into the rotor eye to create a tracer pulse. Simultaneously, samples were taken at the liquid outlets and analyzed by means of UV-spectroscopy continuously until the absorption value of the samples returned to zero. In both RPBs, the RTD was measured twice. For the RTD experiments in the RPB 1.0 design, a rotational speed of 600 rpm and a buffer flow rate of 54.0 l h^{-1} were used. The RPB was equipped with a 600-mm rotor, packing configuration A, and an FF-III nozzle for the buffer. For the RTD experiments in the RPB 2.0 design, a rotational speed of 1200 rpm and a buffer flow rate of 126.6 l h^{-1} were used to reflect an improved design and operation, as further discussed in chapter 7.

The RPB was equipped with a 600-mm rotor, packing configuration E, and an FF-I nozzle for the buffer.

The E functions and F functions obtained for the RPB 1.0 and the RPB 2.0 design according to Eqs. (55) and (57) are shown in Fig. 70 and Fig. 71, respectively. The corresponding RTD parameters are shown in Fig. 72 as mean values with sample standard deviation.

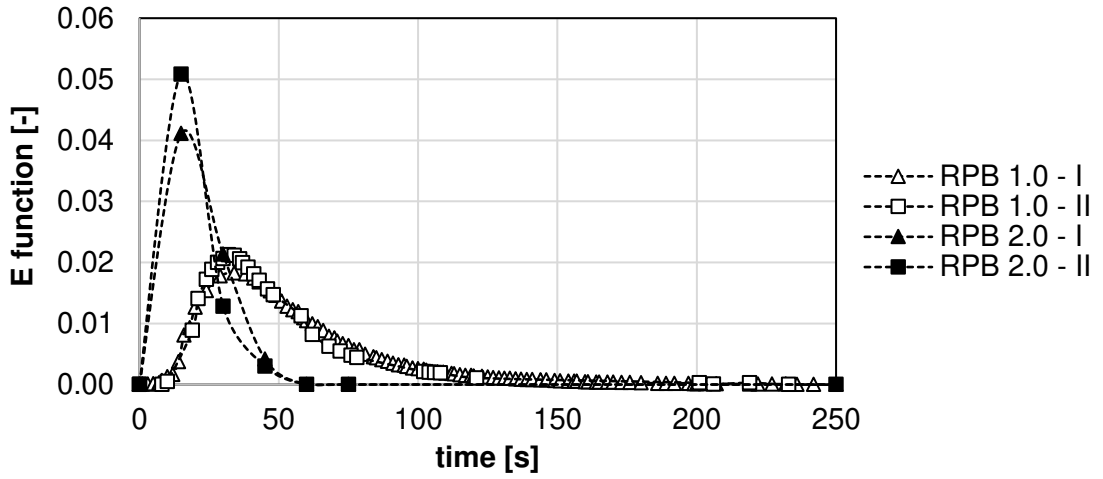

Fig. 70. E function for the RTD experiments in the RPB 1.0 and the RPB 2.0 design.

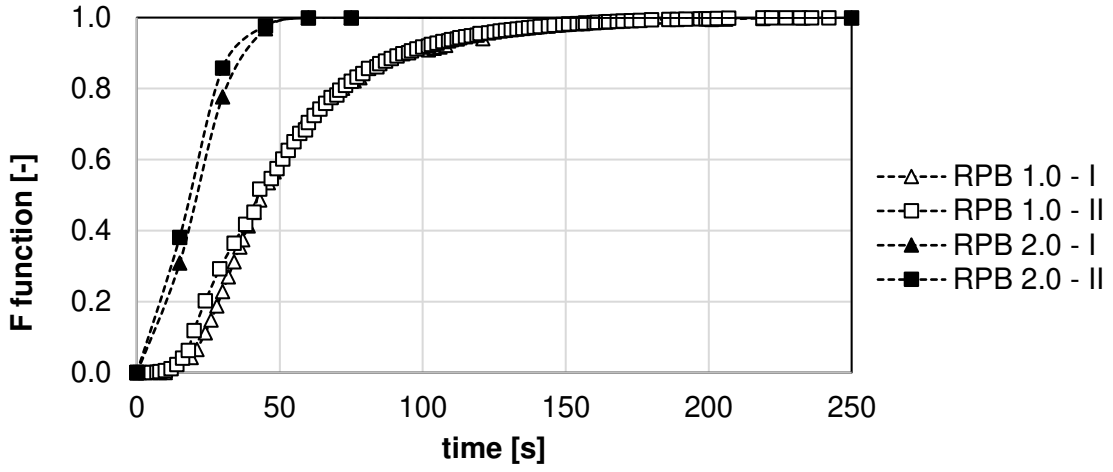

Fig. 71. F function for the RTD experiments in the RPB 1.0 a and the RPB 2.0 design.

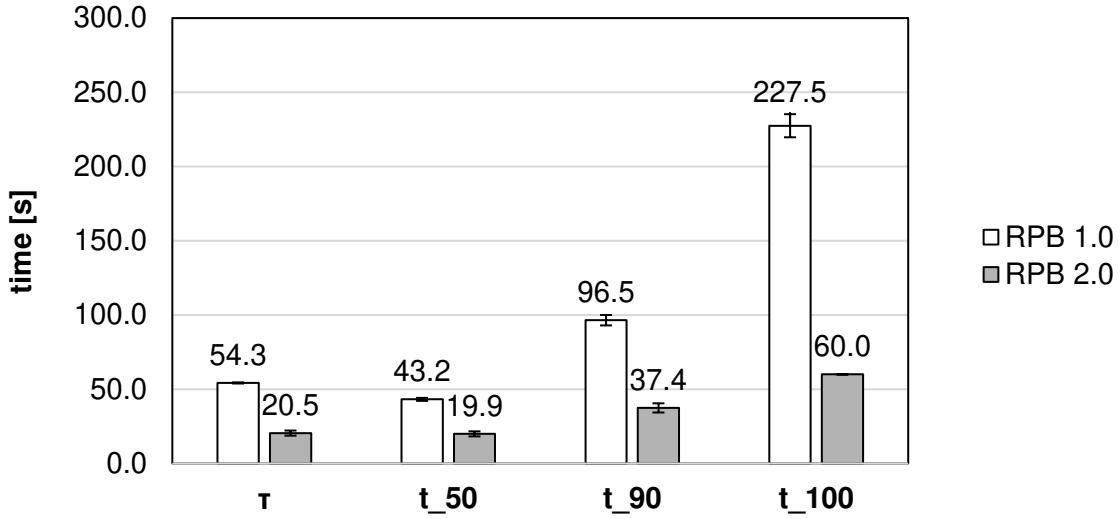

Fig. 72. RTD parameters for the RPB 1.0 and the RPB 2.0 design. Displayed are the average values obtained from the runs shown in Fig. 70 and Fig. 71. Error bars depict the sample standard deviation.

As shown in Fig. 70 to Fig. 72, a very broad RTD is obtained for the RPB 1.0 design. In particular, a long tailing period can be observed. Thus, 50 % of the tracer has left the RPB within the first 43.2 s, on average, while some tracer molecules stay in the RPB 1.0 for up to 227.5 s. This leads to an average hydraulic residence time of 54.3 s. This observation can be explained by the influence of three design parameters on the RTD. First, the distance between the rotor and RPB casing is comparatively large in the RPB 1.0 design (Fig. 5) so that droplets are washed off the casing's surface slowly. Second, the bottom of the RPB casing is flat and partially uneven, so that liquid can stand on the casing bottom for a longer time without flowing into the liquid outlets or form liquid pockets. Third, the liquid outlets are relatively small in comparison to the surface area of the casing bottom and the size of the rotor (Chapter 2.4.1).

In contrast, the RTD curves for the RPB 2.0 design (Fig. 6) reflect an improved RPB design and operation (Chapter 7). As can be obtained from Fig. 70 to Fig. 72, the tailing is significantly reduced so that all liquid elements leave the RPB within 60.0 s, on average. This was achieved by a smaller distance between the rotor and RPB casing, as well as an inclined casing bottom with significantly larger liquid outlets (Chapter 2.4.2).

C.6 Modeling Equations

In this chapter, the model equations of the incorporation model and the IEM model are presented in more detail.

With respect to the incorporation model, *Fournier, Falk, and Villermaux* expressed the concentrations of each species j in the reactional volume 2 (Eq. (35)) in the following set of equations (Eqs. (59) – (63)) for the Villermaux-Dushman protocol (Fournier et al. 1996a):

$$\frac{dn_{H^+}}{dt} = -r_1 V_2 - 6r_2 V_2 \tag{59}$$

$$\frac{dn_{I^-}}{dt} = C_{I_0^-}\frac{dV_2}{dt} - 5r_2 V_2 - r_3 V_2 \tag{60}$$

$$\frac{dn_{IO_3^-}}{dt} = C_{IO_{3,0}^-}\frac{dV_2}{dt} - r_2 V_2 \tag{61}$$

$$\frac{dn_{I_2}}{dt} = 3r_2 V_2 - r_3 V_2 \tag{62}$$

$$\frac{dn_{I_3^-}}{dt} = r_3 V_2 \tag{63}$$

The first term on the right-hand side in Eqs. (60) and (61) describes the incorporation of reactants by the growing volume. The other terms on the right-hand side in Eqs. (59) to (63) are reaction terms. r_1, r_2, and r_3 are the reaction rates of reactions (i) – (iii), respectively. The reaction rate r_1 is considered to be infinitely large, whereas the reaction rate r_2 is considered to be dependent on the ionic strength, as presented in detail in chapter 3.2.6.

After inserting the reaction rates, the equation system can be transformed into a dimensionless form (Eqs. (76) – (80)) by using different substitutions (Eqs. (64) – (75)).

$$f_i = \frac{n_i}{n_{H_0^+}} \tag{64}$$

$$\Theta = \frac{t}{t_{mix}} \tag{65}$$

$$g = \frac{V_2(t)}{V_{20}} \tag{66}$$

$$P = \frac{C_{H_2BO_3^-,0}}{C_{H_0^+}} \tag{67}$$

$$Q_1 = \frac{C_{I_0^-}}{C_{H_0^+}} \tag{68}$$

$$Q_2 = \frac{C_{IO_{3,0}^-}}{C_{H_0^+}} \tag{69}$$

$$Da_2 = k_2 t_{mix} C_{H_0^+}^4 \tag{70}$$

$$Da_3 = k_3 t_{mix} C_{H_0^+} \tag{71}$$

$$Da_3' = k_3' t_{mix} \tag{72}$$

$$F_2 = Da_2 \frac{(f_{H^+} f_{I^-})^2 f_{IO_3^-}}{g^4} \tag{73}$$

$$F_3 = Da_3 \frac{f_{I_2} f_{I^-}}{g} \tag{74}$$

$$F_3' = Da_3' f_{I_3^-} \tag{75}$$

Every ordinary differential equation (ODE) must have an initial condition to be solved. The dimensionless time Θ is set to zero. At the very beginning, just protons and no other reagents are located in the Volume V_{20} so that the initial conditions given in Eq. (81) are consistent. With the help of the initial conditions, the ordinary differential equation system can then be solved, e.g. with the help of Matlab, as presented in detail in chapter 5.

$$\frac{df_{H^+}}{d\Theta} = -P\frac{dg}{d\Theta} - 6F_2 \tag{76}$$

$$\frac{df_{I^-}}{d\Theta} = Q_1 \frac{dg}{d\Theta} - 5F_2 - F_3 + F_3' \tag{77}$$

$$\frac{df_{IO_3^-}}{d\Theta} = Q_2 \frac{dg}{d\Theta} - F_2 \tag{78}$$

$$\frac{df_{I_2}}{d\Theta} = 3F_2 - F_3 + F_3' \tag{79}$$

$$\frac{df_{I_3^-}}{d\Theta} = F_3 - F_3' \tag{80}$$

$$\Theta = 0: \quad f_{H^+} = 1\,, \quad f_{I^-} = f_{IO_3^-} = f_{I_2} = f_{I_3^-} = 0 \tag{81}$$

For the IEM model, Eqs. (28) and (29) were used to set up the relevant equations related to the Villermaux-Dushman protocol. The relevant ODEs are given in Eqs. (82) – (86).

$$\frac{dC_{H^+,1}}{dt} = \frac{< C_{H^+} > - C_{H^+,1}}{t_{mix}} - R_{i,1} - 6R_{ii,1} \tag{82}$$

$$\frac{dC_{I^-,1}}{dt} = \frac{< C_{I^-} > - C_{I^-,1}}{t_{mix}} - 5R_{ii,1} - R_{iii,1} \tag{83}$$

$$\frac{dC_{IO_3^-,1}}{dt} = \frac{< C_{IO_3^-} > - C_{IO_3^-,1}}{t_{mix}} - R_{ii,1} \tag{84}$$

$$\frac{dC_{I_2,1}}{dt} = \frac{< C_{I_2} > - C_{I_2,1}}{t_{mix}} + 3R_{ii,1} - R_{iii,1} \tag{85}$$

$$\frac{dC_{I_3^-,1}}{dt} = \frac{< C_{I_3^-} > - C_{I_3^-,1}}{t_{mix}} + R_{iii,1} \tag{86}$$

where R is the reaction rate of the respective species with the indices denoting the corresponding reaction (i to iii) and the considered liquid volume (1 or 2). The equations above all refer to volume (1) while equations for volume (2) are not shown here because they are identical except for different indices. The first term on the right-hand side of Eqs. (82) – (86) describes the increase or the decrease of a species' concentration depending on the difference between its mean concentration and actual concentration. The other terms are again reaction terms where the relevant species is involved. To

transform the ODE-system into a dimensionless form the substitutions used by *Fournier et al.* are used so that the ODE-system given in Eqs. (87) – (91) is obtained (Fournier et al. 1996a).

$$\frac{df_{H^+}}{d\Theta} = < f_{H^+} > - f_{H^+} - < f_{H_2BO_3^-} > - 6Da_2(f_{I^-} - f_{H^+})^2 f_{IO_3^-} \tag{87}$$

$$\frac{df_{I^-}}{d\Theta} = < f_{I_2} > - f_{I_2} - 5Da_2(f_{I^-} - f_{H^+})^2 f_{IO_3^-} - (Da_3 f_{I_2} f_{I^-} - Da_3' f_{I_3^-}) \tag{88}$$

$$\frac{df_{IO_3^-}}{d\Theta} = < f_{IO_3^-} > - f_{IO_3^-} - Da_2(f_{I^-} - f_{H^+})^2 f_{IO_3^-} \tag{89}$$

$$\frac{df_{I_2}}{d\Theta} = < f_{I_2} > - f_{I_2} + 3Da_2(f_{I^-} - f_{H^+})^2 f_{IO_3^-} - (Da_3 f_{I_2} f_{I^-} - Da_3' f_{I_3^-}) \tag{90}$$

$$\frac{df_{I_3^-}}{d\Theta} = Da_3 f_{I_2} f_{I^-} - Da_3' f_{I_3^-} \tag{91}$$

Again, every ODE must have an initial condition to be solved. The dimensionless time Θ is set to zero. In the acidic environment, initially, only protons are present so that the initial conditions are the same as given in Eq. (81). In the buffer environment, there are initially no protons and the initial condition for the dimensionless amounts of iodide and iodate depend on the chosen concentration set.

C.7 Preliminary Investigations on the Choice of Kinetics

In a preliminary investigation on a suitable kinetics model, several approaches were investigated. The resulting sum of squared deviation between experimentally measured X_S values (Fig. 29, FVT-e) and X_S values predicted by twelve different model variants (based on results shown in Fig. 28, FVT-d) for packing configuration E are summarized in Fig. 73. It was differentiated between the linear approach of the incorporation model (Lin), the exponential approach of the incorporation model (Exp), and the IEM model (IEM). Furthermore, with respect to the assumed initial proton concentration, it was differentiated between the assumption of complete dissociation of sulfuric acid at the beginning of the mixing process (CD) and the assumption of incomplete dissociation of sulfuric acid at the beginning of the mixing process (ID). In the latter case, the initial proton concentration was calculated according to Eq. (92) (adapted from *Baqueiro et al.* (Baqueiro et al. 2018)), under the assumption that the first dissociation of sulfuric acid to hydrogen sulfate and protons is complete.

$$C_{H^+} = C_{H_2SO_4} + \frac{-\left(C_{H_2SO_4} + K_{a2}\right) + \sqrt{\left(C_{H_2SO_4} + K_{a2}\right)^2 + \left(4 * K_{a2} * C_{H_2SO_4}\right)}}{2} \qquad (92)$$

where K_{a2} is the second dissociation constant of sulfuric acid ($K_{a2} = 10^{-1.99}$). It should be noted that an incomplete dissociation of sulfuric acid was already considered in the calculation of the revised reaction rate constant k_2 (k2016). Therefore, the number of available protons might be underestimated in the case of additional consideration in the modeling calculations. Finally it was differentiated between the reaction rate constant k_2 suggested by *Guichardon et al.* ((Guichardon et al. 2000), k2000, a function of the ionic strength), the reaction rate constant k_2 suggested by *Guichardon and Ibaseta* ((Guichardon and Ibaseta 2016), k2016, a function of the ionic strength), and a reaction rate constant k_2 fixed at the value of $8.23*10^8$ (k-fixed, independent of the ionic strength of the solution).

Because the lowest sum of squared deviation was obtained for Lin-CD-k2016 and Exp-CD-k2016, these modeling approaches were selected for further investigation in chapter 5.5.2, together with model variant IEM-CD-k2016, for the sake of comparison.

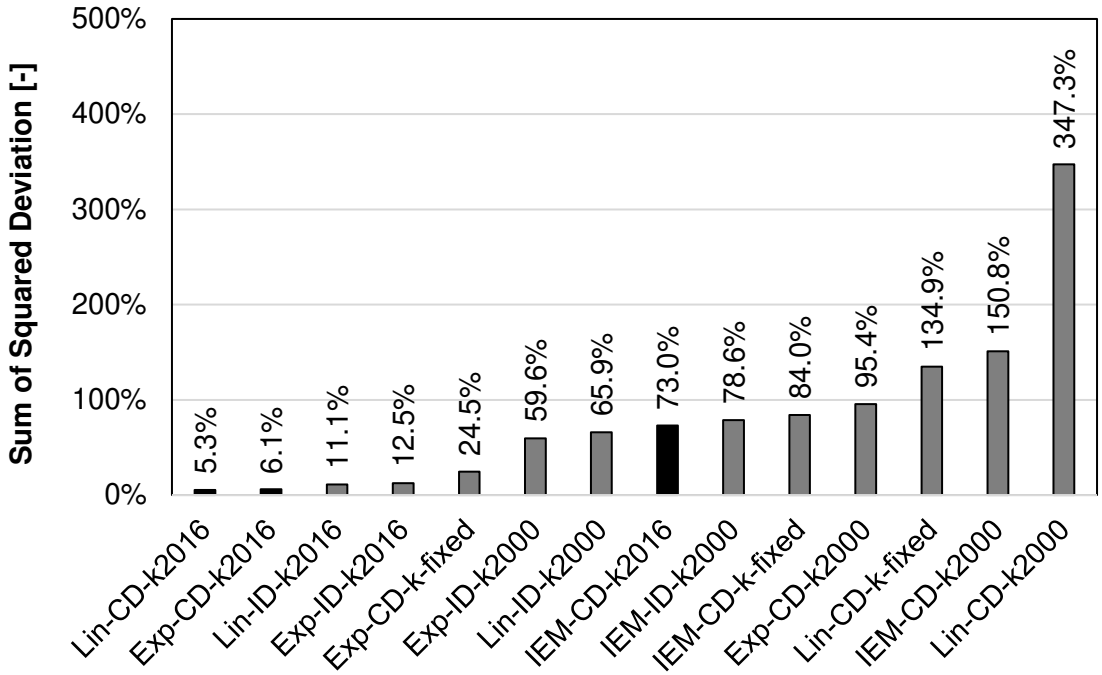

Fig. 73. Sum of squared deviation between experimentally measured X_S values (Fig. 29, FVT-e) and X_S values predicted by twelve different model variants (based on results shown in Fig. 28, FVT-d) for packing configuration E. Model variants investigated further in the chapter 5.5.2 are highlighted in black.

C.8 Schematic Representations

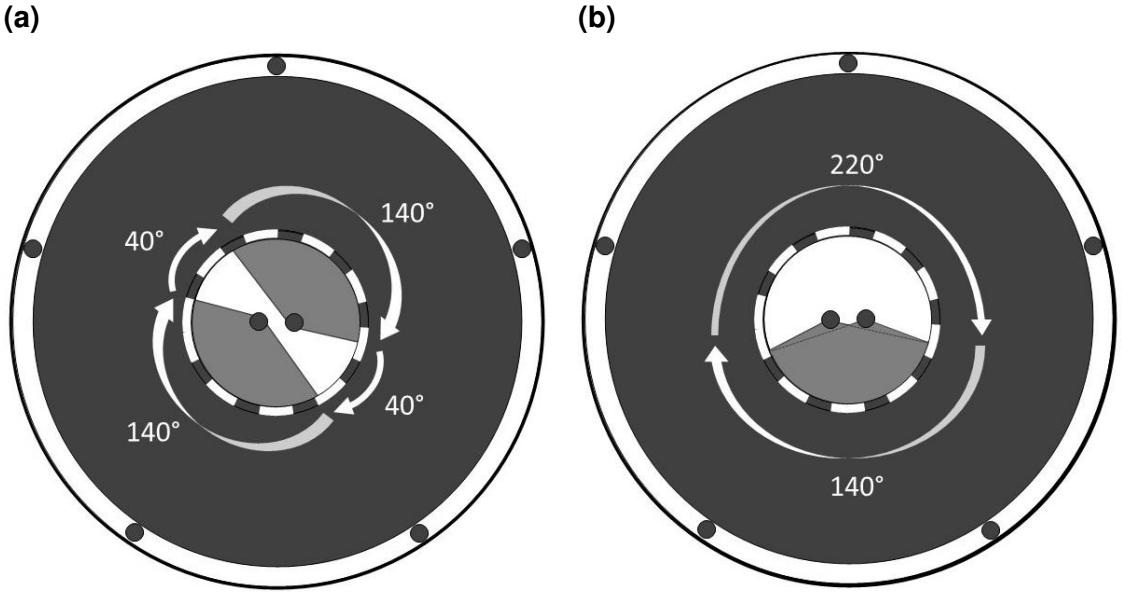

Fig. 74. Schematic representation of the angular distance between the impingement zones for a distribution angle δ = 140°. (a) opposite liquid distribution (φ = 180°); (b) overlapping liquid distribution (φ = 0°).

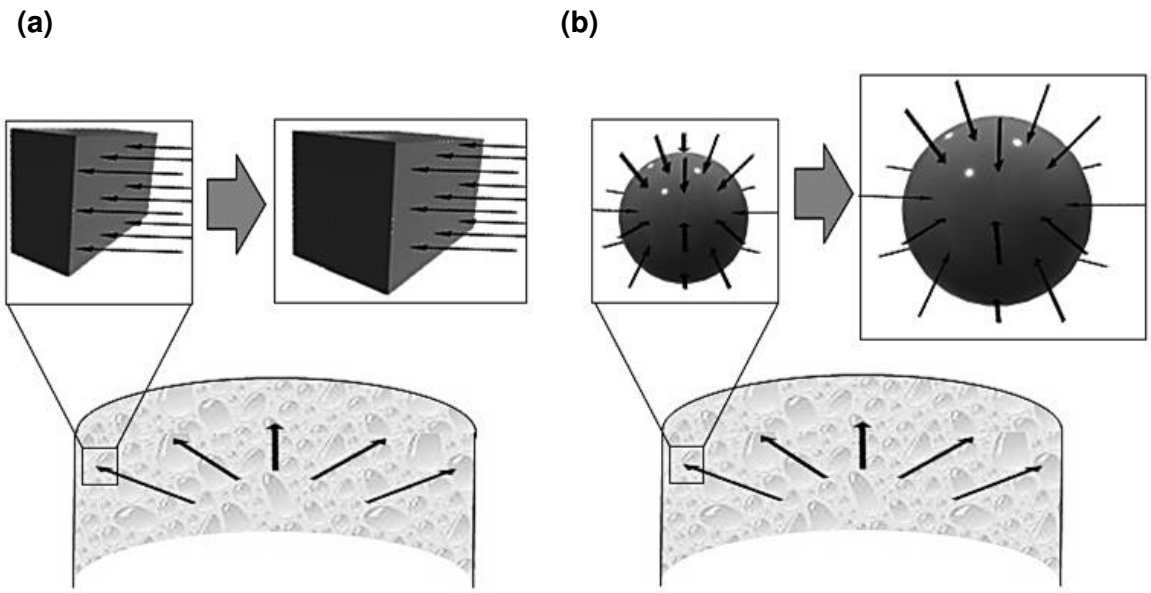

Fig. 75. Schematic representation of growth mechanisms discussed in the modeling section. (a) Two-dimensional growth of liquid aggregates, assumed for larger liquid aggregates, e.g., a film of liquid at the inner packing rim. The surface available for incorporation of additional liquid stays constant over time; (b) Three-dimensional growth of liquid aggregates, assumed for discrete, spherical liquid aggregates, e.g., small droplets at the inner packing rim. The surface available for incorporation of additional liquid increases over time.

D Supporting Information To Chapter 6: Application Case Studies

D.1 MDA Production – Additional Data

Tab. 18. Supplied chemicals used in the MDA experiments.

Chemical	Concentration	Supplier
Aniline	99.7 wt.%	Huntsman Polyurethanes
Formaldehyde	44.0 wt.%	Huntsman Polyurethanes
Hydrochloric acid	37.0 wt.%	Merck

Tab. 19. Overview of the MDA experiments.

Nozzle orientation φ	Circulation flow rate [g min^{-1}]	Formaldehyde flow rate [g min^{-1}]	Rotational speed [rpm]	Total liquid flow rate [l h^{-1}]	Volumetric ratio C/F [-]	RPB start conditions
0°	1000	83	600	64.8	12.4	Cold start
180°	1000	83	600	64.8	12.4	Cold start
180°	1000	83	600	64.8	12.4	Regular
180°	1000	83	1000	64.8	12.4	Regular
180°	1000	83	1200	64.8	12.4	Regular
180°	2000	83	600	124.8	24.8	Regular
180°	3000	83	600	184.8	37.2	Regular
180°	2000	100	600	185.8	31.0	Regular

Tab. 20. Nozzle specifications for the MDA experiments.

Medium	Nozzle
Formaldehyde	Lechler 632.187.16.CA.00.0
Circulation flow (1000 g min^{-1})	Lechler 632.407.16.CA.00.0
Circulation flow (2000 – 3000 g min^{-1})	Lechler 632.567.16.CA.00.0

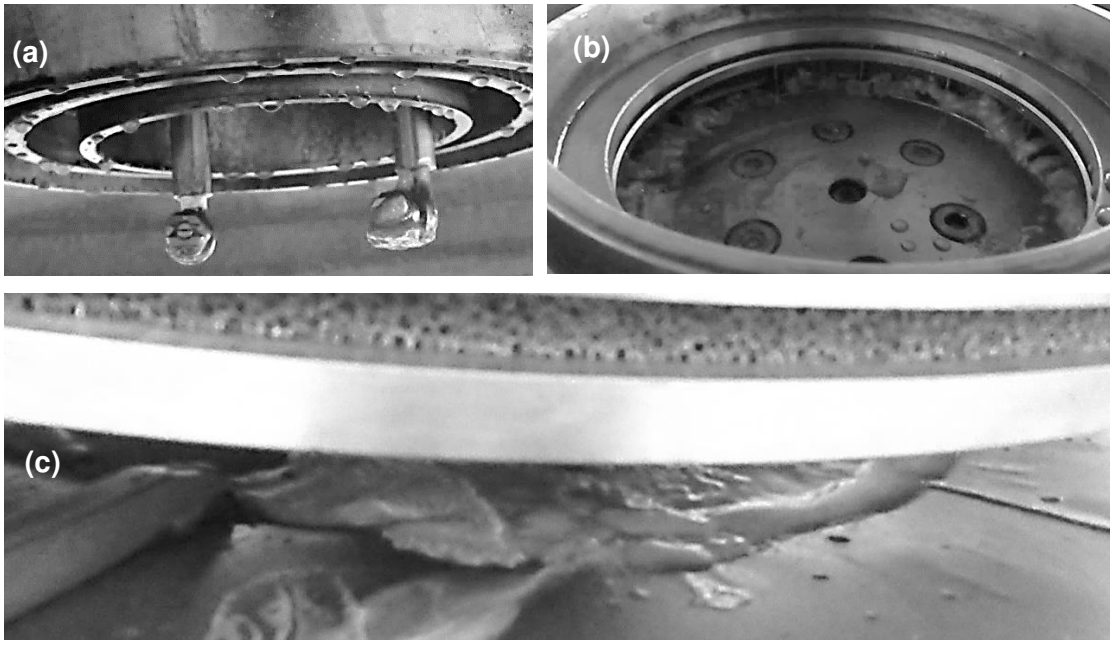

Fig. 76. Fouling observed for an overlapping nozzle orientation (φ = 0°).
(a) Distribution nozzles; (b) Eye ring; (c) RPB casing bottom and liquid outlets.

D.2 MDI Production

During the MDI production, the previously formed MDA reacts with phosgene ($COCl_2$) to form isocyanate, releasing hydrochloride. This phosgenation reaction can be carried out in the liquid or the gas phase and is the most efficient method for a large scale production of isocyanates (Six et al. 2003). Alternative phosgene-free routes, using e.g. carbamate intermediates, are being explored but have not yet reached the same industrial acceptance (Six et al. 2003; van den Berg et al. 2012). Generally, one reactant stream containing an inert organic solvent and the amines are mixed with a second reactant stream containing an excess amount of phosgene. This excess phosgene is necessary to prevent the formation of undesired solid by-products. While gas phase phosgenation offers high selectivity, low phosgene hold-up, and reduced energy demand, it is under practical terms restricted with respect to the workable MDA specifications. In contrast, the reaction can be performed at lower temperatures and without vapourization step with a liquid phase phosgenation (Leschinski et al. 2012). The use of spray nozzles for the distribution of the liquid stream into the center of the rotating packing has been reported to possibly combine the advantages of gas phase and liquid phase phosgenation (Leschinski et al. 2012). Furthermore, applying an RPB to the phosgenation of amines was found to be beneficial, as intensified mass transfer and micromixing allow for the reduction of the amount of solvent and excess phosgene necessary, as well as for a reduced overall energy consumption (Ding et al. 2007a). Despite these benefits, only Yantai Wanhua Polyurethane Co., Ltd, China, one of the largest producers of MDI worldwide (Gal 2012), has reported on the industrial application of RPBs to their MDI production so far. The company has filed patents for both the condensation reaction (Ding et al. 2007b), i.e., the production of MDA, and the phosgenation reaction (Ding et al. 2007a) in RPBs. Based on the application of their RPBs, Yantai Wanhua was reportedly able to increase their MDI production capacity by 50 % from 160,000 to 240,000 metric tons per year (Zhao et al. 2010). At the same time, they claim to have reduced their energy consumption by 20 % and the impurity content of the produced MDI by 30 % (Chen 2009). However, as no details on previous production methods or absolute numbers have been published, the significance of these claims remains vague. In addition, BASF SE (Germany) has filed a patent for the phosgenation of amines in RPBs, where poly- and diamines, for example, such formed in the condensation reaction, could be supplied to an RPB in a liquid stream and brought into contact with phosgene in a gaseous stream (Leschinski et al. 2012). However, no application of this technology on one of their production sites has been publicly communicated so far.

D.3 IIR Production

Another promising application of RPBs for liquid phase reactive mixing is the production of IIR, also called butyl rubber. IIR is a copolymer made from 98.0 wt.% to 98.5 wt.% isobutylene (C_4H_8) units and 1.5 – 2.0 wt.% isoprene (C_5H_8) units (Chen et al. 2009). In order to obtain IIR, a cationic copolymerization between isobutene and isoprene is conducted in liquid chloromethane (CH_3Cl) in the presence of a Friedel-Crafts catalyst, usually aluminum chloride ($AlCl_3$) (Sangalov et al. 2001). Furthermore, this reaction has to run at very low temperatures of around −100°C in order to achieve high molecular weights, which are mandatory for a satisfactory strength of the material (Sangalov et al. 2001). However, while preferably operated at low temperatures, the reaction itself is strongly exothermic. Therefore, excellent heat and mass transfer within the reactor, and especially between the coolant and the reacting liquid phase, are necessary (Zhao et al. 2010). Furthermore, with a reaction rate constant of the polymerization in the range of $10^{5 \pm 1}$ l mol^{-1} s^{-1}, a reactor with an excellent micromixing performance is needed, in order to have a homogenous reaction volume and thus full control over the obtained molecular weight distribution (Chen et al. 2009). While the estimated micromixing times in STRs are in the range of 10^1 ms to 10^2 ms, micromixing times in the order of 10^{-1} ms can be achieved with rotating reactors as SDR and RPBs ((Visscher et al. 2013), Chapter 5.6). Furthermore, the conventional production process in an STR has a mean residence time of 30 min to 60 min, while the mean residence time for the process in an RPB was reportedly reduced to values below one second (Chen et al. 2009). Within this time, a mean molecular weight of 289,000 g mol^{-1}, a low unimodal molecular weight distribution of 1.99, and a single pass conversion of 30 % could be obtained under optimum operating conditions at 1200 rpm and −100°C (Chen et al. 2009) in the pilot plant setup schematically drawn in Fig. 77 (adapted from *Chen et al.* (Chen et al. 2010)). The RPB in this pilot plant had an outer rotor diameter of 258 mm, an inner packing diameter of 150 mm, and an axial height of 50 mm, equipped with wire mesh packing (Chen 2009). The monomers were premixed in concentrations of 2.7 mol l^{-1} isobutylene and 0.05 mol l^{-1} isoprene, while the concentration of the catalyst $AlCl_3$ was adjusted to be 0.011 mol l^{-1}. The two liquid streams were then pumped into the RPB at a volumetric ratio of monomer to catalyst of 10:1 (Chen et al. 2009). In accordance with these results, it was estimated that the production capacity per unit volume can be increased by 2 to 3 orders of magnitude by using RPBs instead of STRs (Chen et al. 2009). Furthermore, the authors demonstrated that the molecular weight could be adjusted as a function of the rotational speed of the RPB: at −100°C, the mean molecular weight increased from 160,000 g mol^{-1} at 600 rpm to 289,000 g mol^{-1} at 1200 rpm. Above this rotational speed, however, the mean molecular weight stayed constant. In an additional study, it

was shown that the consecutive bromination process of IIR could also be intensified in an RPB. Due to the intense micromixing, the production time for high quality brominated IIR could be reduced from 5 min in the conventionally used STR to 2 min in an RPB (Wang et al. 2014). At the same time, the conversion, with respect to 1,4-isoprene, was increased from 80.2 % to 82.6 %, while the selectivity increased from 91.2 % to 91.9 % (Wang et al. 2014). The horizontal-axis RPB used for this process had a radial packing depth of 50 mm, an axial height of 53 mm, and a casing volume of 3 l. The total liquid flow rate of the two introduced solutions was 33 l h^{-1}, at a volumetric ratio of IIR to bromine (Br_2) of 10:1 (Wang et al. 2014).

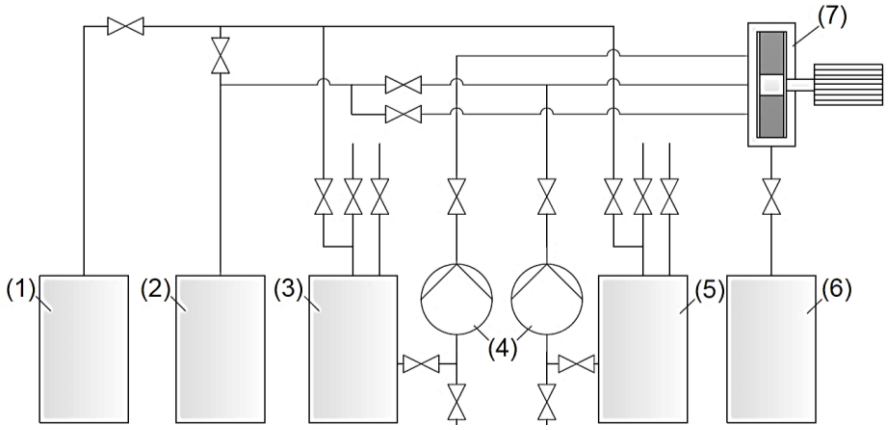

Fig. 77. Schematic diagram for pilot plant setup for IIR production; (1) nitrogen cylinder, (2) coolant tank, (3) isobutylene, isoprene and dichloromethane tank, (4) metering pumps, (5) aluminum trichloride and dichloromethane tank, (6) IIR tank, (7) RPB. Adapted from *Chen et al.* (Chen et al. 2010).

D.4 Liquid-Liquid Extraction – Additional Data

Tab. 21. Chemicals utilized for the liquid-liquid extraction of GVL in chapter 6.3.

Chemicals	Supplier
GVL	Sigma-Aldrich (St. Louis, USA)
Butyl acetate	Sigma-Aldrich (St. Louis, USA)
Acetonitrile	VWR chemicals (Radnor, USA)
Helium	Messer (Bad Soden am Taunus, Germany)
Synthetic air	Messer (Bad Soden am Taunus, Germany)
Hydrogen	Messer (Bad Soden am Taunus, Germany)

Tab. 22. Exemplary data points of the phase equilibrium of water (H_2O), butyl acetate (ButA) and GVL at 22 °C on the outer regression curve of the miscibility gap binodal) shown in Fig. 44, as well as the corresponding solvent capacities K_S and selectivities $S_{S/C}$ along the tie lines, with respect to the solute GVL and the carrier H_2O.

x^R_{H2O} [-]	x^R_{ButA} [-]	x^R_{GVL} [-]	x^E_{H2O} [-]	x^E_{ButA} [-]	x^E_{GVL} [-]	K_{GVL} [-]	S_{GVL/H_2O} [-]
0.999	0.001	0.000	0.156	0.844	0.000	-	-
0.980	0.001	0.019	0.201	0.603	0.196	10.3	50.3
0.965	0.001	0.034	0.250	0.394	0.356	10.5	40.4
0.951	0.002	0.048	0.321	0.250	0.430	9.0	26.5
0.944	0.002	0.053	0.375	0.196	0.429	8.1	20.4
0.936	0.003	0.061	0.423	0.152	0.425	7.0	15.4
0.932	0.003	0.066	0.447	0.134	0.419	6.3	13.2
0.899	0.005	0.096	0.575	0.067	0.358	3.7	5.8
0.901	0.005	0.094	0.582	0.066	0.352	3.7	5.8
0.895	0.005	0.100	0.591	0.062	0.347	3.5	5.3
0.886	0.006	0.108	0.610	0.056	0.334	3.1	4.5

Tab. 23. Molar flow rates and compositions of the concept process presented in chapter 6.3. Exemplary feed composition obtained from *Murat Sen et al.* (Murat Sen et al. 2012).

	$\dot{n}_{GVL}$ [kmol h^{-1}]	$\dot{n}_{H2O}$ [kmol h^{-1}]	$\dot{n}_{ButA}$ [kmol h^{-1}]	$\dot{n}_{total}$ [kmol h^{-1}]
Feed	31.71	229.12	0.00	260.83
Solvent	0.00	0.00	20.00	20.00
	x_{GVL} [-]	x_{H2O} [-]	x_{ButA} [-]	Σx_i[-]
Feed	0.122	0.878	0.000	1.000
Solvent	0.000	0.000	1.000	1.000

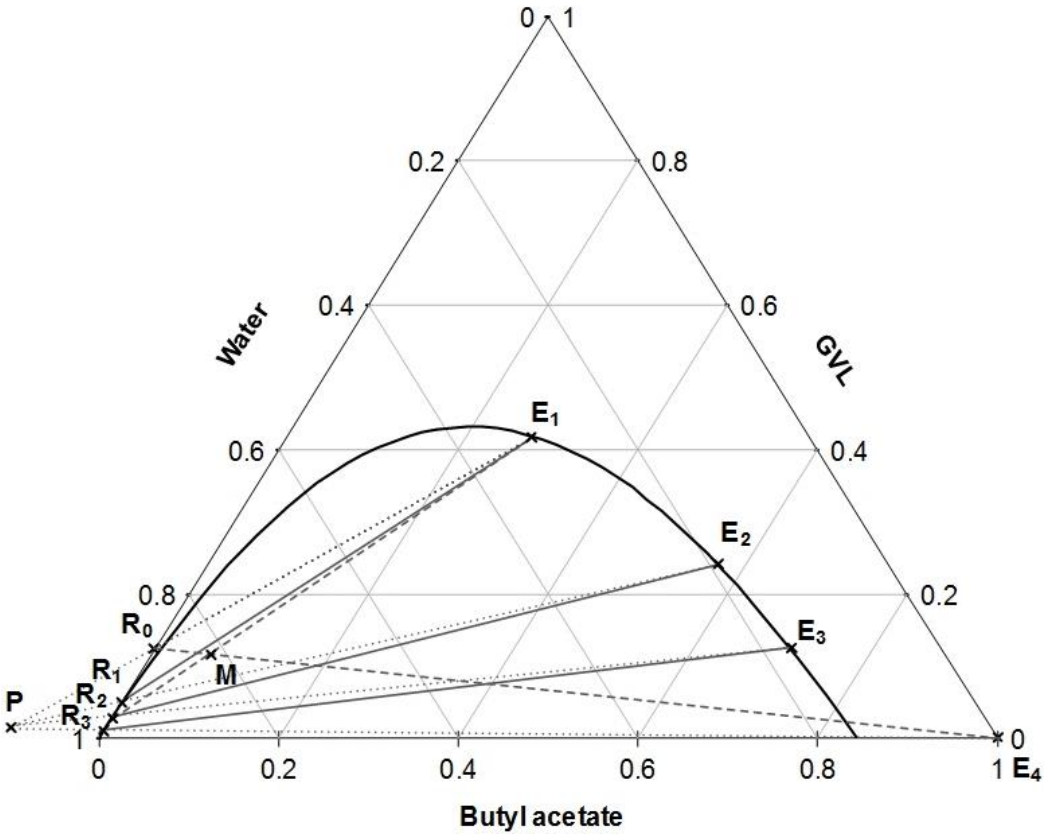

Fig. 78. Stage construction of the three-stage countercurrent concept process for the extraction of GVL from water-rich feed with pure butyl acetate as solvent at 22°C. Raffinate and extract compositions are given as R0 to R3 and E1 to E4, respectively. The mixing point is denoted as M and the pole point is denoted as P. Konodes are given as full lines, helping lines of the mixing point construction are given as dashed lines, and helping lines of the pole construction are given as dotted lines.

D.5 Liquid-Gas Processing – Additional Data

Tab. 24. Specifications of the Andritz RPB used for liquid-gas processing of vegetable oil in chapter 6.4. Further details and dimensions are given in chapter 2.4.

Parameter	**Value**
Manufacturer	Andritz AG, Graz, Austria
Casing	
Casing outer diameter	256 mm
Casing height	160 mm
Rotor	
Rotor type	Centrifuge Basket
Rotor outer diameter	160 mm
Rotor inner diameter	100 mm
Packing	
Packing type	Wire mesh
Packing specific surface area	2983 $m^2\ m^{-3}$
Packing voidage	91.5 %
Packing outer diameter	152 mm
Packing inner diameter	100 mm
Radial packing depth	26 mm
Axial packing height	50 mm

Tab. 25. Specifications of the nozzle used for liquid-gas processing of vegetable oil.

Medium	**Nozzle**
Vegetable oil	Lechler 544.200.16.CA.00.2

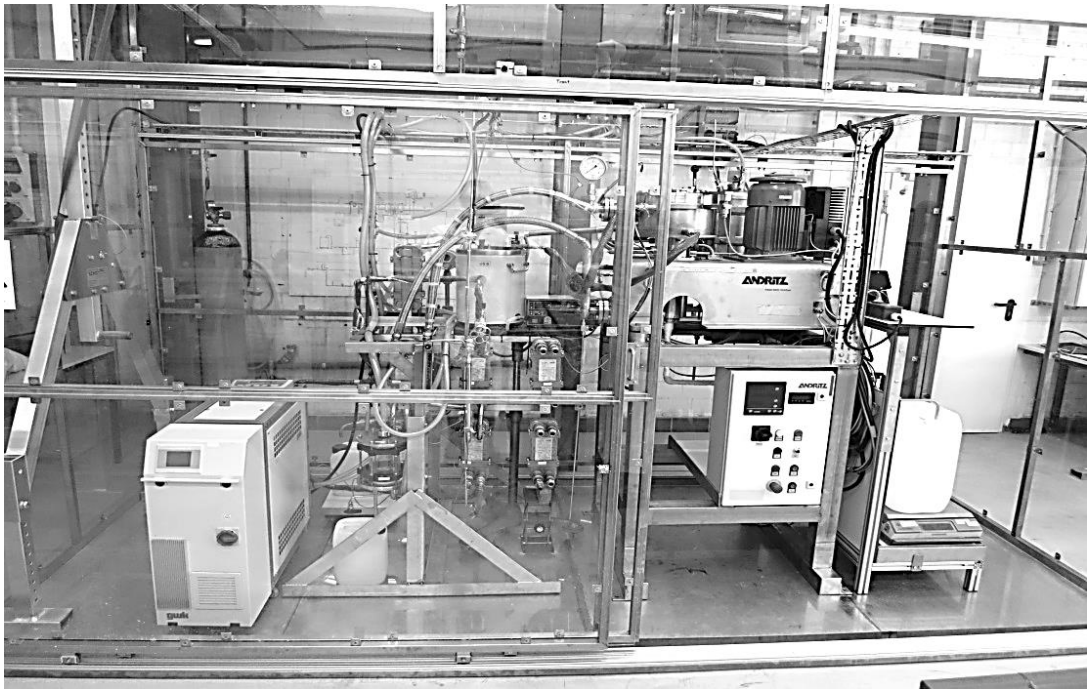

Fig. 79. Photography of the experimental setup used for liquid-gas processing of vegetable oil.

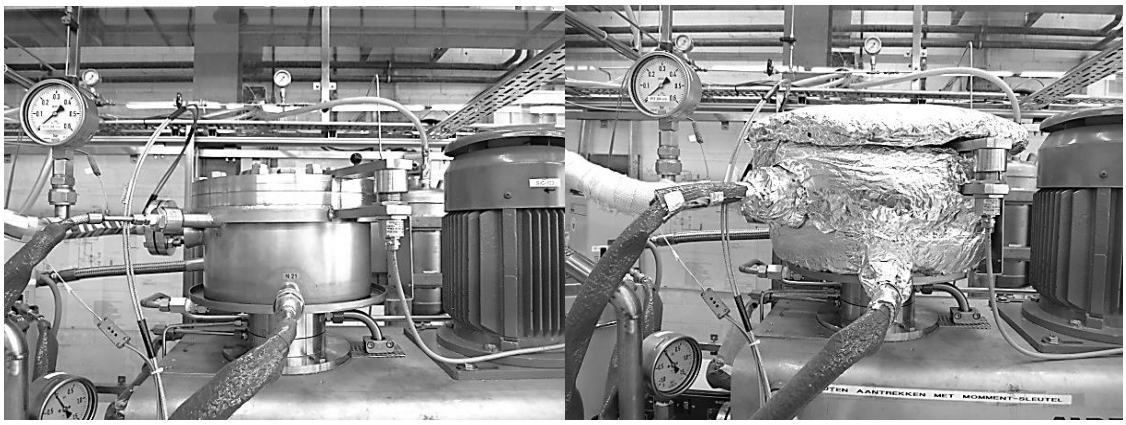

Fig. 80. Photography of the un-insolated (left) and insolated (right) RPB used for liquid-gas processing of vegetable oil.

Tab. 26: Temperatures of the stripping gas and the vegetable oil during the experiments presented in chapter 6.4. Values are given as the average value of all experimental runs ± sample standard deviation.

Sample point	**Temperature [°C]**
Experiments at a mantle heating temperature of **150°C**	
Stripping gas (RPB inlet)	141.7 ± 3.2
Stripping gas (After H1.5)	27.7 ± 1.3
Vegetable oil (RPB inlet)	176.3 ± 1.1
Vegetable oil (After H2.3)	23.7 ± 0.7
Experiments at a mantle heating temperature of **180°C**	
Stripping gas (RPB inlet)	146.1 ± 1.1
Stripping gas (After H1.5)	23.7 ± 0.4
Vegetable oil (RPB inlet)	178.3 ± 0.4
Vegetable oil (After H2.3)	19.3 ± 1.4

E Supporting Information To Chapter 7: Recommendations

Tab. 27. Definitions of the Technology Readiness Levels. Adapted from *Mankins* (Mankins 1995).

TRL	Description
1	Basic principles observed and reported
2	Technology concept and/or application formulated
3	Successful proof-of-concept
4	Components of the technology implemented and successfully tested in a laboratory environment
5	Components of the technology implemented and successfully tested in a relevant environment
6	Complete technology fully tested and validated in a laboratory environment
7	Complete technology fully tested and validated in a relevant environment (prototype, i.e. pilot plant)
8	Successful industrial application of technology
9	Successful long-term industrial application of technology, showing adequate performance and reliability (Proven technology)

PUBLICATIONS

Peer-reviewed paper
Reactive mixing in rotating packed beds: on the packing's role and mixing modeling (2019); Wenzel, D.; Nolte, K.; Górak, A.; Chem. Eng. Proc.: P.I. (143), published online, doi: 10.1016/j.cep.2019.107596
Liquid Distribution and Mixing in Rotating Packed Beds (2019); Wenzel, D.; Ojeda, L.S.; Gerdes, N.; Steinbrink, M.; Górak, A.; Ind. Eng. Chem. Res. 58 (15), pp. 5919-5928
On the Reactant Concentration and the Reaction Kinetics in the Villermaux-Dushman Protocol (2018); Wenzel, D.; Assirelli, M.; Rossen, H.; Lopattschenko, M.; Górak, A.; Chem. Eng. Proc.: P.I. (130), pp. 332-341
Review and Analysis of Micromixing in Rotating Packed Beds (2018), Wenzel, D.; Górak, A.; Chem. Eng. J. (345), pp. 492-506
A guide on the industrial application of rotating packed beds (2018), Neumann, K.; Gladyszewski, K.; Groß, K.; Qammar, H.; Wenzel, D.; Górak, A.; Skiborowski, M.; Chem. Eng. Res. Des. 134, pp. 443-462
Aqueous food-grade and cosmetic-grade surfactant systems for the continuous countercurrent cloud point extraction (2018), Racheva, R.; Rahlf, A.; Wenzel, D.; Müller, C.; Kerner, M.; Luinstra, G.; Smirnova, I.; Sep. Pur. Tech. 202 (2018), pp. 76-85

Patents
Rotierender Ring Reaktor (2019), Wenzel, D.; Górak, A; Application Nr.: DE102017119569A1

Oral and poster presentations
Wenzel, D.; Górak, A., “Rotating Packed Beds: Ein innovatives, modulares und flexibles Mischer-Konzept”, Presentation at Jahrestreffen der ProcessNet Fachgruppen Wärme- und Stoffübertragung, Trocknungstechnik und Mischvorgänge (2019), Essen, Germany
Wenzel, D.; Assirelli, M.; Górak, A., "Liquid Mixing in a Rotating Packed Bed Pilot Plant", Presentation at Mixing XXVI - North American Mixing Forum (NAMF) (2018), San Juan, Puerto Rico
Wenzel, D.; Skiborowski, M.; Górak, A., "Application of Rotating Packed Beds to Liquid Phase Processes", Presentation at 10th World Congress of Chemical Engineering (2017), Barcelona, Spain
Groß, K.; Neumann, K.; Qammar, H.; Wenzel, D., "Current Status of Rotating Packed Beds (RPBs): Applications in Chemical Industry", Poster at Jahrestreffen der ProcessNet Fachgruppen Fluidverfahrenstechnik und Membrantechnik (2017), Köln, Germany
Groß, K.; Wenzel, D.; Neumann, K.; Skiborowski, M.; Górak, A., "Rotating Packed Beds - Vorteile und Herausforderungen", Presentation at Jahrestreffen der ProcessNet-Fachgemeinschaft "Prozess-, Apparate- und Anlagentechnik" 2016 (2016), Karlsruhe, Germany

SUPERVISED THESES AND INTERNSHIPS

Bachelor theses
Rossen, H. F. (2017): Untersuchungen zum Einfluss der Pufferzusammensetzung auf die Segregationsbestimmung innerhalb eines modifizierten Villermaux-Dusham-Protokolls, TU Dortmund University
Lopattschenko, M. (2017): Untersuchungen zur Verwendung verschiedener Säuren innerhalb eines modifizierten Villermaux-Dushman-Protokolls, TU Dortmund University
Steinbrink, M. (2017): Untersuchungen zur Durchmiscung von Flüssigkeiten innerhalb eines Rotating Packed Beds, TU Dortmund University
Bredehorn, E. (2017): Untersuchungen zum Einfluss von Design- und Betriebsparametern auf die Mikrovermischung in Rotating Packed Beds, TU Dortmund University
Minor, A.-J.(2018): Untersuchungen zur Flüssig-Flüssig-Extraktion einer biobasierten Plattformchemikalie, TU Dortmund University
Pyka, T. (2018): Inbetriebnahme und Charakterisierung eines Rotating Packed Beds für Gas-Flüssig-Prozesse, TU Dortmund University

Master theses
Nolte, K. (2018): Modellierung der Durchmischung von Flüssigkeitsströmen innerhalb eines Rotating Packed Beds, TU Dortmund University

Internships
Steinbrink, M. (01/2017): Vertiefungspraktikum „Villermaux-Dushman-Protokoll“, TU Dortmund University
Ojeda, L.S. (07/2017 – 08/2017): DAAD Research Internships in Science and Engineering (RISE), TU Dortmund University
Gerdes, N. (01/2018): Vertiefungspraktikum „Rotating Packed Beds“, TU Dortmund University

DECLARATION

Contents of this thesis were acquired in cooperation with ISPT (Institute for Sustainable Process Technology) within the scope of the research project ImPaCCt (Improved Process Performance by Process Intensification in Centrifugal Contactors).
Parts of this work have been published and have been presented by the author or partly contain measured data evolved from supervised student theses at the Laboratory of Fluid Separations, Faculty of Biochemical and Chemical Engineering, TU Dortmund University. Detailed information is given below.

Chapter	Subchapter	Content	Scientific work
1	1.1	Partly adapted/modified from	A), C), F)
2	2.1-2.2	Partly adapted/modified from	A), C), F)
3	3.1-3.2	Partly adapted/modified from	A), B), C)
	3.3-3.5	Partly adapted/modified from	B)
	3.4	Measured experimental data partly from	a), b)
4	4.1-4.2	Partly adapted/modified from	A), C), F)
	4.3-4.5	Partly adapted/modified from	A)
5	5.1-5.2	Partly adapted/modified from	A), C), F)
	5.3	Partly adapted/modified from	C), F)
	5.4	Measured experimental data partly from	c), d), g)
	5.4-5.5	Partly adapted/modified from	C), F)
	5.6	Partly adapted/modified from	A), C), F)
	5.7	Partly adapted/modified from	C), F)
6	6.1-6.2	Partly adapted/modified from	D)
	6.3	Measured experimental data partly from	e)
	6.4	Measured experimental data partly from	f)
7	7.4	Partly adapted/modified from	D)
	7.5	Partly adapted/modified from	E), F)
8	8.1-8.2	Partly adapted/modified from	A), B), C), F)

Appendix	Subchapter	Content	Scientific work
A		Partly adapted/modified from	B)
B		Partly adapted/modified from	A)
C	C.1-C.4	Partly adapted/modified from	C), F)
	C.4	Measured experimental data partly from	c), d), g)
	C.5	Measured experimental data partly from	c), g)
	C.6-C.8	Partly adapted/modified from	F)
D	D.2-D.3	Partly adapted/modified from	D)
	D.4	Measured experimental data partly from	e)
	D.5	Measured experimental data partly from	f)
E		Partly adapted/modified from	D)

Publications	
A)	Review and Analysis of Micromixing in Rotating Packed Beds (2018), Wenzel, D.; Górak, A.; Chem. Eng. J. (345), pp. 492-506
B)	On the Reactant Concentration and the Reaction Kinetics in the Villermaux-Dushman Protocol (2018); Wenzel, D.; Assirelli, M.; Rossen, H.; Lopattschenko, M.; Górak, A.; Chem. Eng. Proc.: P.I. (130), pp. 332-341
C)	Liquid Distribution and Mixing in Rotating Packed Beds (2019); Wenzel, D.; Ojeda, L.S.; Gerdes, N.; Steinbrink, M.; Górak, A.; Ind. Eng. Chem. Res. 58 (15), pp. 5919-5928
D)	A guide on the industrial application of rotating packed beds (2018), Neumann, K.; Gladyszewski, K.; Groß, K.; Qammar, H.; Wenzel, D.; Górak, A.; Skiborowski, M.; Chem. Eng. Res. Des. 134, pp. 443-462
E)	Rotierender Ring Reaktor (2019), Wenzel, D.; Górak, A; Application Nr.: DE102017119569A1
F)	Reactive mixing in rotating packed beds: on the packing's role and mixing modeling (2019); Wenzel, D.; Nolte, K.; Górak, A.; Chem. Eng. Proc.: P.I. (143), published online, doi: 10.1016/j.cep.2019.107596
Student theses	

a)	Rossen, H. F. (2017): Untersuchungen zum Einfluss der Pufferzusammensetzung auf die Segregationsbestimmung innerhalb eines modifizierten Villermaux-Dusham-Protokolls, TU Dortmund University
b)	Lopattschenko, M. (2017): Untersuchungen zur Verwendung verschiedener Säuren innerhalb eines modifizierten Villermaux-Dushman-Protokolls, TU Dortmund University
c)	Steinbrink, M. (2017): Untersuchungen zur Durchmischung von Flüssigkeiten innerhalb eines Rotating Packed Beds, TU Dortmund University
d)	Bredehorn, E. (2017): Untersuchungen zum Einfluss von Design- und Betriebsparametern auf die Mikrovermischung in Rotating Packed Beds, TU Dortmund University
e)	Minor, A.-J.(2018): Untersuchungen zur Flüssig-Flüssig-Extraktion einer biobasierten Plattformchemikalie, TU Dortmund University.
f)	Pyka, T. (2018): Inbetriebnahme und Charakterisierung eines Rotating Packed Beds für Gas-Flüssig-Prozesse, TU Dortmund University
g)	Nolte, K. (2018): Modellierung der Durchmischung von Flüssigkeitsströmen innerhalb eines Rotating Packed Beds, TU Dortmund University